Dissertation

submitted to the

Combined Faculty of Mathematics, Engineering and Natural Sciences

of Heidelberg University, Germany

for the degree of

Doctor of Natural Sciences

Put forward by

M.Sc. Felix Klaus Ahrens

born in: Viernheim (Germany)

Oral examination: 28 July 2022

Cryogenic read-out system and resonator optimisation for the microwave SQUID multiplexer within the ECHo experiment

Referees: Prof. Dr. Christian Enss
Prof. Dr. Peter Fischer

Abstract

The framework of this thesis is the development of a dedicated microwave SQUID multiplexing read-out system for the ECHo experiment, which aims at the investigation of the effective electron neutrino mass by means of arrays of magnetic microcalorimeters implanted with ^{163}Ho. The first part of this work is focused on the development of the cryogenic microwave read-out system to read out about 6000 microwave SQUID multiplexer (µMUX) channels. Based on simulations employing a developed software package, the best configuration in terms of noise performance, system linearity and power dissipation has been found. A demonstration system has been set up and its conformity with the design targets has been proven experimentally, in particular a system noise temperature of about 4 K could be demonstrated. The second part of this thesis is dedicated to pinpoint the optimal resonator geometry for the µMUX. For the well-established coplanar waveguide (CPW) resonators, an innovative resonance frequency fine-tuning technique has been introduced and demonstrated for the first time, yielding more than a factor of five of improvement in the accuracy of the resonance frequency spacing between neighbouring resonators. Lumped element resonators (LERs), on the other hand, feature a more compact design and an LER-based µMUX theoretically exhibits a better noise performance than a CPW-based µMUX. However, a white magnetic flux noise level of $\sim 0.2\,\mu\Phi_0/\sqrt{\text{Hz}}$ for CPW-based µMUX and $\sim 0.6\,\mu\Phi_0/\sqrt{\text{Hz}}$ for LER-based µMUX has been measured. The difference could be traced back to additional loss mechanisms in the LER accidentally occurring for the investigated devices. A rescaling compensating for these losses reveals a potential white magnetic flux noise level of $\sim 0.2\,\mu\Phi_0/\sqrt{\text{Hz}}$ for both resonator geometries.

Kryogenes Auslesesystem und Resonatoroptimierung für den Mikrowellen-SQUID-Multiplexer innerhalb des ECHo-Experiments

Den Rahmen dieser Arbeit bildet die Entwicklung eines auf Mikrowellen-SQUID-Multiplexern basierenden Auslesesystems für das ECHo-Experiment. Das Ziel des ECHo-Experiments ist die Untersuchung der effektiven Elektron-Neutrinomasse mithilfe von Detektorarrays, die aus mit ^{163}Ho implantierten magnetischen Mikrokalorimetern aufgebaut sind. Der erste Teil der vorliegenden Arbeit ist der Entwicklung eines kryogenen Auslesesystems gewidmet, welches etwa 6000 Mikrowellen-SQUID-Multiplexer-Kanäle auslesen soll. Basierend auf Simulationen mithilfe eines speziell für diesen Zweck entwickelten Software-Pakets wurde der beste Aufbau in Bezug auf das Rauschen, auf die Linearität des Systems und auf die Leistungsdissipation gefunden. Ein Demonstrator wurde aufgebaut und die Konformität mit den angestrebten Entwurfswerten wurde experimentell bestätigt, insbesondere eine Rauschtemperatur von etwa 4 K konnte demonstriert werden. Der zweite Teil der vorliegenden Arbeit konzentriert sich auf die Bestimmung der optimalen Resonatorgeometrie für den Mikrowellen-SQUID-Multiplexer (µMUX). Für die bereits etablierten koplanaren Leitungsresonatoren (CPW) wurde eine innovative Methode zur Anpassung der Resonanzfrequenz erstmalig eingeführt und demonstriert. Dabei konnte die Genauigkeit, mit der der Abstand zwischen benachbarten Resonanzfrequenzen eingestellt werden kann, um mehr als einen Faktor fünf verbessert werden. Resonatoren, die aus konzentrierten Elementen aufgebaut sind (LER), sind deutlich kompakter als CPW-Resonatoren. Zusätzlich weist ein LER-basierter µMUX zumindest theoretisch ein geringeres Rauschniveau auf als ein CPW-basierter µMUX. Es konnte jedoch ein weißes Flussrauschen von $\sim 0.2\,\mu\Phi_0/\sqrt{\text{Hz}}$ für CPW-basierte µMUX-Kanäle und ein weißes Flussrauschen von $\sim 0.6\,\mu\Phi_0/\sqrt{\text{Hz}}$ für LER-basierte µMUX-Kanäle gemessen werden. Dieser Unterschied konnte auf zusätzliche Verlustmechanismen zurückgeführt werden, die unbeabsichtigt in den LER-basierten µMUX-Kanälen auftraten. Eine Reskalierung, die die Verlustmechanismen kompensiert, ergab, dass potentiell mit beiden Resonatorgeometrien ein weißes Flussrauschen von $\sim 0.2\,\mu\Phi_0/\sqrt{\text{Hz}}$ möglich sein sollte.

Contents

1. Introduction

Concluding his lecture with the title "The Schrödinger Equation in a Classical Context: A Seminar on Superconductivity" [Fey63], Richard Feynman observed:

'These then are some illustrations of things that are happening in modern times — the transistor, the laser, and now these [Josephson] junctions, whose ultimate practical applications are still not known. The quantum mechanics which was discovered in 1926 has had nearly 40 years of development, and rather suddenly it has begun to be exploited in many practical and real ways. We are really getting control of nature on a very delicate and beautiful level.'

In fact, the invention of the transistor opened the way for the development of modern semiconductor digital electronics, starting in the 40s of the 20th century. Already in 1926, Julius Edgar Lilienfeld introduced the concept of a *field-effect transistor* (FET) [Lil26], but the first practical transistor device was developed in 1947 by John Bardeen and Walter Brattain at Bell Labs [Bar48], earning them the Nobel prize in physics in 1956.

A somewhat parallel chain of events occurred in the second half of the 20th century, when in 1962 Brian David Josephson proposed a theoretical model for the nowadays so-called Josephson effects, which occur when Cooper pairs tunnel through a barrier between two superconductors named *Josephson junction* after him [Jos62]. Only one year later, at Bell Labs, Philip Anderson and John Rowell performed the first experimental observation of the Josephson tunnel effect [And63] and in 1973 Josephson received the Nobel prize for his prediction.

The Josephson junction is the elementary building block for superconducting electronics, analogously to the role of transistors in semiconductor electronics. Various applications in the field of superconducting electronics have been explored and developed after Josephson's discovery, starting from the invention of *superconducting quantum interference devices* (SQUIDs) [Jak64] and the *rapid single flux quantum* (RSFQ) devices [Lik91], for example. In the last years, the field of quantum technologies based on superconducting electronics is growing exponentially, with important developments towards superconducting quantum computing [Cas17, Nis07, Aru19], microwave amplifiers with quantum-limited noise performance [Esp21] and the multiplexed read-out of cryogenic detectors.

High-resolution cryogenic detectors, such as *transition edge sensors* (TESs) or *mag-*

netic microcalorimeters (MMCs), can be read out by coupling them to a dc SQUID, often employing the so called two-stage set-up [Cla04] to improve the noise performance. This is an efficient read-out strategy as long as the number of detectors is kept low. In the last decade, however, the challenge faced by research groups developing such detectors has progressively shifted from the optimisation of single detector pixels towards the integration of a high number of pixels into detector arrays [Fav20]. A dc SQUID based read-out system with individual wiring becomes unfeasible when dealing with large detector arrays comprising $\geq \mathcal{O}(10^2)$ detectors. On the one hand, the total power dissipated by a large number of dc SQUIDs would locally heat up the detectors placed in close vicinity, ultimately compromising their performance. On the other hand, the number of wires to be installed scales linearly with the number of read-out channels, increasing the system complexity, and leading to an intolerable heat-flow onto the cryogenic platform. Therefore, a completely new read-out approach is necessary, overcoming these limitations.

About twenty years ago, an innovative detector technology was proposed, based on the microwave measurement of the complex impedance of thin superconducting films, which nowadays it is commonly denoted as *microwave kinetic inductance detector* (MKID). In the original paper [Day03], the authors mention the possibility to exploit frequency-division microwave multiplexing to read-out large arrays of these detectors. For that, the superconducting films are shaped as microwave resonators and coupled to a common transmission line. Inspired by microwave multiplexing of MKIDs, the microwave SQUID multiplexer has been developed to read out large arrays of TESs, introducing an rf SQUID that couples each TES to a resonator with a unique resonance frequency [Irw04, Mat11] and transduces detector signals in the TESs into resonance frequency shifts. Efforts are ongoing to develop the microwave SQUID multiplexer for MMCs [Kem12, Weg18b], adapting it to the requirements set by the particular features of these detectors.

MMCs are microcalorimeters based on the magnetic response of a paramagnetic sensor upon a change of temperature. The sensor is thermally connected to a metallic absorber where the particle energy is released, causing an increasing of temperature of the complete detector and, thus, a change of magnetisation of the sensor. The magnetisation signal is finally read out exploiting a SQUID-based read-out system. MMCs exhibit a fast signal rise time below 1 µs, an excellent energy resolution up to 1.6 eV FWHM and an almost linear detector response [Fle05]. Because of these superior detector properties, MMCs have been chosen as detector technology for the Electron Capture in ^{163}Ho (ECHo) experiment.

The ECHo experiment aims to determine the effective electron neutrino mass by analysing the end-point of the electron capture spectrum of ^{163}Ho. In the electron capture process, an electron from an inner atomic shell of the ^{163}Ho atom is cap-

tured by the nucleus, emitting an electron neutrino. The ^{163}Dy daughter atom is left in an excited state and it subsequently reaches the ground state emitting cascades of X-rays and Auger electrons. The available decay energy, corresponding to the Q-value $Q_{\mathrm{EC}} \sim 2.833 \pm 0.030_{\mathrm{stat}} \pm 0.015_{\mathrm{sys}}\, keV$ [Eli15], is shared by the atomic de-excitations of the daughter atom and by the electron neutrino, neglecting the tiny nuclear recoil contribution. The spectrum corresponding to the de-excitation energy is affected by the non-zero neutrino mass, since it effectively reduces the energy available and it shifts the end-point of the spectrum. In order to enhance the sensitivity on the effective neutrino mass, the electron capture spectrum must be measured with a calorimetric approach, i.e. including all the contributions to the de-excitation energy, and the event statistics should be maximised. For that, a large number of MMC detectors, embedding a sufficient amount of ^{163}Ho inside the detector absorber, should be measured in parallel, preserving the high-energy resolution response of the microcalorimeter detectors. For the present phase of the ECHo experiment, ECHo-100k, the target number of detector pixels is about 10^5, each one characterised by a ^{163}Ho activity of about 10 Bq. With such a large number of detectors to be simultaneously operated, a multiplexed detector read-out approach is mandatory. In fact, a dedicated microwave SQUID multiplexing system for the MMCs for ECHo-100k is currently under development and it represents the framework of this thesis.

The work presented here focuses on two fundamental aspects regarding the microwave SQUID multiplexing for ECHo: firstly, pinpointing the optimal microwave resonator geometry for the microwave SQUID multiplexer, and secondly, developing a cryogenic microwave read-out system for the multiplexed detector read-out for ECHo-100k.
For the microwave resonators, two different layouts are considered: coplanar waveguide resonators and lumped element resonators. Coplanar waveguide resonators have successfully been integrated into microwave SQUID multiplexers [Mat11, Kem12, Weg18b] and exhibit a predictable noise performance, which is sufficient to achieve the energy resolution required for ECHo-100k. As the resonance frequency spacing for the microwave SQUID multiplexer is critical to keep crosstalk low, while making most efficient use of the available system bandwidth, in the framework of this thesis an innovative resonance frequency fine-tuning technique for coplanar waveguide resonators has been introduced and demonstrated.
While the integration of lumped element resonators into microwave SQUID multiplexers is still under development, a resonance frequency fine-tuning technique for lumped element resonators is already well-established [Liu17b, McK19, Pal19]. The advantages of the lumped element resonator geometry with respect to the coplanar waveguide resonator geometry are a more compact layout allowing for a higher packing density of resonators on chip, and an improvement in the noise performance of the microwave SQUID multiplexer as predicted by theory. As the noise performance of the microwave SQUID multiplexer plays a crucial role to achieve the required

high energy resolution for ECHo-100k, the noise performance of microwave SQUID multiplexers based on both resonator geometries is compared experimentally in the framework of this thesis with the aim to pinpoint the best resonator geometry.
Additionally, in the scope of this thesis, a dedicated cryogenic microwave read-out system for the microwave SQUID multiplexer has been developed respecting the strict boundary conditions set by the ECHo experiment in terms of noise performance, linearity and power dissipation. The conformity of the read-out system with the design targets has been experimentally demonstrated.

After a short description of the magnetic microcalorimeters employed for the ECHo experiment in chapter 2, highlighting the detectors' building blocks, their working principle and their performance, the microwave SQUID multiplexer, its properties, its production and read-out techniques are introduced in chapter 3. The development of a dedicated cryogenic microwave read-out chain for the ECHo-100k experimental phase is presented in chapter 4. Here, firstly, the dedicated simulation framework developed in the context of this thesis is discussed, secondly, the designed read-out system configuration in terms of cryogenic components and mechanical design is presented, and, finally, the construction of the first read-out demonstrator channel, followed by the experimental assessment of its performance, is described. The last part of this thesis is devoted to pinpointing the optimal resonator geometry for the microwave SQUID multiplexer. In particular, in chapter 5 the innovative tile-and-trim procedure to fine-tune the resonance frequency of coplanar waveguide resonators is described and in chapter 6 the measured noise performance of microwave SQUID multiplexers based on both coplanar waveguide resonators and lumped element resonators is compared and the results are discussed in light of the underlying theoretical model. Finally, chapter 7 provides a conclusion and an outlook.

2. Magnetic microcalorimeters for the ECHo experiment

The Electron-Capture in ^{163}Ho (ECHo) experiment is aiming at the determination of the effective electron neutrino mass employing magnetic microcalorimeters (MMCs). In this chapter, the ECHo experiment is introduced following [Gas17, Man21a], the underlying detector technology is shortly reviewed based on [Fle05, Man21a], and a dc SQUID-based single-channel read-out system for MMCs is presented following [Kem15, Man21b].

2.1 The ECHo experiment

One of the most stringent open questions in particle physics is the determination of the absolute neutrino mass scale. Different approaches are currently being implemented to extract this information, ranging from the search of neutrinoless double-beta decay [Giu12] to cosmological observations [Won11] and to the experiments based on the kinematics of weak decays (β or electron capture processes). The latter is the most direct and model-independent method for the determination of the electron neutrino mass, since it is purely based on kinematics. Here the neutrino is not observed directly, but the energy E_{EC} of all other decay products, which share the available decay energy Q_{EC} with the neutrino[1], can be measured precisely. The minimum energy required to create a neutrino corresponds to its mass m_{ν_e} and, therefore, the maximum energy in the measured beta or electron capture energy spectrum is reduced by that amount: $E_{\mathrm{EC}}^{\mathrm{max}} = Q_{\mathrm{EC}} - m_{\nu_e}c^2$, with the vacuum speed of light c. As a result, the spectrum is distorted by a non-zero neutrino mass, especially in the vicinity of the end-point.

The ECHo experiment aims to determine the effective electron neutrino mass exploiting the electron capture decay of the holmium isotope ^{163}Ho. In this process, an electron from an inner orbital of the holmium atom is captured by the nucleus, transforming a nuclear proton into a neutron under the emission of an electron neutrino ν_e. After this decay, the daughter atom, which is a dysprosium atom (Dy), is left in an excited state and it reaches its ground state by emitting cascades of X-rays and electrons. The decay scheme is the following:

[1] The nucleus recoil is negligible.

$$\begin{aligned} {}^{163}_{67}\mathrm{Ho}_{96} \rightarrow {}^{163}_{66}\mathrm{Dy}^{*}_{97} + \nu_e \\ \rightarrow {}^{163}_{66}\mathrm{Dy}_{97} + E_{\mathrm{EC}} \end{aligned} \tag{2.1}$$

where ν_e is the emitted electron neutrino and E_{EC} is the de-excitation energy that can be measured.

^{163}Ho is characterised by the smallest Q-value among the nuclides that undergo electron capture, $Q_{\mathrm{EC}} = 2.833(30_{\mathrm{stat}})(15_{\mathrm{sys}})\,\mathrm{keV}$ [Eli15]. Since a small Q-value increases the relative number of events in the end-point region, ^{163}Ho is considered the best candidate for the determination of the neutrino mass by means of electron capture spectroscopy [DR82].

In order to perform a competitive experiment to determine the effective electron neutrino mass exploiting the ^{163}Ho electron capture spectrum, there are three main requirements:

- all the contributions to the de-excitation energy must be measured, meaning that a calorimetric approach is necessary;
- the calorimetric electron capture spectrum must be measured with high precision and therefore detectors with excellent energy resolution are a requisite;
- in order to resolve the effect of a non-zero neutrino mass at the end-point of the spectrum, a high statistics measurement is needed.

These requirements can be satisfied using magnetic microcalorimeter (MMC) arrays with embedded ^{163}Ho, as it will be discussed in section 2.2, where also the working principle of these microcalorimeters is presented.

The ECHo experiment is organised in up-scaling phases, gradually increasing the total statistics and therefore the sensitivity on the effective electron neutrino mass. The first phase, ECHo-1k, was a small scale experiment with about 100 MMC pixels to reach a sensitivity below 20 eV. The next phase, ECHo-100k, aims to lower the sensitivity below 3 eV operating about 12000 MMC pixels. The modular approach of the ECHo experiment will allow to scale up to further phases with larger number of pixels. With increasing numbers of detectors to be read out simultaneously, a multiplexed approach becomes crucial.

2.2 Magnetic microcalorimeters

Magnetic microcalorimeters (MMCs) are low temperature detectors based on the magnetic response of a paramagnetic sensor upon a deposition of energy. In the

following the general working principle of MMCs is described and the key detector features for the specific application of the ECHo experiment are discussed. Subsequently, the MMC design for the ECHo-100k experimental phase is shortly illustrated and the direct current Superconducting Quantum Interference Device (dc SQUID) read-out technique is discussed.

2.2.1 Working principle

MMCs consist of a particle absorber, which is placed in good thermal contact with a paramagnetic temperature sensor sitting in a constant magnetic field, as sketched in figure 2.1. The temperature sensor consists of Er^{3+} ions diluted in silver with a concentration of few hundred ppm and is weakly connected to a thermal bath at constant temperature of about 20 mK. When energy is deposited in the absorber, the temperature of the detector increases and, hence, the magnetisation of the paramagnetic sensor decreases. Finally, the change of magnetisation is translated into a change of magnetic flux in a superconducting pick-up coil, which is connected in parallel to the input coil of a dc SQUID, which acts as a very sensitive magnetic flux sensor. Thus, the change of magnetic flux $\delta\Phi$ in the dc SQUID is proportional to the initial energy deposition δE, according to the relation

$$\delta\Phi \propto \delta M = \frac{\partial M}{\partial T}\delta T = \frac{\partial M}{\partial T}\frac{\delta E}{C} \tag{2.2}$$

where δM is the change of magnetisation in the paramagnetic sensor, which depends on the change of temperature δT according to the magnetisation response of the sensor $\partial M/\partial T$, and C is the detector heat capacity [Fle05].

Along with their large bandwidth, their almost quantum limited noise performance and their intrinsic compatibility with operational temperatures in the millikelvin range, dc SQUIDs are well suited for the read-out of MMC detectors. The general working principle of a dc SQUID is shortly discussed in section 2.2.4.

2.2.2 Detector properties

MMCs have been chosen as detector technology for the ECHo experiment since they meet the main requirements presented in section 2.1. First of all, it has been demonstrated that it is possible to implant the ^{163}Ho source into MMCs and, therefore, to perform a calorimetric measurement of the ^{163}Ho electron capture spectrum [Gas13]. For the ECHo-100k phase, a ^{163}Ho activity of 10 Bq per pixel is planned [Man21a]. As MMCs are characterised by a fast response with an intrinsic rise time shorter than 100 ns [Kem18], minimising the fraction of pile-up events on the rise of the signal,

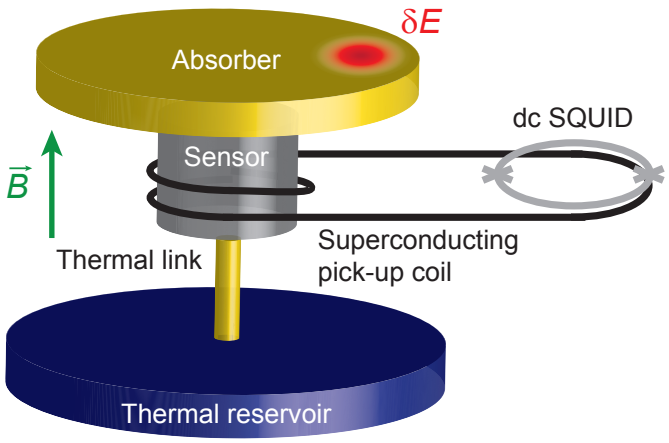

Figure 2.1: Schematic drawing of an MMC detector, consisting of a particle absorber, a paramagnetic sensor weekly connected to a thermal bath and a superconducting pick-up coil connected to a dc SQUID loop. This figure is based on a work in [Man21a].

which otherwise pose a source of background events. Furthermore, the calibration function of MMCs is almost ideally linear for energies up to 10 keV, with deviations below 1 % - which can be well described by the thermodynamic model of the detector [Sik20]. Finally, MMCs developed for X-ray spectroscopy have shown an excellent energy resolution of 1.6 eV FWHM at 5.9 keV [Kem18], which is comparable with the best values presently reached by any kind of cryogenic detector at this energy scale. The energy resolution is first and foremost limited by the noise level of the read-out chain, which therefore must be minimised. Additional suppressible effects - among others, crosstalk between the different detector pixels and fluctuations of the detector base temperature - can further worsen the achievable energy resolution. However, the fundamental limit on the energy resolution can be calculated considering only the irreducible thermodynamic fluctuations of the energy content in the different subsystems of the calorimeter, leading to the following relation [Fle05]:

$$\Delta E_{\mathrm{FWHM}} \propto \sqrt{C_{\mathrm{e}}} T \left(\frac{1}{\beta(1-\beta)} \frac{\tau_{\mathrm{r}}}{\tau_{\mathrm{d}}} \right)^{1/4} \tag{2.3}$$

where C_{e} is the electronic contribution to the heat capacity of the the detector, T is the operational temperature, $\beta := C_{\mathrm{s}}/(C_{\mathrm{e}} + C_{\mathrm{s}})$, where C_{s} is the spin contribution to the detector heat capacity and, finally, τ_{r} and τ_{d} are the rise time and decay time that describe the detector signal. Consequently, in order to obtain the best possible energy resolution, not only the heat capacity of the detector and the working temperature should be lowered by fabricating micro-scale calorimeters and operating them at

millikelvin temperature, respectively, but also the signal shape and in particular the fast rise time and a comparably slow decay time play a crucial role. Therefore, the read-out chain should on the one hand, guarantee sufficient bandwidth to be able to resolve the fast response of MMC detectors, and on the other hand, exhibit an excellent noise performance in order not to deteriorate the intrinsic energy resolutions of MMCs.

Overall, the presented properties and performance make MMCs the ideal choice as detector technology for the ECHo experiment.

2.2.3 Detector design for ECHo-100k

The detector array designed for the ECHo-100k experimental phase [Man21a] consists of 64 MMC pixels, based on a planar gradiometric geometry. This layout consists of two planar meander-shaped pick-up coils equipped with planar sensors on top [Fle09] as visualised in figure 2.2. Forming a first-order gradiometer, the two pick-up coils with inductance L_{m}, respectively, are connected in parallel to the input coil L_{i} of a highly sensitive magnetic flux sensor, as for instance a dc SQUID with inductance L_{S}. The detector and the dc SQUID do not need to share the same substrate and it is usually convenient to fabricate them separately. In operation, the detector chip and the SQUID chip are connected by aluminium wire-bonds with parasitic wire inductance L_{w}.

In order to align the magnetic moments of the paramagnetic sensor, a weak magnetic field is required, which can be generated by injecting a persistent current into the superconducting circuit formed by the two meander-shaped pick-up coils.

The main advantage related to the choice of a planar gradiometric geometry is the suppression of background events caused by external electromagnetic interference. In fact, since both the pick-up coils contribute to the detector signal but with opposite polarities, identical signals occurring simultaneously in both the detector pixels are cancelled out. A second convenient aspect of this layout is that each pair of pick-up coils are read out by a single dc SQUID read-out channel, effectively implementing an intrinsic multiplexed read-out. Finally, the detector signal is enhanced if compared to other MMC geometries, e.g. cylindrical sensors surrounded by dc SQUID counter-wound loops [Fle09], thanks to the sensor proximity to the pick-up coil, which improves the coupling between the coil and the magnetic moments of the sensor. Furthermore, the indirect coupling between the pick-up coil and the dc SQUID via a separate coil allows to fabricate the MMC detector and the dc SQUID on different substrates, minimising the dc SQUID power dissipation on the detector and the consequent potential temperature increase in the sensor, which would reduce the signal size.

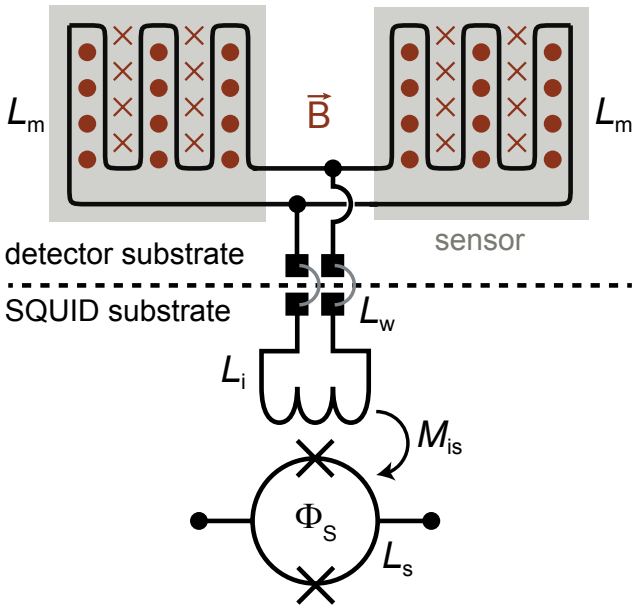

Figure 2.2: Gradiometric planar geometry layout with two detector pixels equipped with two temperature sensors and two meander-shaped pick-up coils underneath. The pick-up coils are in turn coupled to a dc SQUID current sensor which is fabricated on a separate substrate. This figure is adopted from [Man21a].

2.2.4 dc SQUID read-out

The read-out of an MMC detector is usually performed exploiting a dc SQUID, converting the change of magnetic flux in the meander-shaped pick-up coil to a voltage signal. A dc SQUID consists of a superconducting loop which is interrupted by two weak links, the so-called Josephson junctions, as illustrated in figure 2.3a. In order to suppress hysteretic behaviour, the junctions are typically shunted by a resistor [Cla04], as shown in the schematics. Sufficiently low dc currents can flow without dissipation in the dc SQUID loop, since the Cooper pairs can tunnel through the Josephson junctions that separate the two superconducting paths. However, in the case of larger bias currents, quasiparticles partially carry the current through the junctions, leading to a voltage drop V_S across the dc SQUID. The voltage V_S depends on the bias current I_b and on the magnetic flux Φ_S penetrating the dc SQUID loop, as illustrated in the characteristic curves in figure 2.3b. Therefore, a dc SQUID can be used as a magnetic flux to voltage converter. The relation between the voltage across the dc SQUID V_S and the magnetic flux threading the loop Φ_S is however not linear, but periodical, as visible in the second plot of figure 2.3b. In particular, the dc SQUID voltage response upon a change of magnetic flux can be considered linear if the dc SQUID working point is chosen to be at the steepest part of the curve, as marked in figure 2.3b, and if the change in magnetic flux is much smaller than

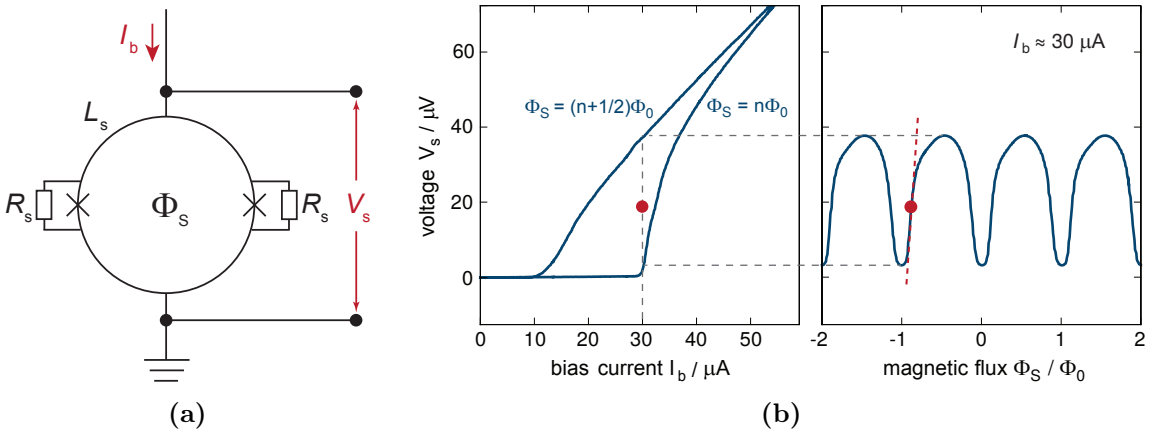

Figure 2.3: **(a)** Schematic of a dc SQUID with the two Josephson junctions represented by the symbol $\times$ and shunted with the resistors R_S. The bias current I_b and the voltage drop V_S across the dc SQUID are shown. **(b)** Current-voltage characteristics (left) of a dc SQUID and corresponding flux-voltage characteristics (right) for a fixed bias current. The magnetic flux is shown in terms of magnetic flux quanta $\Phi_0 = h/2e \approx 2.07 \times 10^{-15}$ Wb. The working point is marked in red. This figure is taken from [Man21a].

$\sim 1/4 \cdot \Phi_0$. For larger magnetic flux changes, the flux-to-voltage conversion exhibits a high non-linearity, which can be overcome by introducing a feedback mechanism that linearises the dc SQUID response.

In order to introduce such a linearisation feedback mechanism and a low temperature amplification stage, the so-called two-stage set-up is exploited [Cla04]. The scheme of a two-stage dc SQUID configuration is depicted in figure 2.4. The signal from the MMC detector is coupled to a first-stage dc SQUID, the output of which is coupled to the input of a second-stage dc SQUID array that serves as low noise amplifier [Kem15].

The first-stage dc SQUID is operated in voltage bias mode, meaning a bias current I_{b1} is run through the load resistor R_g, which is chosen to be much smaller than the dynamical resistance R_{dyn} of the first-stage dc SQUID, maintaining a constant voltage drop over the first-stage dc SQUID and decreasing the power dissipation on the first-stage dc SQUID chip. The second-stage amplifier dc SQUID array consists of 16 dc SQUIDs in series and is operated in current bias mode. As a result, the change of magnetic flux Φ_S penetrating the first-stage dc SQUID loop is converted into an output current which flows through the input coil of the amplifier dc SQUID, creating a change of magnetic flux in the dc SQUID array. The magnetic flux gain G_Φ is given by:

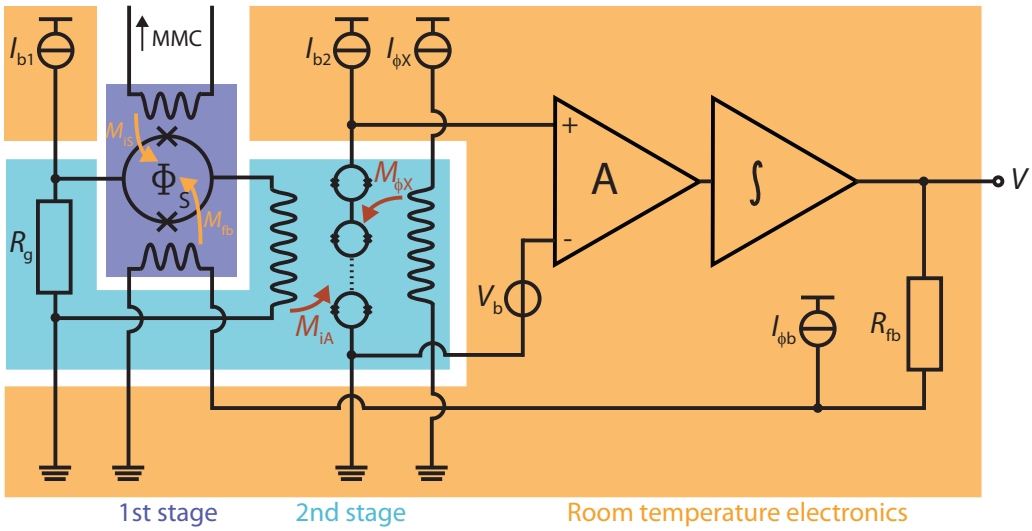

Figure 2.4: Schematic circuit of a two-stage dc SQUID configuration, where the first stage is marked in violet, the second stage is marked in blue and the room temperature electronics is marked in orange. This figure is based on a work in [Man21b].

$$G_\Phi = \frac{M_{\mathrm{iA}}}{M_{\mathrm{dyn}} + R_{\mathrm{g}}/V_\Phi}\,. \tag{2.4}$$

Here, M_{iA} is the mutual inductance between the amplifier dc SQUIDs and the corresponding input coil, V_Φ is the flux-to-voltage transfer coefficient of the first-stage dc SQUID and $M_{\mathrm{dyn}} = R_{\mathrm{dyn}}/V_\Phi$ is the intrinsic current sensitivity of the first-stage dc SQUID. The output voltage of the second stage is amplified using a low-noise amplifier at room temperature and then fed into a voltage integrator, as shown in figure 2.4. The output voltage V_{out} is converted into a feedback current via the feedback resistor R_{fb}. The feedback current runs through a feedback coil coupled to the first-stage dc SQUID with a mutual inductance M_{fb}. In this way, a negative magnetic flux feedback signal is created, which compensates the initial change of magnetic flux in the first-stage dc SQUID. This flux-locked loop feedback mechanism linearises the dc SQUID response, keeping the first-stage dc SQUID at a constant working point [Cla04].

State-of-the-art two-stage dc SQUID set-ups coupled to MMCs, as they were used for the first experimental phase of ECHo [Gas17, Man22], exhibit a large signal bandwidth of $\sim 100\,\mathrm{kHz}$ [Kem15], a white noise level of $\sim 0.3\,\mu\Phi_0/\sqrt{\mathrm{Hz}}$ and a $1/f$-type noise level of $\sim 5.0\,\mu\Phi_0/\sqrt{\mathrm{Hz}}$ at a frequency of $f = 1\,\mathrm{Hz}$ [Man21b].

3. Microwave SQUID multiplexer

This chapter is dedicated to the detailed discussion of the microwave SQUID multiplexer. The need of a multiplexed read-out for large arrays of MMC detectors is discussed in section 3.1, with particular emphasis on the case of the ECHo experiment. After that, in section 3.2, the properties of superconducting resonators are described and the theoretical background of superconducting coplanar waveguide resonators as well as superconducting lumped element resonators is presented. Josephson junctions and rf SQUIDs, being an essential part of the microwave SQUID multiplexer, are introduced in section 3.3. The working principle of the microwave SQUID multiplexer is explained in section 3.4, where also a theoretical description of the microwave SQUID multiplexer is provided. Noise contributions are discussed in section 3.5. A linearisation scheme for the response of the microwave SQUID multiplexer is reviewed in section 3.6, the intended read-out scheme based on a software-defined radio is presented in section 3.7, and the production of the microwave SQUID multiplexer devices used in the scope of this thesis is summarised in section 3.8.

3.1 Read-out of large arrays of MMCs

For experiments using a small number of detector pixels based on magnetic microcalorimeters (MMCs), typically a two-stage dc SQUID-based read-out, as presented in the previous chapter, is employed, since it provides a large read-out bandwidth and its noise performance allows for an excellent energy resolution of few electronvolt FWHM [Fle09, Kem15, Kem18, Man21a]. However, recently, technological progress made the fabrication of large numbers of virtually identical MMC detector pixels possible, and hence, various experiments tend to employ in the order of thousands of detector pixels for different applications, such as the detection of neutral molecule fragments [Gam19, Sch21] or the determination of the of the effective electron neutrino mass [Gas17].

For these experiments, a read-out scheme in which every detector pixel or every pair of detector pixels is read out individually by means of a two-stage dc SQUID set-up is impossible, because the heat dissipation of the set-up, the system complexity and the costs scale linearly with the number of channels to be read out. In fact, each two-stage dc SQUID set-up dissipates heat in the order of $1 - 10\,\mathrm{nW}$ [Dru07], and since the first-stage dc SQUID is situated in close proximity to the detector, this power dissipation can lead to a locally increased temperature compromising the

performance of the MMCs [Kra20]. For thousands of detector pixels and hence, thousands of two-stage dc SQUID set-ups, the power dissipation could even affect the cooling performance of the cryogenic platform, which is typically $\sim 10\,\mu W$ at millikelvin temperature. Additionally, each two-stage dc SQUID set-up requires ~ 10 wires routed from room temperature to millikelvin temperature, which contribute, on the one hand, to the heat flow onto the cryogenic experimental platform, and on the other hand, to the system complexity. Lastly, the financial efforts to set up thousands of read-out chains are become substantial.

These limitations make a multiplexed approach for the read-out of large arrays of MMCs necessary. The optimal multiplexing scheme for a specific experiment can vary, depending on the number of detector pixels, the required energy resolution, the expected event rate, the tolerable level of crosstalk and the tolerable power dissipation in the proximity of the detectors. For the ECHo-100k phase of the ECHo experiment [Gas17], 12000 detector pixels with an activity of 10 Bq/pixel, corresponding to 6000 detector channels, have to be operated and read out simultaneously. In order to limit the unresolved pile-up fraction, the fast rise-time of MMCs should not be excessively affected by the read-out system. Moreover, an energy resolution better than 5 eV FWHM is required to guarantee a sufficient sensitivity.

Several SQUID-based multiplexing techniques have been demonstrated for low temperature detectors, which are discussed in more detail in [Kem12, Weg18a, Ric21]. Time-division multiplexing [Bey09, Por14] is suitable for small detector arrays with a slow detector response and a low event rate, as the available bandwidth per detector channel is inversely proportional to the number of detector channels, and hence, it cannot be employed for the large number of MMCs within ECHo-100k requiring a fast read-out. The presently available code-division multiplexing [Irw10, Nie10, Mor16], which has been developed for transition-edge sensors, cannot be adopted for the MMCs within ECHo-100k either, as the typical read-out schemes would lead to a substantial degradation of the MMCs' energy resolution [Ban12].

A promising technique for the read-out of MMCs within ECHo-100k is microwave SQUID multiplexing [Irw04, Mat11, Nor13], which is a frequency-division multiplexing technique. The signals from different detector channels are modulated onto different microwave carrier frequencies, which allows for the simultaneous and continuous transmission of the detector signals through a single single coaxial cable and a demodulation at room temperature. The modulation is typically achieved by means of an rf SQUID, which limits the power dissipation onto the experimental platform to a few picowatt per channel, meaning that even for $\mathcal{O}(10^5)$ channels, the power dissipation on the experimental platform is kept well below the available cooling power of typically $\sim 10\,\mu W$. Additionally, this technique provides a large bandwidth per detector channel. For these reasons, microwave SQUID multiplexing will be em-

ployed for the MMCs within ECHo-100k, and thus, it represents the framework of this thesis.

3.2 Superconducting microwave resonators

An integral part of microwave SQUID multiplexers are superconducting microwave resonators. In this section, the properties of superconductors in the microwave regime are reviewed, and capacitively coupled and inductively terminated quarter-wave resonators are introduced, following [Kem12, Weg18a, Ric21]. Subsequently, a second superconducting microwave resonator geometry based on lumped elements is presented.

3.2.1 Properties of superconductors in the microwave regime

Superconductors exhibit a vanishing dc resistance at temperatures below the superconducting transition temperature T_c, allowing for a dissipationless flow of dc currents. For ac currents with angular frequency ω, however, superconductors show a finite surface impedance $Z_\mathrm{S} = R_\mathrm{S} + i\omega L_\mathrm{S}$. The surface resistance R_S is a consequence of quasiparticles in the superconductor experiencing accelerations due to time variable electromagnetic field and subsequent scattering processes causing ohmic losses, analogously to conduction electrons in normal conducting metals. Cooper pairs, in contrast, are not subject to those scattering mechanisms and, hence, they flow dissipationless through the superconductor. However, due to their inertia, they cannot follow the time variable electromagnetic field instantaneously, which manifests in the kinetic inductance L_kin of superconductors. Therefore, the surface inductance $L_\mathrm{S} = L_\mathrm{m} + L_\mathrm{kin}$ of a superconductor is comprised not only of the of the magnetic inductance L_m related to the geometry of the superconductor, but also of the kinetic inductance. The number density of quasiparticles in superconductors decreases exponentially with falling temperature, and hence, the surface resistance R_S drops accordingly. Thus, for temperatures far below the superconducting transition temperature T_c, the surface impedance Z_S is dominated by the surface inductance L_S.

The surface impedance Z_S is closely related to the complex conductivity of a superconductor [Glo57]

$$\sigma_\mathrm{S}(\omega, T) = \sigma_1(\omega, T) - i\sigma_2(\omega, T)\,, \tag{3.1}$$

at angular frequency ω and temperature T. The real part $\sigma_1(\omega, T)$ and the imaginary part $\sigma_2(\omega, T)$ can be calculated in relation to the normal conductivity σ_n, employing the Mattis–Bardeen theory [Mat58]. For small angular frequencies $\omega < 2\Delta(T)/\hbar$,

i.e. in case the energy of a single photon is not sufficient to break a Cooper pair with binding energy $2\Delta(T)$, the conductivity ratios are given by

$$\begin{aligned}\frac{\sigma_1}{\sigma_\mathrm{n}} &= \frac{2}{\hbar\omega}\int_{\Delta(T)}^{\infty}\frac{[f(\epsilon)-f(\epsilon-\hbar\omega)][\epsilon^2+\Delta^2(T)+\hbar\omega\epsilon]}{\sqrt{\epsilon^2-\Delta^2(T)}\sqrt{[\epsilon+\hbar\omega]^2-\Delta^2(T)}}\mathrm{d}\epsilon \\ \frac{\sigma_2}{\sigma_\mathrm{n}} &= \frac{1}{\hbar\omega}\int_{\Delta(T)-\hbar\omega}^{\Delta(T)}\frac{[1-2f(\epsilon-\hbar\omega)][\epsilon^2+\Delta^2(T)+\hbar\omega\epsilon]}{\sqrt{\Delta^2(T)-\epsilon^2}\sqrt{[\epsilon+\hbar\omega]^2-\Delta^2(T)}}\mathrm{d}\epsilon\,,\end{aligned} \tag{3.2}$$

where $\hbar$ denotes the reduced Planck constant and $f(x) = (1+e^{x/k_\mathrm{B}T})^{-1}$ indicates the Fermi-Dirac distribution.

Depending on the characteristic length scales inside the superconductor, i.e. the mean free path of the electron l_e, the magnetic penetration depth λ and the superconducting coherence length ξ_0, different relations between the complex conductivity $\sigma_\mathrm{S}(\omega,T)$ and the surface impedance Z_S can be established. For a superconducting film of thickness t in the dirty limit, meaning that the mean free path of the electrons l_e is much smaller than the superconducting coherence length ξ_0, the surface impedance can be expressed as [Kau78]

$$Z_\mathrm{S} = \sqrt{\frac{i\omega\mu_0}{\sigma_\mathrm{S}(\omega,T)}}\coth\left(t\sqrt{i\omega\mu\sigma_\mathrm{S}(\omega,T)}\right)\,, \tag{3.3}$$

which simplifies for $\sigma_2 \gg \sigma_1$ and $T \ll T_\mathrm{c}$ to [Bar09]

$$\begin{aligned}R_\mathrm{S} &= \mu_0\lambda_\mathrm{eff}\omega\beta\frac{\sigma_1}{2\sigma_2} \\ L_\mathrm{S} &= \mu_0\lambda_\mathrm{eff}\,,\end{aligned} \tag{3.4}$$

where $\lambda_\mathrm{eff} = \lambda\coth(t/\lambda)$ denotes the effective magnetic penetration depth. For thin films, the effective magnetic penetration depth is increased with respect to the penetration depth for bulk material $\lambda = 1/\sqrt{\mu_0\omega\sigma_2}$. The parameter $\beta = 1+\frac{2t/\lambda}{\sinh(2t/\lambda)}$ approaches $\beta \approx 2$ in the limits of very thin films, i.e. for $d \to 0$.

3.2.2 Superconducting coplanar waveguides

A coplanar waveguide (CPW) consists a centre conductor of width s and two ground planes in parallel to the centre conductor, which are separated from the centre conductor by slots of width w, as illustrated in figure 3.1. In the case of the microwave

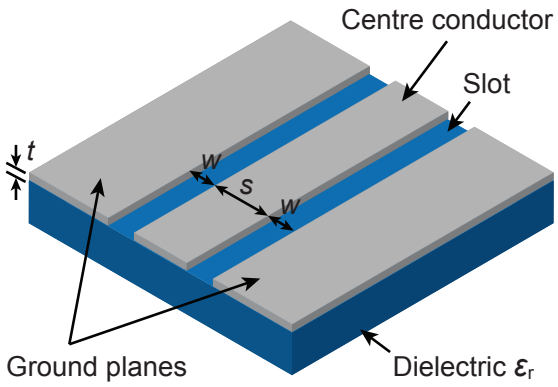

Figure 3.1: Sketch of a coplanar waveguide geometry made from a superconducting film of thickness t placed on top of a dielectric substrate with relative permittivity ε_r. The centre conductor exhibits a width s and the slots a width w. This figure is based on a work in [Ric21].

SQUID multiplexer, these structures are fabricated from a superconducting film of thickness t deposited on a dielectric substrate with relative permittivity ε_r. As the two half-spaces divided by the plane of the superconducting film exhibit different relative permittivities, the wave travelling along the CPW experiences an inhomogeneous medium, for which reason the wave is described by a hybrid of a transverse electromagnetic mode (TEM) and a longitudinal electromagnetic mode. However, for waves on CPWs commonly a quasi-TEM is assumed, as the longitudinal component is typically negligibly small, meaning that the main components of the wave vector $\mathbf{k}$, of the electric field $\mathbf{E}$ and of the magnetic field $\mathbf{B}$ are orthogonal.

The magnetic inductance per unit length L'_m and the capacitance per unit length C' can be calculated involving conformal mapping techniques [Gao08a]. For this, the four geometry dependent quantities $k = s/(s+2w)$ and $k' = \sqrt{1-k^2}$ as well as $k_x = u_1(x)/u_2(x)$ and $k'_x = \sqrt{1-k_x^2}$ are required, where the quantities

$$u_1(x) = \frac{s}{2} + \frac{x}{\pi}\left[1 + \ln\left(\frac{2\pi s}{x}\frac{w}{s+w}\right)\right] \tag{3.5}$$

$$u_2(x) = \frac{s}{2k} - \frac{x}{\pi}\left[1 + \ln\left(\frac{2\pi s}{xk}\frac{w}{s+w}\right)\right] \tag{3.6}$$

are a function of x, the perpendicular distance from the surface of the dielectric substrate. Subsequently, the magnetic inductance per unit length and the capacitance per unit length are calculated as

$$L'_\mathrm{m} = \frac{\mu_0}{4}\frac{\mathrm{K}(k'_{x=t/2})}{\mathrm{K}(k_{x=t/2})} \tag{3.7}$$

$$C' = 2\epsilon_0\frac{\mathrm{K}(k_{x=t})}{\mathrm{K}(k'_{x=t})} + 2\epsilon_0\epsilon_\mathrm{r}\frac{\mathrm{K}(k)}{\mathrm{K}(k')} \tag{3.8}$$

with the the vacuum permittivity $\varepsilon_0 \approx 8.85 \times 10^{-12}\,\mathrm{As/Vm}$ and the complete elliptic integral of the first kind $\mathrm{K}(x)$. Similarly, the kinetic inductance can be derived from the geometry of the CPW [Col92]

$$L'_\mathrm{kin} = (g_\mathrm{c} + g_\mathrm{g})\mu_0\lambda_\mathrm{eff} \tag{3.9}$$

with the contribution g_c arising from the centre conductor and the contribution g_g from the ground planes:

$$g_c = \frac{1}{4s(1-k^2)\mathrm{K}^2(k)} \left[\pi + \ln\left(\frac{4\pi s}{t} \left(\frac{w}{s+w} \right)^k \right) \right] \tag{3.10}$$

$$g_g = \frac{k}{4s(1-k^2)\mathrm{K}^2(k)} \left[\pi + \ln\left(\frac{4\pi s}{tk} \left(\frac{w}{s+w} \right)^{1/k} \right) \right] . \tag{3.11}$$

Finally, the characteristic impedance Z_0 of the CPW and the phase velocity of the wave in the CPW v_p are given by

$$Z_0 = \sqrt{\frac{L'}{C'}} \tag{3.12}$$

$$v_p = \frac{1}{\sqrt{L'C'}} \tag{3.13}$$

with the total inductance per unit length $L' = L'_m + L'_{kin}$.

3.2.3 Superconducting inductively terminated CPW quarter-wave resonators

A superconducting quarter-wave resonator based on a CPW geometry can be implemented by shorting one end of a superconducting CPW-based transmission line with length l_r to ground, while leaving the other end open. Such a configuration will exhibit resonances for $l_r = (2n-1)\lambda^{(n)}/4$, where $\lambda^{(n)}$ indicates the resonant wavelength corresponding to the mode number n. As the according resonance frequency for the n-th mode is given by $f_0^{(n)} = v_p/\lambda^{(n)}$, for the base mode $n = 1$, the resonance frequency yields

$$f_0 = \frac{1}{4l_r\sqrt{L'C'}} , \tag{3.14}$$

where the mode number has been omitted to simplify the notation. If such a resonator is coupled to a microwave transmission line via a coupling capacity C_c, as sketched in figure 3.2, the resonator can be read out by measuring the scatter parameter S_{21} between the two ports of the transmission line. The termination in a load inductor L_T facilitates the coupling of further elements to the resonator, such as non-hysteretic, unshunted rf SQUIDs in the case of a microwave SQUID multiplexer based on quarter-wave resonators. The loaded impedance of such a quarter-wave resonator is given by [Col92]

$$Z = \frac{1}{i\omega C_c} + Z_0 \frac{i\omega L_T + Z_0 \tanh(\gamma l_r)}{Z_0 + i\omega L_T \tanh(\gamma l_r)} , \tag{3.15}$$

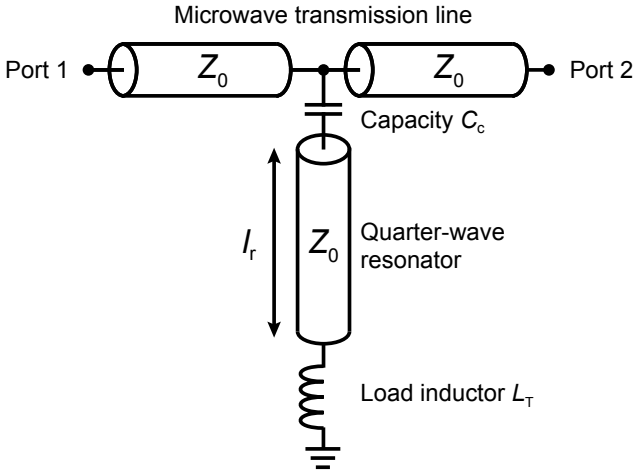

Figure 3.2: Schematic of a quarter-wave resonator of length l_r, which is coupled to a transmission line via a capacity C_c, and inductively terminated in a load inductor L_T. The resonator and the transmission line exhibit the same characteristic impedance Z_0. This figure is based on a work in [Weg18a].

where $\omega = 2\pi f$ denotes the angular frequency and $\gamma = \alpha + i\beta$ the complex propagation constant with the attenuation constant α and the phase constant $\beta = \omega/v_\mathrm{p}$. Finally, the scatter parameter $S_{21} = 2/(2 + Z_0/Z)$ [Poz98] as a function of frequency f can be expressed as [Bar09]

$$S_{21}(f) = \frac{S_{21}^{\min} + 2iQ_\mathrm{l}\frac{f-f_\mathrm{r}}{f_\mathrm{r}}}{1 + 2iQ_\mathrm{l}\frac{f-f_\mathrm{r}}{f_\mathrm{r}}} \tag{3.16}$$

with the minimum transmission $S_{21}^{\min} = Q_\mathrm{l}/Q_\mathrm{i}$, which characterises the transmission of the resonator on resonance $f = f_\mathrm{r}$. For $2\pi f_0 C_\mathrm{c} Z_0 \ll 1$ and $2\pi f_0 L_\mathrm{T} \ll Z_0$, the resonance frequency can be expressed as [Mat11]

$$f_\mathrm{r} = \frac{f_0}{1 + 4f_0(C_\mathrm{c}Z_0 + L_\mathrm{T}/Z_0)}\,. \tag{3.17}$$

The loaded quality factor Q_l is a measure for the stored energy in the resonator in relation to the energy loss per period. It can be calculated according to

$$\frac{1}{Q_\mathrm{l}} = \frac{1}{Q_\mathrm{i}} + \frac{1}{Q_\mathrm{c}} \tag{3.18}$$

with the intrinsic quality factors Q_i and the coupling quality factor Q_c. The intrinsic quality factor Q_i accounts for loss mechanisms within the resonator, such as radiative losses $1/Q_\mathrm{rad}$ [Maz04], dielectric losses $1/Q_\mathrm{TLS}$ [Gao08b] and quasiparticle losses $1/Q_\mathrm{QP}$ [Gao08c]. Radiative losses are dependent on the resonator geometry and can be minimised by reducing the characteristic CPW centre conductor width s [Maz04]. Quasiparticle losses are connected to the scattering of quasiparticles, as discussed above, and hence, they are expected to decrease drastically with falling temperature. Therefore, for the quarter-wave resonators employed in the framework

of this thesis, which are operated well below the superconducting transition temperature T_c, neither radiative losses nor quasiparticle losses are expected to play a crucial role, but dielectric losses are assumed to dominate. At low temperatures, dielectric losses are mostly governed by the resonant energy absorption of two-level systems (TLS), which are present in the dielectric materials in the vicinity of the resonator [McR20]. The coupling quality factor Q_c for a capacitively coupled quarter-wave resonator is given by [Mat11]

$$Q_c = \frac{2\pi}{(2Z_0\omega_r C_c)^2}\,, \tag{3.19}$$

where $\omega_r = 2\pi f_r$ is the angular resonance frequency.

The loaded quality factor Q_l determines the resonator bandwidth Δf for a given resonance frequency f_r via

$$\Delta f = \frac{f_r}{Q_l}\,. \tag{3.20}$$

In order not to locally heat up the experimental set-up for ECHo-100k, compromising the MMC performance, for the microwave SQUID multiplexer the lowest possible power dissipation is intended, and hence, the highest possible intrinsic quality factor $Q_i \to \infty$ is preferred. In this limit $Q_l \approx Q_c$ holds true, as follows from equation (3.18). Therefore, according to equations (3.19) and (3.20), for a given resonance frequency f_r, the resonator bandwidth Δf can be adjusted by tuning the corresponding coupling capacity C_c.

Additionally, the capacitive coupling impacts the power of the standing wave inside the resonator P_{rf} in dependence on the power of the read-out tone P_{rf} applied to the microwave transmission line. For frequencies $f \approx f_r$ close to the resonance frequency, the relation

$$P_{res} = \frac{2}{\pi}\frac{Q_l^2}{Q_c}P_{rf} \tag{3.21}$$

can be derived for a quarter-wave resonator [Bar09]. In this case, the amplitude of the current running through the inductive load is given by [Mat11]

$$I_T = \sqrt{\frac{16}{\pi}\frac{Q_l^2}{Q_c}\frac{P_{rf}}{Z_0}}\,. \tag{3.22}$$

3.2.4 Superconducting lumped element resonators

In figure 3.3a, an alternative planar resonator layout is presented, which is more compact than a CPW-based quarter-wave resonator layout. It is comprised of lumped elements, i.e. elements which are much smaller than the resonant wavelengths, forming a tank circuit, and hence, this resonator configuration is called lumped element

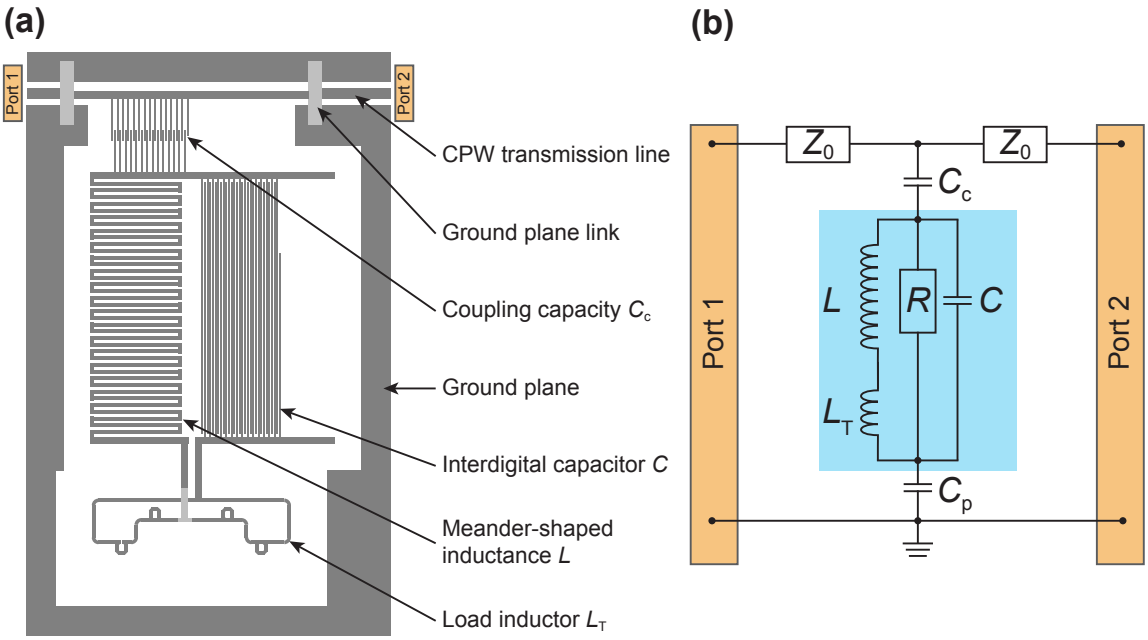

Figure 3.3: **(a)** Layout of a planar lumped element resonator (LER) comprised of an interdigital capacitor C, a meander-shaped inductance L and an inductive load L_T. The resonator is coupled to a transmission line via a coupling capacity C_c. **(b)** Equivalent circuit of the lumped element resonator. Losses are accounted for by the resistance R and the parasitic coupling to the ground plane is characterised by the capacity C_p. The transmission line exhibits a characteristic impedance Z_0. This figure is inspired by a work in [Pal19].

resonator (LER). An interdigital capacitor C is connected in parallel to an inductance formed by a meander-shaped inductor L and a load inductor L_T. Further components, such as non-hysteretic unshunted rf SQUIDs, can be coupled to the resonator via the load inductor. The resonator itself is coupled capacitively to a CPW-based transmission line via an interdigital coupling capacitor C_c, which allows for a read-out of the resonator by means of a microwave transmission measurement between the two ports indicated in the figure. The capacitive coupling of the resonator to the transmission line causes, however, an asymmetry in the transmission line, which could potentially lead to the formation of spurious modes, such as the coupled slot-line mode. In order to suppress these spurious modes and the associated loss mechanisms, such as radiative losses, it proved to be useful to connect the ground planes on either side of the transmission line's centre conductor by means of superconducting links shortly before and after the coupling capacity, as indicated in figure 3.3a [Wil16, Her17].

An equivalent circuit for the LER coupled to a transmission line with characteristic impedance Z_0 is shown in figure 3.3b. This circuit model also takes into account losses

inside the resonator, modelled as resistance R, and a parasitic capacitive coupling to the ground planes via a capacity C_p. For the actual resonator, marked in the light blue box, the impedance is given by

$$Z_\mathrm{res}(\omega) = \left(\frac{1}{R} + i\omega C + \frac{1}{i\omega(L + L_\mathrm{T})} \right)^{-1} , \tag{3.23}$$

where $\omega = 2\pi f$ denotes the angular frequency. Taking into account the capacitive coupling, the input impedance reads

$$Z_\mathrm{in}(\omega) = \frac{1}{i\omega C_\mathrm{c}^\mathrm{eff}} + Z_\mathrm{res}(\omega) , \tag{3.24}$$

with the effective coupling capacity $C_\mathrm{c}^\mathrm{eff} = C_\mathrm{c} C_\mathrm{p}/(C_\mathrm{c} + C_\mathrm{p})$. The resonance frequency of such a tank circuit can be derived as [Poz98]

$$f_\mathrm{r} = \frac{\omega_\mathrm{r}}{2\pi} = \frac{1}{2\pi\sqrt{(L + L_\mathrm{T})(C + C_\mathrm{c}^\mathrm{eff})}} , \tag{3.25}$$

where ω_r denotes the angular resonance frequency.

Analogously to the CPW-based quarter-wave resonators, the complex scatter parameter S_{21} of LERs can be determined, yielding again equation (3.16). However, the expression for the coupling quality factor, and hence, for the loaded quality factor, is different from the expression found for CPW-based quarter-wave resonators.

In the following, expressions for the coupling quality factor Q_c and for the amplitude I_T of the current running in the load inductor L_T are derived, both for an LER with a finite intrinsic quality factor Q_i and for an LER in the limit $Q_\mathrm{i} \to \infty$.

Superconducting, lossy LERs

Lossy LERs exhibit a finite intrinsic quality factor Q_i, which accounts for all loss mechanisms inside the resonator, such as radiative losses, dielectric losses and quasiparticle losses. In the equivalent circuit, shown in figure 3.3b, losses are accounted for by the resistance R, which is related to the intrinsic quality factor via [Poz98]

$$Q_\mathrm{i} = \frac{R}{\omega_\mathrm{r}(L + L_\mathrm{T})} . \tag{3.26}$$

For a finite resistance R, the input impedance Z_in of the LER, given by equation (3.24), exhibits a real part, which is - on resonance - significantly larger than the imaginary part. Therefore, on resonance, the input impedance can be expressed as

$$Z_\mathrm{in}(\omega_\mathrm{r}) \approx \mathrm{Re}(Z_\mathrm{in}(\omega_\mathrm{r})) = \frac{R}{1 + R\left(\omega_\mathrm{r} C - \frac{1}{\omega_\mathrm{r}(L+L_\mathrm{T})}\right)^2} . \tag{3.27}$$

Using equations (3.25) and (3.26), and the condition[1] $Q_\mathrm{i} \gg C/C_\mathrm{c}^\mathrm{eff} \sim \mathcal{O}(10)$, this expression simplifies to

$$Z_\mathrm{in}(\omega_\mathrm{r}) \approx \frac{1}{Q_\mathrm{i}\omega_\mathrm{r}^3(L+L_\mathrm{T})(C_\mathrm{c}^\mathrm{eff})^2}\,. \tag{3.28}$$

Subsequently, the scatter parameter on resonance $S_{21}(\omega_\mathrm{r}) = 2/(2+Z_0/Z_\mathrm{in}(\omega_\mathrm{r}))$ can be expressed in terms of equation (3.28). Additionally, from equation (3.16) follows that on resonance $S_{21}(\omega_\mathrm{r}) = S_{21}^\mathrm{min} = Q_\mathrm{l}/Q_\mathrm{i}$ holds true. Equating these two expressions for the scatter parameter, replacing the loaded quality factor Q_l with equation (3.18), and solving for the coupling quality factor Q_c yields

$$Q_\mathrm{c} = \frac{2}{Z_0\omega_\mathrm{r}^3(L+L_\mathrm{T})(C_\mathrm{c}^\mathrm{eff})^2}\,, \tag{3.29}$$

which does not exhibit any dependence on R or Q_i, and hence, it can be set by adjusting the geometry of the resonator and of the couplers.

The amplitude I_T of the current $i_\mathrm{T}(\omega, t) = I_\mathrm{T}(\omega)\sin(\omega t)$, running in the load inductor L_T upon a microwave signal applied at port 1 with voltage amplitude V_rf, is an important quantity, when coupling further devices to the load inductor, such as rf SQUIDs. For the circuit shown in figure 3.3b, the current amplitude I_T can be derived following Kirchhoff's circuit laws:

$$I_\mathrm{T}(\omega) = \frac{V_\mathrm{rf}}{\omega^2(L+L_\mathrm{T})C_\mathrm{c}^\mathrm{eff}}\frac{1-i\omega C_\mathrm{c}^\mathrm{eff}Z_\mathrm{in}}{2Z_\mathrm{in}+Z_0}\,. \tag{3.30}$$

On resonance, i.e. for $\omega = \omega_\mathrm{r}$, the input impedance Z_in can be expressed in terms of equation (3.28), and the imaginary part of the current amplitude I_T is negligibly small for $Q_\mathrm{i} \gg C/C_\mathrm{c}^\mathrm{eff} \sim \mathcal{O}(10)$. Hence, with the help of equations (3.18) and (3.29) the expression for I_T simplifies to

$$I_\mathrm{T} = V_\mathrm{rf}\sqrt{\frac{Q_\mathrm{l}^2}{2Q_\mathrm{c}\omega_\mathrm{r}(L+L_\mathrm{T})Z_0}}\,. \tag{3.31}$$

Superconducting, lossless LERs

In the limit $Q_\mathrm{i} \to \infty$, the above derivation does not hold true, as on resonance the input impedance vanishes: $Z_\mathrm{in}(\omega_\mathrm{r}) = 0$. However, for frequencies close to the resonance frequency, the input impedance can be approximated by its Taylor series expansion around ω_r up to first order:

$$Z_\mathrm{in}(\omega) = Z_\mathrm{in}(\omega_\mathrm{r}) + \left.\frac{\partial Z_\mathrm{in}(\omega)}{\partial\omega}\right|_{\omega=\omega_\mathrm{r}} \cdot(\omega-\omega_\mathrm{r}) + \mathcal{O}\left((\omega-\omega_\mathrm{r})^2\right)\,. \tag{3.32}$$

[1] This condition should easily be met for the planar niobium-based superconducting microwave resonators. Intrinsic quality factors up to $Q_\mathrm{i} \sim \mathcal{O}(10^7)$ have been demonstrated [Nog19].

In this approximation, for a frequency $\omega = \omega_\mathrm{r} \pm \Delta\omega/2$, where $\Delta\omega$ denotes the bandwidth of the resonance, the input impedance yields

$$Z_\mathrm{in}(\omega_\mathrm{r} \pm \Delta\omega/2) \approx \frac{\pm i\Delta\omega}{\omega_\mathrm{r}^4 (L + L_\mathrm{T})(C_\mathrm{c}^\mathrm{eff})^2} \,. \tag{3.33}$$

The transmission $|S_{21}(\omega_\mathrm{r} \pm \Delta\omega/2)|^2 = |2/(2 + Z_0/Z_\mathrm{in}(\omega_\mathrm{r} \pm \Delta\omega/2))|^2$ can thus be expressed in terms of equation (3.33). Additionally, from equation (3.16) follows that $|S_{21}(\omega_\mathrm{r} \pm \Delta\omega/2)|^2 = \frac{1}{2}(1 + (S_{21}^\mathrm{min})^2) \to \frac{1}{2}$ for $Q_\mathrm{i} \to \infty$. Equating the two expressions for the transmission, using that $\omega_\mathrm{r}/\Delta\omega = Q_\mathrm{l} = Q_\mathrm{c}$ for $Q_\mathrm{i} \to \infty$, and finally, solving for the coupling quality factor Q_c yields

$$Q_\mathrm{c} = \frac{2}{Z_0 \omega_\mathrm{r}^3 (L + L_\mathrm{T})(C_\mathrm{c}^\mathrm{eff})^2} \,, \tag{3.34}$$

which is exactly the same expression, as found for the lossy LER above. For large Q_i, the resonator bandwidth can be adjusted by adjusting the Q_c, for instance via the coupling capacitance.

Starting from equation (3.30), the current amplitude I_T in the limit $R \to \infty$ yields

$$I_\mathrm{T}(\omega) = \frac{V_\mathrm{rf}}{\left(1 - \frac{\omega^2}{\omega_\mathrm{r}^2}\right)\left(Z_0 - \frac{i}{\omega}\sqrt{2\omega_\mathrm{r}^3 (L + L_\mathrm{T}) Z_0 Q_\mathrm{c}}\right) + \frac{\omega^2}{\omega_\mathrm{r}^2}\sqrt{\frac{2\omega_\mathrm{r}(L+L_\mathrm{T})Z_0}{Q_\mathrm{c}}}} \,, \tag{3.35}$$

where equations (3.25) and (3.34) have been used for simplifications. On resonance, i.e. for $\omega = \omega_\mathrm{r}$, this expression simplifies to

$$I_\mathrm{T}(\omega_\mathrm{r}) = V_\mathrm{rf}\sqrt{\frac{Q_\mathrm{c}}{2\omega_\mathrm{r}(L + L_\mathrm{T})Z_0}} \,, \tag{3.36}$$

which resembles equation (3.31). In fact, in the limit $Q_\mathrm{l} = Q_\mathrm{c}$, the two equations are identical.

3.2.5 Representations of resonances

When characterising a transmission line, to which a CPW quarter-wave resonator or an LER is coupled, the resulting scatter parameter S_{21} can be visualised as presented in figure 3.4. Here, as an example, the shown data has been simulated, employing equation (3.16) for a resonator with resonance frequency $f_\mathrm{r} = 6\,\mathrm{GHz}$, loaded quality factor $Q_\mathrm{l} = 6000$ and intrinsic quality factor $Q_\mathrm{i} = 70000$. In figure 3.4a, the scatter parameter is plotted in the complex plane, where the axes represent the real part $\mathrm{Re}(S_{21})$ and the imaginary part $\mathrm{Im}(S_{21})$ of the scatter parameter, respectively. The resulting resonance circle is characterised by its centre

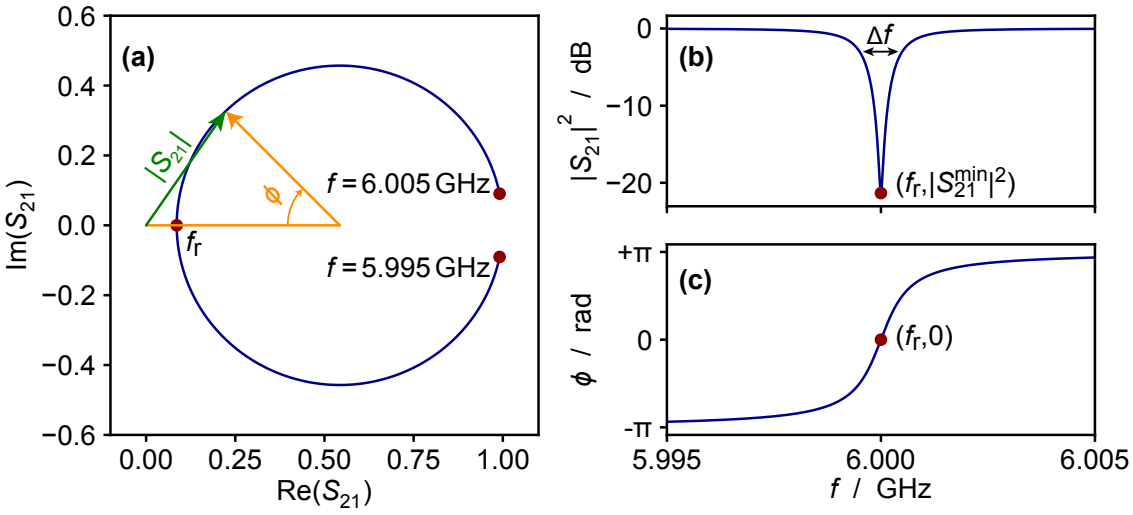

Figure 3.4: Different representations of the scatter parameter S_{21} and derived quantities in a frequency window of 10 MHz around a resonance at $f_\mathrm{r} = 6\,\mathrm{GHz}$ with loaded quality factor $Q_\mathrm{l} = 6000$ and intrinsic quality factor $Q_\mathrm{i} = 70000$: **(a)** resonance circle $S_{21}(f)$ in the complex plane, **(b)** Transmission $|S_{21}|^2$ and **(c)** resonator phase ϕ in dependence on the frequency f.

point $(x_\mathrm{c}, 0)$, where $x_\mathrm{c} = (1 + S_{21}^\mathrm{min})/2$, and by its radius $r = 1 - x_\mathrm{c}$. On resonance, the the scatter parameter $S_{21}(f_\mathrm{r}) = S_{21}^\mathrm{min} = Q_\mathrm{l}/Q_\mathrm{I}$ is real-valued. For frequencies $f \to \pm\infty$, the scatter parameter approaches the off-resonance point $(1, 0)$. The transmission $|S_{21}|^2 = [\mathrm{Re}(S_{21})]^2 + [\mathrm{Im}(S_{21})]^2$ is shown in figure 3.4b as a function of frequency f. The minimal transmission $|S_{21}^\mathrm{min}|^2$ is reached on resonance. The bandwidth $\Delta f = f_\mathrm{r}/Q_\mathrm{l}$ is indicated in the plot, and the transmission yields $|S_{21}(f_\mathrm{r} \pm \Delta f/2)|^2 = (1 + (S_{21}^\mathrm{min})^2)/2$. The resonator phase is defined as $\phi = \mathrm{arctan2}(\mathrm{Im}(S_{21}), (x_\mathrm{c} - \mathrm{Re}(S_{21})))$, where the function arctan2(y, x) denotes the 2-argument arctan, which is valid in all four quadrants of the Cartesian plane. In figure 3.4c, the resonator phase is plotted as a function of frequency. On resonance, the resonator phase is $\phi = 0$.

In a real measurement, the scatter parameter S_{21} is not only determined by the resonator parameters f_r, Q_l and Q_i, but it is also subject to environmental influences, introduced by components in between the resonator and the measurement device, such as cables, attenuators and amplifiers. In particular, the system attenuation or gain a leads to a decrease or increase of the radius of the resonance circle, the system phase offset α rotates the resonance circle in the complex plane and the cable delay τ twists the resonance circle. In order to extract the resonator parameters from a measured complex transmission S_{21}, these environmental influences have to be taken into account and corrected for. For this, the model

$$S_{21}(f) = ae^{i\alpha}e^{-2\pi i f\tau}\left[1 - \frac{\frac{Q_\mathrm{l}}{|Q_\mathrm{c}|}e^{i\phi_0}}{1 + 2iQ_\mathrm{l}\frac{f-f_\mathrm{r}}{f_\mathrm{r}}}\right], \tag{3.37}$$

is numerically fitted to the data, employing a dedicated algorithm [Pro15]. The term in the square brackets corresponds to an ideal resonator, while the prefactor describes the above mentioned environmental influences. This model takes also into account a potential impedance mismatch between the transmission line and the resonator, which is modelled by introducing a complex coupling quality factor $Q_\mathrm{c} = |Q_\mathrm{c}|e^{-i\phi_0}$. For a perfect impedance match, i.e. for $\phi_0 = 0$, the resonator term in the square brackets is identical to equation (3.16).

3.3 Non-hysteretic unshunted rf SQUIDs

The presence of a non-linear inductance is the key element to achieve the modulation of high-frequency carrier signals in the microwave SQUID multiplexer. The non-linear inductance can be introduced by a Josephson junction within a non-hysteretic unshunted rf SQUID, that is coupled to the microwave resonators of the multiplexer. In this section, the expression of the non-linear inductance of a Josephson junction is derived and the working principle of a non-hysteretic unshunted rf SQUID is reviewed, following [Kem12, Weg18a].

3.3.1 Non-linear inductance of a Josephson junction

A Josephson junction consists of two superconductors, which are weakly coupled. If, for instance, an isolating layer between two superconductors is sufficiently thin, the macroscopic wave function of the two superconductors overlap, allowing for coherent tunnelling of Cooper pairs. The Josephson junction is characterised by a critical current I_c. If an external current $I_\mathrm{S} \leq I_\mathrm{c}$ is applied to the Josephson junction, not exceeding the critical current, the total current flowing through the barrier is carried only by Cooper pairs. In this scenario, a phase difference φ appears over the Josephson junction, which satisfies the following relation, in accordance with the first Josephson equation [Jos62]:

$$I_\mathrm{S} = I_\mathrm{c}\sin\varphi\,. \tag{3.38}$$

This phase can be expressed in terms of the phase difference $\varphi_2 - \varphi_1$ of the two superconductors, and in terms of the magnetic vector potential $\mathbf{A}(\mathbf{r})$ inside the tunnel barrier of the Josephson junction:

$$\varphi = \varphi_2 - \varphi_1 - \frac{2\pi}{\Phi_0}\int_1^2 \mathbf{A}(\mathbf{r})\mathrm{d}\mathbf{l} \tag{3.39}$$

The relation between the time evolution of the phase difference $\dot{\varphi}$ and the voltage drop V across the junction is given by the second Josephson equation [Jos62]:

$$\dot{\varphi} = \frac{2\pi}{\Phi_0}V \tag{3.40}$$

where Φ_0 denotes the magnetic flux quantum.

Considering an alternating current with amplitude I_S smaller than the critical current I_c of the junction, using the time derivative of equation (3.38) and inserting it in equation (3.40), the voltage drop V results to be:

$$V = \frac{\Phi_0}{2\pi I_\mathrm{c}\cos\varphi}\dot{I}_\mathrm{S}\,. \tag{3.41}$$

The proportionality factor linking the voltage and the time derivative of the current is by definition an inductance, which can then be written as [Jos64]:

$$L(\varphi) \coloneqq \frac{\Phi_0}{2\pi I_\mathrm{c}\cos\varphi} = \frac{L_\mathrm{J}}{\cos\varphi} \tag{3.42}$$

where L_J is the Josephson inductance and $L(\varphi)$ indicates a phase-dependent non-linear inductance.

3.3.2 Working principle of non-hysteretic unshunted rf SQUIDs

A non-hysteretic unshunted rf SQUID consists of a superconducting loop with a characteristic inductance L_S, interrupted by a single Josephson junction. The inductance of the junction is given by the above derived equation (3.42).

Figure 3.5a shows a schematic of a non-hysteretic unshunted rf SQUID inductively coupled to a coil characterised by an inductance L_T and by a mutual inductance M_T between the coil and the rf SQUID loop.

Taking into account the quantisation of flux inside a closed superconducting loop, with the help of equation (3.39), the following expression can be derived:

$$\varphi + \frac{2\pi\Phi_\mathrm{tot}}{\Phi_0} = 2\pi n \quad \text{with} \quad n \in \mathbb{Z} \tag{3.43}$$

where Φ_tot is the total flux through the rf SQUID loop.

Inserting equation (3.43) into the first Josephson equation (equation (3.38)), the supercurrent I_S flowing through the rf SQUID in dependence on the total magnetic flux Φ_tot yields

$$I_\mathrm{S} = -I_\mathrm{c} \sin\left(2\pi \frac{\Phi_\mathrm{tot}}{\Phi_0}\right) \tag{3.44}$$

where the total magnetic flux Φ_tot accounts for the applied flux $\Phi_\mathrm{ext} = M_\mathrm{T} I_\mathrm{T}$ generated by applying a current I_T through the coil represented by L_T in figure 3.5a, and the screening flux $\Phi_\mathrm{scr} = L_\mathrm{S} I_\mathrm{S}$ induced by the screening current I_S:

$$\Phi_\mathrm{tot} = \Phi_\mathrm{ext} + \Phi_\mathrm{scr}\,. \tag{3.45}$$

Normalising the total magnetic flux and the external magnetic flux by writing the phase values $\varphi_\mathrm{tot} = 2\pi\Phi_\mathrm{tot}/\Phi_0$ and $\varphi_\mathrm{ext} = 2\pi\Phi_\mathrm{ext}/\Phi_0$, and introducing the screening parameter $\beta_\mathrm{L} = 2\pi L_\mathrm{S} I_\mathrm{c}/\Phi_0 = L_\mathrm{S}/L_\mathrm{J}$, the normalised total magnetic flux can be written as

$$\varphi_\mathrm{tot} = \varphi_\mathrm{ext} - \beta_\mathrm{L} \sin\varphi_\mathrm{tot}\,. \tag{3.46}$$

Hence, the behaviour of an rf SQUID significantly depends on its screening parameter β_L, as shown in figure 3.5b. When $\beta_\mathrm{L} \leq 1$, the relation between the total magnetic flux and the external magnetic flux is bijective and, in this case, the rf SQUID is defined as non-hysteretic. On the other hand, when β_L takes larger values, i.e. when $L_\mathrm{S} > L_\mathrm{J}$, a single value of the external flux is not linked uniquely to a single value of the total flux, leading to a hysteretic behaviour of the rf SQUID.

For the operation of the microwave SQUID multiplexer, typically the rf SQUID is inductively coupled to a resonator, such as an LC circuit or a quarter-wave resonator, operated with an alternating current. The periodic change in the non-linear Josephson inductance

$$L(\varphi_\mathrm{tot}) = \frac{\Phi_0}{2\pi I_\mathrm{c} \cos\varphi_\mathrm{tot}}\,, \tag{3.47}$$

derived from equation (3.42), induces a shift in the resonance frequency $f_\mathrm{r}(\varphi_\mathrm{tot})$ of the resonator.

In case the rf SQUID is hysteretic, i.e. $\beta_\mathrm{L} > 1$, the mapping between the external flux and the total flux is not unique and therefore transitions occur between different total flux states. This causes power dissipation mechanisms in the rf SQUID which turn out to be periodically dependent on the total flux, leading to a modulation of

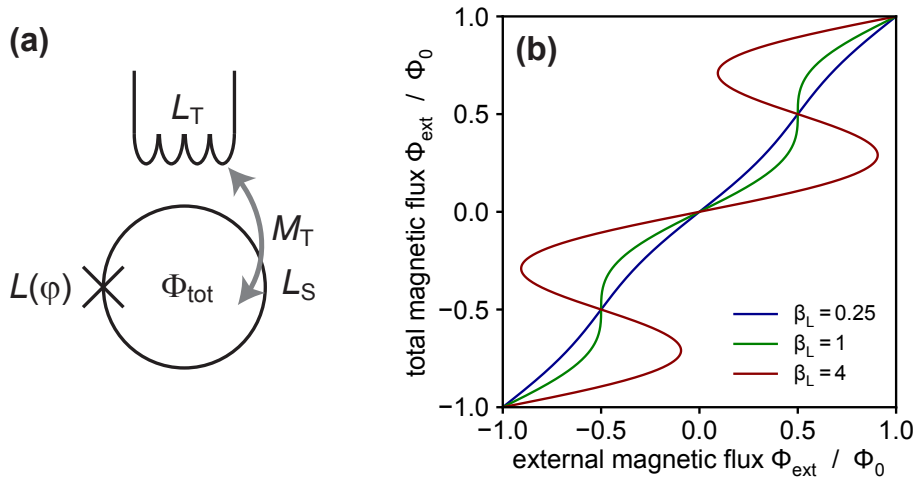

Figure 3.5: **(a)** Schematics of a non-hysteretic unshunted rf SQUID with inductance L_S, inductively coupled to a coil with inductance L_T. The mutual inductance between the coil and the rf SQUID is represented by the arrow and it is denoted by M_T. **(b)** Plot showing the relation between the total magnetic flux Φ_{tot} through the rf SQUID loop and the external magnetic flux Φ_{ext} for different values of the screening parameter β_L.

the loaded quality factor $Q_l = Q_l(\varphi_{tot})$. On the other hand, in the non-hysteretic mode, i.e. $\beta_L \leq 1$, the rf SQUID can be considered as quasi-dissipationless and the loaded quality factor becomes flux-independent.

3.4 Working principle of the microwave SQUID multiplexer

In the following, the working principle of a microwave SQUID multiplexer is introduced, following [Kem12, Weg18a]. In figure 3.6, a microwave SQUID multiplexer based on N quarter-wave resonators is sketched. Each channel i, with $i = 1, ..., N$, is comprised of a CPW quarter-wave resonator, which is inductively terminated by a load inductor L_T. The load inductor of each channel is coupled to a non-hysteretic, unshunted rf SQUID. The i-th resonator exhibits a lengths $l_{r,i}$ and is coupled to a common transmission line via a coupling capacity $C_{c,i}$. Each channel exhibits a unique resonance frequency, which can be adjusted by the resonator length $l_{r,i}$. Additionally, the bandwidth of each resonator can be tuned by the coupling capacity $C_{c,i}$. In a microwave SQUID multiplexer based on LERs, the basic set-up is the same as in the case of the-CPW-based microwave SQUID multiplexer, however, the resonance frequencies are tuned by adjusting the meandering inductance L or the interdigital capacity C.
Each rf SQUID consists of a superconducting loop with inductance L_S, which is

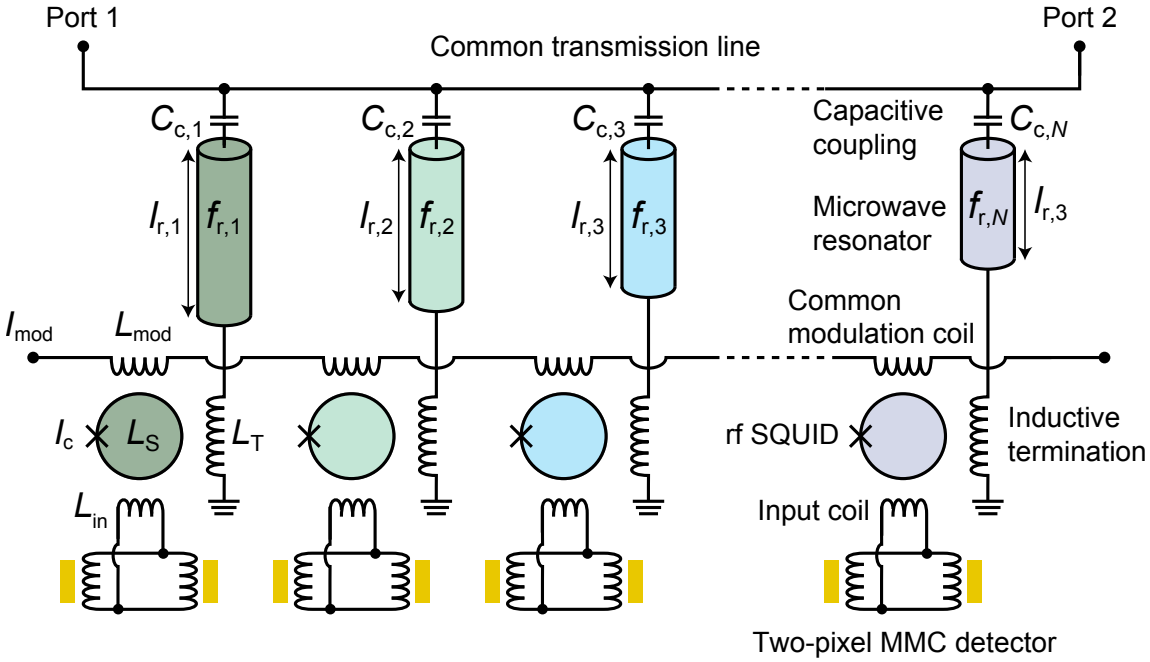

Figure 3.6: Sketch of a microwave SQUID multiplexer based on N quarter-wave resonators. Each channel i ($i = 1, ..., N$) is characterised by a unique resonance frequency, and is coupled capacitively to a common transmission line and inductively to an rf SQUID. Each rf SQUID is coupled inductively to a common modulation line and to an individual MMC detector comprised of two pixels, marked in yellow. This figure is taken from [Weg18a].

interrupted by a Josephson junction with critical current I_c. Gradiometric MMC detectors, comprised of two pixels each, are coupled inductively to the rf SQUIDs, forming superconducting flux transformers with the input coils L_{in} of the rf SQUIDs. Moreover, all rf SQUIDs are coupled to a common modulation coil, which allows for a simultaneous change of the magnetic flux Φ_{ext} in all rf SQUIDs by injecting a modulation current I_{mod} into the common modulation coil.

According to equation (3.47), a non-hysteretic, unshunted rf SQUID acts as a parametric inductance, as the inductance of the Josephson junction exhibits a dependence on the magnetic flux. Therefore, the state of the MMC affects the inductance of the rf SQUID. As the rf SQUID is coupled inductively to the load inductor L_T of a resonator, the corresponding resonance frequency will exhibit a dependence on the state of the MMC. Hence, the state of the MMC can be measured by tracking the resonance frequency.

This tracking could in principle be achieved by means of a vector network analyser, however, as this method is comparably slow, the time resolution achievable with the microwave SQUID multiplexer would be reduced significantly. An alternative read-

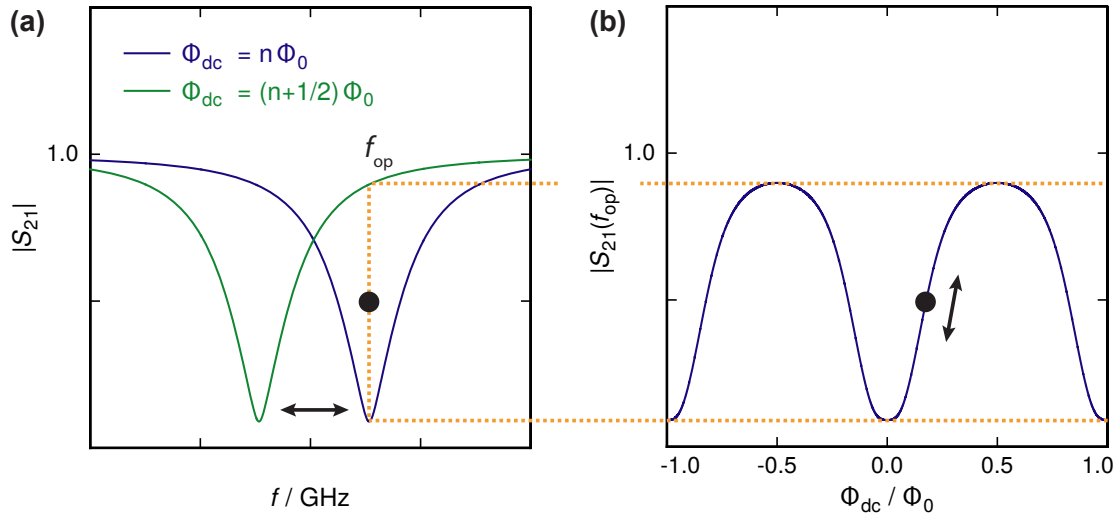

Figure 3.7: A resonator of the microwave SQUID multiplexer is probed with fixed power and fixed read-out frequency f_{op}. From the measured transmission $|S_{21}(\Phi_{\mathrm{dc}}, f_{\mathrm{op}})|$, the flux state Φ_{dc} can be inferred. **(a)** Resonance curves for $\Phi_{\mathrm{dc}} = n\Phi_0$ and $\Phi_{\mathrm{dc}} = (n + 1/2)\Phi_0$ and **(b)** the resulting transmission $|S_{21}(\Phi_{\mathrm{dc}}, f_{\mathrm{op}})|$ for varying flux Φ_{dc}. This figure is adopted from [Weg18a].

out scheme for a multiplexer SQUID multiplexer channel is based on the excitation of the corresponding resonance by applying a sinusoidal microwave carrier with an operational frequency f_{op} and a fixed power at port 1, and on the simultaneous measurement of the transmission $|S_{21}(f_{\mathrm{op}})|$ at port 2. The measurement concept is visualised in figure 3.7. The transmission $|S_{21}(f)|$ for an arbitrary multiplexer channel is shown in figure 3.7a for two values of the magnetic flux Φ_{dc} externally applied to the rf SQUID. As explained above, the resonance frequency $f_{\mathrm{r}}(\Phi_{\mathrm{dc}})$ depends on the magnetic flux state of the rf SQUID coupled inductively to the load inductor of the resonator. The shown resonance curves correspond to the limiting cases $\Phi_{\mathrm{dc}} = n\Phi_0$ and $\Phi_{\mathrm{dc}} = (n + 1/2)\Phi_0$, for which the resonance frequency is at its maximum and minimum, respectively. Due to the flux dependence of the resonance frequency $f_{\mathrm{r}}(\Phi_{\mathrm{dc}})$, the transmitted signal $|S_{21}(\Phi_{\mathrm{dc}}, f_{\mathrm{op}})|$ also exhibits a flux dependence, as visualised in figure 3.7b. Therefore, the state of the MMC coupled inductively to the rf SQUID can be monitored by continuously measuring the transmission at a fixed read-out frequency f_{op}. Applying a waveform composed of N sinusoidal carriers with frequencies $f_{\mathrm{op},i}$ $(i = (1, ..., N))$, adjusted to the resonance of the i-th multiplexer channel, to port 1 of the multiplexer, and monitoring the transmission at port 2 allows for a simultaneous and continuous read-out of all MMC detectors coupled to the microwave SQUID multiplexer.

Different models have been developed to describe the microwave SQUID multiplexer quantitatively [Mat11, Kem12, Weg21]. The results relevant to this thesis are sum-

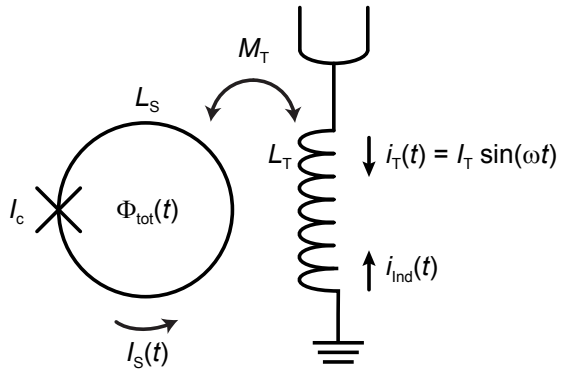

Figure 3.8: Schematic representation of a non-hysteretic, unshunted rf SQUID coupled to the load inductor of a superconducting, inductively terminated quarter-wave resonator. This figure is taken from [Weg18a].

marised in the following. In figure 3.8, an inductively terminated quarter-wave resonator with load inductor L_T is coupled to an rf SQUID with inductance L_S and critical current of the Josephson junction I_c. The total magnetic flux threading the rf SQUID $\Phi_\mathrm{tot}(t)$ includes the contributions from the externally applied magnetic flux $\Phi_\mathrm{ext}(t)$, the screening flux $\Phi_\mathrm{scr}(t) = L_\mathrm{S} I_\mathrm{S}(t)$ caused by the screening currents following equation (3.44), and the rf magnetic flux $\Phi_\mathrm{rf} = M_\mathrm{T} I_\mathrm{T}$ introduced by the ac currents $i_\mathrm{T} = I_\mathrm{T} \sin(\omega t)$ in the load inductor of the resonator. Therefore, following from equation (3.44), the current running in the rf SQUID is given by

$$I_\mathrm{S}(t) = -I_\mathrm{c} \sin\left(\varphi_\mathrm{ext} + \varphi_\mathrm{rf} \sin(\omega t) + \beta_\mathrm{L} \frac{I_\mathrm{S}(t)}{I_\mathrm{c}}\right), \tag{3.48}$$

where the notation of normalised magnetic fluxes $\varphi_i = 2\pi\Phi_i/\Phi_0$ with the magnetic flux quantum Φ_0 is used. Due to the inductive coupling of the rf SQUID to the load inductor of the resonator, a current $i_\mathrm{ind}(t, \varphi_\mathrm{ext}, \varphi_\mathrm{rf})$ in the load inductor is induced by the current I_S in the rf SQUID. Therefore, the total current running in the load inductor is the sum of $i_\mathrm{T}(t)$ and $i_\mathrm{ind}(t, \varphi_\mathrm{ext}, \varphi_\mathrm{rf})$. Under the assumption that these two contributions are in phase, the effective load inductance of the resonator, i.e. the inductance of the system comprised of the load inductor and the rf SQUID, can be calculated as

$$L_\mathrm{T,eff}(\varphi_\mathrm{ext}, \varphi_\mathrm{rf}) = L_\mathrm{T} \left[1 + \frac{i_\mathrm{ind}(t, \varphi_\mathrm{ext}, \varphi_\mathrm{rf})}{i_\mathrm{T}(t)}\right]. \tag{3.49}$$

Consequently, the resonance frequency of a microwave SQUID multiplexer channel based on a quarter-wave resonator, following equation (3.17), can be expressed as

$$f_\mathrm{r}(\varphi_\mathrm{dc}, \varphi_\mathrm{rf}) = \frac{f_0}{1 + 4 f_0 (C_\mathrm{c} Z_0 + L_\mathrm{T,eff}(\varphi_\mathrm{ext}, \varphi_\mathrm{rf})/Z_0)}. \tag{3.50}$$

The derivation for $L_\mathrm{T,eff}$ holds true also for microwave SQUID multiplexers based on LERs, and hence, the corresponding resonance frequency follows from equation (3.25), yielding

$$f_\mathrm{r} = \frac{1}{2\pi \sqrt{(L + L_\mathrm{T,eff}(\varphi_\mathrm{ext}, \varphi_\mathrm{rf}))(C + C_\mathrm{c}^\mathrm{eff})}}. \tag{3.51}$$

Due to the recursive structure of equation (3.48), to date no analytic solution has been found for $L_{\mathrm{T,eff}}$, however, approximate solutions can be found for certain cases.

3.4.1 Approximation for $L_{\mathrm{T,eff}}$ in the limit of small read-out powers

For small read-out powers, and hence for a small current amplitude I_{T} in the load inductor, the normalised rf magnetic flux $\varphi_{\mathrm{rf}} = 2\pi I_{\mathrm{T}} M_{\mathrm{T}}/\Phi_0$ can be neglected in equation (3.48). For a non-hysteretic rf SQUID, i.e. for $\beta_{\mathrm{L}} < 1$, the effective load inductance can be derived, resulting in

$$L_{\mathrm{T,eff}}(\varphi_{\mathrm{ext}}) = L_{\mathrm{T}} - \frac{M_{\mathrm{T}}^2}{L_{\mathrm{S}}} \frac{\beta_{\mathrm{L}} \cos\left(\varphi_{\mathrm{dc}}(\varphi_{\mathrm{ext}})\right)}{1 + \beta_{\mathrm{L}} \cos\left(\varphi_{\mathrm{dc}}(\varphi_{\mathrm{ext}})\right)}\,, \tag{3.52}$$

where the normalised dc magnetic flux $\varphi_{\mathrm{dc}} = \varphi_{\mathrm{ext}} - \beta_{\mathrm{L}} \sin(\varphi_{\mathrm{dc}})$, threading the rf SQUID, takes into account the externally applied flux as well as a magnetic flux resulting from screening currents in the rf SQUID.

For a microwave SQUID multiplexer based on CPW quarter-wave resonators, following a first order Taylor series expansion of equation (3.50), the resulting flux dependent resonance frequency can be expressed as

$$f_{\mathrm{r}}(\varphi_{\mathrm{ext}}) \approx f_0 - 4 f_0^2 \left[C_{\mathrm{c}} Z_0 + \frac{L_{\mathrm{T}}}{Z_0} - \frac{M_{\mathrm{T}}^2}{Z_0 L_{\mathrm{S}}} \frac{\beta_{\mathrm{L}} \cos\left(\varphi_{\mathrm{dc}}(\varphi_{\mathrm{ext}})\right)}{1 + \beta_{\mathrm{L}} \cos\left(\varphi_{\mathrm{dc}}(\varphi_{\mathrm{ext}})\right)} \right] \tag{3.53}$$

with a maximum resonance frequency shift of

$$\Delta f_{\mathrm{r}}^{\mathrm{max}} \approx \frac{4 f_0^2 M_{\mathrm{T}}^2}{Z_0 L_{\mathrm{S}}} \frac{2\beta_{\mathrm{L}}}{1 - \beta_{\mathrm{L}}^2}\,. \tag{3.54}$$

Analogously, for a microwave SQUID multiplexer based on LERs, following a first order Taylor series expansion of equation (3.51), the flux dependent resonance frequency can be expressed as

$$f_{\mathrm{r}}(\varphi_{\mathrm{ext}}) \approx f_{\mathrm{r},0} \left(1 + \frac{M_{\mathrm{T}}^2}{2 L_{\mathrm{S}} (L + L_{\mathrm{T}})} \frac{\beta_{\mathrm{L}} \cos\left(\varphi_{\mathrm{dc}}(\varphi_{\mathrm{ext}})\right)}{1 + \beta_{\mathrm{L}} \cos\left(\varphi_{\mathrm{dc}}(\varphi_{\mathrm{ext}})\right)} \right)\,, \tag{3.55}$$

where the bare resonance frequency $f_{\mathrm{r},0}$ is given by equation (3.25). The maximum resonance frequency shift yields

$$\Delta f_{\mathrm{r}}^{\mathrm{max}} \approx \frac{f_{\mathrm{r},0} M_{\mathrm{T}}^2}{2 L_{\mathrm{S}} (L + L_{\mathrm{T}})} \frac{2\beta_{\mathrm{L}}}{1 - \beta_{\mathrm{L}}^2}\,. \tag{3.56}$$

3.4.2 Generalised approximation of $L_{\mathrm{T,eff}}$

For arbitrary values of the normalised rf magnetic flux φ_{rf} threading a non-hysteretic rf SQUID ($\beta_{\mathrm{L}} < 1$), an approximate solution for $L_{\mathrm{T,eff}}$ can be found by expanding

equation (3.48) in β_L up to second order, solving for I_S and expanding the solution once more in β_L, which has been demonstrated in [Weg18a, Weg21]. Finally, this so-called revised model of the microwave SQUID multiplexer yields

$$L_{\mathrm{T,eff}}(\varphi_\mathrm{ext}, \varphi_\mathrm{rf}) = L_\mathrm{T} - \frac{M_\mathrm{T}^2}{L_\mathrm{S}} \frac{2\beta_\mathrm{L}}{\varphi_\mathrm{rf}} \sum_{i,j} p_{i,j}(\varphi_\mathrm{ext}, \varphi_\mathrm{rf}) \tag{3.57}$$

with the summands

$$p_{i,j}(\varphi_\mathrm{ext}, \varphi_\mathrm{rf}) = a_{i,j} \beta_\mathrm{L}^{b_{i,j}} \cos\big(c_{i,j}\varphi_\mathrm{ext}\big) J_1(c_{i,j}\varphi_\mathrm{rf}) \,, \tag{3.58}$$

where i denotes the Taylor expansion order, j the different contributions of each order, and $J_1(x)$ the Bessel function of first kind. The numeric values of the parameters $a_{i,j}$, $b_{i,j}$ and $c_{i,j}$ are summarised in table A.1 in the appendix up to $i = 10$ [Weg21].

Consequently, for a microwave SQUID multiplexer based on CPW quarter-wave resonators, the flux dependence of the resonance frequencies can be expressed as

$$f_\mathrm{r}(\varphi_\mathrm{ext}, \varphi_\mathrm{rf}) \approx f_0 - 4f_0^2 \left(C_\mathrm{c} Z_0 + \frac{L_\mathrm{T}}{Z_0} - \frac{M_\mathrm{T}^2}{Z_0 L_\mathrm{S}} \frac{2\beta_\mathrm{L}}{\varphi_\mathrm{rf}} \sum_{i,j} p_{i,j}(\varphi_\mathrm{ext}, \varphi_\mathrm{rf}) \right) . \tag{3.59}$$

For a microwave SQUID multiplexer channel based on an LER, the flux dependent resonance frequency is given by

$$f_\mathrm{r}(\varphi_\mathrm{ext}, \varphi_\mathrm{rf}) \approx f_{\mathrm{r},0} \left(1 + \frac{M_\mathrm{T}^2}{2L_\mathrm{S}(L + L_\mathrm{T})} \frac{2\beta_\mathrm{L}}{\varphi_\mathrm{rf}} \sum_{i,j} p_{i,j}(\varphi_\mathrm{ext}, \varphi_\mathrm{rf}) \right) . \tag{3.60}$$

3.4.3 Bandwidth and maximum frequency shift

In order to characterise a multiplexer in terms of maximum frequency shift $\Delta f_\mathrm{r}^\mathrm{max}$ in relation to the resonator bandwidth Δf, the dimensionless parameter

$$\eta = \frac{\Delta f_\mathrm{r}^\mathrm{max}}{\Delta f} \tag{3.61}$$

is introduced. For a microwave SQUID multiplexer exhibiting a too large value of η, the transmission $|S_{21}(\Phi_\mathrm{dc}, f_\mathrm{op})|$ at the read-out frequency f_op becomes partially flux insensitive, while a microwave SQUID multiplexer with too small values of η suffers from a reduced signal amplitude [Weg18a]. The ratios $\eta \approx 0.8$ [Mat17] and $\eta \approx 1.0$ [Weg18a] proved to be good compromises.

3.5 Noise contributions

In order not to deteriorate the excellent intrinsic energy resolution of MMCs, the noise contributions from the read-out system have to be minimised. The noise power

density spectra, measured for microwave SQUID multiplexer-based read-out systems, can exhibit both frequency independent white noise components and $1/f$-type noise components. As it will be explained in section 3.6, due to the flux-ramp modulation-based linearisation scheme for the response of the microwave SQUID multiplexer, the $1/f$-type noise components will be greatly suppressed during regular operation of the microwave SQUID multiplexer [Mat12, Ric21]. Therefore, among the noise contributions of the microwave read-out system, the dominant white noise component will have the most significant impact on the achievable energy resolution within ECHo-100k.

3.5.1 System noise

The read-out power applied to a microwave SQUID multiplexer channel for the read-out of MMCs is typically in the order of $P_{\mathrm{rf}} \approx -70\,\mathrm{dBm}$. In order not to be limited by the thermal noise of the room temperature components processing the signal from the microwave SQUID multiplexer, a low-noise amplification is needed. While the $1/f$-type noise contribution of typical semi-conductor-based low-noise amplifiers is suppressed by the flux-ramp modulation, the white noise contribution of these amplifiers has major impact on the overall white noise performance of the microwave read-out chain.

The white noise contribution of the microwave read-out chain, including the low-noise amplifiers, can be expressed in terms of a noise temperature $T_{\mathrm{N,system}}$, which will be explained in more detail in chapter 4. In order to quantify the impact of the corresponding apparent voltage noise $S_{V,\mathrm{system}} = 4k_{\mathrm{B}}T_{\mathrm{N,system}}Z_0$ acting on the transmission line of the microwave SQUID multiplexer, the system noise is typically referenced to the rf SQUID in terms of apparent magnetic flux noise. For this, the transfer coefficient $V_\Phi^{\max}$ is required, which translates an infinitesimal change of flux in the rf SQUID to an infinitesimal change of the voltage amplitude V_{rf} of the read-out signal on resonance at an optimal working point $\Phi_{\mathrm{ext}} = \Phi_{\mathrm{ext}}^{\mathrm{opt}}$. The transfer coefficient can be derived [Mat11, Weg18a], yielding

$$V_\Phi^{\max} = V_{\mathrm{rf}} \left(\frac{\partial \,\mathrm{Im}(S_{21})}{\partial f} \right)_{f=f_{\mathrm{r}}} \left(\frac{\partial f_{\mathrm{r}}}{\partial \Phi_{\mathrm{ext}}} \right)_{\Phi_{\mathrm{ext}}=\Phi_{\mathrm{ext}}^{\mathrm{opt}}} . \tag{3.62}$$

In the following, the system noise in terms of apparent magnetic flux noise is derived for a microwave SQUID multiplexer based on CPW quarter-wave resonators, as well as for a microwave SQUID multiplexer based on LERs.

For a microwave SQUID multiplexer based on CPW quarter-wave resonators, the voltage amplitude V_{rf} of the read-out signal on the transmission line can be expressed in terms of the rf magnetic flux Φ_{rf}, applying equation (3.22) and the relations

$P_{\mathrm{rf}} = V_{\mathrm{rf}}^2/(2Z_0)$ and $\Phi_{\mathrm{rf}} = I_{\mathrm{T}} M_{\mathrm{T}}$:

$$V_{\mathrm{rf}}^{\mathrm{CPW}} = \frac{\Phi_{\mathrm{rf}} Z_0}{M_{\mathrm{T}}} \sqrt{\frac{\pi}{8} \frac{Q_{\mathrm{c}}}{Q_{\mathrm{l}}^2}} \,. \tag{3.63}$$

The derivative of the imaginary part with respect to frequency can be derived from equation (3.16). On resonance, i.e. for $f = f_{\mathrm{r}}$, this yields

$$\left(\frac{\partial \,\mathrm{Im}(S_{21})}{\partial f} \right)_{f=f_{\mathrm{r}}} = \frac{2Q_{\mathrm{l}}^2}{f_{\mathrm{r}} Q_{\mathrm{c}}} \,. \tag{3.64}$$

The change of the resonance frequency upon a change of flux can be calculated from equation (3.59), resulting in

$$\left(\frac{\partial f_{\mathrm{r}}^{\mathrm{CPW}}}{\partial \Phi_{\mathrm{ext}}} \right)_{\Phi_{\mathrm{ext}}=\Phi_{\mathrm{ext}}^{\mathrm{opt}}} = \frac{4 f_0^2 M_{\mathrm{T}}^2}{Z_0 L_{\mathrm{S}}} \frac{2\beta_{\mathrm{L}}}{\Phi_{\mathrm{rf}}} \sum_{i,j} \left. \frac{\partial p_{i,j}}{\partial \varphi_{\mathrm{ext}}} \right|_{\Phi_{\mathrm{ext}}=\Phi_{\mathrm{ext}}^{\mathrm{opt}}} \,. \tag{3.65}$$

Therefore, the transfer coefficient is given by

$$V_{\Phi}^{\mathrm{max,CPW}} = \sqrt{32\pi \frac{Q_{\mathrm{l}}^2}{Q_{\mathrm{c}}}} \frac{f_0^2}{f_{\mathrm{r}}} \frac{M_{\mathrm{T}}}{L_{\mathrm{s}}} \beta_{\mathrm{l}} \sum_{i,j} \left. \frac{\partial p_{i,j}}{\partial \varphi_{\mathrm{ext}}} \right|_{\Phi_{\mathrm{ext}}=\Phi_{\mathrm{ext}}^{\mathrm{opt}}} \,, \tag{3.66}$$

yielding the apparent magnetic flux noise

$$S_{\Phi,\mathrm{system}}^{\mathrm{CPW}} = \frac{S_{V,\mathrm{system}}}{(V_{\Phi}^{\mathrm{max}})^2} = \frac{k_{\mathrm{B}} T_{\mathrm{N,system}} Z_0 L_{\mathrm{S}}^2 Q_{\mathrm{c}}}{8\pi Q_{\mathrm{l}}^2 M_{\mathrm{T}}^2 \beta_{\mathrm{L}}^2} \frac{f_{\mathrm{r}}^2}{f_0^4} \left(\sum_{i,j} \left. \frac{\partial p_{i,j}}{\partial \varphi_{\mathrm{ext}}} \right|_{\Phi_{\mathrm{ext}}=\Phi_{\mathrm{ext}}^{\mathrm{opt}}} \right)^{-2} \,. \tag{3.67}$$

For a microwave SQUID multiplexer based on LERs, the voltage amplitude V_{rf} can be derived from equation (3.31), using the relations $P_{\mathrm{rf}} = V_{\mathrm{rf}}^2/(2Z_0)$ and $\Phi_{\mathrm{rf}} = I_{\mathrm{T}} M_{\mathrm{T}}$:

$$V_{\mathrm{rf}}^{\mathrm{LER}} = \frac{\Phi_{\mathrm{rf}}}{M_{\mathrm{T}}} \sqrt{4\pi f_{\mathrm{r},0} Z_0 (L + L_{\mathrm{T}}) \frac{Q_{\mathrm{c}}}{Q_{\mathrm{l}}^2}} \,. \tag{3.68}$$

The derivative of the imaginary part with respect to frequency can be derived from equation (3.16) and yields once more equation (3.64).
The change of the resonance frequency upon a change of flux can be calculated from equation (3.60), resulting in

$$\left(\frac{\partial f_{\mathrm{r}}^{\mathrm{LER}}}{\partial \Phi_{\mathrm{ext}}} \right)_{\Phi_{\mathrm{ext}}=\Phi_{\mathrm{ext}}^{\mathrm{opt}}} = \frac{f_{\mathrm{r},0} M_{\mathrm{T}}^2}{2 L_{\mathrm{S}} (L + L_{\mathrm{T}})} \frac{2\beta_{\mathrm{L}}}{\Phi_{\mathrm{rf}}} \sum_{i,j} \left. \frac{\partial p_{i,j}}{\partial \varphi_{\mathrm{ext}}} \right|_{\Phi_{\mathrm{ext}}=\Phi_{\mathrm{ext}}^{\mathrm{opt}}} \tag{3.69}$$

Therefore, the transfer coefficient for a microwave SQUID multiplexer based on LERs is given by

$$V_{\Phi}^{\mathrm{max,LER}} = \sqrt{16\pi \frac{Q_{\mathrm{l}}^2}{Q_{\mathrm{c}}} \frac{f_{\mathrm{r},0} Z_0}{L + L_{\mathrm{T}}}} \frac{M_{\mathrm{T}}}{L_{\mathrm{s}}} \beta_{\mathrm{l}} \sum_{i,j} \left. \frac{\partial p_{i,j}}{\partial \varphi_{\mathrm{ext}}} \right|_{\Phi_{\mathrm{ext}}=\Phi_{\mathrm{ext}}^{\mathrm{opt}}} \,, \tag{3.70}$$

yielding the apparent magnetic flux noise

$$S_{\Phi,\mathrm{system}}^{\mathrm{LER}} = \frac{S_{V,\mathrm{system}}}{\left(V_\Phi^{\max}\right)^2} = \frac{k_\mathrm{B} T_{\mathrm{N,system}} L_\mathrm{S}^2 (L + L_\mathrm{T}) Q_\mathrm{c}}{4\pi Q_\mathrm{l}^2 M_\mathrm{T}^2 \beta_\mathrm{L}^2 f_{\mathrm{r},0}} \left(\sum_{i,j} \left. \frac{\partial p_{i,j}}{\partial \varphi_\mathrm{ext}} \right|_{\Phi_\mathrm{ext}=\Phi_\mathrm{ext}^\mathrm{opt}} \right)^{-2} . \quad (3.71)$$

Comparison of the system noise for CPW-based and LER-based multiplexers

In order to compare the apparent magnetic flux noise of the two different microwave SQUID multiplexer configurations, equations (3.67) and (3.71) can be rewritten using the radius of the resonance circle $r = Q_\mathrm{l}/2Q_\mathrm{c}$ and the parameter $\eta_0 := \lim_{\varphi_\mathrm{rf}\to 0} \eta$. For the microwave SQUID multiplexer based on CPW quarter-wave resonators, this yields

$$S_{\Phi,\mathrm{system}}^{\mathrm{CPW}} = \frac{k_\mathrm{B} T_{\mathrm{N,system}} L_\mathrm{S}}{4 r \eta_0 \omega_\mathrm{r} (\beta_\mathrm{L} - \beta_\mathrm{L}^3)} \left(\sum_{i,j} \left. \frac{\partial p_{i,j}}{\partial \varphi_\mathrm{ext}} \right|_{\Phi_\mathrm{ext}=\Phi_\mathrm{ext}^\mathrm{opt}} \right)^{-2} \left(\frac{2 f_\mathrm{r}}{f_0} \right)^2 , \quad (3.72)$$

and for the microwave SQUID multiplexer based on LERs, this results in

$$S_{\Phi,\mathrm{system}}^{\mathrm{LER}} = \frac{k_\mathrm{B} T_{\mathrm{N,system}} L_\mathrm{S}}{4 r \eta_0 \omega_\mathrm{r} (\beta_\mathrm{L} - \beta_\mathrm{L}^3)} \left(\sum_{i,j} \left. \frac{\partial p_{i,j}}{\partial \varphi_\mathrm{ext}} \right|_{\Phi_\mathrm{ext}=\Phi_\mathrm{ext}^\mathrm{opt}} \right)^{-2} . \quad (3.73)$$

Based on these two equations, in figure 3.9, the expected system noise for CPW-based and LER-based microwave SQUID multiplexers in units of apparent magnetic flux noise is plotted as a function of the microwave read-out power. For both cases, the resonance frequency $f_\mathrm{r} = 6\,\mathrm{GHz}$, the bandwidth $\Delta f = 1\,\mathrm{MHz}$, the screening parameter $\beta_\mathrm{L} = 0.6$ and the rf SQUID inductance $L_\mathrm{S} = 45\,\mathrm{pH}$ have been assumed. Additionally, $\eta_0 = 1$ and the limit of high intrinsic quality factors, i.e. $r \to 1/2$, have been considered. The external flux bias has been set to $\Phi_\mathrm{ext}^\mathrm{opt} = 0.38\,\Phi_0$ and the system noise temperature to 4 K. For the CPW-based microwave SQUID multiplexer $f_0 = 6.7\,\mathrm{GHz}$ and for the LER-based microwave SQUID multiplexer $L + L_\mathrm{T} = 2.2\,\mathrm{nH}$ have been assumed. All of these values are typical values for a microwave SQUID multiplexer for the read-out of MMCs. At low read-out powers, the system noise in units of apparent magnetic flux noise decreases with increasing microwave read-out power, until a minimum is reached. At powers beyond the minimum, the flux noise level increases dramatically, because the transfer coefficient $V_\Phi^{\max}$ approaches zero due to the power dependence of the resonance frequency shift. After the zero-crossing of the transfer coefficient, the flux noise level drops, reaches a minimum, and diverges again at the next zero-crossing, and so on. Since the noise levels associated with the minima increase with increasing microwave power, the optimal read-out power in terms of system noise is the microwave power corresponding to the first

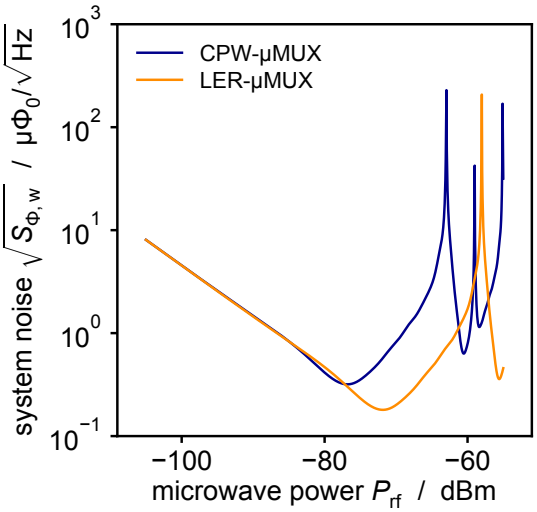

Figure 3.9: Simulated system noise in units of apparent magnetic flux noise for a microwave SQUID multiplexer based on CPW quarter-wave resonators (CPW-μMUX) and a microwave SQUID multiplexer based on LERs (LER-μMUX). The simulation parameters are reported in the main text.

minimum. As can be seen in figure 3.9, the first minimum of the system noise level associated with the CPW-base microwave SQUID multiplexer is at a lower microwave power and at a higher flux noise level than the minimum associated to the LER-based microwave SQUID multiplexer. In fact, for the CPW-based microwave SQUID multiplexer, the minimum is located at $P_{\text{rf}} = -76.8\,\text{dBm}$ and exhibits a flux noise level of $0.33\,\mu\Phi_0/\sqrt{\text{Hz}}$, while for the LER-based microwave SQUID multiplexer, the minimum is at $P_{\text{rf}} = -71.8\,\text{dBm}$ with a flux noise level of $0.18\,\mu\Phi_0/\sqrt{\text{Hz}}$. The reason for the different noise levels can be found comparing equations (3.72) and (3.73): the two equations differ by a factor $(2f_\text{r}/f_0)^2$ with $2f_\text{r} > f_0$.
The two equations reach their respective first minimum at the same rf magnetic flux $\Phi_{\text{rf}}^{\text{opt}}$. However, comparing equation (3.63) and (3.68), the rf power needed to create the flux $\Phi_{\text{rf}}^{\text{opt}}$ in the rf SQUIDs depends on the type of resonator, which explains the shift in microwave power P_{rf} of the two minima.

Summarising, microwave SQUID multiplexers based on LERs are expected to feature a better system noise performance than CPW-based microwave SQUID multiplexers, while requiring a higher microwave read-out power.

3.5.2 Further noise contributions

Both the capacitance per unit length of a CPW resonator (equation (3.8)) and the interdigital capacity of an LER (compare [Igr04]) depend on the relative permittivity ε_r of the dielectric materials in close proximity to the resonators, such as the wafer substrate. At low temperatures, fluctuating two-level systems present in the dielectric materials [And72] affect the relative permittivity, and consequently the capacity of the resonators, which manifests in a frequency noise S_{f_r} and translates into an apparent magnetic flux noise in the rf SQUID. This noise contribution features

typically a $1/f$-type spectral noise power density [Maz04, Gao08a, Bar09]. Due to the flux-ramp modulation read-out scheme, which will be used for the linearisation of the microwave SQUID multiplexer response within ECHo-100k, this contribution will be greatly suppressed.

The rf SQUID itself is subject to intrinsic noise contributions resulting from fundamental SQUID properties [Ryh89]. These contribution are, however, negligible, if compared to the expected system noise [Weg18a].

3.6 Flux-ramp modulation

MMCs exhibit an almost ideal response upon an energy input, meaning an almost linear relation between the energy input and the magnetic flux signal. The minor deviation from the linear response is well described by a quadratic function that can be calculated *a priori*, according to the thermodynamic model of the detector [Fle05, Kem18]. The output signal of a microwave SQUID multiplexer, on the other hand, is periodic in dependence on the magnetic flux threading the rf SQUID, as depicted in figure 3.7b. In order to maintain the almost ideal detector response, a linearisation scheme for the response of the microwave SQUID multiplexer is required. A feedback system, which maintains an optimal working point for each rf SQUID, comparably to the feedback technique for dc SQUIDs introduced in chapter 2, is not feasible, as for each rf SQUID additional wires would be required. An alternative linearisation scheme for the response of the microwave SQUID multiplexer is the so-called flux-ramp modulation [Mat12].

This approach is explained in the following with the help of figure 3.10. All rf SQUIDs of the microwave SQUID multiplexer are modulated simultaneously by a sawtooth shaped modulation current $I_{\mathrm{mod}}(t)$, which is injected into the common modulation coil of the rf SQUIDs (figure 3.10a). For this, the repetition rate of the sawtooth is chosen to be significantly larger than the bandwidth of the detector, so that the external flux $\Phi_{\mathrm{ext}}(t)$ appears quasi-static within one period of the modulation current. The amplitude of the sawtooth is chosen to induce an integer number of flux quanta Φ_0 in the rf SQUID. In this way, within the time window of one flux-ramp, a periodic signal A can be measured, which corresponds to the transmission $|S_{21}|$ for the microwave SQUID multiplexer (figure 3.10b). The shape of this periodic signal depends on the design parameters of the microwave SQUID multiplexer. If a quasi-static flux $\Delta\Phi_{\mathrm{ext}}$ is induced in the rf SQUID, which is depicted as an offset in the modulation current in figure 3.10a, the periodic transmission $|S_{21}|$ within one time window of the flux-ramp is shifted by a phase $\Delta\phi$, as shown in figure 3.10b. Since the change in phase $\Delta\phi$ is proportional to the flux $\Delta\Phi_{\mathrm{ext}}$, it can be exploited to perform a linearised read-out of the microwave SQUID multiplexer. By continuously

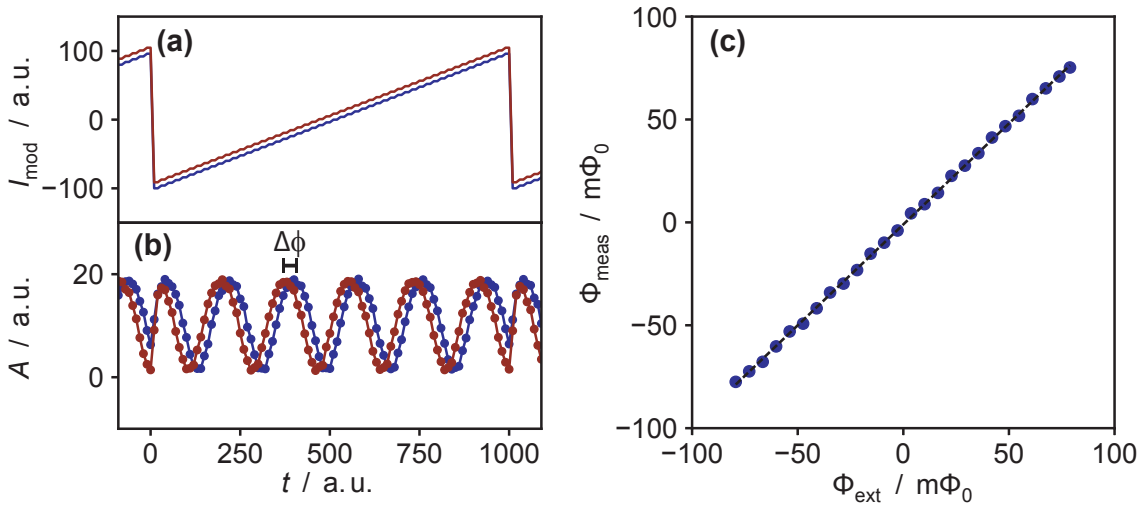

Figure 3.10: Visualisation of the working principle of the flux-ramp modulation on the basis of measurements performed with a dc SQUID. **(a)** Sawtooth-shaped modulation current I_{mod} in the modulation coil and **(b)** the resulting signal amplitude A. The blue colour indicates the situation for an external magnetic flux $\Phi_{\mathrm{ext}} = 0$, while the red colour stands for $\Phi > 0$, which is simulated by biasing the modulation current I_{mod}. **(c)** The measured flux Φ_{meas}, which has been determined from the phase shift $\Delta\phi$, is plotted as a function of the externally applied flux Φ_{ext}. The linear relation is highlighted by the numerical fit. This figure is taken from [Ric21].

monitoring the phase shift in succeeding time windows of the flux-ramp, an external magnetic flux signal $\Phi_{\mathrm{ext}}(t)$, such as a detector signal, can be reconstructed from the individual quasi-static fluxes $\Delta\Phi_{\mathrm{ext}}$.

Besides the linearisation of the response of the microwave SQUID multiplexer, the flux-ramp modulation provides a suppression of $1/f$-type noise contributions after the rf SQUID, as the signal is modulated onto a carrier with higher frequency, i.e. the frequency of the periodic transmission $|S_{21}|$ [Mat12]. In this way, the potential influence of the $1/f$-type noise contribution, for instance from two-level systems, amplifiers or mixers, is greatly reduced. Compared to a read-out scheme of the microwave SQUID multiplexer in which the working point is fixed at the steepest point of the transmission (figure 3.7b), the white noise contributions are enhanced for a flux-ramp modulated read-out. One reason for this is that at the beginning of each time window of the flux-ramp, several data points cannot be used for the determination of the phase due to the occurrence of transients at the flux-ramp reset. For an ideal, sinusoidal transmission $|S_{21}|$, the white noise is enhanced by a factor $\sqrt{2/\alpha}$, where α denotes the fraction of data points which are used for the determination of the phase within one time window of the flux-ramp [Mat12, Leh07].

3.7 Software-defined radio

To read out a microwave SQUID multiplexer, the transmission of all channels has to be measured simultaneously at individual read-out frequencies. For characterisation measurements, as they are carried out in the scope of this thesis, a homodyne read-out system is sufficient. For this, a signal generator provides a read-out frequency signal, which subsequently is modulated by the multiplexer. The output signal is mixed with a reference signal from the same signal generator in an I/Q mixer at room temperature. The mixing product in the base band at $f = 0\,\mathrm{Hz}$ is digitised and then analysed. A more detailed description of this read-out method can be found in chapter 6. In principle, the homodyne read-out system can be scaled up to read out more than one microwave SQUID multiplexer channel. For this, the signals of multiple signal generators providing suitable read-out frequencies are combined to a waveform, which is subsequently modulated by the microwave SQUID multiplexer. The output signal has to be filtered by band-pass filters in order to separate the different frequency components. The individual frequencies are then down-converted by I/Q mixers and, finally, they are digitised. This method would, however, require one signal generator and one I/Q mixer per per multiplexer channel, which increases the system complexity and the costs dramatically for large numbers of multiplexer channels.

An alternative read-out method is the software-defined radio, meaning the software-based generation and analysis of multiple read-out frequencies, which is commonly used in telecommunication, and whose application to the frequency-domain multiplexed read-out of low temperature detectors has been demonstrated for microwave kinetic inductance detectors [Maz04], transition-edge sensors [Nor13] and magnetic microcalorimeters [Ric21]. In figure 3.11, the working principle of a software-defined radio-based read-out of a microwave SQUID multiplexer is illustrated. A field programmable gate array (FPGA) is connected to a digital-to-analogue converter (DAC) and to an analogue-to-digital converter (ADC), controlling the output signal of the DAC and processing the data from the ADC. The DAC can be used for the generation of arbitrarily shaped signals, and hence, it is used for the generation of a frequency comb. For the microwave SQUID multiplexer, typically, frequencies in the range between 4 GHz and 8 GHz are required. For this, DACs with a sufficiently large bandwidth and a sufficiently low signal-to-noise ratio would be needed, but they are not available. Therefore, the frequency comb is generated in the MHz-band with an appropriate frequency spacing suited to the channels of the microwave SQUID multiplexer, and subsequently up-converted into the GHz-band by means of an I/Q mixer and a local oscillator. The usage of an I/Q mixer provides the possibility to make use of the frequency band above the frequency band above and below the frequency of the local oscillator, respectively . For this, the phase of the read-out

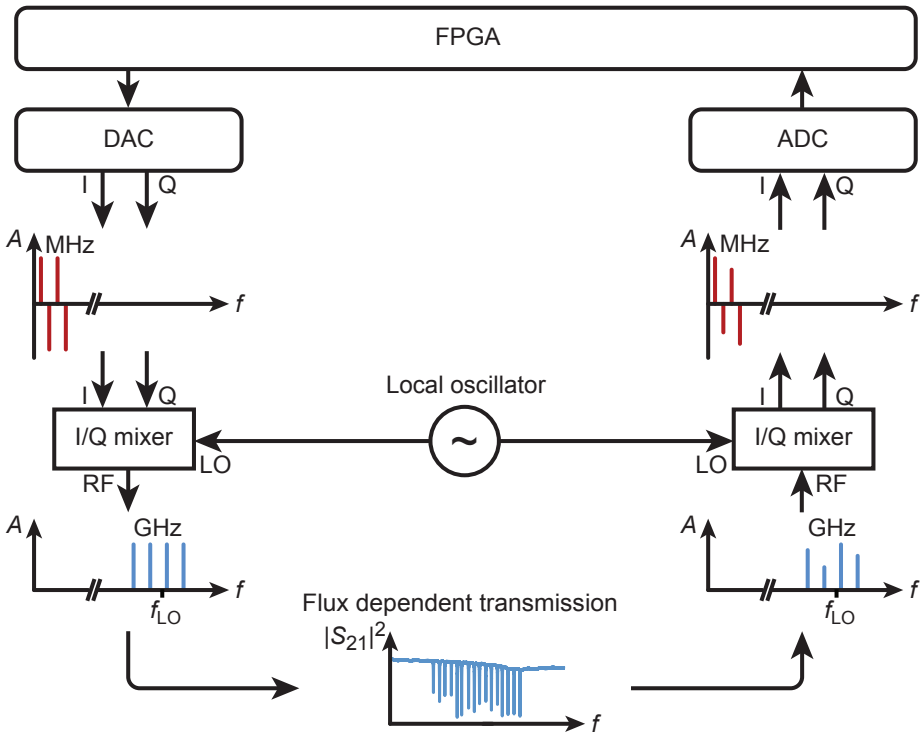

Figure 3.11: Working principle of the software-defined radio-based read-out of a microwave SQUID multiplexer. The frequency comb is generated in the MHz-band by a digital-to-analogue converter (DAC), up-converted into the GHz band by means of an I/Q mixer and a local oscillator. After the modulation of the signal, a down-conversion into the MHz-band is performed, applying again an I/Q mixer. Finally, the signal is digitised with the help of an analogue-to-digital converter (ADC). An FPGA controls the converters and processes the data. This figure is adopted from [Ric21].

signals has to be adjusted by the DAC. The read-out signals are fed into the cryogenic part of the microwave read-out chain, where their amplitude is successively attenuated, to reach the required read-out power on the multiplexer chip. Here, the frequency comb is modulated depending on the magnetic flux states of the respective rf SQUIDs. Afterwards, the frequency comb is amplified in the cryogenic read-out chain and fed into a second I/Q mixer, where with the help of the local oscillator, the frequency comb is down-converted into the MHz band. After digitisation by the ADC, the FPGA separates the different frequency components by means of digital band-pass filters, and finally, the amplitude of the signals is determined.

For ECHo-100k, a software-defined radio system is currently being developed [San19, Kar20], and based on a prototype, a multichannel software-defined radio-based read-out of the microwave SQUID multiplexer for MMCs has already been demonstrated [Ric21].

3.8 Microfabrication

The microfabrication of the microwave SQUID multiplexer devices used in the framework of this thesis has been performed in the cleanroom facility of the Kirchhoff-Institute for Physics, Heidelberg University. The microwave SQUID multiplexer chips have been microfabricated on wafer scale, employing 3" silicon wafers with a 255 nm thick thermal oxide layer as substrate. Seven microfabrication layers have been required for the production of the microwave SQUID multiplexer, as summarised in table 3.1.

fabrication steps				
#	structure	material	thickness	structuring process
1	bottom electrodes of JJs, transmission lines, resonators, ground planes, SQUID loops and electrical leads	Nb	250 nm	sputt. + dry etching
2	tunnel barrier of JJs	$Al - Al_x$	20 nm	sputt. + wet etching
3	top electrodes of JJs	Nb	125 nm	sputt. + dry etching
4	first isolation	SiO_2	100 nm	sputt. + lift-off
5	second isolation	SiO_2	200 nm	sputt. + lift-off
6	filter resistances	Au:Pd	260 nm	sputt. + lift-off
7	coupling coil, modulation coil, electrical leads, ground plane links	Nb	600 nm	sputt. + lift-off

Table 3.1: Microfabrication steps for the production of the microwave SQUID multiplexer. Each structuring process includes a microlithographic step that is not explicitly reported in the table.

The process starts with a sputter deposition[2] of 250 nm of niobium, followed by a microlithographic structuring and dry etching[3] to fabricate the bottom electrodes of the Josephson Junctions (JJs), the transmission lines, the resonators, the ground planes, the SQUID loops and some electrical leads. The tunnel barriers of the JJs and the top electrodes are completed with a trilayer process, involving the sputter deposition, microlithography and wet etching of an $Al - AlO_x$ layer and a sputter deposition, microlithography and dry etching of the second niobium layer. Subsequently, two

[2] All the sputter deposition processes described here are performed with a UHV sputter system by DCA Instruments Oy, Turku, Finland.

[3] All the dry etching processes described here are performed with an SF_6-based ICP-RIE etch step employing the cryogenic ICP-RIE etch system SI 500 C by Sentech Instruments GmbH, Berlin, Germany.

SiO_2 layers are sputter deposited, structured and lifted off, to ensure a reliable isolation between crossing electrical leads. As next step, filter resistances made of an Au:Pd layer with a thickness of 260 nm are sputtered deposited, structured and lifted off. Note that these filter resistances are not present on the devices used within this thesis, but other microwave SQUID multiplexer devices from the same wafer feature them [Ric21]. Finally, the remaining niobium structures, including the coupling coils and the modulation coils, the structures linking the ground planes, and some electrical leads are fabricated via sputter deposition, microlithography and lift-off of a 600 nm thick niobium layer. More details regarding the microfabrication steps can be found in [Ric21].

4. Cryogenic microwave read-out chain for ECHo-100k

The ECHo-100k phase of the ECHo experiment aims at reaching a sensitivity below 3 eV on the effective electron neutrino mass [Gas17]. Under the assumption of an energy resolution below 5 eV FWHM for each read-out channel, during the 3 years measurement campaign for ECHo-100k, about 10^{13} electron capture events have to be acquired in order to achieve this goal [Man21a]. Hence, the planned total ^{163}Ho activity for the ECHo-100k phase is 100 kBq. Each detector pixel is planned to be loaded with an amount of ^{163}Ho corresponding to an activity of 10 Bq, which is set by constraints in terms of the unresolved pile-up fraction, i.e. the fraction of events in a detector channel occurring simultaneously within the smallest resolved time unit and therefore being unidentifiable as distinct events. From these value it is easy to calculate that at least 10000 detector pixels are needed for the data acquisition during the ECHo-100k phase. Including diagnostic pixels for sensing local temperature variations and performing *in situ* background measurements, in total 12000 detector pixels have to be read out, which corresponds to 6000 microwave SQUID multiplexer (µMUX) channels.

The total system bandwidth needed for the read-out of 6000 µMUX channels is set by the number of µMUX channels itself and by the frequency spacing between neighbouring µMUX channels. To mitigate crosstalk due to the extended Lorentzian tails of the resonance curves of neighbouring µMUX channels, for the ECHo-100k phase the spacing between neighbouring channels is set to the tenfold resonator bandwidth [Weg18a, Mat19]. In turn, the resonator bandwidths are designed to be 1 MHz each, which is a practical compromise between a fast read-out able to resolve the intrinsic signal rise time of MMCs and a finite available system bandwidth per microwave read-out chain. Hence, altogether a total system bandwidth of 60 GHz is required for the ECHo-100k experimental phase. As the bandwidth of a single read-out chain will be limited to frequencies between 4 GHz and 8 GHz, corresponding to the bandwidth of the used low-noise amplifiers as discussed below, in total 15 cryogenic microwave read-out chains are required, each of which accounts for 400 µMUX channels.

In the following sections, firstly, the requirements on the cryogenic microwave read-out chain are introduced, which is followed by the discussion of the design process leading to the final layout of the cryogenic microwave read-out chain for ECHo-100k, involving dedicated simulations. Subsequently, the mechanical design is presented

and, finally, the characterisation measurements of an ECHo-100k demonstrator channel are discussed demonstrating the target performance.

4.1 Requirements on the cryogenic microwave read-out chain

The 15 cryogenic microwave read-out chains for ECHo-100k are subject to constraints and requirements set by the specifications of the ECHo experiment, the employed cryogenic platform and the commercially available microwave hardware. In the following, the key points considered for the design of the cryogenic microwave read-out chains are briefly introduced.

System noise The energy resolution of the ECHo-100k detector with implanted ^{163}Ho source operated with dc SQUID read-out is well below the required energy resolution of 5 eV FWHM for the ECHo-100k phase [Gri22]. In order to maintain the energy resolution below 5 eV FWHM when utilising µMUX read-out, uttermost care has to be taken to minimise the noise contributions from the read-out system, as they directly impact the signal-to-noise ratio and, ultimately, the achievable energy resolution. The target for the µMUX-based read-out is to reach a white noise performance, which is comparable to the white noise performance of state-of-the-art dc SQUID-based read-out systems for MMCs with an apparent white magnetic flux noise level of $\sim 0.3\,\mu\Phi_0/\sqrt{\text{Hz}}$ [Man21b]. Consequently, for a cryogenic microwave read-out chain involving an ideal LER-µMUX as simulated in section 3.5, the system noise temperature has to be $\lesssim 11$ K. For a real and, hence, non-ideal µMUX device, exhibiting a finite intrinsic quality factor, the system noise temperature has to be accordingly lower to reach the same overall noise performance. Therefore, the design goal is a system noise temperature of ~ 4 K, which imposes strict requirements on the noise performance of the first amplifier after the µMUX, as discussed below.

Microwave power The microwave power ratings of the SDR system and the optimal microwave read-out power per carrier on chip set limits on the the attenuation between the input of the cryogenic read-out chain and the µMUX (referred to as Tx attenuation of cryogenic microwave read-out chain), as well as on the the effective gain between the µMUX and the output of the cryogenic read-out chain (referred to as Rx gain of the cryogenic read-out chain). For this, additional room temperature microwave components, such as power combiners and cables, connecting the SDR system and the cryogenic microwave read-out chain, have to be taken into consideration.
The optimal microwave read-out power for an ideal LER-µMUX as simulated in section 3.5.1 is -71.8 dBm per µMUX channel on the transmission line of the µMUX

chip, while the output microwave power provided by the SDR system corresponds to $-19.0\,\mathrm{dBm}$ per read-out tone[1]. Therefore, the maximum total attenuation between the output of the SDR system and the µMUX cannot fall below $-52.8\,\mathrm{dB}$. Taking into account the attenuation of the additional room temperature components and cables, the Tx attenuation of the cryogenic read-out chain is required to take values between $-40.0\,\mathrm{dB}$ and $-45.0\,\mathrm{dB}$.
The maximum admissible microwave power at the input of the SDR system is $-35.0\,\mathrm{dBm}$ per read-out tone, which limits the tolerable amplification between the µMUX and the input of the SDR system to $+36.8\,\mathrm{dB}$. Taking into account the attenuation of the additional room temperature components and cables, the Rx gain of the cryogenic read-out chain, i.e. the gain between the µMUX and the output of the cryogenic microwave read-out chain, can take values up to $+40\,\mathrm{dB}$.

Heat load The cryogenic platform holding the ECHo-100k experimental set-up is a BF-XLD-series cryogen free dilution refrigerator system[2]. It is comprised of multiple stages, namely the 300 K plate, the 50 K plate, the 4 K plate, the still plate, the coldplate and the mixing chamber plate, each of which is providing a lower temperature than the preceding stage under normal operation. Note that the names of the first three stages reflect the respective temperature ranges and not the actual temperatures, e.g. for the cryogenic platform employed for the ECHo experiment, the temperatures are typically $T_{300\,\mathrm{K}} \approx 296\,\mathrm{K}$, $T_{50\,\mathrm{K}} \approx 57\,\mathrm{K}$ and $T_{4\,\mathrm{K}} \approx 3.5\,\mathrm{K}$, respectively.
A two stage pulse tube cooler[3] thermally connected to the 50 K plate and the 4 K plate provides a cooling power of $P_{\mathrm{cool}}^{4\,\mathrm{K}} = 1.35\,\mathrm{W}$ at $T_{4\,\mathrm{K}} = 4.2\,\mathrm{K}$ and $P_{\mathrm{cool}}^{50\,\mathrm{K}} = 40\,\mathrm{W}$ at $T_{50\,\mathrm{K}} = 45\,\mathrm{K}$. To reach the ECHo-100k operational temperature of 20 mK, the cryogenic platform is equipped with a $^3\mathrm{He}/^4\mathrm{He}$ dilution unit providing a cooling power[4] of $P_{\mathrm{cool}}^{\mathrm{MXC}} \gtrsim 14\,\mu\mathrm{W}$ to the mixing chamber (MXC) plate of the cryostat at $T_{\mathrm{MXC}} = 20\,\mathrm{mK}$. The cooling power on the coldplate is up to $P_{\mathrm{cool}}^{\mathrm{cp}} \lesssim 300\,\mu\mathrm{W}$ at a temperature of $T_{\mathrm{cp}} \approx 120\,\mathrm{mK}$, whereas the still plate requires a power input of up to $P_{\mathrm{heat}}^{\mathrm{still}} \lesssim 30\,\mathrm{mW}$ in order to maintain the circulation of the $^3\mathrm{He}/^4\mathrm{He}$ dilution cycle. Care has to be taken that the heat load associated with the microwave read-out chains installed on a cryogenic platform does not exceed the cooling capability of the individual stages of the cryogenic platform, respectively. For this, three major sources

[1] This holds true for a waveform composed of multiple cosinusoidal waves with no relative initial phase shifts, as periodically all the cosinusoidal waves interfere constructively. By engineering a waveform with optimised phase shifts, potentially more microwave power per channel is available. This information was received in private communication with N. Karcher.
[2] Bluefors Oy, Helsinki, Finland
[3] PT415-RM Cryocooler, Cryomech Inc., Syracuse, NY, USA
[4] https://bluefors.com/products/xld-dilution-refrigerator/ (retrieved 16 May 2022)

of thermal load onto the stages of the cryogenic platform have to be considered: firstly, passive microwave components, such as cables and attenuators, lead to a read-out power dependent signal dissipation and thereby to a heating effect. Secondly, active components, i.e. microwave amplifiers, exhibit a read-out power independent dissipation due to dc voltages and currents defining the amplifiers' working points. Thirdly, microwave cables connecting different temperature stages of the cryogenic platform act as thermal link between those stages causing a heat flow onto the colder stage.

Intermodulation distortion Any microwave amplifier exhibits a limited linear amplification regime because of physical limitations to the underlying amplification mechanism, i.e. the amplifier gain is decreasing with increasing input signal powers. This non-linearity gives rise to intermodulation distortion causing third-order and higher-order frequency mixing products of the read-out tones. Unlike harmonic distortion, which would cause mixing products at integer multiples of the read-out frequencies and therefore outside the relevant frequency band composed by the read-out tones, the intermodulation distortion creates amongst others unwanted spurious in-band tones. The number of third-order modulation tones grows almost quadratically with the number of read-out tones. For the 400 read-out tones per read-out chain required for ECHo-100k, this leads to a pseudo-noise floor caused by the sheer number of intermodulation tones. In order to avoid signal degradation due to the pseudo-noise floor, the microwave amplifiers employed for the cryogenic microwave read-out chain for ECHo-100k need to exhibit a sufficiently low level of intermodulation distortion.

Mechanical design The geometry of the cryogenic platform sets restrictions on the available space for the cryogenic microwave read-out chains in terms of distance between the different temperature stages and in terms of cross-section defined by the flanges in the temperature stages allowing for cable feedthroughs. Additionally, a modular design for the cryogenic read-out chain is favourable, since it permits the installation of an arbitrary number of read-out channels and enables an easy scale-up for potential future extensions of the ECHo experiment.

Costs The design of the cryogenic microwave read-out chain needs to respect the financial limits set by the available budget within ECHo-100k, which imposes for instance restrictions on the use of superconducting coaxial cables, as the associated costs per unit length typically exceed the corresponding costs for normal conducting cables by at least one order of magnitude.

4.2 Design of the cryogenic microwave read-out chain

In order to design a cryogenic microwave read-out chain with an optimal noise performance while fulfilling all the boundary conditions discussed above, the cryogenic read-out chain has to be modelled in terms of attenuation, gain and noise performance, as well as in terms of power dissipation and heat flow. Subsequently, the read-out chain can be simulated, the influence of single components and of their physical properties on the performance can be studied and the design of the read-out chain can be optimised accordingly.

In the following, firstly, the calculation of the noise in cascaded two-port networks, of the intermodulation distortion in amplifiers, and of the rate of heat flow in coaxial cables are explained. Then, a generic design of the cryogenic microwave read-out chain acting as a basis for a numeric optimisation process is introduced, and the results of the numeric optimisation process and the final layout of the cryogenic microwave read-out chain for the ECHo-100k phase are discussed. Finally, a mechanical design of the cryogenic microwave read-out chain is presented.

4.2.1 Calculation of the noise in cascaded two-port networks

Practically, all devices used for the cryogenic microwave read-out chain can be modelled as two-port networks, meaning as electrical network with two ports, each consisting of a pair of terminals, as indicated in figure 4.1a. Such a general two-port network is characterised by the complex-valued scatter matrix S with components S_{ij} relating the incident wave a_j at port j to the reflected wave b_i at port i. Therefore, for instance, the forward transmission from port 1 to port 2 is described by the matrix component S_{21}. For the noise analysis of the cryogenic microwave read-out chain, some simplifications can be assumed. Firstly, for the employed coaxial components, the outer conductor is grounded, for which reason at each port of the corresponding two-port network one terminal is omitted in the following, as indicated in figure 4.1b. Secondly, for the noise analysis it can be assumed that the microwave signal is following the read-out chain in a unidirectional fashion, which is why for all employed two-port microwave components an input (port 1) and an output (port 2) can be defined. Therefore, in terms of signal amplification or damping, each device is characterised by its forward power gain or attenuation $G = |S_{21}|^2$. For directional devices, such as microwave amplifiers, the definition of an input and an output is obvious, but here it is also extended to devices such as attenuators and cables. The noise power P_{N} of a two-port network in a frequency band B can be expressed in terms of its noise temperature T_{N}, which corresponds to the physical temperature of a resistor exhibiting a Johnson-Nyquist noise power equivalent to the noise power of

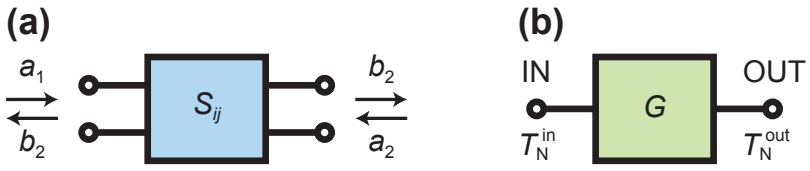

Figure 4.1: **(a)** General two-port network characterised by its scatter matrix S with components S_{ij} relating the incident waves a_j at port j to the reflected waves b_i at port i. Each port consists of two terminals. **(b)** Simplified directional two-port network characterised by its power gain or attenuation $G = |S_{21}|^2$ and its noise temperature at the input port and output port.

the two-port network:

$$P_\mathrm{N} = k_\mathrm{B} T_\mathrm{N} B \,, \tag{4.1}$$

where k_B is the Boltzmann constant. For electrical two-port networks it is common practice to use the input noise temperature $T_\mathrm{N}^\mathrm{in} = T_\mathrm{N}$ as reference value, whereas the output noise temperature is given by $T_\mathrm{N}^\mathrm{out} = T_\mathrm{N} G$. Passive microwave components, such as attenuators, often correspond to electrical networks of ohmic resistors, for which reason the dominant noise source is Johnson-Nyquist noise, i.e. thermal noise. Therefore, the noise temperature of a passive microwave component is related to the physical temperature T_phys of the component via

$$T_\mathrm{N} = T_\mathrm{phys} \frac{1-G}{G} \,, \tag{4.2}$$

as demonstrated in [Poz98]. For active components, such as amplifiers, the noise temperature is dependent on the physical process underlying the amplification and, hence, it is not possible to find a generalised relation between the physical temperature and the noise temperature. For commercially available semiconductor-based low-noise amplifiers in the lower GHz-frequency range, noise temperatures as low as 1.1 K have been reached[5].

For a cascade of k microwave components, the total noise temperature is given by

$$T_\mathrm{N,tot} = T_\mathrm{N,1} + \frac{T_\mathrm{N,2}}{G_1} + \frac{T_\mathrm{N,3}}{G_1 G_2} + \cdots + \frac{T_\mathrm{N,k}}{G_1 G_2 \cdots G_{k-1}} \,, \tag{4.3}$$

where $T_{\mathrm{N},i}$ denotes the noise temperature of the i-th component in the cascade and G_i the corresponding gain or attenuation [Fri44]. This equation is not only important for the calculation of the noise performance of multistage signal chains, but it also

[5] https://lownoisefactory.com/product/lnf-lnc0-6_2a/ (retrieved 16 May 2022)

illustrates the importance of a first stage low-noise amplification in signal chains, as in this case the noise temperature T_1 of the amplifier dominates and the noise temperatures of all succeeding amplifiers are at least suppressed by a factor of G_1.

4.2.2 Calculation of the intermodulation distortion in amplifiers

For an ideal amplifier with voltage gain a_1, the output voltage signal v_{out} is related to the input voltage signal v_{in} via $v_{\text{out}} = a_1 v_{\text{in}}$. However, for a real device, physical limits to the amplification process result in a limited linear response regime at small input voltages. Beyond that regime, the gain decreases for increasing input voltages, until a saturation is reached and the level of the output voltage becomes independent from the amplitude of the input signal. This gain compression can be modelled by a power series in the input voltage v_{in} motivated by the Taylor expansion of the underlying amplification function:

$$v_{\text{out}} = a_0 + a_1 v_{\text{in}} + a_2 v_{\text{in}}^2 + a_3 v_{\text{in}}^3 + \dots . \tag{4.4}$$

The Taylor expansion coefficient a_0 describes a dc offset voltage and a_1 the linear voltage gain. All the expansion coefficients for higher powers of v_{in} account for non-linearities of the amplifier. For a microwave signal $v_{\text{in}} = A_{\text{in}} \cos(\omega t)$ with frequency ω and amplitude A_{in}, the cubic term in equation (4.4) generates

$$a_3 v_{\text{in}}^3 = a_3 A_{\text{in}}^3 \left(\frac{3}{4} \cos(\omega t) + \frac{1}{4} \cos(3\omega t) \right) \tag{4.5}$$

after application of standard trigonometric identities. This expression exhibits terms with frequencies ω and 3ω, implying frequency mixing. On the one hand, merging the term with frequency ω with the linear term in equation (4.4) yields

$$v_{\text{out},\omega} = a_1 \left(1 + \frac{3\,a_3}{4\,a_1} A_{\text{in}}^2 \right) v_{\text{in}} \tag{4.6}$$

which indicates an amplitude dependent gain, meaning that for $a_3 < 0$ a at large amplitudes A_{in} a gain compression occurs, as expected for real amplifiers. On the other hand, the frequency mixing in equation (4.5) generates spurious tones in the output frequency spectrum of the amplifier. For instance, for an input signal composed of two carriers with identical amplitude A_{in} and closely spaced frequencies ω_1 and ω_2, the cubic term additionally introduces tones with the output frequencies $\omega_3^{\pm} = 2\omega_1 \pm \omega_2$ and $\omega_4^{\pm} = 2\omega_2 \pm \omega_1$, where ω_3^- and ω_4^- neighbour the carrier frequencies ω_1 and ω_2 [Poz98]. These parasitic, unwanted intermodulation products are

unavoidable, but their extent depends on the applied input voltage and the amplifier characteristics. The amplitude of those spurious tones grows with A_{in}^3, whereas the hypothetically uncompressed output signal amplitude at frequencies ω_1 and ω_2 scales with A_{in}. Therefore, a hypothetical intercept point of these two contributions can be defined, the so-called third-order intercept point (IP3), quantifying the intermodulation distortion. The corresponding input power $IIP3$ results in

$$IIP3 = \frac{1}{2Z_0}\left(A_{\mathrm{in}}^{\mathrm{IP3}}\right)^2 \quad \text{with} \quad A_{\mathrm{in}}^{\mathrm{IP3}} = \sqrt{\left|\frac{4\,a_1}{3\,a_3}\right|} \tag{4.7}$$

where Z_0 is the characteristic impedance [Poz98]. For a cascade of two amplifiers with $IIP3'$ and $IIP3''$ and power gains G' and G'', respectively, the overall input third-order intercept point $IIP3$ can be calculated according to [Poz98]

$$IIP3 = \left(\frac{1}{IIP3'} + \frac{G'}{IIP3''}\right)^{-1}. \tag{4.8}$$

It is worth noting that besides third-order intermodulation, also any other term in equation (4.4) with order ≥ 2 leads to frequency mixing. For carrier frequencies between 4 GHz and 8 GHz, the second-order term only leads to spurious frequencies outside of this frequency band, whereas all higher orders cause parasitic in-band tones amongst others. However, their respective amplitudes decrease with increasing order, and hence, the third-order contribution dominates.

For a waveform composed of N sinusoidal tones, a total of $2N(N-1)$ third-order intermodulation tones are created [Hen18]. For the 400 read-out tones per read-out chain for ECHo-100k, this implies more than 3×10^5 third-order intermodulation tones, which lead to the formation of an irreducible pseudo-noise floor. In order to suppress the impact of this pseudo-noise floor on the signal-to-noise ratio, microwave amplifiers with the highest possible $IIP3$ are preferred.

4.2.3 Calculation of the rate of heat flow in coaxial cables

The rate of heat flow through a homogeneous object with constant cross-sectional area A and length l can be calculated as

$$\dot{Q} = \frac{A}{l}\int_{T_1}^{T_2} \Lambda(T)\mathrm{d}T \tag{4.9}$$

where T_1 and T_2 are the temperatures at the two ends of the object. The thermal conductivity Λ can in general be comprised of multiple contributions, which depend

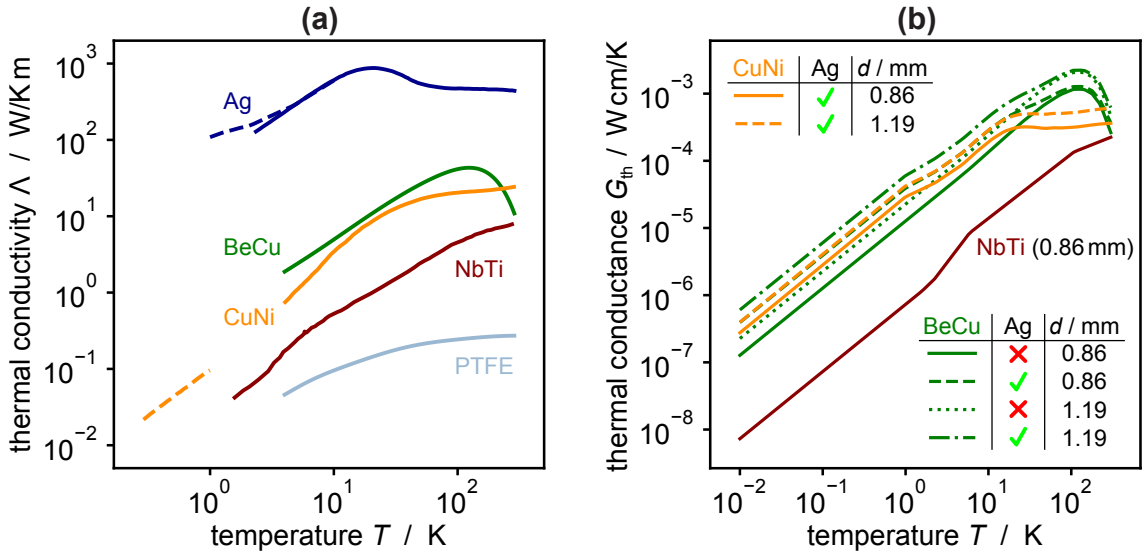

Figure 4.2: **(a)** Measured thermal conductivities of selected materials relevant for the selection of coaxial cables for ECHo-100k. Sources: Ag [Smi95, Coa19], BeCu [Mar02], CuNi [Pob92, Ho78], PTFE [Mar02], NbTi [Fla78]. **(b)** Modelled thermal conductances of selected coaxial cables. The inset tables indicate the layout of the coaxial cables in terms of outer diameter d and optional silver (Ag) coating of the centre conductor.

on the material properties and temperature. For dielectric materials the thermal conductivity is mostly governed by phonons, which in crystals ideally leads to a $\Lambda_{\mathrm{ph}} \propto T^3$ dependence at low temperatures. For normal conducting metals, additionally, the contribution of the conduction electrons has to be considered, ideally causing a $\Lambda_{\mathrm{el}} \propto T$ dependence at low temperatures. In superconducting metals, Cooper-pairs do not contribute to the thermal conductivity, since they do not carry any entropy, however, quasiparticles transport heat. As below the superconducting transition temperature the number of quasiparticles drops fast with decreasing temperature, the thermal conductivity decreases as well.

In the temperature range between 0 K and 300 K the thermal conductivities of the considered cable materials are subject to physical phenomena not covered by basic models. For this reason, for the calculation of the rate of heat flow through the coaxial cables experimental values of the thermal conductivity are considered, where available. In figure 4.2a measured values of the thermal conductivity for selected materials common to low temperature coaxial cables are shown. The general layout of the coaxial cables considered for the cryogenic microwave read-out chain is sketched in figure 4.3. The centre conductor with diameter d_{centre} consists either of normal conducting alloys such as beryllium-copper (BeCu) or copper-nickel (CuNi) and can optionally exhibit a $\sim 4\,\mu\mathrm{m}$ thick silver (Ag) coating, or, alternatively, it can consist

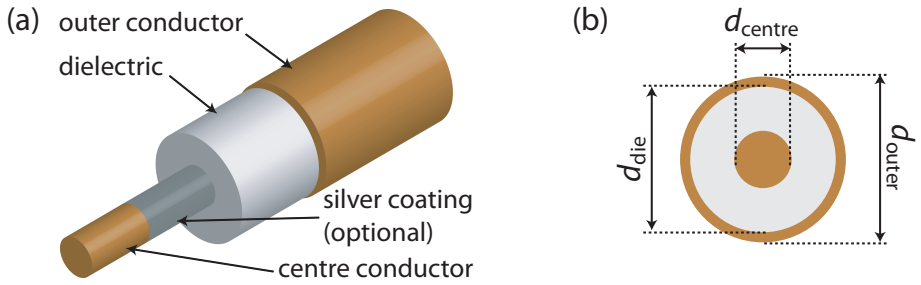

Figure 4.3: **(a)** Schematic structure of a coaxial cable. **(b)** Cross-section of a coaxial cable with diameter of the centre conductor d_{centre}, outer diameter of the dielectric d_{die} and outer diameter of the outer conductor d_{outer}.

of the superconducting alloy niobium-titanium (NbTi). The dielectric material with outer diameter d_{die} is made of polytetrafluoroethylene (PTFE). The outer conductor is made of the same alloy as the centre conductor and features an outer diameter d_{outer}. To calculate the rate of heat flow of a composite object, such as a coaxial cable, the total thermal conductance has to be considered, which is defined as

$$G_{th,tot} = \sum_i G_{th,i} = \sum_i A_i \Lambda_i \tag{4.10}$$

where the index i runs over all components with individual thermal conductivity Λ_i and cross-section A_i. In figure 4.2b the thermal conductance of all coaxial cables considered for the ECHo-100k cryogenic microwave read-out chain, modelled according to equation (4.10), is presented. The underlying thermal conductivity data is taken from figure 4.2a for the temperature range covered there. For very low temperatures, however, no measured data is available, for which reason an extrapolation $G_{th} \propto T$ has been performed, motivated by the dominant electronic contribution to the thermal conductivity in normal conducting metals at lowest temperatures. In a conservative approximation, the same extrapolation has been performed for the superconducting NbTi cable. Due to its phononic nature, the contribution of the dielectric material to the thermal conductance is expected to be negligible at lowest temperatures in any case.

The producer of the coaxial cables specifies the thermal conductance of the cables at a temperature of 4 K and, hence, the plausibility of the modelled thermal conductances is verified by comparing the values obtained from the models at 4 K to the values provided by the producer. For BeCu-based cables the maximum deviation is 1.8 %, for CuNi-based cables 7.7 % and for the NbTi-based cable 3.7 %. These values indicate a reasonable agreement, which is fully sufficient for the purpose of estimating the rate of heat flow between different temperature stages of the cryogenic platform caused by the coaxial cables linking them thermally.

Finally, following from equations (4.9) and (4.10), the rate of heat flow through a coaxial cable can be expressed as

$$\dot{Q}_{\text{cable}} = \sum_i \frac{A_i}{l} \int_{T_1}^{T_2} \Lambda_i(T) \mathrm{d}T = \frac{1}{l} \int_{T_1}^{T_2} G_{\text{th}}(T) \mathrm{d}T \tag{4.11}$$

where l is the length of the coaxial cable, G_{th} is the thermal conductance of the cable as modelled above, and T_1 and T_2 are the temperatures of the two stages of the cryogenic platform thermally linked by the coaxial cable. Obviously, for equation (4.11) to hold true, the two ends of the cable need to exhibit the exact temperatures of the respective stages of the cryogenic platform. In particular, a not well thermalised centre conductor could lead to a significantly increased rate of heat flow onto colder stages exhibiting low cooling powers. Potentially, this could compromise the successful operation of the µMUX or of the entire cryogenic platform. Therefore, one important aspect in designing the cryogenic microwave read-out chain is the mitigation of excess heat flow through the centre conductors of coaxial cables, which will be addressed below.

4.2.4 General layout of the cryogenic microwave read-out chain

For the optimisation of the design of the cryogenic microwave read-out chain, firstly, a generic layout for the read-out chain is set up. By varying the material of the cables and the attenuation or gain of microwave components, such as attenuators, directional couplers and amplifiers, different configurations of the read-out chain can be simulated. The simulation results in terms of noise temperature, attenuation or gain, and heat load of all possible configurations within the generic layout are fed into a database. By the application of cuts on the database, layout configurations fulfilling all boundary conditions can be extracted. Among these suitable configurations, the one with the best noise performance is chosen for the cryogenic read-out chain for ECHo-100k.

In figure 4.4, the generic layout for the microwave read-out chain for ECHo-100k is depicted. The six temperature stages of the cryogenic platform are indicated by six different colours. The colour of each microwave component reflects to which platform the component is mounted and, hence, which temperature it is assumed to exhibit. Coaxial cables connecting different stages of the cryogenic platform are depicted with a colour gradient, as they will exhibit a temperature gradient. The cables and components depicted on the left side, i.e. between the input of the cryogenic read-out chain (IN) and the microwave SQUID multiplexers (µMUX), are referred to as Tx branch of the read-out chain, as this part of the read-out chain is dedicated to sending the read-out frequency comb generated by the SDR system to the µMUX.

The Tx branch needs to attenuate the signal level provided by the SDR system to the input level required at the µMUX, while keeping the added noise level as small as possible. The Rx branch, comprised of the cables and components between the µMUX and the output of the cryogenic read-out chain (OUT), has the task to amplify the signal, which has been modulated by the µMUX, to the required input power level of the SDR system, maintaining the best possible signal-to-noise ratio. Additionally, the intermodulation distortion introduced by the amplification has to be kept at a minimum. Both the Tx branch and the Rx branch are required to keep the heat load onto the stages of the cryogenic platform well below the respective cooling powers.

In the following, the role of the different components of the cryogenic microwave read-out chain is motivated and discussed and the possible range of variation during the optimisation is specified.

Amplifiers

As indicated by equation (4.3), a low-noise signal amplification immediately after the µMUX is essential for a good noise performance of the read-out chain. Within the ECHo-100k phase, the use of superconducting microwave amplifiers with quantum limited noise performance, such as travelling wave parametric amplifiers [Esp21], is not intended, and therefore, semiconductor-based ultra-low noise amplifiers, such as high-electron-mobility transistor (HEMT) amplifiers, are considered as first stage amplifiers for the cryogenic microwave read-out chain. Respecting the minimum bandwidth of 4 GHz per amplifier required for ECHo-100k, the best amplifier in terms of noise performance is the LNF-LNC4_8C[6] with a noise temperature of 1.5 K, a gain of +42 dB, an $IIP3$ of −44 dBm and a specified frequency range between 4 GHz and 8 GHz. However, the total signal power applied to the µMUX is −45.8 dBm for 400 read-out tones, and the attenuation between the µMUX, and the first stage amplifier should be as small as possible, which is why the $IIP3$ of this amplifier model is insufficient. Therefore, a customised version with a considerably higher $IIP3$, the LNF-LNC4_8C_LG, is chosen as amplifier (amp, Rx, 1) for the cryogenic microwave read-out chain. At a reference frequency of 6 GHz it is specified to exhibit a gain of +23 dB and a noise temperature of 1.9 K. For this customised amplifier, the $IIP3$ is not specified by the producer, but the improvement compared to the standard version of the amplifier is expected to be in the order of 25 dB, i.e. $IIP3 \approx -19\,\mathrm{dBm}$, which is confirmed by the findings presented in section 4.3.3. The power dissipation of this customised amplifier is $\sim 10\,\mathrm{mW}$, i.e. in total $\sim 150\,\mathrm{mW}$ are dissipated by the HEMT amplifiers of all 15 read-out chains, and therefore, the amplifier cannot be

[6] Low Noise Factory AB, Gothenburg, Sweden

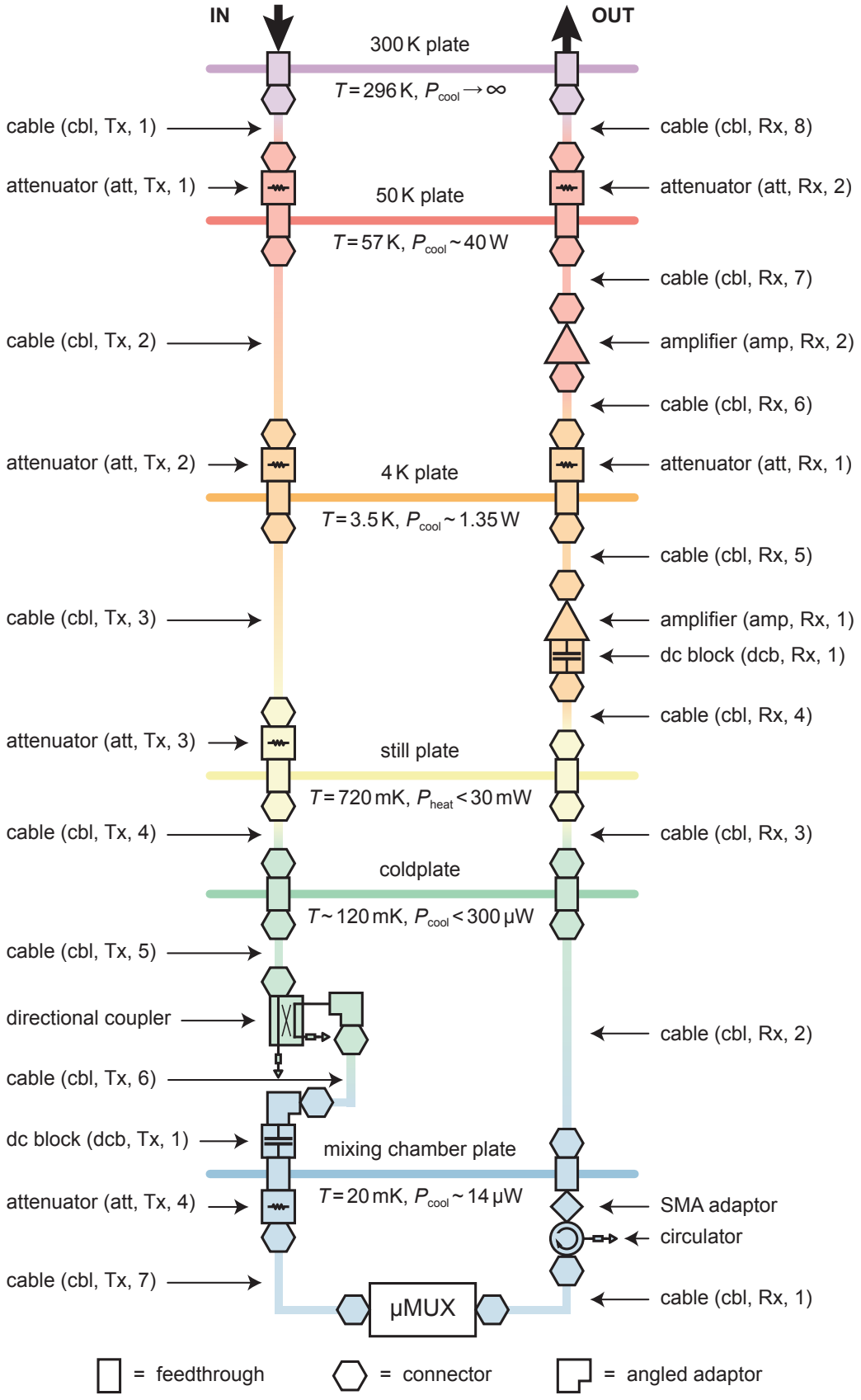

Figure 4.4: General layout of the cryogenic microwave read-out chain. A detailed description is given in the main text.

mounted on the three coldest stages of the cryogenic platform, but only on the 4 K plate, which is providing a sufficient cooling power. As all microwave components between the µMUX and the first stage amplifier contribute significantly to the total noise temperature of the read-out chain, the attenuation of these components has to be kept at a minimum. Additionally, since the gain of the customised HEMT amplifier is not sufficient to amplify the signal coming from the µMUX to the level required at the input of the SDR system, a second low-noise amplifier is needed in the Rx branch. According to equation (4.8) and considering the performance of the first stage amplifier, the $IIP3$ of the second stage amplifier should be considerably larger than 0 dBm in order not to dominate the overall intermodulation performance of the read-out chain. For the simulation, two options have been considered for the second stage low-noise amplifier: a custom made cryogenic low-noise amplifier[7] with a gain of +13.5 dB, a noise temperature of 26.5 K and an $IIP3$ of +7 dBm at a reference frequency of 6 GHz, which is dissipating 60 mW per unit, i.e. 0.9 W for all 15 channels, and which would be mounted at the 50 K plate of the cryogenic platform as amplifier (amp, Rx, 2), or alternatively, a commercial room-temperature low-noise amplifier[8] with a gain of +20.6 dB, a noise temperature of 125 K and an $IIP3$ of +7.5 dBm at a reference frequency of 6 GHz, which would be positioned at the output of the cryogenic read-out chain.

Attenuators

In the design of the cryogenic microwave read-out chain, attenuators fulfil two purposes. Firstly, in the Tx branch, they decrease the power level of the incoming frequency comb of the SDR system in order to match the power level required at the µMUX. Secondly, as attenuators exhibit a galvanic connection between their outer conductor and their centre conductor, they establish a thermal link between the stages of the cryogenic platform and the centre conductor, which allows for a cooling of the otherwise thermally almost isolated centre conductors of all microwave components.

In the Tx branch, the attenuators (att, Tx, 1) to (att, Tx, 4) are placed on the 50 K plate, the 4 K plate, the still plate and the mixing chamber plate, respectively. In terms of noise performance, the largest attenuation should occur at lowest temperatures, according to equation (4.2), but this would also imply a considerable heat load at lowest temperatures due to a large signal power dissipation. Therefore, as the coldest temperature stages have the lowest cooling power, some attenuation has to occur at higher temperatures. To find the best attenuation values, in the simulation

[7] ASU 40K 1-8 GHz wideband LNA, Arizona State University, Tempe, AZ, USA
[8] ZX60-83LN-S+, Mini-Circuits, Brooklyn, NY, USA

(att, Tx, 1) to (att, Tx, 3) are varied between 0 dB and 20 dB attenuation in steps of 1 dB, respectively, and (att, Tx, 4) is varied between 0 dB and 6 dB attenuation in steps of 1 dB.

In the Rx branch, no attenuators are placed between the µMUX and the first stage amplifier, as they would compromise the noise performance according to equation (4.3). As a consequence, it has to be accepted, that potentially the centre conductors of the coaxial cables between the µMUX and the first amplifier are not well thermalised. On the 4 K plate and the 50 K plate, i.e. after the first amplifier, however, a thermalisation of the centre conductors is necessary and feasible. Therefore, the attenuators (att, Rx, 1) and (att, Rx, 2) are varied between 0 dB and 6 dB attenuation in steps of 1 dB. Note that an attenuation of 0 dB implies the utilisation of a 0 dB attenuator, which provides a galvanic connection between the outer conductor and the centre conductor and exhibits at most an attenuation of −0.3 dB, according to the specifications of the manufacturer[9].

Coaxial cables

To connect the microwave components mounted on different stages of the cryogenic platform and to connect spatially separated microwave components on the same stage, coaxial cables are required. The coaxial cables contribute, on the one hand, to the attenuation of the read-out chain and, hence, to the noise, and, on the other hand, to the heat flow between stages at different temperatures. For this reason, the cable materials and diameters at all stages have to be chosen with care. The materials of the considered cables[10] include the normal conducting alloys BeCu and CuNi, as well as the superconducting alloy NbTi. Additionally, an optional silver coating for the centre conductors of the normal conducting coaxial cables has been considered, which reduces the specific attenuation, i.e. the attenuation per cable length, compared to the uncoated cables, but enhances the thermal conductance of the cables as indicated in figure 4.2. In particular, for CuNi-based coaxial cables, only cables with silver coated centre have been considered because of the high specific attenuation of bare CuNi cables. Similarly to the effect of the silver coating, among the two considered cable diameters, a cable with a diameter of 1.19 mm exhibits a smaller specific attenuation and a larger thermal conductance if compared to a cable of the same material and a diameter of 0.86 mm. Considering that the costs per unit length of the superconducting cables is more than one order of magnitude higher than the costs per unit length of normal conducting cables, coaxial cables

[9] Attenuator 18AH-0, APITech, Marlborough, MA, USA

[10] SC-086/50-B-B, SC-119/50-B-B, SC-086/50-SB-B, SC-119/50-SB-B, SC-086/50-SCN-CN, SC-119/50-SCN-CN and SC-086/50-NbTi-NbTi by COAX CO., LTD., Aoba-ku, Yokohama-shi, Kanagawa, Japan

made from NbTi are employed only, where strictly necessary and normal conducting coaxial cables elsewhere.

As mentioned above, the attenuation between the µMUX and the first stage amplifier at the 4 K stage of the cryogenic platform needs to be kept at a minimum in order not to compromise the noise performance of the read-out chain. Therefore, for the cables (cbl, Rx, 1) to (cbl, Rx, 4), superconducting coaxial cables made from NbTi with a diameter of 0.86 mm and negligible attenuation and, hence, vanishing noise temperature, are employed. After the first stage amplification, the contribution of the noise temperature of subsequent attenuating microwave components to the noise temperature of the read-out chain is suppressed and, hence, it is not necessary to employ superconducting cables after the first stage amplifier. Additionally, the temperature of the Rx cables (cbl, Rx, 6) to (cbl, Rx, 8) is above the superconducting transition temperature $T_c \sim 10\,\mathrm{K}$ of NbTi. Therefore, for all cables after the first stage amplifier, only the normal conducting coaxial cable options are considered during the simulations.

For the Tx branch of the read-out chain, the noise performance of the coaxial cables is not critical as the attenuating microwave components in the Tx branch will dominate its noise performance. Therefore, for the cables (cbl, Tx, 1) to (cbl, Tx, 5) only normal conducting cable options are considered during the simulations. The length of the cable (cbl, Tx, 6) is comparably small, as discussed in section 4.2.6, and, hence, following from equation (4.11), the rate of heat flow for that cable is large. Therefore, in order to avoid a rate of heat flow onto the mixing chamber plate which is comparable to the cooling power of that stage, the cable material with the smallest thermal conductance, i.e. NbTi, is chosen for the cable (cbl, Tx, 6) and the cable diameter is set to 0.86mm. The cable (cbl, Tx, 7) does not need to fulfil any particular requirements in terms of heat transport as it connects microwave components which are thermally coupled to the same stage. Also in terms of attenuation or noise, this cable does not play a critical role. Therefore, as a practical, economic and mechanically robust solution, a hand-flex coaxial cable[11] is employed, which has proven to be suitable for this application in [Ric21] and [Ihs21].

A coaxial cable connecting two different temperature stages of the cryogenic platform exhibits a temperature gradient, which has to be taken into account for the calculation of the noise temperature and of the attenuation of the cable. The exact temperature profile along the cable is subject to multiple factors as for instance the temperatures of the two stages, the thermal conductivity as a function of temperature of both the conductor material and the dielectric material, the cable geometry, and the dissipated signal power in the coaxial cable. For the sake of simplicity and in first approximation, a linear temperature profile along the cables is assumed for

[11] 086 model series, Mini-Circuits, Brooklyn, NY, USA

all simulations. For the calculation of the attenuation and the noise temperature of a coaxial cable with length l and temperature dependent specific attenuation $\tilde{G}(T)$, the cable is modelled as a cascade of $n \gg 1$ attenuators, each corresponding to a cable segment of length l/n. The physical temperature T_i of the i-th attenuator in the cascade is determined by the linear temperature profile of the cable, while the attenuation is given by $G_i = \tilde{G}(T_i) \cdot l/n$. Consequently, the noise temperature of the i-th attenuator is calculated by equation (4.2), i.e. $T_{\mathrm{N},i} = T_i(1-G_i)/G_i$. Finally, the noise temperature of the coaxial cable is calculated with equation (4.3) for the noise temperature of cascaded two-port networks, while the total attenuation factor of the cable is given by $G = G_1 G_2 \cdots G_n$. For the simulations, the specific attenuation $\tilde{G}(T)$ has been obtained by interpolating data provided by the manufacturer of the cables, and $n = 30$ has proven to be sufficiently accurate. The length l of each cable is determined by geometric constraints, such as the distance between the microwave components which are connected by the cable, and by an individual buffer preventing potential damage from the cable due to thermal contraction during the cooldown of the set-up.

The rate of heat flow through a coaxial cable connecting two different temperature stages is calculated by equation (4.11) assuming a perfect thermalisation in first approximation. Additionally, in a most conservative approach, for the simulations it is assumed that the signal power dissipated in the cables adds to the heat flow, i.e. the dissipation is assumed to act entirely as heat load onto the colder stage of the two stages connected by the cable.

Further microwave components

Directional coupler In the framework of cryogenic read-out chains, a directional coupler interrupts galvanically the centre conductor of the read-out chain and terminates the two ends of the centre conductor, caused by the interruption, in matched and well-thermalised terminations. In this way, the heat flow arising from a comparably warm and potentially even not well thermalised centre conductor is interrupted and dumped entirely at the directional coupler. In this way, a decent thermalisation of the subsequent centre conductor is guaranteed by the well thermalised terminations. This would be particularly important close to the µMUX on the mixing chamber plate, as a hot centre conductor of the read-out chain could heat up the experimental set-up consisting of the µMUX and the MMCs, which could compromise their performance. For an ideal, unterminated directional coupler no signal losses occur in the coupler itself. However, if two ports are terminated in matched loads, the directional coupler acts as a lossy attenuator in terms of attenuation and noise temperature [GG04]. Therefore, no directional coupler can be employed in the Rx branch close to the µMUX, where attenuating components would compromise the

noise performance of the read-out chain. In the Tx branch of the read-out chain, the noise performance of the directional coupler is not critical, but the power dissipation upon the attenuation has to be taken into account. The power dissipation of the total 15 directional couplers of all read-out chains for ECHo-100k would exceed the cooling power of the mixing chamber plate. Therefore, a directional coupler is inserted into the read-out chain at the coldplate of the cryogenic platform, where the cooling power is sufficient. For the simulation, cryogenic directional couplers[12] with 6 dB coupling, 10 dB coupling and 20 dB coupling have been considered.

dc blocks Similarly to directional couplers, dc blocks[13] are employed to mitigate heat flow, however, they do not provide a thermalisation of the centre conductor. As they interrupt both the centre conductor and the outer conductor and exhibit a comparably small insertion loss of $\lesssim 0.5\,\mathrm{dB}$, they are particularly suitable for reducing the rate of heat flow upon the power dissipation of amplifiers in the Rx branch. For this reason, the dc block (dcb, Rx, 1) is placed right before the first stage amplifier. To mitigate the rate of heat flow onto the mixing chamber plate in the Tx branch further, the dc block (dcb, Tx, 1) is located before the Tx feedthrough of the mixing chamber plate. For the simulation, in terms of attenuation and noise temperature, the dc blocks are modelled as lossy attenuators.

Circulator In order to isolate the µMUX from the noise of the first stage amplifier, a circulator[14] with an insertion loss of $< 0.2\,\mathrm{dB}$ is interconnected, whose third port is terminated in a matched load. Such a circulator configuration is called isolator. In forward direction, i.e. in direction from the µMUX to the HEMT amplifier, the isolator acts as an attenuator in terms of noise temperature and attenuation [GG04], whereas in backwards direction, the noise coming from the HEMT amplifier is suppressed by $\geq 22\,\mathrm{dB}$ and, hence, the noise acting on the µMUX is dominated by the isolator's cold termination.

Feedthroughs, connectors, adaptors Several small microwave components with minimal loss, which can be modelled as lossy attenuators, are employed in the cryogenic read-out chain. Feedthroughs[15] provide mechanical and thermal anchoring of the attached microwave components and feed the conductors through the stages of the cryogenic platform. For the 300 K stage hermetically sealed feedthroughs[16] are

[12] QMC-Cryocoupler, Quantum Microwave Inc., Cohasset, MA, USA
[13] dc block inner/outer (model: 8039), APITech, Marlborough, MA, USA
[14] LNF-CIC4_8A, Low Noise Factory AB, Gothenburg, Sweden
[15] SF-SF50+, Mini-Circuits, Brooklyn, NY, USA
[16] PE9184, Pasternack, Irvine, CA, USA

used. Cable connectors[17] are chosen according to the cable diameter and cable material. An adaptor[18] is employed to attach the circulator to the feedthrough. In the final set-up, this adaptor might need to be replaced by a superconducting coaxial cable for geometric reasons, however, this change would practically not affect the simulation results. Due to the limited space between the coldplate and the mixing chamber plate, angled adaptors[19] are required to fit the cables.

4.2.5 Simulation results

In order to find the most suitable layout for the cryogenic microwave read-out chain for the ECHo-100k phase, the performances of numerous layout options at a reference frequency of 6 GHz have been simulated in terms of noise temperature, Tx attenuation, Rx gain and power dissipation on each stage of the cryogenic platform, employing a dedicated Python-based simulation program, which has been developed within the framework of this thesis. Each layout option is characterised by a unique combination of attenuators and cable types at each stage, and by the attenuation of the directional coupler and the presence or absence of a second stage amplifier at the 50 K stage. Among all possible layout options, highly implausible options have been excluded from the simulations, as for instance those with extremely high or extremely low attenuation. After this selection, for the remaining 1.3×10^6 options, a simulation has been performed. The results of each simulation have been stored in a layout database, from which the most suitable layout could be extracted by the application of the following four selection criteria:

- the Tx attenuation and the Rx gain have been limited to values compatible with the required microwave power on the µMUX chip and the power specifications of the SDR system;

- the heat load onto each stage of the cryogenic platform has been restricted to 20 % of the respective cooling power. On the one hand, this criterion takes into account a possible underestimation of the heat load due to potentially not well thermalised centre conductors. On the other hand, not the entire cooling power of each stage is available for the cryogenic microwave read-out chain because of the presence of further components on the stages, such as dc cable ribbons and mechanical connections;

[17] AX-086P/SD, AX-086P/SDLS/NbTi and Ax-119P by COAX CO., LTD., Aoba-ku, Yokohama-shi, Kanagawa, Japan

[18] SM-SM50+, Mini-Circuits, Brooklyn, NY, USA

[19] Angled SMA coupling (model: 0409059), BKL-ELECTRONIC Kreimendahl GmbH, Lüdenscheid, Germany

- besides the superconducting coaxial cables with diameter $d_{\text{outer}} = 0.86\,\text{mm}$ and the hand-flex coaxial cable, only two additional cable types have been permitted, in order to maintain an efficient and economic cable manufacture and assembly;
- for simplicity, the number of attenuator types has been limited to three.

After the application of those criteria, the remaining results have been sorted by noise performance, and the layout with the best performance has been chosen for ECHo-100k.

In figure 4.5a the final layout is visualised. The simulations indicated that the noise performance of layouts with a cryogenic second-stage amplifier is typically better than the noise performance of the corresponding set-ups with room-temperature amplifiers by a factor of ~ 2, and hence, the cryogenic second-stage amplifier is chosen for the microwave read-out chain. As expected, also the usage of 0 dB attenuators in the Rx branch proved to be essential for a sufficient noise performance while providing a thermalisation path to the centre conductors. In the Tx branch the attenuation is distributed over all stages and it consists of one $-10\,\text{dB}$ attenuator at the 50 K plate and one at the 4 K plate, a $-6\,\text{dB}$ attenuator at the still plate, a -10 dB directional coupler at the cold plate and a 0 dB attenuator at the mixing chamber plate. This configuration is a trade-off between the best noise performance and the available cooling power. Due to the constraint of a limited number of cable types, for the Tx branch, only one cable type is employed between the 300 K plate and the directional coupler at the coldplate, namely BeCu cables with a diameter of $d_{\text{outer}} = 0.86\,\text{mm}$. By design, the coaxial cables between the directional coupler and the first stage amplifier are made from NbTi with a diameter of 0.86 mm, except for the hand-flex coaxial cable connecting the µMUX to the Tx branch, as discussed in section 4.2.4. For the Rx branch, BeCu coaxial cables with a diameter of 1.19 mm and a silver coated centre conductor are employed between the first stage amplifier and the 300 K plate. This result reflects once more the need for a low attenuation in the Rx branch, in order to obtain an optimal noise performance.

The expected Tx attenuation and the expected Rx gain as a function of frequency for the final layout of the cryogenic microwave read-out chain are plotted in figure 4.5b. Due to the frequency dependent attenuation of the coaxial cables, the Tx attenuation ranges between $-42.1\,\text{dB}$ at $f = 4\,\text{GHz}$ and $-44.4\,\text{dB}$ at $f = 8\,\text{GHz}$. In order to obtain the optimal microwave read-out power on chip for all read-out tones at all frequencies, the frequency dependent Tx attenuation can easily be compensated by adjusting the signal power provided by the SDR system as a function of frequency. In the Rx branch, the total gain is not only subject to the frequency dependent attenuation of the microwave cables, but also to the frequency dependent gain of the

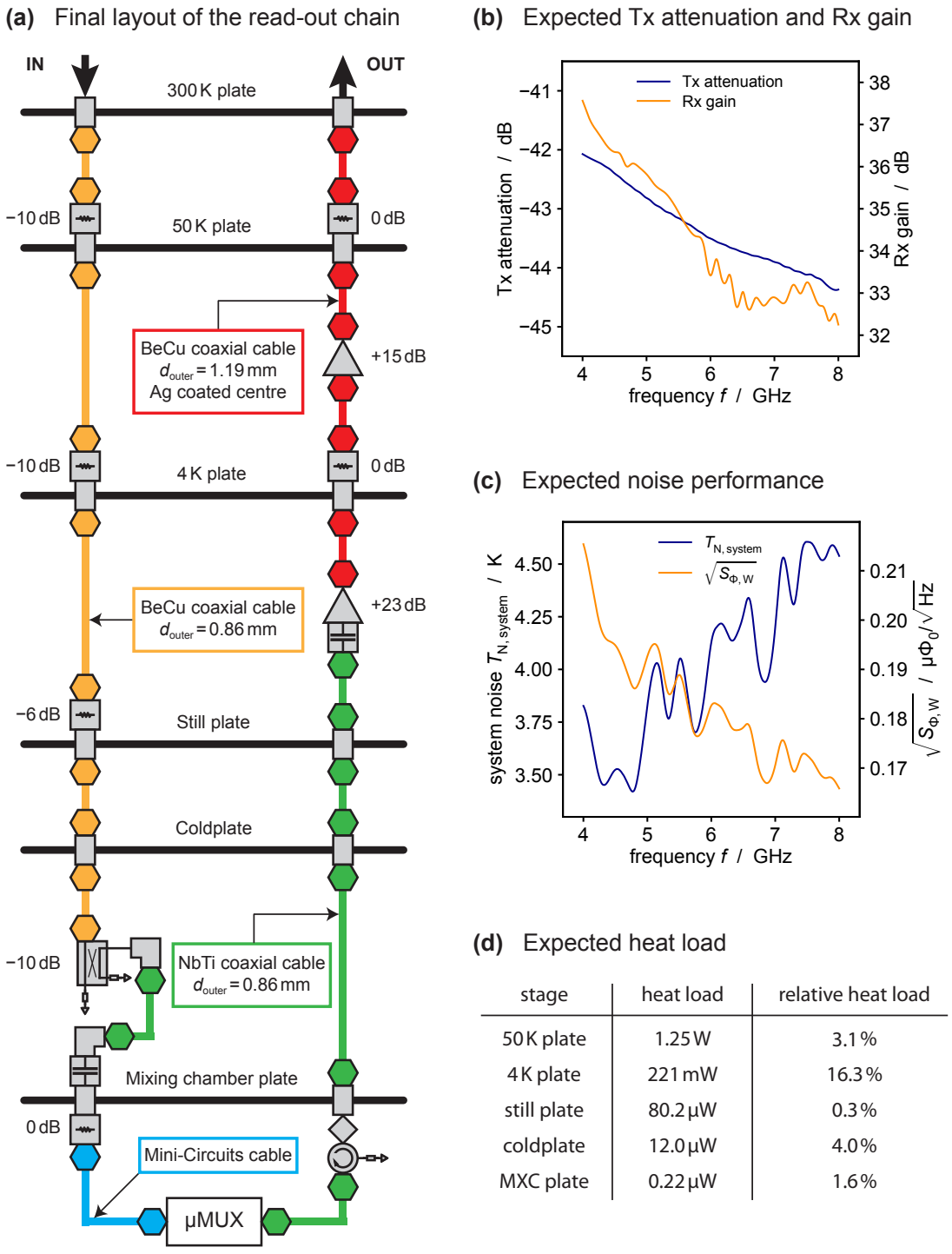

stage	heat load	relative heat load
50 K plate	1.25 W	3.1 %
4 K plate	221 mW	16.3 %
still plate	80.2 μW	0.3 %
coldplate	12.0 μW	4.0 %
MXC plate	0.22 μW	1.6 %

Figure 4.5: **(a)** Final layout of the cryogenic microwave read-out chain. The pictograms symbolising microwave components are identical to those used in figure 4.4. **(b)** Simulated Tx attenuation (IN → μMUX) and Rx gain (μMUX → OUT). **(c)** Simulated noise performance. The μMUX parameters used for calculation of the apparent white magnetic flux noise $\sqrt{S_{\Phi,W}}$ are reported in the main text. **(d)** Simulated heat load onto the stages of the cryogenic platform. The relative heat load is the ratio of the expected heat load and of the cooling power of the respective stage.

amplifiers, and ranges between +37.6 dB at $f = 4\,\mathrm{GHz}$ and +32.3 dB at $f = 8\,\mathrm{GHz}$. The small oscillations visible at frequencies above $\sim 6\,\mathrm{GHz}$ arise from a similar feature in the gain of the second stage amplifier.

The system noise temperature $T_{\mathrm{N,system}}$, plotted in figure 4.5c, is the noise temperature of the entire read-out system, i.e including the SDR system, referenced to the µMUX chip. It takes values between 3.4 K and 4.6 K and increases, by trend, with increasing frequency. This behaviour is mostly a consequence of the decreasing Rx amplification. The oscillations in $T_{\mathrm{N.system}}$, are caused by the interplay of the frequency dependent gains of the two amplifiers and the frequency dependent attenuations of the microwave cables.

For a given µMUX configuration, the white apparent magnetic flux noise level corresponding to the system noise temperature $T_{\mathrm{N.system}}$ can be calculated employing equations (3.72) and (3.73). Accordingly, for an ideal µMUX based on lumped element resonators with intrinsic quality factor $Q_{\mathrm{i}} \to \infty$, matching parameter $\eta_0 = 1$, SQUID screening parameter $\beta_{\mathrm{L}} = 0.6$, SQUID inductance $L_{\mathrm{S}} = 45\,\mathrm{pH}$ and resonance frequency $4\,\mathrm{GHz} \leq f_{\mathrm{r}} \leq 8\,\mathrm{GHz}$, the apparent magnetic flux noise $\sqrt{S_{\Phi,\mathrm{W}}}$ is shown in figure 4.5c. In contrast to $T_{\mathrm{N.system}}$, by trend, the white apparent magnetic flux noise decreases with increasing frequency, because $S_{\Phi,\mathrm{W}} \propto T_{\mathrm{N.system}}/f_{\mathrm{r}}$. The values for the apparent white magnetic flux noise range between $0.166\,\mu\Phi_0/\sqrt{\mathrm{Hz}}$ and $0.215\,\mu\Phi_0/\sqrt{\mathrm{Hz}}$, which is comparable to the white flux noise level of state-of-the-art dc SQUID-based read-out systems for MMCs [Man21b].

The expected performance of the final cryogenic microwave read-out system with 15 read-out chains in terms of heat load onto the stages of the cryogenic platform is summarised in figure 4.5d. Note that the numbers presented in the table only hold exactly true under the assumption of perfectly thermalised centre conductors and components, and might therefore be somewhat larger in the real set-up. Excluding the 4 K stage, the relative heat load on any other stage of the cryogenic platform, i.e. the ratio of the heat load and the cooling power of the respective stage, is $\leq 4\,\%$. For the 4 K stage, the dominant heat load is the power dissipation of the first stage amplifiers, which dissipate in total 150 mW. Therefore, the heat load on the 4 K stage restricted to signal dissipation and the thermal conductance of the cables corresponds to 71 mW, accounting for a relative heat load of 5.3 %. Thus, even if the real heat load due to thermal conductance and signal dissipation was one order of magnitude larger on all stages than the corresponding simulated heat load, the cooling performance of the cryogenic platform would still not be compromised. As a conclusion, it is safe to assume that the heat load caused by the real cryogenic read-out system will be compatible with the cooling performance of the cryogenic platform. Even an upgrade of the number of read-out chains for a potential future phase of the ECHo experiment seems feasible in terms of heat load. In this case, the bottleneck would be the cooling

power of the 4 K stage, which, however, could be boosted by the installation of a second pulse tube cooler.

4.2.6 Mechanical design

The layout of the dedicated cryogenic platform for the ECHo experiment sets requirements and restrictions on the mechanical design of the cryogenic microwave read-out chain. The largest port on the 300 K plate of the cryogenic platform, which allows for a straight connection through all subjacent temperature stages, is a DN 100 ISO-K flange with an inner diameter of 102 mm, which defines the circular cross-section available for the required 15 microwave read-out chains. The distance between the 300 K plate and the mixing chamber plate is ~ 1.0 m, and hence, a cylindrical volume is established, which is usable for the placing of the read-out chains.

In figure 4.6a, the dedicated design for the mechanical set-up of the read-out chains for ECHo-100k is depicted true to scale. It is structured in a modular way, allowing for the installation of up to 16 individual coaxial read-out chains. For the sake of clarity, only four read-out chains are shown in the figure. The vacuum-tight 300 K flange is made from stainless steel and it features 16 pairs of hermetically sealed coaxial feedthroughs, which allow for the connection of the SDR system to the cryogenic microwave read-out chain. All other flanges are made from tempered OFHC[20] copper, in order to ensure a sufficient thermalisation of components and cables attached to them, and they exhibit standard coaxial feedthroughs. Additionally, they feature through holes for the installation of support structures for microwave components, and slits for the feedthrough of dc power cables for the cryogenic low-noise amplifiers. As the semi-rigid coaxial cables connecting the different temperature stages potentially experience a different thermal contraction during the cool down of the cryogenic platform than the platform itself, a cable length buffer preventing potential damage is needed. For the cables connecting the 300 K flange with the 50 K flange, this buffer consists of a loop, while for all other cables the buffer is implemented in the S-shaped configuration of the cables.

The mechanical design of the section containing the second stage amplifiers, i.e. the section between the 50 K flange and the 4 K flange, is very similar to the design of the section containing the first stage amplifier, and hence, only the latter is discussed here. Figure 4.6b shows a zoom onto that section of the read-out chains connecting the 4 K flange and the still flange. The first stage amplifiers, i.e. the HEMT amplifiers, are mechanically and thermally connected to the 4 K flange via a modular support structure made from OFHC copper. For the sake of simplicity, the dc power cables for the amplifiers are omitted in the figure. Due to space constraints, not

[20] Oxygen-free high thermal conductivity

all amplifiers are mounted at the same height, causing the coaxial cable lengths to vary slightly between different read-out chains. Simulations of the noise performance showed that these length variations do not impact the performance of the read-out chains significantly.

Between the still flange and the cold flange, only coaxial cables are mounted to provide a connection between the section above and the section below.

The zoom onto the section of the read-out chains between the cold flange and the mixing chamber flange, visualised in figure 4.6c, shows the tightly packed layout of the read-out chains at this stage. The directional couplers are mounted to a modular OFHC copper structure providing mechanical support and thermal anchoring. The coaxial cables connecting the directional couplers to the subjacent dc blocks are very short, and hence, the use of superconducting NbTi coaxial cables at this stage is motivated by maintaining the heat flow onto the mixing chamber stage at a minimum, as discussed above. In order to make most efficient use of the available space, two angled adaptors per read-out chain are employed between the directional coupler and the dc block.

The section below the mixing chamber (MXC) flange provides the interface to the experimental holder[21] where the detector chips and the respective µMUX chips for the ECHo-100k phase are placed.

A dedicated stand has been designed, which allows for the installation and testing of the entire 15 read-out chains outside the cryogenic platform. After approval, the set-up, with the exception of the 300 K flange, can be inserted laterally into a dedicated slot of the cryogenic platform.

4.3 Experimental characterisation

Based on the results of the above discussed simulations of the cryogenic microwave read-out chain for ECHo-100k and based on the above presented mechanical design of the read-out chain, a demonstration read-out chain has been manufactured and assembled on the dedicated cryogenic platform for the ECHo experiment. Exploiting this demonstration read-out chain, the compliance of the cryogenic microwave read-out chain with the performance goals has been demonstrated.

[21] Currently under development.

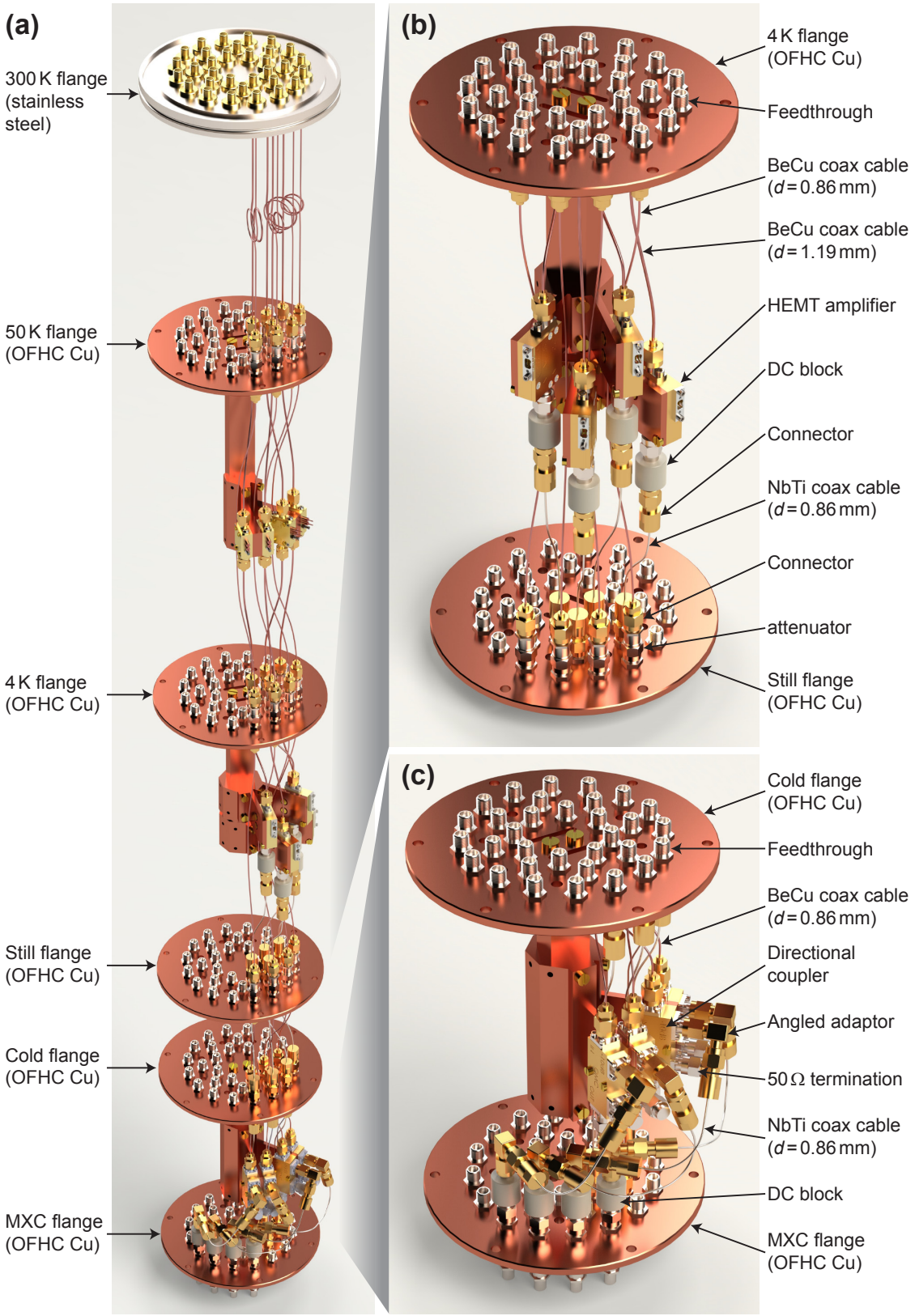

Figure 4.6: **(a)** Mechanical design of the cryogenic microwave read-out chain with zooms onto **(b)** the section between the 4 K flange and the still flange, and **(c)** the section between the cold flange and the mixing chamber (MXC) flange. For the sake of clarity only four channels are shown.

4.3.1 Attenuation, gain and noise performance

After the assembly of the demonstration read-out chain on the cryogenic platform, the first characterisation at room temperature in terms of attenuation and gain of the read-out chain has been carried out by means of a vector network analyser[22]. The attenuation of the Tx branch and the gain of the Rx branch have been measured separately and the corresponding results are presented in figure 4.7. For comparison, the theoretically expected Tx attenuation and Rx gain are also plotted in the same figure. The underlying simulations have been carried out employing the dedicated simulation program developed for the design process of the cryogenic microwave read-out chain, however, setting the temperatures of all stages of the cryogenic platform, of all coaxial cables and of all microwave components to 300 K. As the attenuation of the coaxial cables and the gain of the two involved low-noise amplifiers are temperature dependent, the simulated Tx attenuation and the simulated Rx gain deviate from the simulated curves shown in figure 4.5b. In particular, at 300 K the NbTi-based coaxial cables are normal conducting and their specific attenuation of $-24.0\,\mathrm{dB/m}$ at 300 K decreases the effective Rx gain drastically. The agreement between the measured and the simulated Tx attenuation is satisfactory. The deviations around 4.7 GHz and 7.6 GHz are smaller than 2.3 dB and originate most likely from minor microwave reflections at the connections of microwave components within the Tx branch of the read-out chain. For the Rx branch, the simulated gain is about 2 dB smaller than the measured gain, which could be traced back to an enhanced HEMT amplifier gain at 300 K with respect to the gain specified by the producer. The oscillations in the Rx gain curve are characterised by a similar amplitude as the deviations in the Tx attenuation curve and are most likely caused by a similar effect. Considering that the attenuation or gain of each employed microwave component is specified only with a limited accuracy - for instance, the employed $-10\,\mathrm{dB}$-attenuators are specified with an attenuation accuracy of $\pm 0.5\,\mathrm{dB}$ - the match between the measured Tx attenuation and Rx gain and the corresponding simulated curves is satisfying.

In standard operation mode, the two branches of the cryogenic microwave read-out chain cannot be characterised separately anymore, as the cryogenic microwave read-out chain is enclosed inside the vacuum can of the cryogenic platform. Therefore, only the transmission of the entire cryogenic read-out chain, i.e. the series of the Tx branch, the experimental holder carrying the µMUX and the Rx branch, can be measured by means of a vector network analyser. In order to characterise the cryogenic microwave read-out chain in standard operation, an experimental holder carrying the µMUX chip *ECHo-MUX-04-6A* has been mounted onto the mixing chamber plate of the cryogenic platform, connected to the read-out chain, and cooled down to the intended operational temperature of $T_{\mathrm{MXC}} = 20\,\mathrm{mK}$. A detailed description of this

[22] R&S ZNB8, Rohde & Schwarz GmbH & Co. KG, Munich, Germany

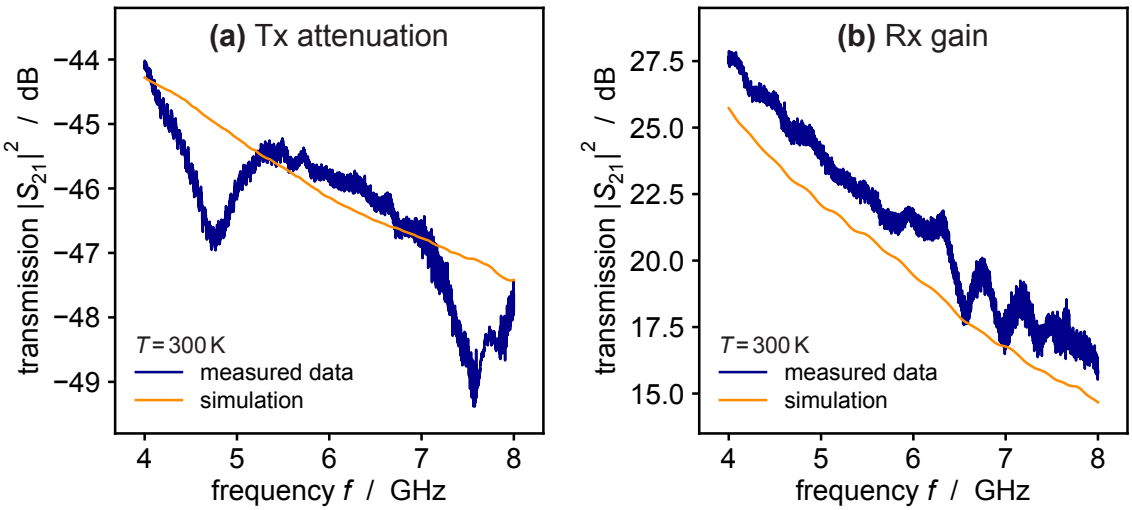

Figure 4.7: **(a)** Tx attenuation and **(b)** Rx gain of the cryogenic microwave read-out chain at room temperature.

set-up is given in section 6.1. In figure 4.8, the measured transmission of this set-up for frequencies between 4 GHz and 8 GHz is plotted. Note that the 14 sharp resonances correspond to superconducting resonators of the µMUX chip, as discussed in section 6.2, and hence, they are not a feature of the read-out chain. For comparison, the theoretically expected transmission of the cryogenic microwave read-out chain is plotted in the same figure. The slight deviations of the simulated from the measured transmission are most likely caused, on the one hand, by effects similar to those responsible for the deviations of the data at 300 K presented above, and on the other hand, by minor signal reflections due to imperfections of the experimental holder, as for instance the transition from the microwave circuit board to µMUX chips implemented with manually placed aluminium bonding wires. Overall, given the limited precision of the simulation due to the finite accuracy of the specified properties of the employed microwave components and due to the neglect of imperfections, the measured transmission of the cryogenic microwave read-out chain and the simulated transmission agree reasonably well.

In the course of the noise performance measurements for the microwave SQUID multiplexer, presented in chapter 6, the Tx attenuation of the set-up in standard operation mode at the resonance frequencies of the µMUX channels could be estimated. The results thereof are summarised in table 6.4, presented in section 6.2.3, and the plausibility of the simulated Tx attenuation of the cryogenic microwave read-out is discussed in section 6.4.1. Additionally, the amplitude and phase noise performance of the investigated µMUX channels is consistent with the system noise predicted for the respective µMUX channels by the above simulations, as explained in section 6.4.1, indicating that the simulated system noise temperatures are plausible.

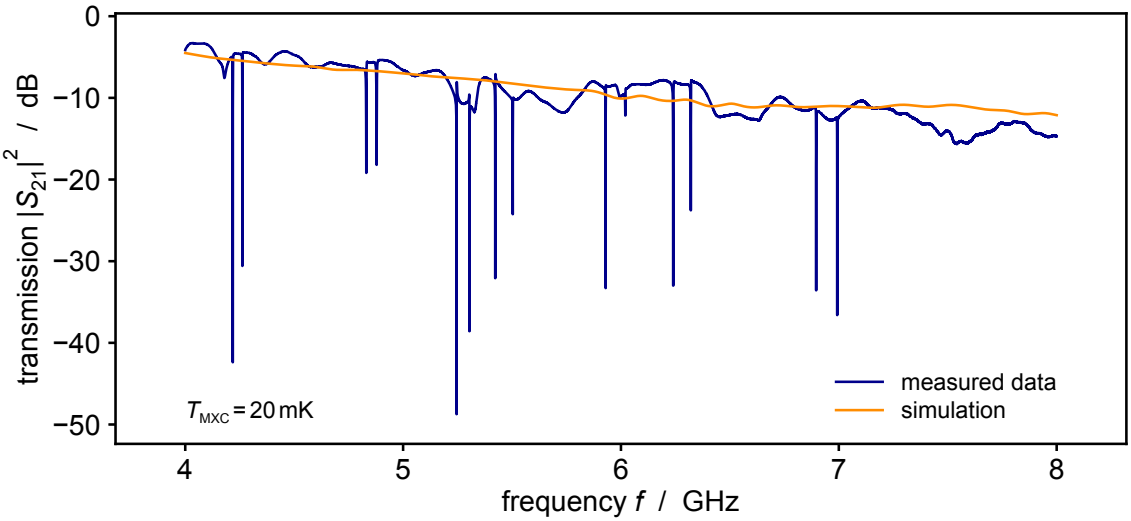

Figure 4.8: Measured transmission (blue curve) of the cryogenic microwave read-out chain with experimental set-up carrying the µMUX chip *ECHo-MUX-04-6A*. The 14 sharp resonances correspond to some of the microwave resonators of the µMUX chip. The orange curve indicates the simulated transmission of the cryogenic microwave read-out chain.

4.3.2 Heat load

A detailed characterisation of the installed demonstration read-out chain in terms of heat flow and power dissipation has not been feasible within the scope of this thesis. In particular, as the simulated heat load onto the cryogenic platform caused by a single channel is 15 times smaller than the values listed in figure 4.5d, the relative heat load onto the mixing chamber is in the order of 0.1 % and onto the 4 K plate in the order of 1.1 %, which basically negligible.

Instead, in order to mimic the impact of the heat load caused by 15 cryogenic microwave read-out chains onto the cryogenic platform, all stages of the cryogenic platform have been equipped with ohmic heaters temporarily. The power dissipated in the heaters has been varied in multiples of the simulated values for the heat load, listed in figure 4.5d, in order to investigate the performance of the cryogenic platform under increasing heat load. It turned out, that up to a power dissipation corresponding to the fivefold simulated heat load, a stable operation of the cryogenic platform with a mixing chamber temperature $T_{\mathrm{MXC}} \leq 20\,\mathrm{mK}$, i.e. the intended operational temperature for ECHo-100k, was possible. For higher heat loads, the limited cooling performance of the 4 K plate lead to instabilities in the operation of the cryogenic platform, such as temperature oscillations and an escalating flow of the $^3\mathrm{He}/^4\mathrm{He}$ mixture in the dilution cycle. Overall, this performance test indicates that, even if the heat load caused by the 15 real cryogenic read-out chains was up to five times

larger than simulated, for instance due to potentially not well thermalised centre conductors of coaxial cables, the cooling performance of the cryogenic platform would still suffice.

4.3.3 Intermodulation distortion

In the following, the intermodulation distortion in the cryogenic microwave read-out chain is characterised in terms of the $IIP3$ of the cascade of the two low-noise amplifiers. For that purpose, the sinusoidal signals of two microwave signal generators[23] with carrier frequencies f_1 and f_2 and identical amplitude A_{in} have been combined and applied to the input of the cryogenic microwave read-out chain. The resulting frequency spectrum at the output of the read-out chain has been recorded with a real time signal analyser (RSA)[24]. The carrier frequencies have been varied between 4 GHz and 8 GHz in steps of 50 MHz, keeping a spacing of $f_2 - f_1 = 100\,\text{MHz}$. For each frequency setting, the generated carrier power has been varied between $-30\,\text{dBm}$ and $+19\,\text{dBm}$ in steps of 1 dBm. In figure 4.9a, exemplarily, the recorded power spectrum for $f_1 = 4.0\,\text{GHz}$ and $f_2 = 4.1\,\text{GHz}$ is shown for a generated carrier power of $P_{\text{tone}}^{\text{set}} = 3\,\text{dBm}$. The carriers are visible as peaks at their respective carrier frequencies f_1 and f_2. Additional, equidistantly spaced peaks are present and they can be attributed to intermodulation distortion in the set-up. The peaks associated with third-order intermodulation (IM3) neighbour the carrier peaks. Peaks corresponding to an increasing order of intermodulation exhibit a decreasing amplitude and are increasingly distant in frequency space from the carriers. For the given generated carrier power, the fifth-order intermodulation (IM5) is the highest observable order of intermodulation, as the amplitudes of any higher-order intermodulation are lower than the noise floor of the RSA at $\sim -90\,\text{dBm}$. For each recorded spectrum, the carrier power arriving at the RSA is extracted, as well as the power of the spurious tones corresponding to the third-order intermodulation, i.e. the dominant contribution to intermodulation distortion. Knowing the total attenuation of the microwave set-up, as well as the attenuations of the signal chain before the first stage amplifier and after the second stage amplifier from simulations, the carriers' input power can be referenced to the input of the first stage amplifier and the measured tone powers can be referenced to the output of the second stage amplifier. In figure 4.9b, for carrier frequencies $f_1 = 4.0\,\text{GHz}$ and $f_2 = 4.1\,\text{GHz}$, the measured total carrier power at the output of the second stage amplifier is plotted as a function of the total carrier power applied to the input of the first stage amplifier. For low powers, the input and output power are related linearly, indicating a constant gain. For higher powers, however, as expected a gain compression occurs. The measured total power

[23] R&S SMA100B and R&S SMF100A, Rohde & Schwarz GmbH & Co. KG, Munich, Germany
[24] RSA5115B, Tektronix Inc., Beaverton, OR, USA

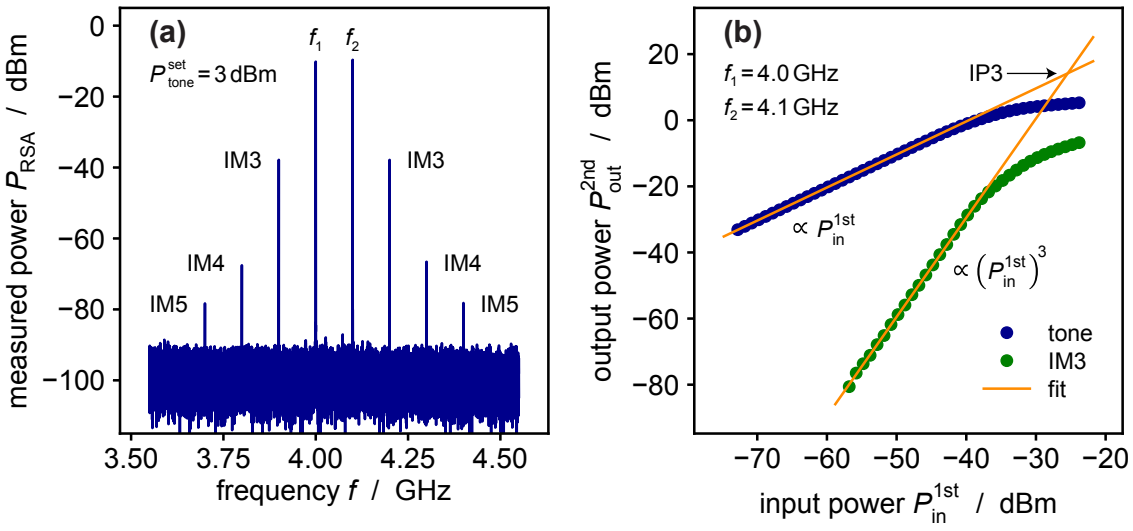

Figure 4.9: **(a)** Power spectrum as recorded by the real-time spectrum analyser (RSA) for tones $f_1 = 4.0\,\text{GHz}$ and $f_2 = 4.1\,\text{GHz}$ and generated tone powers $P^{\text{set}}_{\text{tone}} = 3\,\text{dBm}$. The spurious frequencies caused by intermodulation (IM) are marked with their respective order. **(b)** Total tone power (blue circles) and total IM3 power (green circles) at the output of the 2nd stage amplifier as a function of the total tone power at the input of the 1st stage amplifier. The orange lines are fits to the uncompressed parts of the respective data.

of the third-order intermodulation tones, referenced to the output of the second stage amplifier, is plotted in figure 4.9b, too. In accordance to the expectation, for low powers a cubic relation is found and at higher powers a compression is observed. In order to extract the third-order intercept point (IP3), the data related to the carriers is fitted numerically for low powers with a linear function, and the data related to the intermodulation tones is fitted with a cubic function at low powers, as shown in figure 4.9b. These fit curves are then extrapolated to high powers, where they intersect in the third-order intercept point (IP3), which characterises the intermodulation related to the cascade of the first stage amplifier and the second stage amplifier. For each pair of carrier frequencies f_1 and f_2, the input power $IIP3$ at the IP3 has been extracted from the corresponding fits. In figure 4.10, the $IIP3$ obtained in this way is plotted for carrier frequencies $4\,\text{GHz} \leq f_1 \leq 8\,\text{GHz}$. As the input power of the carriers at the first stage amplifier is calculated from the generated carrier power based on the simulated attenuation of the set-up, a systematic error is introduced, because the total simulated attenuation deviates slightly from the measured total attenuation as already observed in section 4.3.1. Averaging the $IIP3$ over all frequencies yields $\langle IIP3 \rangle = -21 \pm 2\,\text{dBm}$. Based on equation (4.8) with the second stage $IIP3$ of $+7\,\text{dBm}$ at $6\,\text{GHz}$ and the first stage gain of $+23\,\text{dB}$, the first stage $IIP3$ yields $-19 \pm 3\,\text{dBm}$, which is compatible with the expected performance.

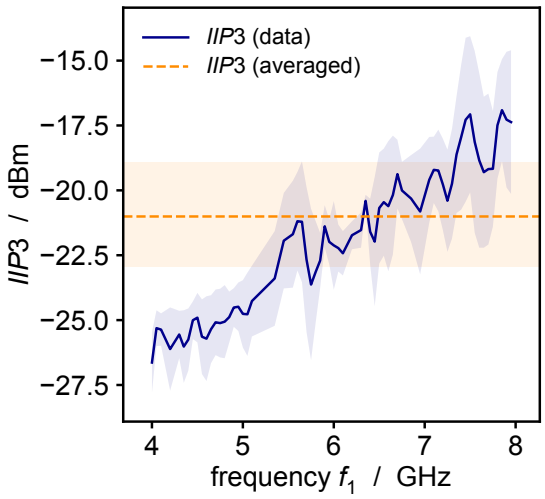

Figure 4.10: The input third-order intercept point $IIP3$, extracted from the measured output tone powers and IM3 powers, is plotted as a function of the input tone frequency f_1 as blue curve with associated uncertainty (light blue band). The average $IIP3$ is shown as dashed orange line with corresponding uncertainty (light orange band).

In order to understand the impact of the measured third-order intermodulation in terms of pseudo-noise, the apparent pseudo-noise power on the µMUX chip has to be estimated. For this, firstly, the total carrier power at the input of the first stage amplifier is calculated. The optimal read-out power on chip is −71.8 dBm per carrier, however, part of the power is reflected by the corresponding resonance of the µMUX and does not reach the first stage amplifier. For a µMUX channel with intrinsic quality factor $Q_\mathrm{i} \sim 10^5$ and a fixed optimal read-out frequency, i.e. a read-out frequency for which the transmission change is maximal during flux-ramp-modulation, the transmission averaged over one period of the flux-ramp-modulation is −6.3 dB. Additionally, the microwave components between the µMUX and the input of the first stage amplifier account for an attenuation of −1.3 dB. Hence, for 400 carriers, the total signal power at the input of the first stage amplifier yields −53.4 dBm, which is −32.4 dB below the $\langle IIP3 \rangle$. Consequently, the apparent total IM3 power at the input of the first stage amplifier is −97.2 dB below the $\langle IIP3 \rangle$. On the µMUX chip, this corresponds to an apparent total IM3 power of −119.5 dBm for IM3 tones with frequencies $f_\mathrm{IM3} = |2f_1 - f_2|$ for any f_1 and any f_2 between 4 GHz and 8 GHz, meaning for f_IM3 between 0 GHz and 12 GHz. Assuming that the sheer number of all IM3 tones in its entirety acts as white pseudo-noise, equation (4.1) can be employed to calculate a corresponding pseudo-noise temperature of $T_\mathrm{N,IM3} = 6.8\,\mathrm{mK}$. If compared to the system noise temperature shown in figure 4.5c, the pseudo-noise temperature arising from third-order intermodulation is basically negligible. Hence, third-order intermodulation does not deteriorate the noise performance of the microwave read-out chain significantly.

4.3.4 Final remarks and outlook

In conclusion, the cryogenic microwave read-out chains for ECHo-100k has been designed based on simulations in order to fulfil the required performance in terms of attenuation, gain, noise, power dissipation and intermodulation distortion. A mechanical design has been established and a demonstration read-out chain has been set up. The compliance of the performance of the demonstration read-out chain with the design goals has been demonstrated experimentally.

Currently, the assembly of the full cryogenic microwave read-out system comprised of 15 individual read-out chains is carried out and will be put in operation in the near future.

For potential future experimental phases of the ECHo experiment, the modular structure of the mechanical design permits an easy scale-up. The cryogenic platform exhibits four ports allowing for a lateral insertion of read-out systems, and hence, a total of 64 microwave read-out chains could be installed, which corresponds to the read-out of 51200 detector pixels. For that, it might be necessary to upgrade the cryogenic platform with an additional pulse-tube cooler in order to provide sufficient cooling power at the 4 K stage, as discussed above.

If for future experimental phases of the ECHo experiment stricter requirements apply on the noise performance, on the one hand, the first stage amplification needs to happen immediately after the µMUX, meaning on the mixing chamber plate, and on the other hand, the noise performance of the first stage amplifier should ideally be quantum-noise-limited. Therefore, it could be considered to employ travelling wave parametric amplifiers (TWPAs) [Esp21]. Current TWPAs, however, typically exhibit significantly lower saturation powers than semiconductor-based amplifiers, such as the HEMT amplifiers used for the current read-out chains, and therefore, the applied input power would need to be reduced with respect to the input power applied to the HEMT amplifiers. One way to accomplish this, is the use of tone-tracking [Hen18], where the read-out frequencies provided by the SDR system are not fixed, but are dynamically kept at the minima of the corresponding resonance curves by a feedback mechanism. In this way, most of the microwave power applied to the µMUX is reflected and, hence, does not reach the input of the first stage amplifier.

5. Tile-and-trim resonance frequency adjustment for the µMUX

The available frequency band of the cryogenic microwave read-out chain for the ECHo-100k experimental phase is limited by the available frequency band of the low-noise HEMT amplifier, i.e. it is restricted to frequencies between 4 GHz and 8 GHz. To make most efficient use of the available frequency band, the resonance frequencies of the microwave SQUID multiplexer (µMUX) channels should be packed as tightly as possible, while maintaining a sufficiently large resonance frequency spacing to mitigate crosstalk due to the extended tails of the Lorentzian line shape of the resonance curves [Mat19]. For matching resonator bandwidth Δf and maximum frequency shift $\Delta f_\mathrm{r}^\mathrm{max}$, i.e. for $\eta = 1$, ideally, the resonance frequencies should be equidistantly distributed with a spacing corresponding to the tenfold resonator bandwidth in order to reach a crosstalk level below 10^{-4} [Weg18a, Mat19].

In principle the resonance frequencies of superconducting microwave resonators can be adjusted accurately based on electromagnetic simulations. In practice, however, the resonance frequencies of microfabricated µMUX devices typically exhibit deviations from the target equidistant resonance frequency spacing, compromising either the crosstalk performance of the µMUX or the packing density of resonance frequencies within the available frequency band. These deviations are due to thickness inhomogeneities of the deposited film constituting the superconducting resonators or due to fabrication tolerances in the structure size of these microfabricated resonators. As it is very difficult to overcome these limitations to such an extent that they would not significantly affect the resonance frequency placing anymore, a more practical solution consists in the application of a tile-and-trim technique after fabrication. This approach takes into account systematic influences on the resonance frequency placing and compensates for them.

For bare superconducting lumped element resonators (LERs) a tile-and-trim technique has been introduced and demonstrated [Liu17b, McK19, Pal19]. Later it could also be established for LER-based µMUX [Obe20, Nei21]. For inductively terminated quarter-wave coplanar waveguide (CPW) resonators, however, no resonance frequency adjustment technique has been reported in literature yet, to the best of my knowledge. In the following sections, firstly, the tile-and-trim technique for LERs is reviewed and secondly, a similar technique for CPW resonators is introduced and demonstrated for the first time. Finally, the resonance frequency placing in a tile-and-trim fashion for the µMUX within ECHo-100k is discussed.

5.1 Tile-and-trim process for LER

The resonance frequency of a bare LER is determined by the meandering inductance L, the interdigital capacitance C and the coupling capacitance $C_\mathrm{c}^\mathrm{eff}$ describing the capacitive coupling to the transmission line and to the ground plane of the µMUX chip. If C is expressed in terms of the number of capacitance fingers N_C and the specific capacitance $\tilde{C}$ per finger, i.e. $C = \tilde{C}N_\mathrm{C}$, the resonance frequency reads

$$f_\mathrm{r} = \frac{1}{2\pi\sqrt{L(\tilde{C}N_\mathrm{C} + C_\mathrm{c}^\mathrm{eff})}} = \frac{k(N_\mathrm{C})}{2\pi\sqrt{L\tilde{C}N_\mathrm{C}}} \tag{5.1}$$

with the function $k(N_\mathrm{C}) = (1+C_\mathrm{c}^\mathrm{eff}/\tilde{C}N_\mathrm{C})^{-1/2}$. Note that the number of capacitance fingers N_C is not necessarily an integer, but rather a positive rational number. For two resonance frequencies f_r^i and f_r^f with identical L, $C_\mathrm{c}^\mathrm{eff}$ and $\tilde{C}$, but different number of fingers N_C^i and N_C^f, respectively, the ratio of the resonance frequencies is given by

$$\frac{f_\mathrm{r}^\mathrm{i}}{f_\mathrm{r}^\mathrm{f}} = \sqrt{\frac{N_\mathrm{C}^\mathrm{f}}{N_\mathrm{r}^\mathrm{i}}}\,\frac{k\big(N_\mathrm{r}^\mathrm{i}\big)}{k\big(N_\mathrm{r}^\mathrm{f}\big)} \approx \sqrt{\frac{N_\mathrm{C}^\mathrm{f}}{N_\mathrm{r}^\mathrm{i}}}\,. \tag{5.2}$$

The approximation holds true because $k\big(N_\mathrm{r}^\mathrm{i}\big) \approx k\big(N_\mathrm{r}^\mathrm{f}\big) \approx 1$. Equation (5.2) suggests that a change of number of resonance fingers relates in a straight forward manner to a change in resonance frequency. This observation lays the foundation to the implementation of a resonance frequency adjustment technique. After the microfabrication of a lumped element resonator, the initial resonance frequency f_r^i is measured at low temperatures. As the initial number of capacitance fingers N_C^i is known, the final number of capacitance fingers N_C^f for the desired final resonance frequency f_r^f can be calculated. The difference ΔN_C is accordingly determined by

$$\Delta N_\mathrm{C} = N_\mathrm{C}^\mathrm{i} - N_\mathrm{C}^\mathrm{f} = N_\mathrm{C}^\mathrm{i}\left[1 - \left(\frac{f_\mathrm{r}^\mathrm{i}}{f_\mathrm{r}^\mathrm{f}}\right)^2\right]. \tag{5.3}$$

From a microfabrication point of view, it is easier to reduce the number of fingers ($\Delta N_\mathrm{C} > 0$) via a microlithographic tile-and-trim process, than to increase the number of fingers. The consecutive steps of such a tile-and-trim process are sketched in figure 5.1 using the example of a niobium-based LER as in [Pal19, Obe20, Nei21]. Initially (1), the LER with known number of capacitance fingers N_C^i is characterised at temperatures far below the superconducting transition temperature of the resonator material, i.e. in the case of niobium far below 9.2 K, in order to determine the initial resonance frequency f_r^i. Afterwards, the chip is prepared for the resonance

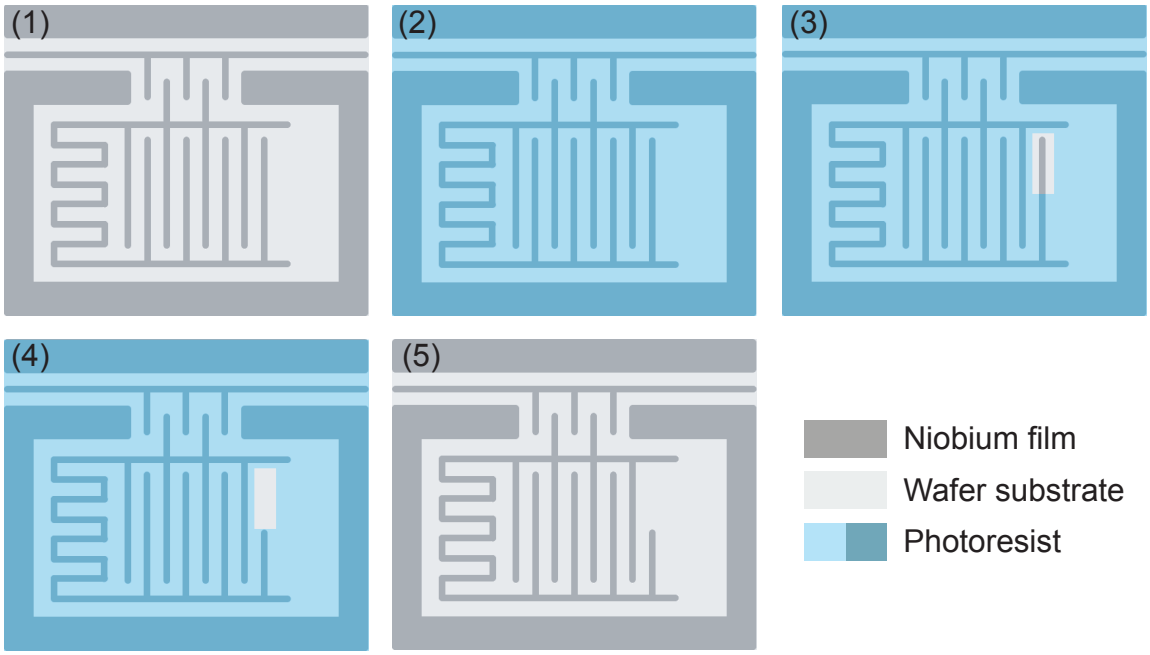

Figure 5.1: Sketch of the microfabrication steps for the tile-and-trim process for a niobium-based lumped element resonator. The figure is taken from [Pal19].

frequency adjustment procedure by coating it with a photoresist (2). A window is opened in the photoresist (3) uncovering the last ΔN_C capacitance fingers, i.e. typically a fraction of one finger. An SF_6-based inductively coupled plasma reactive ion etching process step is applied to remove the niobium of the part of the capacitance finger, which is not covered with photoresist (4). Finally (5), the photoresist is removed and the LER is characterised once more at low temperatures to check to which extent the resonance frequency placing could be improved.

5.2 Tile-and-trim process for CPW resonators

For an inductively terminated quarter-wave CPW resonator as depicted in figure 5.2, correcting the resonance frequency by adjusting the inductance per unit length L' or the capacitance per unit length C' of the CPW geometry is not feasible, as the precision in terms of spatial resolution needed for the corresponding microlithographic tile-and-trim process cannot be reached with standard photolithographic techniques. A more practical, yet not satisfactory approach to change the resonance frequency f_r of an inductively terminated quarter-wave CPW resonator is the adjustment of the coupling capacitance C_c between the resonator and the transmission line, as follows from equation (3.17). This, however, would also impact the coupling quality factor Q_c, according to equation (3.19), and thereby the resonator bandwidth Δf. An ap-

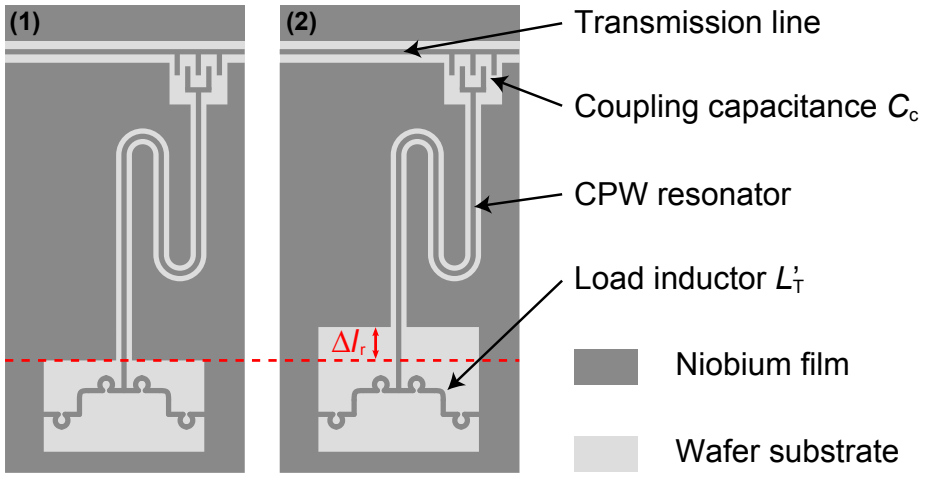

Figure 5.2: Sketch of the CPW resonator geometry considered for the tile-and-trim technique **(1)**. The structure depicted in **(2)** represents the same resonator geometry as in **(1)** with a shifted niobium ground plane at the load inductor. The shift is characterised by the length Δl_r. The figure is adopted from [Nei21].

proach to correct f_r while leaving Q_c unaffected is the adjustment of the resonator length l_r. The length of the CPW's centre conductor can obviously not be changed, but the ground planes surrounding the centre conductor could be adjusted as illustrated in 5.2 (2). Effectively, both l_r and the terminating inductance L_T would change causing a shift in the resonance frequency. A resonance frequency adjustment process based on this last approach is introduced and demonstrated in the following.

5.2.1 Theoretical background

As introduced in section 3.2, for a bare quarter-wave CPW resonator the resonance frequency $f_0 = 1/(4l_r\sqrt{L'C'})$ is entirely determined by the resonator's length l_r, the inductance per unit length L' and the capacitance per unit length C'. If such a quarter-wave resonator is on one end coupled to a microwave transmission line via a coupling capacitance C_c and on the other end terminated in an inductance L_T, the resonance frequency is given by

$$f_r = \frac{f_0}{1 + 4f_0\left[C_c Z_0 + \frac{L_T}{Z_0}\right]}, \tag{5.4}$$

where $Z_0 = \sqrt{L'/C'}$ denotes the characteristic impedance of the CPW [Mat11]. Shortening the ground plane close to the load inductor, as indicated in figure 5.2, by the distance Δl_r yields a shorter CPW resonator with a new bare resonance frequency

$$f_0' = \frac{1}{4\left(l_\mathrm{r} - \Delta l_\mathrm{r}\right)\sqrt{L'C'}} = f_0 \frac{l_\mathrm{r}}{l_\mathrm{r} - \Delta l_\mathrm{r}} \,. \tag{5.5}$$

Additionally, the loop size of the load inductor L_T increases and therefore, the new load inductance can in first order be approximated by

$$L_\mathrm{T}' = L_\mathrm{T} + \lambda \Delta l_\mathrm{r} \tag{5.6}$$

with some positive coefficient λ. Substituting f_0 with f_0' and L_T with L_T' in equation (5.4) yields the new resonance frequency

$$f_\mathrm{r}' = \frac{f_0}{1 + 4 f_0 \left[C_\mathrm{c} Z_0 + \frac{L_\mathrm{T}}{Z_0} + \Delta l_\mathrm{r} \left(\frac{\lambda}{Z_0} - \sqrt{L'C'} \right) \right]} \,. \tag{5.7}$$

Applying the expansion $\frac{a}{1+4ax} \approx a - 4a^2 x$ for $x \ll \frac{1}{4a}$, the total shift of the resonance frequency upon a shift of the edge of the ground plane is

$$\Delta f_\mathrm{r} = f_\mathrm{r}' - f_\mathrm{r} = -\kappa \frac{\Delta l_\mathrm{r}}{l_\mathrm{r}^2} \quad \text{with} \quad \kappa = \frac{\lambda - L'}{4L'\sqrt{L'C'}} \,. \tag{5.8}$$

Therefore, for a quarter-wave CPW resonator with measured resonance frequency f_r and known resonator length l_r, a new resonance frequency f_r' can be obtained by trimming the edge of the ground plane by Δl_r, applying the same microfabrication steps as for the tile-and-trim process for LERs as described in section 5.1.

The knowledge of κ is crucial for a successful application of this tile-and-trim technique for CPWs. In order to make an *a priori* prediction on κ, the three quantities L', C' and λ need to be determined. Both L' and C' can be derived analytically from the CPW geometry employing, for instance, conformal mapping techniques [Sim01, Gao08a]. For the coefficient λ an analytic determination is not trivial, as λ depends strongly on the geometry of the terminating coupling inductance and the surrounding ground planes. However, its determination can be carried out involving an inductance calculation software, varying the distance Δl in the simulated design and extracting λ by fitting equation (5.6) to the simulation results for L_T'. As, however, L', C' and λ and therefore also κ are subject to the same unavoidable inaccuracies during microfabrication that lead to the deviations of the resonance frequencies from their respective design values. Therefore, a more practical way accounting for systematic deviations in L', C' and λ is the experimental determination of κ, e.g. by performing κ-calibration measurements as presented below.

5.2.2 Calibration measurement

The approach chosen for the experimental determination of κ in the framework of this thesis is to microfabricate a dedicated κ-calibration chip alongside the chip to be post-processed, on the same wafer. In order to minimise the impact of the variation of material parameters over the wafer, as for instance the impact of niobium film thickness variations, these two chips are positioned directly next to each other in the wafer layout.

The κ-calibration chip (No. 1-3) of the wafer *ECHo-CPW-Trim* was microfabricated following the description given in 3.8. It features 16 superconducting niobium-based quarter-wave CPW resonators coupled capacitively to a common CPW microwave transmission line and terminated inductively as sketched in figure 5.2. The designs of all 16 resonators differ from each other only by the position of the edge of the ground plane at the terminating coupling inductance. For the first resonator the design of the ground plane is as for the standard CPW-µMUX chips and therefore, it acts as a reference resonator. For the remaining 15 resonators the edge of the ground plane is shifted upwards along the resonator by an additional 16 µm with respect to the preceding resonator, meaning that the ground plane of the last resonator is shifted by 240 µm compared to the ground plane of the reference resonator. The design of the inductive termination is identical to the load inductor design of a full µMUX chip. The κ-calibration chip was characterised at a temperature of $T = 4.2\,\mathrm{K}$ in a

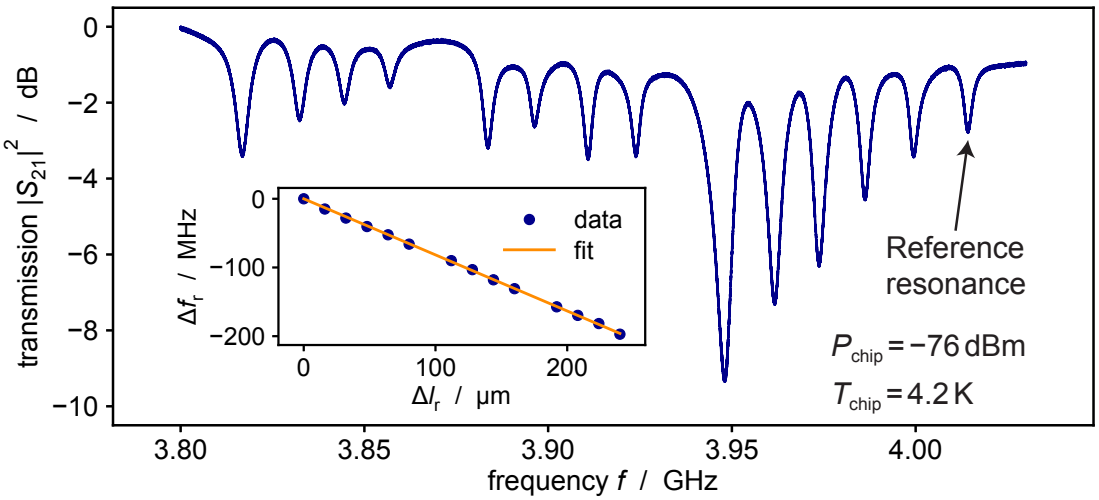

Figure 5.3: The transmission spectrum of the κ-calibration chip (No. 1-3) measured at a temperature of $T_{\mathrm{chip}} = 4.2\,\mathrm{K}$ and with a microwave power on chip of $P_{\mathrm{chip}} = -76\,\mathrm{dBm}$. In the inset the measured deviation from the reference resonance frequency is plotted as a function of the corresponding ground plane shift. The orange line is a numerical fit to the data.

liquid helium transport vessel employing a vector network analyser. The measured transmission spectrum is presented in figure 5.3. Only 14 out of the 16 expected resonances are visible, as for two resonators microscopic non-removable residuals of photoresist from the microlithographic fabrication procedure compromised the functionality of the resonators. Applying the fit-algorithm explained in section 3.2.5 [Pro15] to the measured resonance curves yields the resonance frequencies of each resonator. Subsequently, the resonance frequency deviations Δf_r with respect to the reference resonance frequency were determined. In the inset of figure 5.3 the resonance frequency deviations Δf_r are plotted as a function of the length variation Δl_r of the ground plane with respect to the ground plane position of the reference resonator. The error of the data is estimated based on the fit error of the underlying resonance frequencies and it is smaller than the marker size in the plot. Equation (5.8) is numerically fitted to the data where by design $l_\mathrm{r} = 7084\,\mu\mathrm{m}$ is the length of the reference resonator. The fit curve is depicted as solid orange line in the inset of figure 5.3. The matching of the fit curve and the measured data points confirms the proportionality of Δf_r and Δl_r predicted by equation (5.8). Finally, the fit yields $\kappa = 4.10 \times 10^7\,\mathrm{Hz{\cdot}m}$, which corresponds to a specific frequency shift of $817\,\mathrm{kHz}/\mu\mathrm{m}$ for the given resonator length.

5.2.3 Demonstration of the tile-and-trim technique for CPW resonators

The *ECHo-CPW-Trim* wafer features the demonstrator chip (No. 1-2) for the proof of concept for the resonance frequency adjustment process for CPW resonators. Like the κ-calibration chip it consists of 16 superconducting niobium-based quarter-wave CPW resonators coupled capacitively to a common CPW microwave transmission line and terminated inductively. In contrast to the κ-calibration chip, the resonators of the demonstrator chip vary in resonator length l_r, but feature all the same terminating coupling inductance design, i.e. $\Delta l_\mathrm{r} = 0$. In that, the design of the demonstrator chip is identical to the design of µMUX chips, however without rf SQUIDs. The intended resonance frequency spacing is 10 MHz as for the µMUX chips for the ECHo-100k phase of the ECHo experiment.

After microfabrication, the demonstrator chip was characterised at a temperature of 4.2 K in a liquid helium transport vessel using a vector network analyser. The measured transmission spectrum is shown as blue curve in figure 5.4, which exhibits an irregular spacing of the resonances. To obtain an equidistant resonance frequency spacing, firstly, for each resonator with index $i \in \{1, 2, ..., 16\}$ the resonance frequency $f_{\mathrm{r},i}$ was extracted applying the resonance fitting algorithm introduced in section 3.2.5, and secondly a new set of resonance frequencies $f'_{\mathrm{r},i} < f_{\mathrm{r},i}$ for $i \in \{1, 2, ..., 16\}$ with $f'_{\mathrm{r},i+1} - f'_{\mathrm{r},i} = 10\,\mathrm{MHz}$ was defined. Based on equation (5.8) the individual trimming lengths $\Delta l_{\mathrm{r},i} = (f_{\mathrm{r},i} - f'_{\mathrm{r},i}) l^2_{\mathrm{r},i}/\kappa$ were determined. Here the

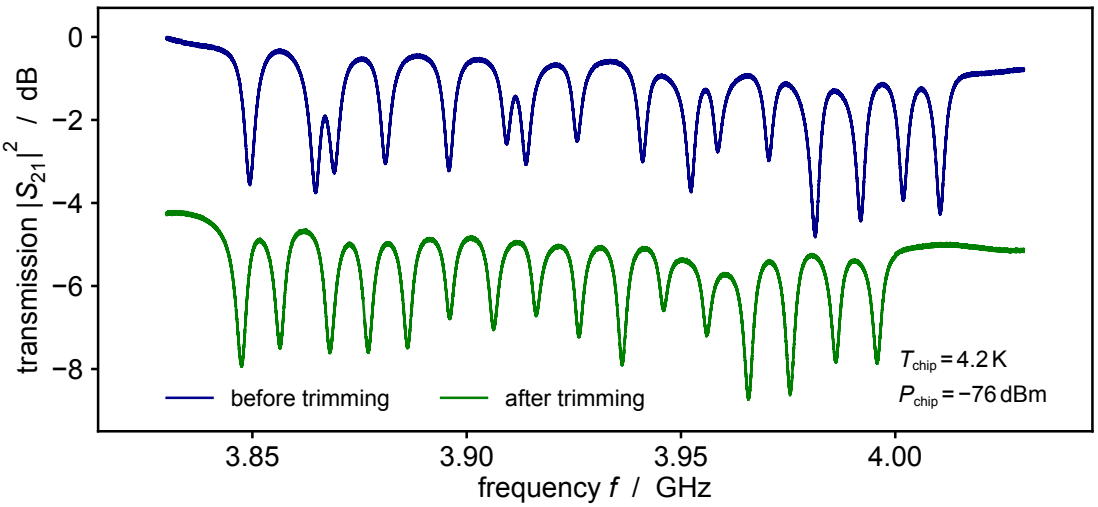

Figure 5.4: The transmission spectrum of the CPW resonator chip (No. 1-2) before (blue curve) and after (green curve) the trimming procedure. The green curve is shifted intentionally by −4 dB for the sake of clarity.

κ-value measured in the calibration experiment was used and the resonator lengths $l_{\mathrm{r},i}$ were known by design. A microlithographic tile-and-trim process involving the same microfabrication steps as for the tile-and-trim process for LERs described in section 5.1 was performed in order to shift the edges of the niobium-based ground planes upwards by the length $\Delta l_{\mathrm{r},i}$. Following the tile-and-trim process, the demonstrator chip (No. 1-2) was characterised once more at a temperature of $T = 4.2\,\mathrm{K}$ utilising a vector network analyser. The resulting transmission spectrum is depicted as green curve in figure 5.4. Note that the curve is intentionally shifted by −4 dB for the sake of clarity. Already by bare eye the ameliorated resonance frequency spacing is evident. In order to quantify the improvement, the extracted resonance frequencies before and after the tile-and-trim process in dependence of the resonator index were numerically fitted with a linear function representing an equidistant spacing. The corresponding data and fits are presented in figure 5.5a. The slopes of the linear fits reveal an average frequency spacing of 10.82 MHz before the tile-and-trim process and 9.89 MHz after. Taking the intended resonance frequency spacing of 10 MHz as a reference, the tile-and-trim process leads to a considerable improvement. For the mitigation of Lorentzian crosstalk, besides the average resonance frequency spacing, also the mean scatter is an important figure of merit. It is quantified as the standard deviation from the average frequency spacing. In figure 5.5b the residuals of the measured resonance frequencies with respect to their corresponding fit curves are visualised using the same colour code as before. The dashed blue and green lines indicate one standard deviation for the measured resonance frequencies before and after trimming, respectively, from the corresponding fit curves. The mean scatter

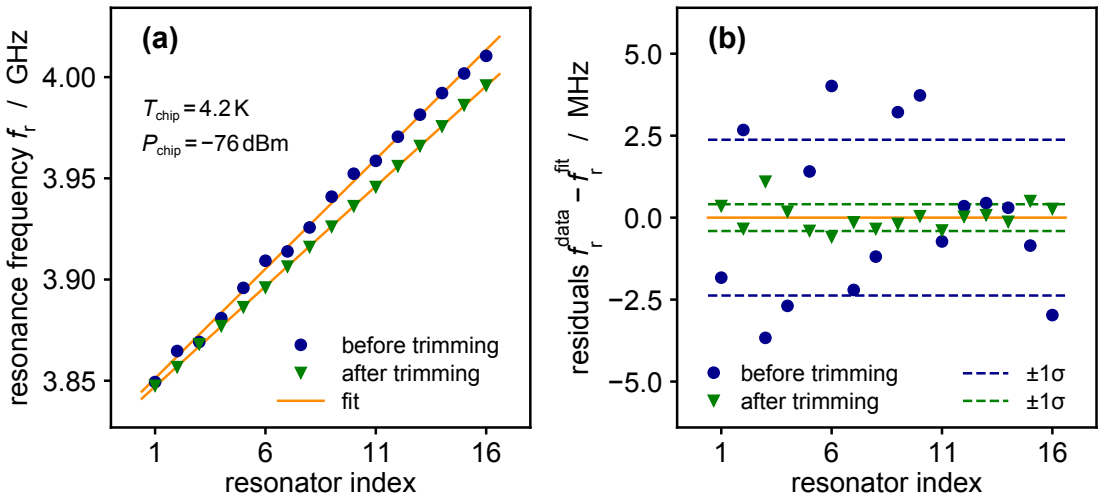

Figure 5.5: Resonance frequencies extracted from the spectra in figure 5.4 as a function of the resonator index **(a)** in blue (green) from the transmission spectrum before (after) the resonance frequency adjustment. The orange lines indicate linear fits to the data. The residuals of both data sets with respect to the corresponding fits are shown in **(b)**. The dashed blue (green) lines represent a 1σ deviation of the initial (adjusted) resonance frequencies from the fit. The orange line marks the target of zero deviation.

before trimming takes a value of 2.38 MHz, whereas after trimming it reaches a value of 0.41 MHz indicating an improvement by a factor of 5.8. Compared to the mean scatter of 0.67 MHz observed after a tile-and-trim process adjusting the resonance frequencies of LERs [Pal19], the resonance frequency adjustment process for CPWs yields competitive results.

5.3 Post-production resonance frequency adjustment within ECHo-100k

Within the scope of this thesis, the tile-and-trim technique for the resonance frequency adjustment for superconducting quarter-wave CPW resonators with inductive termination by trimming the ground plane has been introduced and demonstrated for the first time. Based on this result, the same technique has been applied to adjust the resonance frequencies of a full CPW-µMUX chip [Nei21]. Therefore, by now, for both the LER-µMUX and the CPW-µMUX effective post-production resonance frequency adjustment techniques are available.

For the practical implementation of a tile-and-trim resonance frequency adjustment for the µMUX for ECHo-100k, the process for LER-µMUX as discussed in section

5.1 could be adopted one-to-one. For the CPW-µMUX, however, the process as demonstrated above would require a refinement avoiding the need for κ-calibration chips, as otherwise the use of the process is limited for the following reason: on the one hand, a large number of κ-calibration chips per wafer allows for a decent monitoring of κ variations over the wafer enabling a precise post-production resonance frequency adjustment in a tile-and-trim fashion. On the other hand, a large number of κ-calibration chips limits the area per wafer available for the actual µMUX chips, lowering the fabrication efficiency. A small number of κ-calibration chips per wafer obviously inverts the problem. These issues can easily be overcome by designing CPW-µMUX chips with intrinsic calibration. Instead of designing 16 resonators per chip which all differ in l_r but exhibit $\Delta l_\mathrm{r} = 0$, for instance four values for l_r and four values for Δl_r could be chosen, resulting in 16 combinations exhibiting 16 different initial resonance frequencies. For each group of resonators with identical l_r and different Δl_r, a value for κ could be determined and subsequently a resonance frequency adjustment in a tile-and-trim fashion could be carried out without the need for dedicated κ-calibration chips.

For ECHo-100k, the microfabrication of the µMUX, the first characterisation, the post-production resonance frequency adjustment and the second characterisation have to be carried out on a wafer scale as a single chip treatment is not feasible, considering the required total number of fully working µMUX chips. For this, the transmission lines and the modulation lines of multiple µMUX chips on a wafer have to be connected in series, respectively, such that all chips can be characterised in a single measurement. Due to fabrication tolerances, resonance collisions and swaps can occur and even the loss of entire µMUX channels is possible. As this potentially compromises an effective post-production resonance frequency adjustment, a resonance identification strategy independent from the resonance frequency is required, which allows for a mapping from a measured resonance curve to a physical resonator.

The planar superconducting microwave resonators employed for microwave kinetic inductance detectors (MKIDs) are typically coupled to a common transmission line and are read out by frequency-division multiplexing, similarly to the µMUX-resonators, and hence, they exhibit similar requirements in terms of equidistant resonance frequency spacing. For this reason, the above described tile-and-trim process for LERs has been established for MKIDs in the first place [Liu17b, McK19]. However, also for MKID-resonators fabrication tolerances can lead to resonance frequency collisions, swaps and loss of entire resonators. Therefore, a resonance identification technique for MKID-resonators has been developed [Liu17a]. The resonator-to-frequency mapper for MKIDs consists of a cryogenic array of light emitting diodes (LEDs), which is arranged in such a way that each MKID-resonator faces exactly one LED. Therefore, switching on a given LED will dissipate power in the corresponding MKID-resonator,

causing a breaking of Cooper pairs creating excess quasiparticles. The associated change in kinetic inductance leads to a measurable shift in the resonance frequency of the illuminated MKID-resonator, and hence this signature allows for a precise mapping between a physical resonator and a measured resonance frequency.

In contrast to MKID-resonators, µMUX-resonators exhibit a comparably small kinetic inductance. Consequently, the change in kinetic inductance upon irradiation of a µMUX-resonator leads to a significantly smaller change in resonance frequency, which is not sufficient to make practical use of the above described LED-based mapping technique. Therefore, a dedicated resonator identification technique for µMUX-resonators has been developed, which is sketched in figure 5.6. The rf SQUID of each µMUX channel i is coupled to the common transmission line via an individual mutual inductance $M_{\mathrm{mod},i}$, which is achieved by shunting the standardised modulation inductance L_{mod} with an individual inductance $L_{\mathrm{par},i}$ for all channels but the first. Running a modulation current sweep through the common modulation line will lead to an individually different modulation of the magnetic flux in each rf SQUID due to the different mutual inductances. Consequently, the flux-dependent resonance

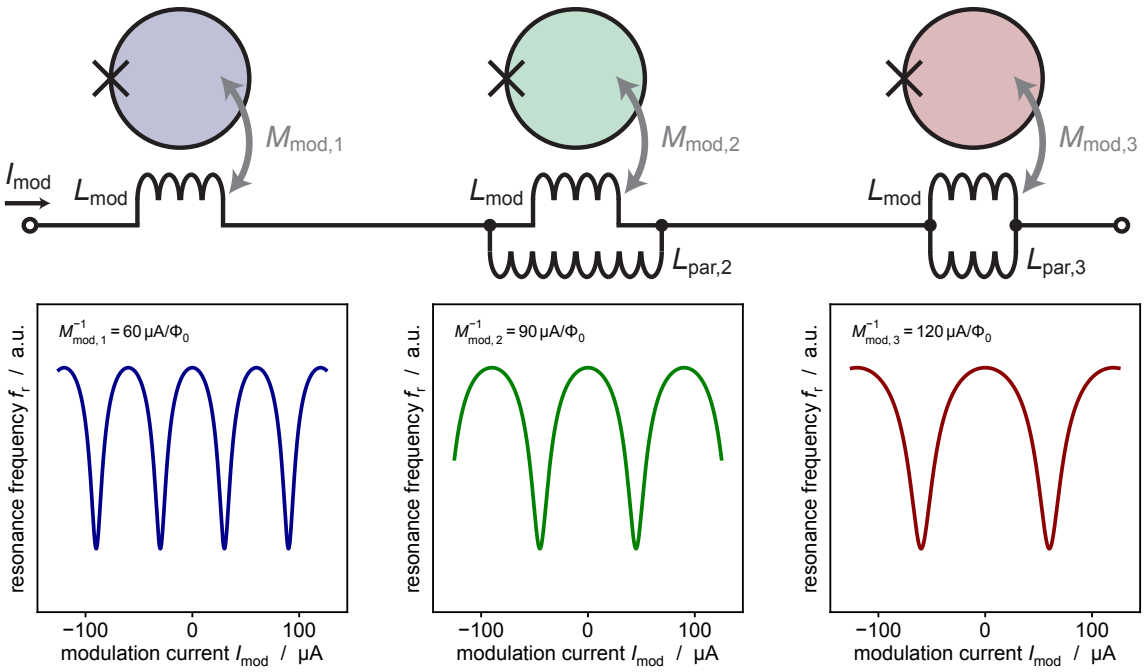

Figure 5.6: Sketch of an inductive coupling scheme allowing for the identification of µMUX channels. Each channel i exhibits an individual mutual inductance $M_{\mathrm{mod},i}$ between the rf SQUID and the common modulation line. Hence, the resonance frequency modulation upon a modulation current sweep exhibits a characteristic periodicity for each µMUX channel, as visualised in the plots below the respective rf SQUIDs. For the sake of simplicity the resonators coupled to the rf SQUIDs have been omitted in the figure.

frequencies of the resonators coupled to the rf SQUIDs exhibit a characteristic modulation with individual periodicity, as visualised in the plots of figure 5.6. This periodicity serves as a signature for each µMUX channel and allows for a complementary resonator identification independently from the value of resonance frequency. As for the operation of the µMUX with flux-ramp modulation, every µMUX channel should ideally exhibit the same mutual inductance M_{mod}, after the resonator identification, the parallel inductances $L_{\mathrm{par},i}$ can be easily removed during the etching step of the tile-and-trim resonance frequency adjustment procedure, leaving every µMUX channel with identical mutual inductances M_{mod}. The implementation of this identification scheme has been demonstrated for both LER-µMUX and CPW-µMUX chips [Obe20, Nei21] along with an automatised full characterisation algorithm for an arbitrary number of µMUX channels, providing photolithographic masks for the post-production resonance frequency adjustment.

Beyond ECHo-100k and microwave SQUID multiplexing in general, the post-production resonance frequency adjustment technique developed within the scope of this thesis can be applied to any superconducting inductively terminated quarter-wave CPW resonator.

6. Noise performance of the microwave SQUID multiplexer

In order to define the final microwave SQUID multiplexer (µMUX) design for the ECHo-100k phase of the ECHo experiment, the most suitable microwave resonator geometry has to be pinpointed. Besides the aspects related to the resonator size and the feasibility of a resonance frequency fine-tuning, a key point is the noise performance of µMUX channels based on different resonator geometries. Therefore, in this chapter the noise performance of µMUX channels based on coplanar waveguide resonators (CPW-µMUX channels) is compared to the noise performance of µMUX channels based on lumped element resonators (LER-µMUX channels). For that, first of all the experimental set-up and the design of the µMUX chip under investigation are introduced, followed by the discussion of a basic experimental characterisation of the µMUX chip. Afterwards, the measurement and the data analysis flow for the noise measurements are explained. Finally, the measured data is presented and the resulting noise performance of LER-µMUX channels and that of CPW-µMUX channels are compared and discussed.

6.1 Experimental set-up

A single µMUX chip featuring both LER-µMUX channels and CPW-µMUX channels is cooled down to millikelvin temperatures in the dry dilution refrigerator dedicated to the ECHo experiment, in order to compare the noise performance of µMUX channels based on the two different resonator geometries under the same experimental conditions. For this, the µMUX chip is characterised applying a homodyne read-out scheme.

6.1.1 µMUX chip *ECHo-MUX-04-6A*

The layout of the chip *ECHo-MUX-04-6A* employed for all noise measurements in the framework of this thesis has been designed especially for the investigation of the noise performance of LER-µMUX channels compared to that of CPW-µMUX channels [Ihs21]. A to-scale schematic representation of the chip layout revealing the dimensions of the chip and of the 16 resonators fabricated on the chip is shown in figure 6.1. The first eight channels are based on LERs of which the channels ch01, ch02, ch05 and ch06 are fully-fledged LER-µMUX channels, i.e. they are equipped

with rf SQUIDs. The channels ch03, ch04, ch07 and ch08, are bare LER channels, i.e. without rf SQUID, and they fulfil only diagnostic purposes which are not relevant to this thesis. The remaining eight channels are CPW based channels of which the channels ch09, ch10, ch13, ch14 are featuring rf SQUIDs, whereas the channels ch11, ch12, ch 15 and ch16 are again merely bare resonator channels. All 16 resonators are coupled to a common transmission line based on a CPW geometry, into which an rf signal can be fed in via the contact pad labelled with 'IN' and from which the signal modulated by the 16 resonator channels can be read out via the contact pad 'OUT'. All rf SQUIDs are coupled to a common modulation line which can be contacted via the contact pads marked with +I/-I on the short sides of the chip.

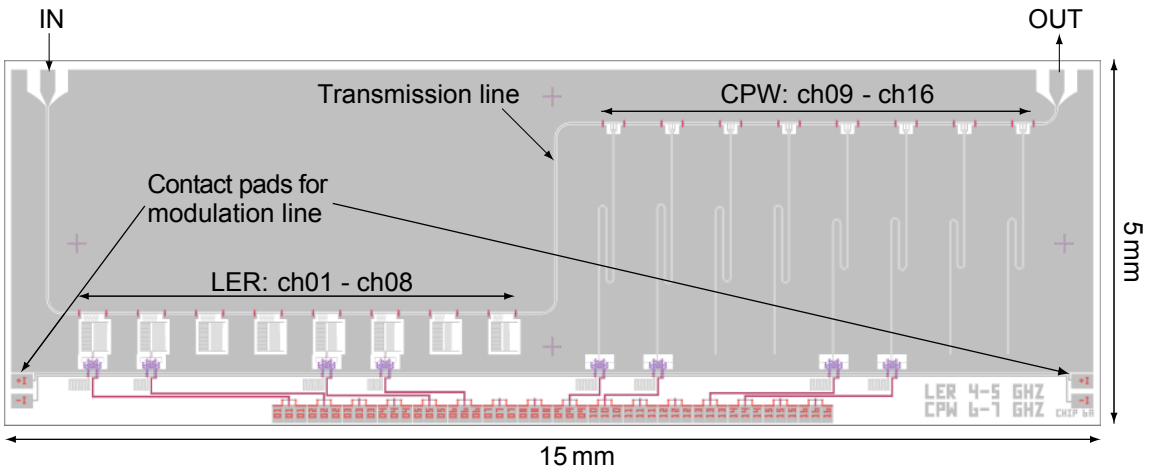

Figure 6.1: To-scale layout of the µMUX chip *ECHo-MUX-04-6A*, which is used for all noise measurements presented within the framework of this thesis. The figure is taken from [Ihs21].

Resonator geometries

Figure 6.2a provides a detailed to-scale view onto the design of the LER-µMUX channel ch06. The LER is comprised of a meandering inductance L and an interdigital capacitance C. The value of $L = 2\,\mathrm{nH}$ is fixed for all resonators following the design presented in [Pal19] and the resonance frequency $f_\mathrm{r} = 1/2\pi\sqrt{(L + L_\mathrm{T})(C + C_\mathrm{c}^\mathrm{eff})}$ is set by varying the number of fingers of the C and by adjusting the number of fingers of the coupling capacitor C_c, which couples the resonator to the transmission line. The effective coupling capacity $C_\mathrm{c}^\mathrm{eff} = C_\mathrm{c}C_\mathrm{p}/(C_\mathrm{c} + C_\mathrm{p})$ takes also into account the parasitic capacity C_p between the resonator and the surrounding ground planes. According to equation (3.34), $C_\mathrm{c}^\mathrm{eff}$ determines the coupling quality factor Q_c for a fixed resonator inductance, and therefore, in the limit $Q_\mathrm{c} \approx Q_\mathrm{l}$, i.e. $Q_\mathrm{i} \gg Q_\mathrm{c}$, it sets the bandwidth $\Delta f = f_\mathrm{r}/Q_\mathrm{l}$. For all LERs, the bandwidth is designed to be

$\Delta f \approx 1\,\mathrm{MHz}$. The LER in figure 6.2a is coupled to the rf SQUID via the load inductor L_T, whose design is identical for all LER-µMUX channels. An overview over all target LER-µMUX resonance frequencies is given in table 6.1.

In Figure 6.2b the schematic drawing of the CPW-µMUX channel ch10 is shown, which is based on a CPW quarter-wave resonator geometry. The width of the conductor is set to $s = 10\,\mu\mathrm{m}$ and the gap between the conductor and the ground plane

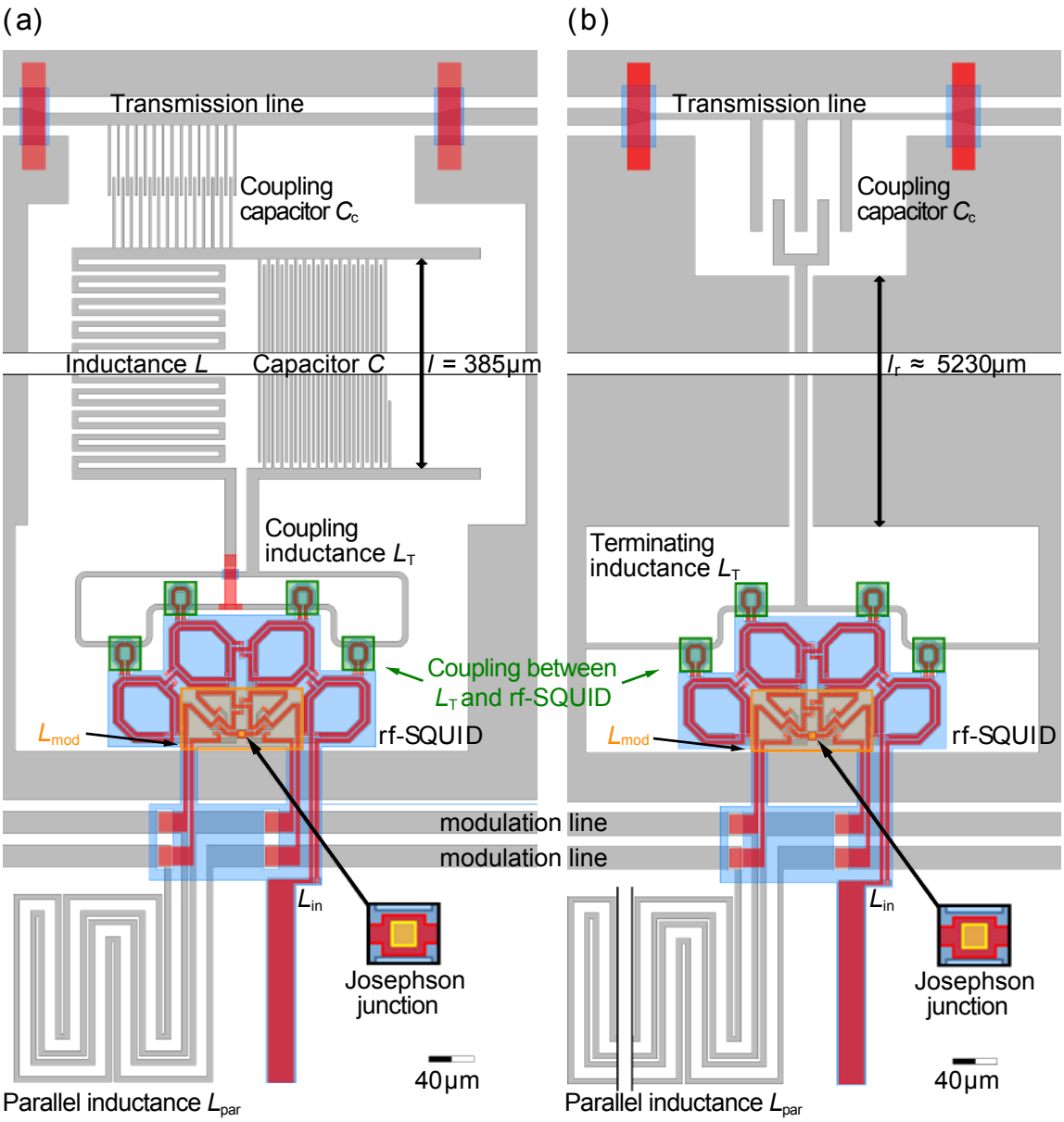

Figure 6.2: **(a)** Sketch of the LER-µMUX channel ch06 and **(b)** of the CPW-µMUX channel ch10 to scale. The indicated design details are explained in the main text. The figure is adopted from [Ihs21].

is set to $w = 6\,\mu\text{m}$. The characteristic impedance of $L' = 4.15062 \times 10^{-7}\,\text{H/m}$ and the characteristic capacitance of $C' = 1.63848 \times 10^{-10}\,\text{F/m}$ can were determined following the calculations in section 3.2.2. Hence, the characteristic impedance is $Z_0 = \sqrt{L'/C'} \approx 50\,\Omega$. The resonator length l_r of the centre conductor of the CPW is used as a parameter to design the bare resonance frequency $f_0 = 1/4l_\text{r}\sqrt{L'C'}$ and it varies between 43 mm and 53 mm, for the CPW-µMUX channels, corresponding to bare resonance frequencies between $\sim 5.7\,\text{GHz}$ and $\sim 6.7\,\text{GHz}$. The actual resonance frequencies are expected to be lower due to the coupling capacity C_c between the resonator and the transmission line, and the presence of the load inductor L_T, as follows from equation (3.17). In order to confine the CPW resonators between the transmission line and the rf SQUIDs, it is necessary to wind the resonators in a trombone-like fashion as visualised in figure 6.1. The capacitive coupling C_c of the resonator to the common transmission line is implemented as IDC, as introduced in [Her17]. Analogously to the LER channels, the bandwidth is set to $\Delta f \approx 1\,\text{MHz}$ following equation (3.19) by adjusting the length of the IDC fingers. The inductance L_T couples the resonator to the rf SQUID and its design is identical for all CPW-µMUX channels. An overview over all target CPW-µMUX resonance frequencies is given in table 6.1.

	ch01	ch02	ch05	ch06	ch09	ch10	ch13	ch14
f_r / GHz	3.81	3.86	4.76	4.81	5.22	5.30	6.01	6.09
$\Delta f_\text{r}^\text{mod}$ / MHz	0.59	0.59	0.73	0.73	1.98	2.05	2.69	2.77

Table 6.1: The design values for the resonance frequencies f_r of the eight µMUX channels of the chip presented in figure 6.1, and the corresponding expected modulation amplitudes $\Delta f_\text{r}^\text{mod}$.

rf SQUID design

The rf SQUID with inductance L_S is comprised of four parallel inductances being connected in one prominent point featuring the Josephson junction. In order to suppress unwanted signals caused by time-dependent homogeneous magnetic fields in the rf SQUID, the four parallel inductances are set up as a first order gradiometer. The inductances L_T, L_mod and L_in representing the load inductor of the resonator, the inductance of the modulation line and the inductance of the input line, respectively, are coupled in a non-gradiometric fashion to the rf SQUID. The mutual inductance $M_\text{T} = k_\text{T}\sqrt{L_\text{T}L_\text{S}}$ between the load inductor of the resonator and the rf SQUID is identical for all µMUX channels with the same resonator geometry. However, the mutual inductance M_T of LER-µMUX channels is not identical to the mutual inductance M_T of CPW-µMUX channels due to the different design of L_T. The

inductance L_{mod} of the modulation line is shunted with an inductance L_{par} which can be used for a resonance frequency-independent resonator identification, as introduced in section 5.3. Since, however, this feature is not needed for the experiments carried out in the framework of this thesis, and since it complicates the data analysis due to the formation of closed superconducting loops [Ihs21], all parallel inductances L_{par} have been removed, applying a post-production step based on ICP-RIE[1] similar to the process discussed in chapter 5. The mutual inductance $M_{\mathrm{mod}} = k_{\mathrm{mod}}\sqrt{L_{\mathrm{mod}}L_{\mathrm{S}}}$ is identical for all LER-µMUX channels and for all CPW-µMUX channels, respectively. The input lines of the rf SQUID have not been used for the measurements presented in this thesis, which is why a detailed discussion of L_{in} is omitted. However, during regular operation of the µMUX, an MMC channel would be connected to the input lines. The values of all inductances and couplings have been calculated with the software InductEx[2]. The results of these calculations are reported in table 6.2. The expected modulation amplitudes $\Delta f_{\mathrm{r,CPW}}^{\mathrm{mod}} = 4f_0^2 M_{\mathrm{T}}^2/(Z_0 L_{\mathrm{S}})$ and $\Delta f_{\mathrm{r,LER}}^{\mathrm{mod}} = f_{\mathrm{r}} M_{\mathrm{T}}^2/(2L_{\mathrm{S}}(L+L_{\mathrm{T}}))$ are calculated from the simulated inductances, are reported for all µMUX channels in table 6.1.
The chip *ECHo-MUX-04-6A* has been microfabricated on the wafer *ECHo-MUX-04* in the cleanroom of the Kirchhoff-Institute for Physics[3] following the fabrication steps described in section 3.8.
The Josephson junction is a window-type junction comprised of a Nb/Al-AlO_x/Nb trilayer structure. Setting the window size and thereby the junction area to $4\times4\,\mu\mathrm{m}^2$, and manufacturing the thickness of the AlO_x-layer, so that the critical current density is $j_{\mathrm{c}} = 21.5\,\mathrm{A/cm}^2$, the junction exhibits a critical current of $I_{\mathrm{c}} = 4.25\,\mu\mathrm{A}$. The rf SQUID screening parameter is thus expected to be $\beta_{\mathrm{L}} \sim 0.6$.

resonator geometry	L_{S} / pH	L_{T} / pH	M_{T}^{-1} / µA/Φ_0	M_{mod}^{-1} / µA/Φ_0
LER	45.6	202.9	371.9	77.2
CPW	45.7	191.3	351.1	73.1

Table 6.2: The simulated inductances and couplings for the µMUX channels in dependence of the resonator geometry.

6.1.2 Experimental holder

For the characterisation of the µMUX chip *ECHo-MUX-04-6A* and all subsequent measurements, a dedicated experimental holder was employed, which is presented in figure 6.3. The holder is made from oxygen-free copper, which has been annealed at

[1] Inductively Coupled Plasma - Reactive-Ion Etching
[2] SUN Magnetics (Pty) Ltd, Stellenbosch, South Africa
[3] Kirchhoff-Institute for Physics, Heidelberg University, Heidelberg, Germany

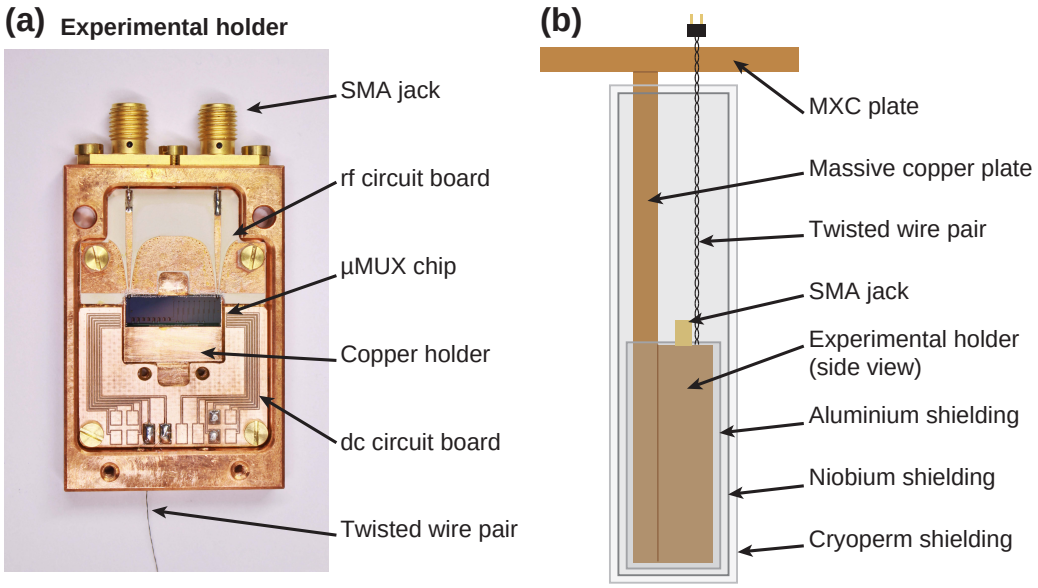

Figure 6.3: **(a)** The experimental holder supporting the chip *ECHo-MUX-04-6A* and featuring the rf and dc connections to the chip via two dedicated circuit boards. **(b)** Sketch of the position of the experimental holder with respect to the mixing chamber plate of the cryogenic platform and to the three shields screening the holder from magnetic fields.

800 °C under vacuum for 24 hours. The consequential enhanced thermal conductivity and the absence of hydrogen ensure a sufficient cooling of the µMUX chip, which is glued[4] onto the holder. The holder is equipped with a custom rf circuit board based on copper laminated Rogers RO3010[5]. The dielectric constant of Rogers RO3010 resembles the dielectric constant of silicon, which enables the possibility to design the CPW structure size on the circuit board exactly as large as the CPW structure size of the connection pads on the µMUX chip, thus minimising microwave reflections at the transition from the circuit board to the chip and vice versa. On the rf circuit board a tapering, starting from a CPW on the side of the circuit board facing the chip, via grounded CPW, to micro strip on the side of the circuit board facing the connector, is implemented maintaining a characteristic impedance of $Z_0 = 50\,\Omega$. Vias in the rf circuit board provide a connection between the top ground plane and the bottom ground plane of the board and therefore a connection of all ground planes to the experimental holder. The layout of the rf circuit board was designed based on simulations carried out with Sonnet[6]. The connection between the rf lines on the µMUX chip and the rf circuit board are implemented using aluminium wire bonds. Also the ground planes of the µMUX chip and of the rf circuit board are connected

[4] GE 7031 by GVL Cryoengineering Dr. George V. Lecomte GmbH, Stolberg, Germany
[5] Rogers Corporation, Rogers, Connecticut, USA
[6] Sonnet Software, Syracuse, New York, USA

in the same way. The micro strips on the rf circuit board are soldered to the centre conductors of SMA jacks, which provide the connection to external rf cables. The housing of the jacks is screwed to the experimental holder. A second circuit board is mounted into the experimental holder, which provides the connection between the modulation line of the chip and a twisted wire pair for modulation currents. The wires are made from NbTi in a CuNi matrix, and the twisting ensures a minimal loop size of the wires, reducing the interference of unwanted external electromagnetic signals. The experimental holder is closed with a lid and mounted onto a massive support plate, both of which are made from annealed oxygen-free copper. As indicated in the schematic set-up in figure 6.3, the massive copper plate is screwed to the mixing chamber (MXC) plate of a dry dilution refrigerator providing a thermal connection to the experimental holder. The set-up is screened from external magnetic fields by multiple shields. The innermost shield is a single continuous piece of aluminium foil, which is superconducting at millikelvin temperatures, wrapped around the holder, leaving free only the SMA connectors and the twisted wire pair. A second shield made from a niobium cylinder, open only on one side, forms a superconducting cup, providing further screening. The cup shape was chosen to provide an aspect ratio of ~ 5 between the depth at which the µMUX chip is located in the shield and the diameter of the shield, in order to ensure sufficient screening. Around the niobium shield, another shield with a similar aspect ratio made from Cryoperm[7] is placed, which exhibits a large magnetic permeability at low temperatures. The aluminium shield, the niobium shield and the Cryoperm shield are all thermally well coupled to the massive copper plate, which is connecting the experimental holder to the MXC plate. The vacuum can of the cryostat used for all measurements presented within this thesis features an additional soft ferromagnetic shield with a large magnetic permeability at room temperature. In the course of the measurements for this thesis, it proved to be necessary to employ all the mentioned shields in order to screen the experimental set-up sufficiently against unwanted magnetic interference.

6.1.3 Measurement set-up

To characterise the µMUX chip under investigation and to measure the noise performance of LER-µMUX channels and CPW-µMUX channels, the experimental holder housing the chip *ECHo-MUX-04-6A* has been mounted onto the mixing chamber (MXC) plate of the cryogen-free dilution refrigerator[8] equipped with the prototype ECHo-100k rf read-out chain described in chapter 4. The two SMA connectors of the experimental holder have been connected to the microwave read-out chain. Additionally, to create a connection to the modulation coil of the µMUX chip, the twisted

[7] VACUUMSCHMELZE GmbH & Co. KG, Hanau, Germany
[8] BF-XLD-SERIES, Bluefors Oy, Helsinki, Finland

wire pair connected to the dc circuit board of the holder, has been connected to another twisted wire pair, contained in a ribbon cable routing a set of multiple wires from the MXC plate to the room temperature stage of the cryostat. The wires of the ribbon cable are made from Alloy-30[9], which provides a low electrical resistance while maintaining a reasonably low thermal conductivity [All17]. The ribbon cables are thermally connected to heat sinks at every temperature stage of the cryostat [Man21b]. The experimental holder has been cooled down to the operational temperature of the ECHo experiment of $T_{\mathrm{MXC}} = 20\,\mathrm{mK}$. The temperature of the MXC plate was stabilised by means of a PID controller[10] acting on a heater mounted onto the MXC plate.

The room temperature part of the measurement set-up is chosen according to the type of measurements being performed: for basic characterisations of the µMUX chip a vector network analyser (VNA) based read-out scheme is used. For the investigation of the noise performance of the µMUX chip, however, the VNA based set-up is not suitable, as the available VNA device contributes significantly to the system noise [Ihs21]. Instead, a homodyne read-out scheme is the method of choice for all noise measurements carried out in the framework of this thesis.

Vector network analyser based read-out scheme

The measurement set-up for basic characterisation measurements of the µMUX chip is based on a commercially available VNA[11], which is connected to the input and output of the cryogenic microwave read-out chain described in chapter 4. A commercial SQUID electronics[12] is used as a software controlled low-noise precision current source at room temperature to feed modulation currents into the modulation line of the µMUX chip via the above mentioned ribbon cable. Both the SQUID electronics and the VNA are connected to a PC allowing for software controlled and fully automatised frequency sweep measurements over a wide range of rf powers and dc modulation currents.

Homodyne read-out scheme

In figure 6.4, the homodyne read-out scheme is sketched, which is used for all noise measurements presented in this thesis. A signal generator[13] with an external rubid-

[9] Isabellenhütte, Dillenburg, Germany
[10] LS372 resistance bridge by Lake Shore Cryotronics, Inc., Westerville, OH, USA
[11] R&S ZNB8, Rohde & Schwarz GmbH & Co. KG, Munich, Germany
[12] XXF-1, Magnicon GmbH, Hamburg, Germany
[13] R&S SMA100B, Rohde & Schwarz GmbH & Co. KG, Munich, Germany

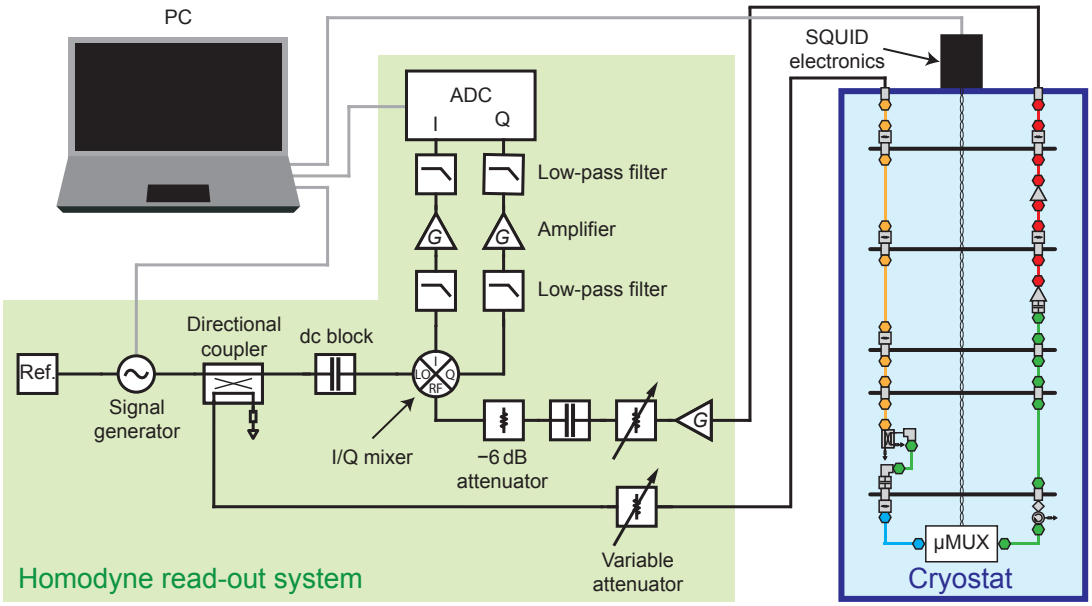

Figure 6.4: Sketch of the homodyne read-out system at room temperature connected to the prototype ECHo-100k cryogenic rf read-out chain mounted inside a cryostat. The rf signal generator, the SQUID electronics providing the modulation current, and the ADC are software controlled.

ium frequency standard[14] serves as local oscillator (LO) with a fixed signal power of $P_{\mathrm{LO}} = +14\,\mathrm{dBm}$ and a variable frequency f_{LO}. The LO signal is split by a 10 dB directional coupler, the transmitted signal propagates through a dc block (inner and outer block) to the LO port of a double balanced I/Q mixer[15], where it serves as reference signal. The coupled signal propagates from the directional coupler through a signal path, including amongst others the μMUX chip, before reaching the RF port of the I/Q mixer, i.e. the coupled signal carries the measurement information. In detail, starting from the directional coupler, the coupled signal passes through a variable attenuator, which allows for an adjustment of the signal power, and afterwards through the Tx branch of the cryogenic rf read-out chain, reaching the transmission line of the μMUX chip, where it experiences modulation due to the μMUX channels coupled to the transmission line. The modulated signal propagates further through the Rx branch of the cryogenic rf read-out chain getting amplified by a cascade of low-noise amplifiers: two amplifiers in the cryogenic rf read-out chain, as discussed in chapter 4, and two amplifiers[16] at room temperature, which are merged into one pictogram in figure 6.4. Subsequently, the signal passes through another variable attenuator with the purpose of counterbalancing the first variable attenuator, in or-

[14] SRS FS725, Stanford Research Systems, Sunnyvale, CA, USA
[15] MLIQ-0416, Marki Microwave, Inc., Morgan Hill, CA, USA
[16] B&Z Technologies, East Setauket, NY, USA

der to keep the power input at the RF port of the I/Q mixer constant. The second variable attenuator is followed by a dc block (inner and outer block) and a −6 dB attenuator. The purpose of the dc blocks at the LO port and the RF port of the mixer is to prevent the formation of ground loops, whereas the purpose of the −6 dB attenuator is to dampen interference effects caused by the signal leakage from the LO port to the RF port due to finite mixer isolation. The LO signal and the RF signal at the I/Q mixer exhibit the same frequency f_{LO}, yielding I and Q signals with frequencies $2f_{\mathrm{LO}}$ and 0 Hz. As for the further analysis only the dc component of both the I and the Q signal is relevant, the $2f_{\mathrm{LO}}$ component is cut off with a pair of low-pass filters[17]. The filtered I and Q signals are amplified separately with a two channel custom made low-noise battery amplifier before being filtered by yet another pair if low-pass filters, which acts as an anti-aliasing filter with a cutoff frequency $f_{\mathrm{c}} \approx 100\,\mathrm{kHz}$. Finally, the I and Q voltage signals are digitised with an analogue-to-digital converter[18] (ADC). As in the case of the VNA based read-out scheme, a SQUID electronics serves as a low-noise precision current source for dc currents applied to the modulation line of the µMUX chip. The SQUID electronics, the signal generator and the ADC are connected to a PC allowing for software controlled measurements. For this purpose, a dedicated Python-based data acquisition and analysis library has been developed, which includes automatised calibration measurements, frequency sweep measurements as a function of the modulation current, and noise measurements, as well as data calibration routines and resonance fitting routines. The corresponding data acquisition and analysis flow is presented in section 6.3.

6.2 Characterisation of the chip *ECHo-MUX-04-6A*

A detailed characterisation of the µMUX chip *ECHo-MUX-04-6A* is necessary to test the performance of the microwave resonators and the rf SQUIDs on chip and to extract characteristic parameters for each channel. For these characterisation measurements, the VNA based measurement set-up described in section 6.1.3 has been employed. In figure 6.5, the transmission spectrum of the µMUX chip is shown, i.e. the absolute square of the scatter parameter $S_{21}(f)$. As for all subsequent measurements, the temperature was set to $T_{\mathrm{MXC}} = 20\,\mathrm{mK}$. The microwave power on the transmission line of the chip was estimated to be $P_{\mathrm{rf}} \sim -70\,\mathrm{dBm}$ at $f = 5.5\,\mathrm{GHz}$. The resonances corresponding to the 16 resonator channels of the µMUX chip, introduced in figure 6.1, could be identified and are highlighted in the spectrum: the resonances marked in dark green correspond to the LER channels equipped with an rf SQUID, i.e. LER-µMUX channels, the dark red colour represents the bare LER chan-

[17] EWT-56-0478, EWT, Salisbury, MD, USA
[18] NI USB-6361 Multifunction I/O Device, National Instruments, Austin, TX, USA

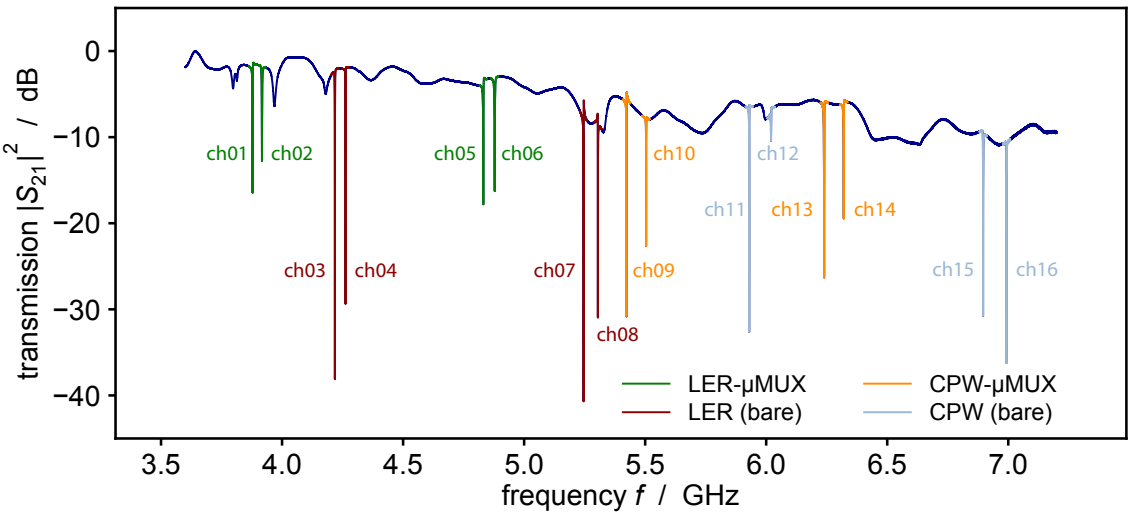

Figure 6.5: Transmission spectrum of the µMUX chip *ECHo-MUX-04-6A* at $T = 20\,\mathrm{mK}$ measured with a VNA. The channel numbers associated with the highlighted resonances correspond to the channel numbers introduced in the chip design shown in figure 6.1.

nels, the orange colour stands for CPW channels with rf SQUID, i.e. CPW-µMUX channels, and the light blue colour indicates CPW channels without rf SQUID. The positions f_{min} of the transmission minima corresponding to the resonances are in reasonable agreement with the designed resonance frequencies. It is worth noticing that the resonances associated with LER-µMUX channels (ch01, ch02, ch05, ch06) have significantly lower internal quality factors than the bare LER channels (ch03, ch04, ch07, ch08). As the only difference is the presence or absence of the coupling to an rf SQUID, the additional losses leading to a reduced internal quality factor in case of the LER-µMUX channels is presumably due to the coupling of the LERs to the rf SQUIDs. Similar effects have been observed in previous works [Pal19, Ihs21], however, the exact mechanism is not understood yet and subject of ongoing research. An analogue effect in case of CPW based channels has not been observed.

6.2.1 Dependence of the resonance frequency on the external magnetic flux bias

In order to get insight into the rf SQUID parameters, the dependence of the eight fully-fledged µMUX channels on external magnetic flux biases has been investigated. The easiest way to change the external magnetic flux threading the rf SQUIDs in a controlled way is the adjustment of the current I_{mod} running through the modulation line and, hence, through the inductance L_{mod}. Therefore, for each µMUX channel, the resonance curve, i.e. the complex scatter parameter $S_{21}(f)$ in a 20 MHz

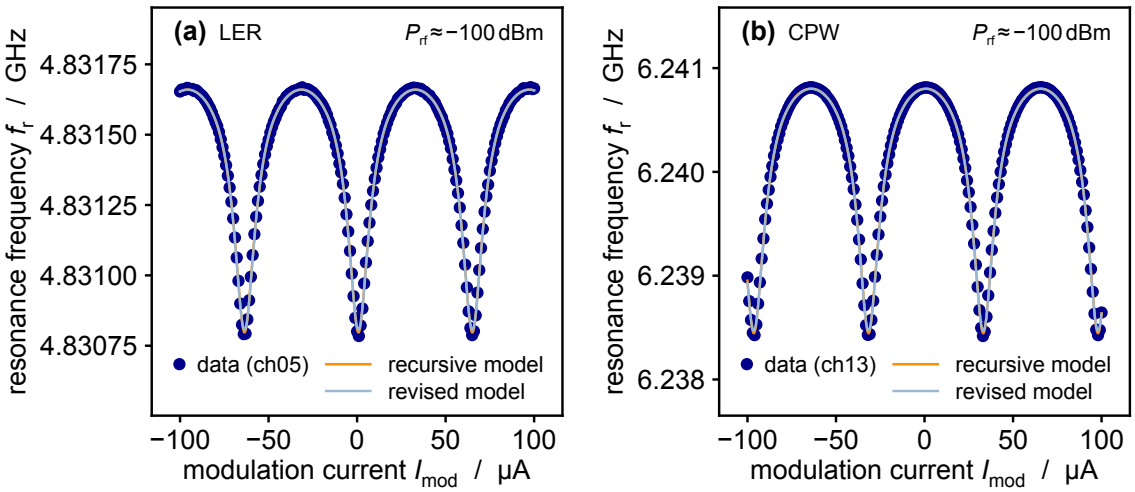

Figure 6.6: Dependence of the resonance frequency f_r on the applied modulation current I_{mod} **(a)** for the LER-µMUX channel ch05 and **(b)** for the CPW-µMUX channel ch13. For both data sets, numerical fits based on the recursive model (eq. (6.2), orange curves) and based on the revised model (eq. (6.3), light blue curves) have been performed. Note that due to the great agreement of the two models the orange curve is hardly visible.

window around the transmission minimum, has been measured as a function of the modulation current I_{mod}. Fitting the obtained complex $S_{21}(f)$ parameter curves with the algorithm described in section 3.2.5 [Pro15] yields the characteristic resonator parameters f_r, Q_l, Q_i and Q_c as a function of I_{mod}. In figure 6.6, the resonance frequency of the LER-µMUX channel ch05 and the resonance frequency of the CPW-µMUX channel ch13 are plotted as a function of the modulation current I_{mod} for a fixed microwave power $P_{rf} = -100\,\mathrm{dBm}$ on the transmission line of the µMUX chip[19]. Both curves are numerically fit with a function motivated by equations (3.53), (3.59), (3.55) and (3.60):

$$f_r(I_{mod}) = f_r^{off} + \Delta f_r^{mod} D(\varphi_{ext}(I_{mod}), \varphi_{rf}(P_{VNA})) \tag{6.1}$$

where - in case of the LER-µMUX channels - the resonance frequency f_r^{off} is given by equation (3.25) and the modulation amplitude is $\Delta f_r^{mod} = f_r^{off} M_T^2/(2(L+L_T)L_S)$, whereas in for the CPW-µMUX channels the resonance frequency f_r^{off} is given by equation (3.17) and $\Delta f_r^{mod} = 4 f_0^2 M_T^2/(L_S Z_0)$. The dimensionless modulation function $D(\varphi_{ext}, \varphi_{rf})$ is model dependent and provides the dependence of the resonance frequencies on the magnetic flux and thereby on the applied modulation current I_{mod} via the normalised external magnetic flux $\varphi_{ext} = 2\pi I_{mod} M_{mod}/\Phi_0 + \varphi_{off}$. The precise

[19] The error bars of the presented data are smaller than the marker size of the data points, for which reason no error bars are visible in the presented data

knowledge of the mutual inductance M_{mod} and the normalised magnetic flux offset φ_{off} are crucial to control the magnetic flux state of the rf SQUID in the following measurements. Both M_{mod} and φ_{off} are fit parameters along with $f_{\mathrm{r}}^{\mathrm{off}}$, $\Delta f_{\mathrm{r}}^{\mathrm{mod}}$ and the screening parameter β_{L}, which enters $D(\varphi_{\mathrm{ext}}, \varphi_{\mathrm{rf}})$.

In case of the basic µMUX model for negligible microwave powers, according to equation (3.52) the modulation function is given by

$$D_{\mathrm{basic}}(\varphi_{\mathrm{ext}}) = \frac{\beta_{\mathrm{L}} \cos(\varphi_{\mathrm{tot}}(\varphi_{\mathrm{ext}}))}{1 + \beta_{\mathrm{L}} \cos(\varphi_{\mathrm{tot}}(\varphi_{\mathrm{ext}}))} \tag{6.2}$$

where, following from equation (3.46), the normalised total magnetic flux for vanishing microwave power is $\varphi_{\mathrm{tot}} = \varphi_{\mathrm{ext}} - \beta_{\mathrm{L}} \sin(\varphi_{\mathrm{tot}})$. The implicit structure of the equation for φ_{tot} does not allow for an analytic solution $\varphi_{\mathrm{tot}}(\varphi_{\mathrm{ext}})$. In previous works, the expression has been approximated as $\varphi_{\mathrm{tot}} \approx \varphi_{\mathrm{ext}} - \beta_{\mathrm{L}} \sin(\varphi_{\mathrm{ext}})$ [Weg18a] which works well for small β_{L}, however, for $\beta_{\mathrm{L}} \sim 0.5$ this approximation is inaccurate. In the framework of this thesis, a different approach has been chosen for the measurements presented in this thesis. The Python function modelling φ_{tot} for the fitting routine has been set up in a recursive fashion with a recursion depth N_{rec}, i.e. the function inserts itself into itself N_{rec} times before returning the result, using φ_{ext} as starting point for the recursion. Ultimately, this leads to the expression $\varphi_{\mathrm{tot}} = \varphi_{\mathrm{ext}} - \beta_{\mathrm{L}} \sin(\varphi_{\mathrm{ext}} - \beta_{\mathrm{L}} \sin(...(\varphi_{\mathrm{ext}} - \beta_{\mathrm{L}} \sin(\varphi_{\mathrm{ext}}))...))$. The dependence of φ_{tot} on N_{rec} has been investigated for $0 < \beta_{\mathrm{L}} < 1$ and $0 < N_{\mathrm{rec}} < 1000$, yielding the result that for any $\beta_{\mathrm{L}} < 1$ a recursion depth of $N_{\mathrm{rec}} \sim 100$ is sufficient. The orange fit curves in figure 6.6 were obtained using this basic µMUX model with the recursive approach to φ_{tot}.

In order to take into account the rf magnetic flux dependence of the interplay between the rf SQUID and the microwave resonator, the revised µMUX model as introduced in section 3.4.2 has to be considered [Weg21]. Following from equation (3.57), the modulation function can be expressed as expansion

$$D_{\mathrm{revised}}(\varphi_{\mathrm{ext}}, \varphi_{\mathrm{rf}}) = \frac{2\beta_{\mathrm{L}}}{\varphi_{\mathrm{rf}}} \sum_{i,j} p_{i,j}(\varphi_{\mathrm{ext}}, \varphi_{\mathrm{rf}}) \tag{6.3}$$

with summands $p_{i,j}(\varphi_{\mathrm{ext}}, \varphi_{\mathrm{rf}}) = a_{i,j} \beta_{\mathrm{L}}^{b_{i,j}} \cos\big(c_{i,j}\varphi_{\mathrm{ext}}\big) J_1(c_{i,j}\varphi_{\mathrm{rf}})$, where i indicates the order of the Taylor expansion and j addresses different contributions within one expansion order. The expansion coefficients up to $i = 10$ are summarised in the appendix in table A.1. $J_1(x)$ is the first Bessel function of first kind. Using this revised µMUX model to fit the data shown in figure 6.6 yields the light blue fit curves. Note that these fit curves are in such great agreement with the fit curves obtained with the basic µMUX model (with recursive approach to φ_{tot}) that they

channel	$f_\mathrm{r}^\mathrm{off}$ / GHz	$\Delta f_\mathrm{r}^\mathrm{mod}$ / MHz	β_L	M_mod^{-1} / µA/Φ_0	Φ_off / Φ_0
ch01 (LER)	3.8784	0.833	0.56	63.8	0.27
ch02 (LER)	3.9170	0.383	0.47	63.8	0.01
ch05 (LER)	4.8314	0.733	0.46	64.3	0.49
ch06 (LER)	4.8786	0.736	0.46	64.4	0.25
ch09 (CPW)	5.4232	1.598	0.45	64.5	-0.26
ch10 (CPW)	5.5035	1.638	0.45	64.6	0.49
ch13 (CPW)	6.2402	2.009	0.46	64.8	-0.01
ch14 (CPW)	6.3211	2.059	0.46	64.6	0.00

Table 6.3: Parameters for all µMUX channels of the chip *ECHo-MUX-04-6A* resulting from the magnetic flux dependence fits in the limit $\Phi_\mathrm{rf} \to 0$. The quantity Φ_off is not a property set by the µMUX chip but depends on the magnetic flux penetrating the rf SQUID at the onset of superconductivity. All other listed quantities are properties of the respective µMUX channels.

cover them almost entirely. This visual agreement is backed by the agreement of the fit parameters obtained with the two different models, which are fully compatible within the fit error. This holds true not only for the two µMUX channels presented exemplarily in figure 6.6, but for all µMUX channels on the chip under investigation.

For the shown data, the microwave power on the transmission line of the chip is $P_\mathrm{rf} \approx -100\,\mathrm{dB}$, which corresponds to $\Phi_\mathrm{rf} \lesssim 5\,\mathrm{m}\Phi_0$ for the given µMUX channels. At higher microwave powers the agreement between the two models for $D(\varphi_\mathrm{ext}, \varphi_\mathrm{tot})$ gets worse and eventually breaks down, as the basic µMUX model does not include any microwave power dependence and, hence, is only valid for small microwave powers and thereby for $\Phi_\mathrm{rf} \to 0$. For this reason, in the following only the revised µMUX model is considered unless noted otherwise.

The fit results for all channels are summarised in table 6.3. The resonance frequencies $f_\mathrm{r}^\mathrm{off}$ of the LER-µMUX channels (CPW-µMUX channels) are $\sim 2\,\%$ (4 %) below the design values listed in table 6.1, which is a reasonable agreement and sufficient for the experiments carried out within the scope of this thesis. The values for the inverse mutual inductance M_mod^{-1} show a great homogeneity over all channels, however, they deviate by up to 16 % from the design values listed in table 6.2. The largest systematic uncertainty in the simulation of the mutual inductance M_mod arises from the parasitic distance between the inductances L_mod and L_S, which accounts for the physical distance of the inductances, given by the thickness of the SiO_2-based isolation layer in between, and for the magnetic penetration depth of the niobium films constituting the inductances. Hence, a deviation from the target SiO_2 thickness or from the expected magnetic penetration depth are the most likely cause for the observed mismatch.

The deviation of the modulation amplitudes $\Delta f_\mathrm{r}^\mathrm{mod} = 4 f_0^2 M_\mathrm{T}^2/(L_\mathrm{S} Z_0)$ of the CPW-µMUX channels from the respective targets values, reported in table 6.1, is between 20 % and 25 %. As the measured resonance frequencies match well the expectation, and hence also f_0, which cannot be measured directly, is expected to match the expectation, the main cause for the observed deviations is most likely due to the term $M_\mathrm{T}^2/L_\mathrm{S}$. The contributions from M_T and L_S to the deviation cannot be disentangled. However, as L_S is in first order only dependent on the coil geometry of the rf SQUID, while M_T is subject to effects similar to the ones, that already lead to the deviations in M_mod, it is more likely that the main component of the deviation is due to M_T.
For the modulation amplitudes $f_\mathrm{r}^\mathrm{mod} = f_\mathrm{r}^\mathrm{off} M_\mathrm{T}^2/(2(L + L_\mathrm{T})L_\mathrm{S})$ of the LER-µMUX channels, the deviation of the channels ch01 and ch02 from the respective target values listed in table 6.1 is around 40 % , while for the deviation of the channels ch05 and ch06 is below 1 %. Deviations in the order of 25 % have been found for another LER-µMUX device from the same wafer in an independent measurement [Ihs21]. The exact cause for the large scatter in $\Delta f_\mathrm{r}^\mathrm{mod}$ is not understood, it might be related to the above mentioned issues occurring when coupling an rf SQUID to an LER, however, further investigation is needed. As the designed resonance frequencies match well the measured ones, it can be assumed that both $f_\mathrm{r}^\mathrm{off}$ and $L + L_\mathrm{T}$ are not the main cause for the deviations in the modulation amplitude. Hence, once more, most likely the deviation arises from the term $M_\mathrm{T}^2/L_\mathrm{S}$.
For each µMUX channel an experimentally determined value for $M_\mathrm{T}^2/L_\mathrm{S}$ can be derived from the measured modulation amplitude, and subsequently an experimentally determined value for M_T can be identified, assuming the simulated value for L_S. In the further analysis, these experimentally determined values are used instead of the simulated ones.
The SQUID hysteresis parameter $\beta_\mathrm{L} = 2\pi I_\mathrm{c} L_\mathrm{S}/\Phi_0$ matches the design value for ch01, however for all the other channels it is $\sim 20\,\%$ smaller than the designed value. As a 20 % deviation between the SQUID inductance L_S of ch01 and L_S of any other channel seems implausible due to their identical geometry, this deviation is necessarily caused by a difference in the critical currents I_c of the different µMUX channels, which could be caused by tolerances in the fabrication of the junction windows or by inhomogeneities in the AlO_x layer forming the junction's tunnel barrier.
The values of the magnetic flux offset Φ_off are reflecting the magnetic flux state of the rf SQUID at the onset of superconductivity when cooling the set-up to millikelvin temperatures and, therefore, they are no properties set by the µMUX chip. The knowledge of both Φ_off and the mutual coupling M_mod allow for the precise preparation of any desired magnetic flux state in the rf SQUID in subsequent measurements by injecting an adequate modulation current I_mod.

6.2.2 Determination of the most flux sensitive state of the µMUX

For the determination of the magnetic flux noise of a µMUX channel, it is essential to know for which optimal external magnetic flux bias $\Phi_{\mathrm{ext}}^{\mathrm{opt}}$ the change in resonance frequency f_{r} upon a change in external magnetic flux Φ_{ext} is extremal. Therefore, following from equation (6.1), for the model dependent modulation function $D(\varphi_{\mathrm{ext}}, \varphi_{\mathrm{rf}})$, the relation

$$\left.\frac{\partial^2 D(\varphi_{\mathrm{ext}}, \varphi_{\mathrm{rf}})}{\partial \varphi_{\mathrm{ext}}^2}\right|_{\varphi_{\mathrm{ext}}=\varphi_{\mathrm{ext}}^{\mathrm{opt}}} = 0 \tag{6.4}$$

has to hold true, where the normalised optimal external magnetic flux bias is given by $\varphi_{\mathrm{ext}}^{\mathrm{opt}} = 2\pi\Phi_{\mathrm{ext}}^{\mathrm{opt}}/\Phi_0$. In order to obtain $\Phi_{\mathrm{ext}}^{\mathrm{opt}}$, equation (6.4) has to be solved numerically for a given model of $D(\varphi_{\mathrm{ext}}, \varphi_{\mathrm{rf}})$. In case of the revised µMUX model, the magnetic flux bias $\Phi_{\mathrm{ext}}^{\mathrm{opt}}$ depends on both the SQUID hysteresis parameter β_{L} and the normalised rf magnetic flux φ_{rf}. As φ_{rf} for a given microwave power at the input of the cryogenic microwave read-out chain is known only with the uncertainties corresponding to the uncertainties in the Tx attenuation of the cryogenic read-out chain, an approximation which is independent of the rf magnetic flux has been chosen: equation (6.4) has been solved numerically for smallest microwave powers, assuming the basic µMUX model including the recursive approach presented in section 6.2.1. The value found for $\Phi_{\mathrm{ext}}^{\mathrm{opt}}$ is accurate in this limit and, hence, also the corresponding modulation current $I_{\mathrm{mod}}^{\mathrm{opt}} = \Phi_{\mathrm{ext}}^{\mathrm{opt}}/M_{\mathrm{mod}}$ is accurate in this limit. Subsequently, for a given µMUX channel, $I_{\mathrm{mod}}^{\mathrm{opt}}$ found in this way is used to create the approximate optimal external magnetic flux bias of that µMUX channel at any microwave power.

6.2.3 Dependence of the resonance frequency on the microwave power

As demonstrated in [Weg18a, Weg21] and discussed in section 3.4, the resonance frequency of a µMUX channel exhibits a dependence on the microwave power applied to the transmission line of the µMUX chip. As this effect implicates a microwave power dependent maximal resonance frequency shift $\Delta f_{\mathrm{r}}^{\mathrm{max}}$, which in turn impacts the noise performance of the µMUX, the microwave power dependencies of the resonance frequencies of all eight µMUX channels of the chip *ECHo-MUX-04-6A* are investigated in the following. Similarly to the above discussed measurements of the external magnetic flux dependence, for each µMUX channel the complex $S_{21}(f)$ parameter has been measured in a 20 MHz window around the transmission minima for 51 different microwave powers between −63 dBm and −13 dBm at the input of the cryogenic microwave read-out chain. The measurements at each microwave power for each channel have been performed for three different external magnetic flux biases:

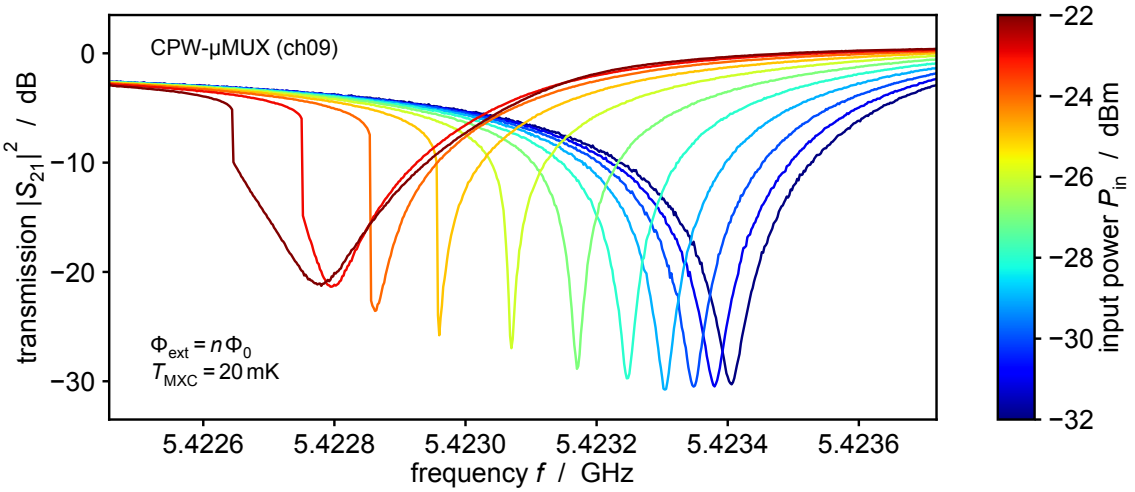

Figure 6.7: The measured resonance curves for the CPW-µMUX channel ch09 for an external magnetic flux bias of $\Phi_{ext} = n\Phi_0$ and for microwave powers applied to the input of the cryogenic read-out chain in the range $-32\,\mathrm{dBm} \leq P_{in} \leq -22\,\mathrm{dBm}$.

firstly, for integer multiples of the magnetic flux quantum ($\Phi_{ext} = n\Phi_0$) and, secondly, for half-integer multiples ($\Phi_{ext} = (n + 1/2)\Phi_0$), as for these two cases the resonance frequency shift is extremal. Thirdly, measurements at an intermediate flux state $\Phi_{ext} = \Phi_{ext}^{opt}$ have been performed, whose definition and significance are explained in section 6.2.2. As for the resonance curves in the previous section, the resonator parameters including the resonance frequency f_r can in principal be extracted from the data by fitting numerically a suitable resonance model to the resonance curves. For low and intermediate microwave powers, the basic resonance model used for the fitting algorithm described in section 3.2.5 matches the data very well and, hence, it can be employed for the extraction of the resonance parameters. For higher microwave powers, however, non-linear effects set in, which cause a deviation from the basic Lorentzian shape of the resonance curves. In figure 6.7, the resonance curves measured for the CPW-µMUX channel ch09 at an external magnetic flux bias of $\Phi_{ext} = n\Phi_0$ for eleven selected microwave powers P_{in} at the input of the cryogenic microwave read-out chain ranging from $-32\,\mathrm{dBm}$ to $-22\,\mathrm{dBm}$ illustrate the transition from a Lorentzian resonance shape on the right side to a distorted resonance shape on the left side, which is reminiscent of the line shape of a Duffing oscillator, exhibiting jumps due to its non-linearity. At least three different mechanisms could potentially contribute to the observed jumps and resonance distortion: in the first place, the Josephson junction in the rf SQUID causes a modulation of the microwave power in the resonator into higher modes, which do not suffice the resonance condition and are thus filtered out, which leads not only to the expected power dependence of the resonance frequency, but also to a distortion of the Lorentzian shape of the

resonance curves at high microwave powers [Weg21]. Secondly, finite losses in the resonator lead to a power dissipation, which in turn can lead to a hysteretic switching between well-defined temperature states of the quasiparticle system in the resonator. This hysteretic switching gives rise to power dependent jumps and distortions of the resonance curves [DV10]. Lastly, a microwave power dependent, dynamical bifurcation between two driven oscillation states of the Josephson junction in the rf SQUID introduces an additional non-linearity [Sid05]. For the presented data, it is still subject to ongoing research to find out, which of those non-linear contributions causes the jumps and the distortion of the resonance curves. Therefore, an exact modelling of the resonance curves at highest microwave powers is currently not possible and, hence, a numerical fitting of these resonance curves is unfeasible.

In order to investigate the power dependence of the µMUX quantitatively at low microwave powers and qualitatively at high microwave powers, a measure for the resonance frequency at any microwave power needs to be defined. The frequency of the transmission minimum f_{min} of any resonance curve can be extracted independently of the distortion of the resonance curve. However, even at low microwave powers, f_{min} does not necessarily coincide with the resonance frequency f_{r} because of potential slight impedance mismatches between the resonators and the transmission line. In the basic resonance model, i.e. equation (3.37), the impedance mismatch is characterised by the angle ϕ_0, which causes a rotation of the complex resonance circle, and, therefore, $\phi_0 = 0$ indicates perfect impedance matching. For a small angle ϕ_0 and a large intrinsic quality factor Q_{i}, the relation $f_{\mathrm{min}} - f_{\mathrm{r}} \approx f_{\mathrm{r}}\phi_0/2|Q_{\mathrm{c}}| \approx \Delta f \cdot \phi_0/2$ follows from equation (3.37), where $|Q_{\mathrm{c}}|$ stands for the real-valued coupling quality factor and Δf for the resonator bandwidth. At low microwave powers, where the resonance curves are purely Lorentzian and both Δf and ϕ_0 are assumed to be constant, all the involved quantities can easily be determined for a given µMUX channel, establishing a fixed difference $\delta f = f_{\mathrm{min}} - f_{\mathrm{r}} = \mathrm{const}$. Subsequently, for all microwave powers, the respective frequency f_{min} can be extracted from the resonance curves, and the pseudo resonance frequency $f_{\mathrm{r}}^{*} = f_{\mathrm{min}} - \delta f$ can be calculated. By construction, at low microwave powers $f_{\mathrm{r}}^{*} = f_{\mathrm{r}}$, whereas at high microwave powers, the pseudo resonance frequency f_{r}^{*} is just a qualitative measure.

In figure 6.8, the pseudo resonance frequencies f_{r}^{*} as a function of the microwave power P_{in} at the input of the cryogenic read-out chain are shown exemplarily for the LER-µMUX channel ch05 and the CPW-µMUX channel ch13. For low powers, the maximum pseudo resonance frequency shift $\Delta f_{\mathrm{r}}^{*,\mathrm{max}} = |f_{\mathrm{r}}^{*}(n\Phi_0) - f_{\mathrm{r}}^{*}((n+1/2)\Phi_0)|$ is basically constant. For higher powers, the maximum pseudo resonance frequency $f_{\mathrm{r}}^{*}(n\Phi_0)$ and the minimum pseudo resonance frequency $f_{\mathrm{r}}^{*}((n+1/2)\Phi_0)$ approach each other until $\Delta f_{\mathrm{r}}^{*,\mathrm{max}} = 0$. Beyond this intersection point, the two extremal pseudo resonance frequencies invert roles until, towards higher powers, they intersect

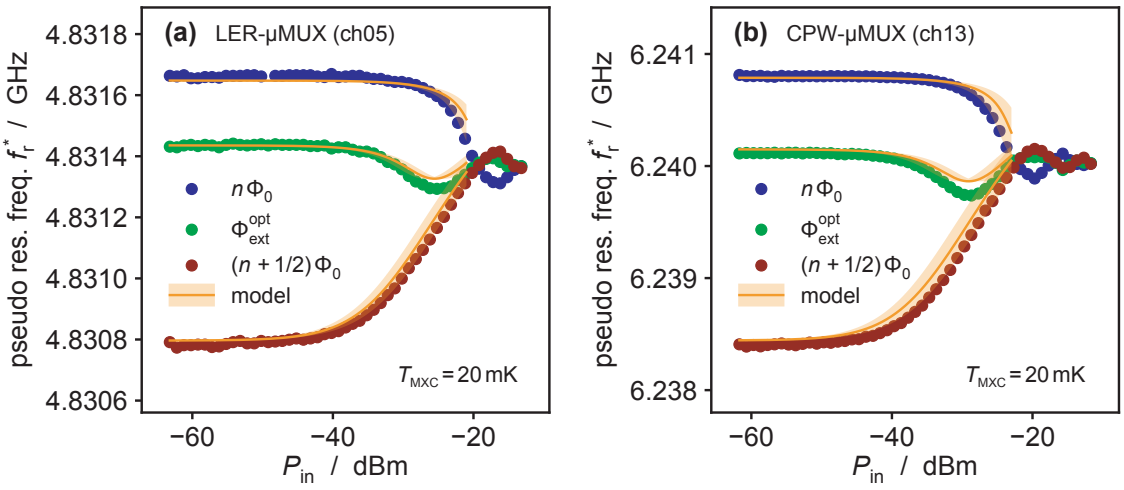

Figure 6.8: The pseudo resonance frequency f_r^* as a function of the microwave power P_{in} applied to the input port of the cryogenic read-out chain **(a)** for the LER-µMUX channel ch05 and **(b)** for the CPW-µMUX channel ch13. The data points in blue were taken with an external magnetic flux bias applied to the rf SQUID corresponding to an integer amount of magnetic flux quanta Φ_0, while the data points in green were taken at an intermediate magnetic flux bias Φ_{ext}^{opt}, and the data points in red at a half integer amount of Φ_0. The orange curves correspond to the revised µMUX model.

again, and so on. The expected white magnetic flux noise performance reflects this behaviour: the microwave powers corresponding to the intersection points, i.e. to $\Delta f_r^{*,max} = 0$, correspond to the microwave powers at which the flux noise diverges, as observed and discussed in section 3.5.1. In between the divergences, local flux noise minima are present. The minimum at lowest power, i.e. considerably before the first divergence, features the lowest possible amount of expected white noise and hence, the corresponding microwave power is considered the optimal read-out power for the microwave SQUID multiplexer. Therefore, the subsequent noise measurements, presented in the sections 6.3 and 6.4, were carried out at low and intermediate microwave powers, for which the non-linearities and the associated distortions of the resonance curves do not play a dominant role.

The revised multiplexer model makes a prediction on the dependence of the resonance frequency on the normalised rf magnetic flux φ_{rf} for which reason equation (6.1) with the revised modulation function $D_{revised}(\varphi_{ext}, \varphi_{rf})$ from equation (6.3) can be utilised to fit the data presented in figure 6.8. In case of an external magnetic flux bias of $n\Phi_0$, the normalised external magnetic flux is $\varphi_{ext} = 0$, whereas an external magnetic flux bias of $(n + 1/2)\Phi_0$ corresponds to $\varphi_{ext} = \pi$. For the intermediate flux bias, the normalised external flux bias is given by $\varphi_{ext} = 2\pi\Phi_{ext}^{opt}/\Phi_0$. For each µMUX channel, the respective resonance frequency f_r^{off}, the modulation amplitude Δf_r^{mod},

and the SQUID hysteresis parameter β_{L} are set to the values found with the external magnetic flux dependence fit in the previous section, and which are listed in table 6.3. The normalised rf magnetic flux is given by $\varphi_{\mathrm{rf}} = 2\pi I_{\mathrm{T}}(P_{\mathrm{rf}})M_{\mathrm{T}}/\Phi_0$ with current $I_{\mathrm{T}}(P_{\mathrm{rf}})$ in the resonator's coupling inductance. In turn, the microwave power P_{rf} on the transmission line of the µMUX chip at frequency f is related to the power P_{in} at the input of the cryogenic read-out chain via $P_{\mathrm{rf}}(f) = P_{\mathrm{in}}(f)G_{\mathrm{Tx}}(f)$ with attenuation factor G_{Tx} representing the frequency dependent Tx attenuation of the cryogenic read-out chain. The only free parameter in the numerical fit to the shown data is the Tx attenuation factor G_{Tx} of the cryogenic read-out chain. The fits of the three different magnetic flux bias states have been performed independently and, additionally, the fit range has been limited to data points corresponding to microwave powers below the first intersection point, as at higher microwave powers the above mentioned jumps in the resonance curves set in. The orange curves in figure 6.8 represent the revised µMUX model curves calculated with the average Tx attenuation obtained from the three independent fits, while the light orange band indicates the associated uncertainty of the average. Qualitatively, the revised µMUX model describes the data very well, the quantitative agreement, however, in particular at higher microwave powers, is rather poor, which is most likely, on the one hand, caused by the deviation of f_{r} from f_{r}^* at higher microwave powers and, on the other hand, by the fact that the revised µMUX model does not take any additional non-linearities into account besides its intrinsic non-linearity. In any case, the mismatch at higher microwave powers demonstrates the presence of some systematic uncertainty in the numerical fits and the obtained Tx attenuation factors $G_{\mathbf{Tx}}$. Because the design value of M_{T} most likely deviates from the actual value, as discussed in the previous section, an additional uncertainty in G_{Tx} is introduced by the occurrence of the mutual inductance M_{T} in the calculation of φ_{rf} from P_{in}.

In table 6.4 the average Tx attenuation obtained from the microwave power dependence fits are reported. Additionally, for comparison, the values for the expected Tx attenuation following from the design of the ECHo-100k cryogenic read-out chain discussed in chapter 4 are listed. For the CPW-µMUX channels ch09, ch13 and ch14, the attenuations obtained from the fits are in reasonable agreement with the simu-

	ch01	ch02	ch05	ch06	ch09	ch10	ch13	ch14
fit	−36.4	−37.3	−37.9	−36.5	−44.9	−48.2	−44.6	−44.0
simulation	−41.9	−41.9	−42.7	−42.7	−43.1	−43.2	−43.6	−43.7

Table 6.4: The attenuation [dB] of the Tx branch of the cryogenic read-out chain extracted by fitting the microwave power dependence of the µMUX. For comparison, the values expected from the simulations described in chapter 4 are listed.

lated values, while the CPW-µMUX channel ch13 exhibits a deviation of 5 dB. The fitted attenuations of the LER-µMUX channels ch01 - ch06 are shifted with respect to the simulated values by 4.6 dB to 6.2 dB. While the deviation for the CPW-µMUX channel ch13 might be caused by an enhanced reflectivity of the set-up inside the experimental holder in this frequency range, and might therefore simply present an outlier, the deviation for the LER-µMUX channels appears more systematic. As the origin of this deviation could not be clarified, the analysis of the noise measurements in section 6.4 has been carried out in two ways: once under the assumption of a Tx attenuation of the cryogenic set-up corresponding to the values found by fitting, and once under the assumption of the simulated Tx attenuation values.

6.3 Noise measurement and data analysis flow

In order to compare the noise performance of LER-µMUX channels to the noise performance of CPW-µMUX channels, the apparent magnetic flux noise of both types of channels has to be investigated over a wide range of microwave read-out powers. To accomplish this, the homodyne read-out system presented in section 6.1.3 and shown in figure 6.4 is employed. For each µMUX channel at each microwave read-out power, a sequence of interdependent measurements has to be performed in order to extract the respective noise performance. The required measurement steps and data analysis steps are discussed in the following.

6.3.1 I/Q mixer calibration

A core piece of the homodyne read-out scheme is an I/Q mixer. For an ideal I/Q mixer, the output voltages at the I port and at the Q port depend only on the input signals provided at the LO port and the RF port. Real I/Q mixers, however, exhibit some non-ideal behaviour, which manifests itself in four parameters characterising the mixer imbalance: a dc voltage offset I_0 at the I port, a dc voltage offset Q_0 at the Q port, a gain imbalance $G_\mathrm{I}/G_\mathrm{Q}$ between the I port and the Q port and a phase deviation $\Delta\phi$ from the orthogonality of the ideal I and Q signals. The output voltage at the I and the Q port, respectively, is then given by

$$\begin{aligned} I &= I_0 + G_\mathrm{I} A \cos(\phi) \\ Q &= Q_0 + G_\mathrm{Q} A \sin(\phi + \Delta\phi) \end{aligned} \tag{6.5}$$

where A stands for the ideal signal amplitude and ϕ for the ideal signal phase, i.e. the relative phase of the input signal at the LO port and the input signal at the RF port.

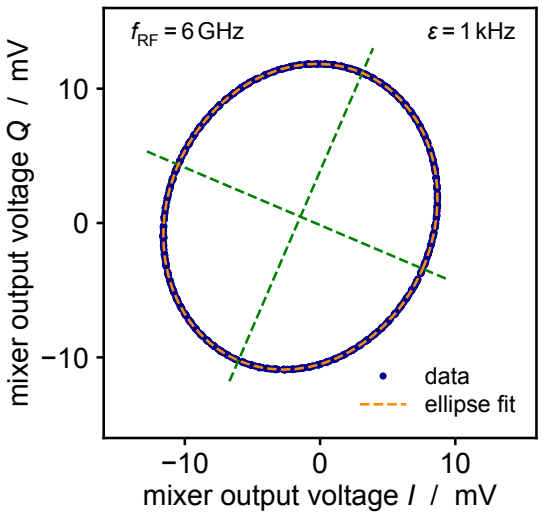

Figure 6.9: I/Q mixer calibration measurement for an RF frequency of $f_{\mathrm{RF}} = 6\,\mathrm{GHz}$, a frequency offset of $\varepsilon = 1\,\mathrm{kHz}$, a microwave power applied to the LO port of $P_{\mathrm{LO}} = 12\,\mathrm{dBm}$ and a microwave power at the RF port of $P_{\mathrm{RF}} = -24\,\mathrm{dBm}$. The dashed orange ellipse is a numerical fit to the data. The dashed green lines indicate the orientation of the ellipse's axes.

Note that for fixed mixer imbalance parameters and fixed A, the set of these two equations parametrises a tilted ellipse in the I/Q plane for $\phi \in [0, 2\pi)$. This fact can be used to determine the mixer parameters and to correct for them in subsequent measurements. The strategy is to carry out a calibration measurement for each RF frequency of interest varying ϕ and numerically fitting the resulting tilted ellipse in the I/Q plane. From the fit parameters, meaning the centre point of the ellipse, the length of the semi-minor axis, the length of the semi-major axis and the tilt angle, the mixer parameters can be calculated.

In the following, the calibration measurement carried out for the I/Q mixer employed in the framework of this thesis is presented. The set-up chosen for the calibration measurement consists of a signal generator[20] connected to the LO port of the I/Q mixer and a second signal generator[21] connected to the RF port of the I/Q mixer. The set-up connected to the I port and the Q port of the I/Q mixer is identical to the one for the final homodyne set-up, i.e. the I and Q signals are low-pass filtered, amplified and, finally, digitised by an ADC as explained in section 6.1.3, and hence, also all potential imbalances caused by components in the signal path between the I/Q mixer and the ADC are accounted for by the calibration. In order to vary the phase ϕ throughout one calibration measurement, the LO frequency f_{LO} and the RF frequency $f_{\mathrm{RF}} = f_{\mathrm{LO}} + \varepsilon$ are chosen to differ by a small amount ε making the phase time dependent $\phi \to \phi + 2\pi\,\varepsilon\,t$. For all calibration measurements in the framework of this thesis $\varepsilon = 1\,\mathrm{kHz}$ has been chosen. In figure 6.9, an exemplary calibration measurement with RF frequency $f_{\mathrm{RF}} = 6\,\mathrm{GHz}$, power input at the LO port $P_{\mathrm{LO}} = 12\,\mathrm{dBm}$ and power input at the RF port $P_{\mathrm{RF}} = -24\,\mathrm{dBm}$ is shown. The dashed orange curve is a tilted ellipse numerically fit to the data. The mixer parameters can

[20] R&S SMA100B, Rohde & Schwarz GmbH & Co. KG, Munich, Germany
[21] R&S SMF100A, Rohde & Schwarz GmbH & Co. KG, Munich, Germany

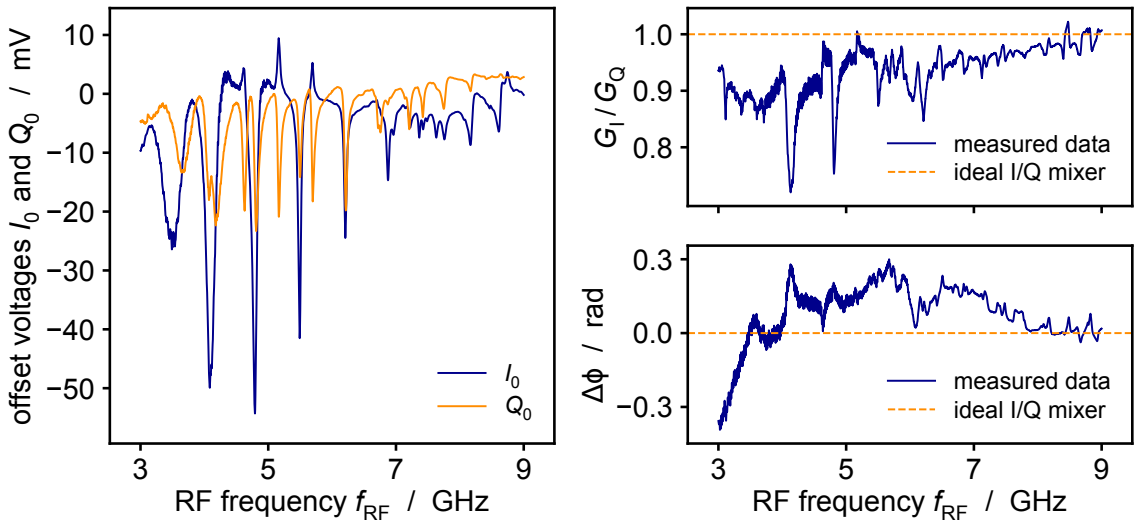

Figure 6.10: The dc offset voltages I_0 and Q_0, the gain imbalance $G_\mathrm{I}/G_\mathrm{Q}$ and the phase offset $\Delta\phi$ determined in a frequency range from 3 GHz to 9 GHz for the I/Q mixer used for all homodyne measurements in this thesis.

be inferred from the fit parameters. As, however, the mixer parameters vary over the accessible frequency range, this calibration measurement has to be repeated for all RF frequencies of interest. In figure 6.10 the calibration parameters are plotted for 75001 equidistantly spaced frequencies between 3 GHz and 9 GHz for the I/Q mixer employed during all homodyne measurements in the course of this thesis.

All data sets $(I_\mathrm{data}, Q_\mathrm{data})$ measured with the homodyne set-up are corrected for the mixer imbalance by subtracting the dc voltage offsets in a first step, transforming the data according to $(I_\mathrm{data}, Q_\mathrm{data}) \rightarrow (I_\mathrm{data} - I_0, Q_\mathrm{data} - Q_0)$. Subsequently, the gain imbalance is multiplied out: $Q_\mathrm{data} \rightarrow Q_\mathrm{data} \cdot G_\mathrm{I}/G_\mathrm{Q}$. The phase and amplitude of the data set in polar coordinates are calculated under consideration of the phase imbalance $\Delta\phi$ according to [Bar09]:

$$\begin{aligned} \phi_\mathrm{data} &= \arctan2(Q_\mathrm{data} - I_\mathrm{data}\sin(\Delta\phi),\, I_\mathrm{data}\cos(\Delta\phi)) \\ A_\mathrm{data} &= \sqrt{\frac{I_\mathrm{data}^2 + Q_\mathrm{data}^2}{\cos^2(\phi_\mathrm{data}) + \sin^2(\phi_\mathrm{data} + \Delta\phi)}} \end{aligned} \tag{6.6}$$

where the function $\arctan2(y, x)$ denotes the 2-argument arctan, which is valid in all four quadrants of the Cartesian plane. Finally, the data set fully corrected for mixer imbalances is given by

$$\begin{aligned} I_{\mathrm{data}}^{\mathrm{corr}} &= A_{\mathrm{data}} \cos(\phi_{\mathrm{data}}) \\ Q_{\mathrm{data}}^{\mathrm{corr}} &= A_{\mathrm{data}} \sin(\phi_{\mathrm{data}}) \end{aligned} \tag{6.7}$$

where the standard transformation from polar coordinates to Cartesian coordinates has been employed.

6.3.2 Determination of environment and resonator parameters

For the precise determination of the magnetic flux noise level of a µMUX channel, it is essential to know how the entire microwave signal path affects the phase and the amplitude of the measured noise signal. Therefore, the cable delay τ, the system attenuation factor a, the system phase angle α have to be determined experimentally. Additionally, the properties of the µMUX channel's resonator, i.e. the resonance frequency, the quality factors Q_l and Q_c and the on-chip impedance mismatch characterised by the angle ϕ_0, need to be known. The resonance frequency defines the frequency f_{RF} of the noise measurement, as the magnetic flux noise is measured on-resonance. The quality factors set the radius $r = Q_\mathrm{l}/(2Q_\mathrm{c})$ of the resonance circle, which is needed to convert I and Q data into resonator phase and resonator amplitude data. One can gain access to all of the above mentioned quantities by measuring the complex transmission $(I + iQ) \propto S_{21}$ in a frequency window around the transmission minimum and numerically fit the model described in section 3.2.5 to the data:

$$S_{21}(f) = a e^{i\alpha} e^{-2\pi i f \tau} \left[1 - \frac{\frac{Q_\mathrm{l}}{|Q_\mathrm{c}|} e^{i\phi_0}}{1 + 2iQ_\mathrm{l} \frac{f - f_\mathrm{r}}{f_\mathrm{r}}} \right] \tag{6.8}$$

In contrast to this model, real systems exhibit a frequency dependent system attenuation $a(f)$ and a frequency dependent phase $\alpha(f)$, introducing a frequency dependent baseline to both the absolute transmission $|S_{21}|^2$ and the corresponding phase transmission. In figure 6.11, as an example, the transmission spectrum $|S_{21}|^2$ calculated from the measured complex-valued data $(I + iQ) \propto S_{21}$ for the LER-µMUX channel ch01 is shown for a frequency band of 20 MHz around the transmission minimum. The non-constant baseline due to the frequency dependent system attenuation a is marked. Several approaches trying to correct for the frequency dependent system parameters $a(f)$ and $\alpha(f)$ before fitting have been tested, all of which have introduced systematic errors which were larger than the systematic error introduced by not correcting for the parameters before the fit. For this reason, in the scope of this thesis no correction has been applied, but the used frequency window for fitting

has been optimised. For large fit windows around the transmission minimum, the frequency dependence of the system parameters $a(f)$ and $\alpha(f)$ impacts the fit results. For small fit windows, on the other hand, the system parameters $a(f)$ and $\alpha(f)$ are assumed quasi-constant, however, due to the reduced amount of available data points, the numerical fit might converge into non-physical solutions, exhibiting, for instance, negative quality factors or resonance frequencies far outside the applied fit window. To find the most suitable fit window for each measured resonance curve, a multitude of fits with different fit window sizes varied in steps of 100 kHz have been performed. Non-physical fits results have been discarded and among the remaining fit results, the respective fit qualities have been ranked in terms of χ^2. The fit results obtained with the best fit window have been used for further measurements and analysis. In case of the exemplary data set for the LER-µMUX channel ch01, the best fit window size is 3.8 MHz, which is indicated in figure 6.11. Additionally, in the figure, the absolute value of the numerical fit to the underlying complex-valued data is plotted.
Even for the best fit windows, a slight deviation between the data and the fit curves remains because of the frequency dependent system parameters $a(f)$ and $\alpha(f)$. In later considerations regarding the measured noise performance of the µMUX, this deviation is taken into account as systematic error.

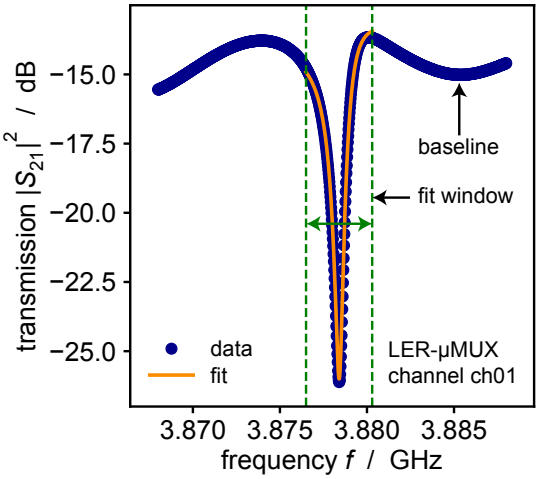

Figure 6.11: Transmission spectrum of the resonance corresponding to to the LER-µMUX channel ch01 in a frequency band of 20 MHz around the transmission minimum. The frequency range used for fitting the resonance is marked by the green arrow. The orange curve represents a numerical fit to the underlying complex I/Q data.

The above described procedure has to be carried out before each measurement of the amplitude noise and phase noise as the system parameters and the resonator parameters change whenever the measurement set-up is altered, e.g. by varying the adjustable attenuators in order to change the microwave power on the µMUX chip or by setting a different external magnetic flux bias in the rf SQUIDs shifting the resonance frequencies.

6.3.3 Measurement of the amplitude noise and the phase noise

For the determination of the amplitude noise and phase noise related to a µMUX channel with a given external magnetic flux bias, a given microwave read-out power and a given read-out frequency f_{RF}, the I/Q mixer's raw output voltages $I_{\mathrm{raw}}(t)$ and $Q_{\mathrm{raw}}(t)$ are sampled at a rate of 500 kS/s for ten seconds. The $I_{\mathrm{raw}}(t)$ and $Q_{\mathrm{raw}}(t)$ traces obtained in that manner have to be corrected for the I/Q mixer imbalances by applying the correction procedure explained in section 6.3.1. In a next step, the resulting $I_{\mathrm{corr}}(t)$ and $Q_{\mathrm{corr}}(t)$ voltage traces need to be calibrated for the system parameters determined with the method discussed in section 6.3.2. The fully calibrated $I_{\mathrm{calib}}(t)$ and $Q_{\mathrm{calib}}(t)$ traces are therefore calculated as

$$(I_{\mathrm{calib}}(t) + i\,Q_{\mathrm{calib}}(t)) = 1 - e^{-i\phi_0}\left[1 - \frac{e^{-i\alpha}e^{2\pi i f_{\mathrm{LO}}\tau}}{a}\,(I_{\mathrm{corr}}(t) + i\,Q_{\mathrm{corr}}(t))\right] \tag{6.9}$$

with the system phase angle α, the cable delay τ, the system attenuation a and the impedance mismatch angle ϕ_0. Note that due to the calibration procedure, $I_{\mathrm{calib}}(t) + i\,Q_{\mathrm{calib}}(t)$ is not a complex voltage but a scatter parameter. Finally, the fully calibrated resonance amplitude trace $A(t)$ and the fully calibrated resonance phase trace $\phi(t)$ can be obtained via [Bar09]

$$\begin{aligned} \phi(t) &= \arctan2(Q_{\mathrm{calib}}(t),\,(x_{\mathrm{c}} - I_{\mathrm{calib}}(t))) \\ A(t) &= \frac{1}{r}\sqrt{[x_{\mathrm{c}} - I_{\mathrm{calib}}(t)]^2 + [Q_{\mathrm{calib}}(t)]^2}\,. \end{aligned} \tag{6.10}$$

The centre of the corresponding resonance circle is at $(x_{\mathrm{c}},\,0)$ in the complex I/Q plane and the radius of the resonance circle is $r = 1 - x_{\mathrm{c}} = Q_{\mathrm{l}}/2Q_{\mathrm{c}}$. The amplitude noise $S_A(f)$ and the phase noise $S_\phi(f)$ are obtained from the Fourier transform of the respective auto-correlation functions, i.e. $S_x(f) = 2\mathcal{F}\{\langle x(t)x(0)\rangle\}$ with $x(t) = A(t)$ and $x(t) = \phi(t)$, respectively.

In figure 6.12, as an example, the phase noise and the amplitude noise of the LER-µMUX channel ch01 are plotted. The corresponding measurement has been carried out on resonance $f_{\mathrm{RF}} = f_{\mathrm{r}}$ at an estimated microwave power of −105 dBm on the transmission line of the µMUX chip. The rf SQUID has been biased with an external magnetic flux in such a way, that the change of the resonance frequency f_{r} is maximal upon a change in external magnetic flux, i.e. $\Phi_{\mathrm{ext}} = \Phi_{\mathrm{ext}}^{\mathrm{opt}}$ as explained in section 6.2.2. Note that the use of anti-aliasing filters with a cut-off frequency $f_{\mathrm{cut}} \sim 100$ kHz cause an artificial drop in the measured noise data for frequencies above f_{cut}. The amplitude noise is mostly characterised by a plateau which can be explained in

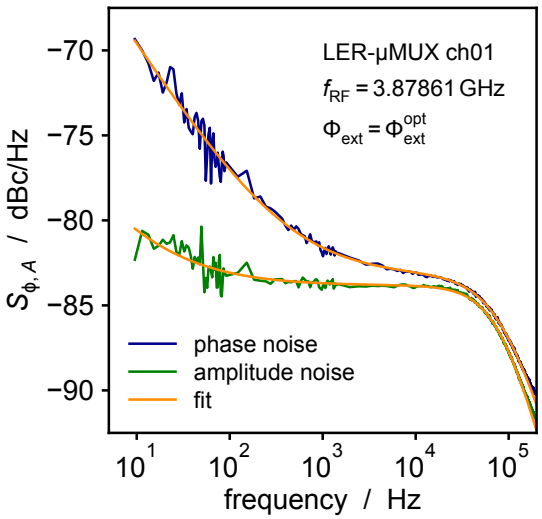

Figure 6.12: Amplitude and phase noise spectra for the LER-µMUX channel ch01 measured on resonance. The rf SQUID has been externally biased to reach the largest magnetic flux sensitivity of the µMUX channel. The orange curves are numerical fits to the data.

terms of white system noise caused by the entirety of the rf components used for the measurement set-up. More details on the microwave read-out chain and the corresponding noise contributions can be found in chapter 4. The phase noise exhibits a high noise level at low frequencies, which falls off towards higher frequencies in a $1/f^{\gamma}$-like manner approaching the white noise level of the amplitude noise. This $1/f^{\gamma}$-type phase noise in superconducting resonators is well understood in terms of two-level tunnelling systems coupling to the electric field of the resonating microwave [Maz04, Gao08a, Bar09]. These tunnelling systems are present in the substrate of the µMUX chip or in the natural niobium oxide layer covering the surface of the niobium layer constituting the resonators. Note that unexpectedly also the shown amplitude noise exhibits to a certain extent a $1/f^{\gamma}$-type noise at low frequencies, which is however compatible with a slight leakage of $1/f^{\gamma}$-type noise from the phase noise to the amplitude noise because of the imperfect I/Q data correction due to the frequency dependent system parameters $a(f)$ and $\alpha(f)$, as discussed in section 6.3.2. The treatment of systematic errors is explained in section 6.3.5. Taking into account the white noise, the $1/f^{\gamma}$-type noise and the filter cut-off at f_{cut}, the measured noise data can be numerically fit by

$$S_{\phi,A}^{\mathrm{fit}}(f) = S_{\phi,A}^{\mathrm{w}} \frac{1 + \left(\frac{f_{\mathrm{cor}}}{f}\right)^{\gamma}}{1 + \left(\frac{f}{f_{\mathrm{cut}}}\right)^{\beta}} \tag{6.11}$$

with white noise level $S_{\phi,A}^{\mathrm{w}}$ and corner frequency f_{cor} at which the contributions of the white noise and the $1/f^{\gamma}$-type noise to the total noise are equal. The exponents $\gamma > 0$ and $\beta > 0$ determine the steepness of the $1/f^{\gamma}$-type noise and the filter cut-off, respectively. In figure 6.12, the numerical fits to the data are shown as orange curves, indicating a good agreement between the data and the model.

The described method to measure the amplitude noise and the phase noise and to extract the parameters characterising the noise by numerically fitting the data is applied to each µMUX channel at each read-out power of interest. The results are presented and discussed in section 6.4.

6.3.4 Measurement of the transfer coefficients

For the determination of the magnetic flux noise S_Φ of the µMUX, a transfer coefficient is required, which converts the measured amplitude and phase noise into units of apparent magnetic flux noise. Since the amplitude transfer coefficient $\partial A/\partial\Phi = \partial A/\partial f \cdot \partial f/\partial\Phi$ vanishes on resonance, as $\partial A/\partial f = 0$ for $f = f_\mathrm{r}$, the phase transfer coefficient $\partial\phi/\partial\Phi$, relating a change in magnetic flux Φ to a change in resonator phase ϕ, is used for the conversion of both phase noise S_ϕ and amplitude noise S_A into units of apparent magnetic flux noise.

The transfer coefficient $\partial\phi/\partial\Phi$ has to be experimentally determined for each noise measurement separately. For this, $I(t)$ and $Q(t)$ traces are measured with the same microwave power P_rf on the transmission line and the same read-out frequency f_RF as for the noise measurement, while varying the external magnetic flux bias minimally around the optimal external magnetic flux bias $\Phi_\mathrm{ext}^\mathrm{opt}$ during the measurement. After correcting the data for I/Q mixer imbalances and for the system parameters, the data can be converted into resonator amplitude traces and resonator phase traces via equation (6.10), analogously to the treatment of the noise I/Q traces. The change in resonator phase upon a change in external magnetic flux can be extracted from the phase trace in order to determine the transfer coefficient.

In figure 6.13, the resonance phase trace measured for the LER-µMUX channel ch01 on resonance for an rf magnetic flux $\Phi_\mathrm{rf} \approx 70\,\mathrm{m}\Phi_0$ is shown. The external magnetic

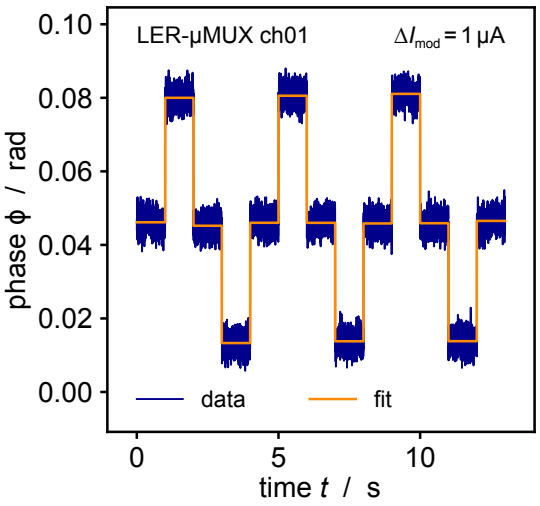

Figure 6.13: The resonator phase trace for the LER-µMUX channel ch01 on resonance with temporally changing external magnetic flux bias. The central phase level corresponds to an external magnetic flux bias of $\Phi_\mathrm{ext} = \Phi_\mathrm{ext}^\mathrm{opt}$, whereas the phase level above and below correspond to an external magnetic flux bias of $\Phi_\mathrm{ext} = \Phi_\mathrm{ext}^\mathrm{opt} \pm M_\mathrm{mod}\Delta I_\mathrm{mod}$.

flux bias was varied according to the sequence $\Phi_{\mathrm{ext}}^{\mathrm{opt}}$, $\Phi_{\mathrm{ext}}^{\mathrm{opt}} + \Delta\Phi$, $\Phi_{\mathrm{ext}}^{\mathrm{opt}}$, $\Phi_{\mathrm{ext}}^{\mathrm{opt}} - \Delta\Phi$, where $\Phi_{\mathrm{ext}}^{\mathrm{opt}}$ is the external magnetic flux bias corresponding to the most magnetic flux sensitive state of the rf SQUID as determined in section 6.2.2. The small change in magnetic flux $\Delta\Phi = M_{\mathrm{mod}}\Delta I_{\mathrm{mod}}$ is obtained by a change of modulation current $\Delta I_{\mathrm{mod}} = 1\,\mu\mathrm{A}$ running through the mutual inductance M_{mod} as found in section 6.2.1. Each step of the sequence was measured for 1 s and the sequence was immediately repeated several times in a row. The central phase level in figure 6.13 corresponds to an external magnetic flux bias of $\Phi_{\mathrm{ext}}^{\mathrm{opt}}$, whereas the upper and lower phase levels correspond to $\Phi_{\mathrm{ext}}^{\mathrm{opt}} \pm \Delta\Phi$, respectively. For an ideal resonator, on resonance, i.e. at $\Phi_{\mathrm{ext}} = \Phi_{\mathrm{ext}}^{\mathrm{opt}}$, a resonator phase of $\phi = 0$ is expected. The deviation of the data from this condition is a consequence of the imperfect I/Q data correction caused by the systematic resonance fit parameter deviations due to the frequency dependent system parameters $a(f)$ and $\alpha(f)$, as explained in section 6.3.2. The treatment of systematic errors is discussed in section 6.3.5.
The data has been numerically fit with a function composed of multiple step functions and the resulting fit curve is depicted in orange in figure 6.13. Finally, the transfer coefficient, i.e. the change in phase ϕ upon a change in magnetic flux Φ, is given by $\partial\phi/\partial\Phi \approx \Delta\phi/\Delta\Phi = \Delta\phi/(M_{\mathrm{mod}}\Delta I_{\mathrm{mod}})$, where $\Delta\phi$ denotes the phase change extracted from the data via the numerical fit.

6.3.5 Systematic errors

As observed in the previous sections, the data processing and analysis is subject to systematic uncertainties introduced by the fitting of the resonance data with frequency dependent system parameters $a(f)$ and $\alpha(f)$. Although care has been taken to limit these systematic effects as discussed in section 6.3.2, the systematic influences could not be mitigated entirely. Consequently, not only the data processing and the data analysis, but also theoretical predictions based on fit parameters extracted from the resonance curves are affected. In the following, the strategy for the data processing, the data analysis and the calculation of theoretical predictions under the influence of systematic uncertainties is discussed.

For the data processing and the data analysis, any compensation for uncertainties would introduce additional systematic uncertainties and, therefore, instead of applying a compensating scheme, a systematic error is taken into account. For that, the quantities of interest, i.e. the white noise levels extracted by fitting from the amplitude and phase noise curves with equation (6.11) have been assigned a systematic error in the order of the deviation of the respective resonance fit curve from the resonance data at $f = f_{\mathrm{r}}$ (via equation (6.8)) and in a careful approach at least 1 dB for those cases, where the deviation is smaller than 1 dB.

For the calculation of theoretical predictions based on resonance fit parameters, such as the theoretically expected white noise level in dependence of the microwave power, another approach has been chosen. In figure 6.14, one of the resonance fit parameters, namely the loaded quality factor Q_l of the LER-µMUX channel ch01, is exemplarily plotted as a function of the microwave power $P_\mathrm{rf}^\mathrm{sim}$ on chip, which has been calculated from the microwave power applied to the input of the cryogenic microwave read-out chain and from the simulated Tx attenuation of the cryogenic read-out chain. The shown data exhibits a relatively large scatter. As the microwave power was changed

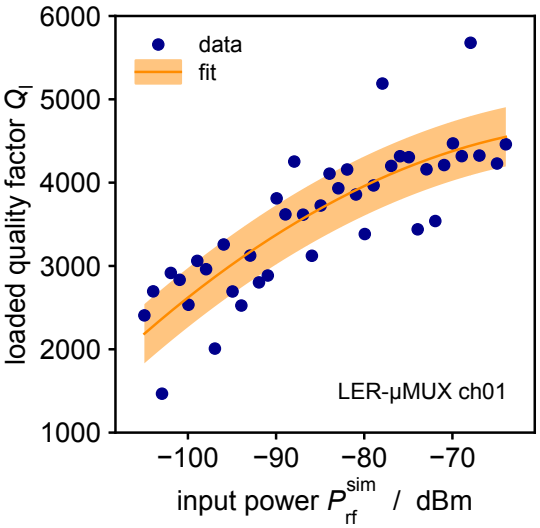

Figure 6.14: The loaded quality factor Q_l of the LER-µMUX channel ch01 as a function of the expected microwave power on chip $P_\mathrm{rf}^\mathrm{sim}$. The orange curve is a quadratic polynomial numerically fitted to the data. The light orange band indicates the average deviation of the data from the fit curve.

with the help of a variable attenuator, as explained in section 6.1.3, the signal path length would vary between measurements at different microwave powers, causing a different set of frequency dependent system parameters $a(f)$ and $\alpha(f)$ at every microwave power[22]. Hence, the systematic uncertainties introduced by $a(f)$ and $\alpha(f)$ vary with the applied microwave power, causing the observed scatter in Q_l. A similar scatter could also be discovered in the resonance frequency f_r, the coupling quality factor Q_c and the internal quality factor Q_i. Consequently, the theoretical predictions based on those resonance fit parameters would exhibit a systematic scatter. Therefore, the scattering fit parameters have been smoothed by fitting a quadratic polynomial to the data. The systematic error of the smoothed data is assumed to be the mean absolute deviation of the data points from the fit. An example of this smoothing is shown in figure 6.14, where the orange curve is a parabola fitted to the data. The light orange band indicates the assumed systematic error. Subsequently, the calculation of theoretical curves, such as the expected white noise level as a func-

[22] For the VNA based measurements presented in section 6.2, the microwave power could be adjusted exploiting the available power output range of the VNA instead of varying the signal path. For this reason, the VNA based measurements do not suffer from a power dependent baseline shape.

tion of applied microwave power, yields smooth curves, and the systematic error of the theoretical curves is derived by means of standard error propagation from the respective errors of the smoothed fit parameter curves.

6.4 Results of the noise measurements

In general, the noise of a µMUX channel is comprised of a $1/f^{\kappa}$-type noise dominating at low frequencies and a frequency-independent white noise as discussed in section 6.3.3. The operation of the µMUX for the ECHo-100k phase of the ECHo experiment will be based on a read-out scheme involving flux-ramp modulation for the linearisation of the rf SQUID response, in which the external flux threading the rf SQUID is modulated with a sawtooth signal with a frequency of typically $\geq 100\,\mathrm{kHz}$ [Mat12, Ric21]. The MMC detector signals are modulated onto this carrier frequency and demodulation occurs in the room temperature electronics, and hence the $1/f^{\kappa}$-type noise of the µMUX is greatly suppressed [Mat12]. Therefore, the white noise contribution of the µMUX will have a significantly larger impact on the achievable energy resolution than the $1/f^{\kappa}$-type noise contribution of the µMUX. As the noise performance measurements carried out in the scope of this thesis are aiming at finding the best microwave resonator geometry for the ECHo-100k read-out system, the following analysis of the noise performance measurements focuses fully on the white noise performance.

For the characterisation of the noise performance of all µMUX channels of the chip *ECHo-MUX-04-6A*, the measurement steps described in the preceding sections have been performed for all eight µMUX channels on resonance with an external flux bias of $\Phi_{\mathrm{ext}} = \Phi_{\mathrm{ext}}^{\mathrm{opt}}$ and for 42 different microwave powers at the input of the cryogenic microwave read-out chain. As the simulated Tx attenuation of the cryogenic microwave read-out chain and the Tx attenuation determined in section 6.2.3 exhibit significant deviations, the following analysis is performed for both sets of Tx attenuations. The microwave power at the input of the cryogenic read-out chain P_{in}, translates hence into two different sets of microwave powers on chip P_{rf}, namely $P_{\mathrm{rf}}^{\mathrm{sim}}$ under the assumption of the simulated Tx attenuations and $P_{\mathrm{rf}}^{\mathrm{fit}}$ assuming the values found in section 6.2.3. The data presented in the following is always plotted as a function of $P_{\mathrm{rf}}^{\mathrm{sim}}$, as a conversion into $P_{\mathrm{rf}}^{\mathrm{fit}}$ can easily be performed with the help of table 6.4.

The input powers have been varied in steps of 1 dB between $P_{\mathrm{in}}^{\mathrm{min}} = -63\,\mathrm{dBm}$ and $P_{\mathrm{in}}^{\mathrm{max}} = -22\,\mathrm{dBm}$, which corresponds to a microwave power on the transmission line of the µMUX chip of $-105\,\mathrm{dBm} \lesssim P_{\mathrm{rf}}^{\mathrm{sim,ch01}} \lesssim -64\,\mathrm{dBm}$ for the LER-µMUX channel ch01 and $-107\,\mathrm{dBm} \lesssim P_{\mathrm{rf}}^{\mathrm{sim,ch14}} \lesssim -66\,\mathrm{dBm}$ for the CPW-µMUX channel ch14 and lies in between these two ranges for all other µMUX channels. Since most of the resonance fits of the CPW-µMUX channel ch09 have not converged, in the following

the data related to this channel is not considered.

6.4.1 Amplitude noise and phase noise of the µMUX

From the phase noise spectra and the amplitude noise spectra measured at 42 different microwave powers for all considered µMUX channels, the corresponding white noise level can be extracted as described in section 6.3.3. The resulting white noise values are summarised in the plots presented in figure 6.15. The blue data points indicate the white noise levels extracted from the phase noise spectra and the green data points the white noise levels from the amplitude noise spectra. The error bars display the systematic error as described in section 6.3.5. The statistical error related to the numerical fitting of the noise spectra, however, is comparably small and, hence, it is neglected. With the exception of a few data points, the white phase noise S_ϕ^{W} and the white amplitude noise S_A^{W} are in good agreement within the errors for all µMUX channels. In those few cases, where S_ϕ^{W} and S_A^{W} are incompatible, most likely the systematic error introduced through the data processing is underestimated. For each µMUX channel, the expected white noise level has been calculated according to [Bar09]

$$S_{\mathrm{expected}}^{\mathrm{w}} = \frac{k_{\mathrm{B}} T_{\mathrm{N,system}}}{r^2 P_{\mathrm{rf}}} \tag{6.12}$$

where k_{B} is the Boltzmann constant and $T_{\mathrm{N,system}}$ stands for the noise temperature of the system, which has been calculated based on equation (4.3) for all relevant frequencies and for each configuration of the homodyne measurement set-up, i.e. for all settings of the variable attenuator. The system noise temperature ranges between 3.4 K and 4.5 K. The radius of the resonance circle $r = Q_{\mathrm{l}}/2Q_{\mathrm{c}}$ is calculated with the smoothed coupling quality factor Q_{c} and the smoothed loaded quality factor Q_{l} determined as in section 6.3.5. P_{rf} denotes the microwave power on the transmission line of the chip. The expected white noise level has been calculated and plotted in figure 6.15 as orange lines for $P_{\mathrm{rf}} = P_{\mathrm{rf}}^{\mathrm{sim}}$ and as red lines for $P_{\mathrm{rf}} = P_{\mathrm{rf}}^{\mathrm{fit}}$. The light orange and the light red bands around the curves display the estimated error of the respective expected white noise curves. The error has been obtained via standard error propagation. To compare the agreement of the measured white noise data with the modelled white noise under the assumption of $P_{\mathrm{rf}} = P_{\mathrm{rf}}^{\mathrm{sim}}$ or $P_{\mathrm{rf}} = P_{\mathrm{rf}}^{\mathrm{fit}}$, the mean absolute deviation is considered as figure of merit. Additionally, the average error of the mean absolute deviation is calculated for comparison. In table 6.5, the according results are reported. For the five µMUX channels ch01, ch05, ch06, ch13 and ch14 the mean absolute deviation for $P_{\mathrm{rf}} = P_{\mathrm{rf}}^{\mathrm{sim}}$ are within the average error, while only for the µMUX channel ch14, the mean absolute deviation for $P_{\mathrm{rf}} = P_{\mathrm{rf}}^{\mathrm{fit}}$ is within the average error. The fact, that the white noise model under the assumption $P_{\mathrm{rf}} = P_{\mathrm{rf}}^{\mathrm{fit}}$ does

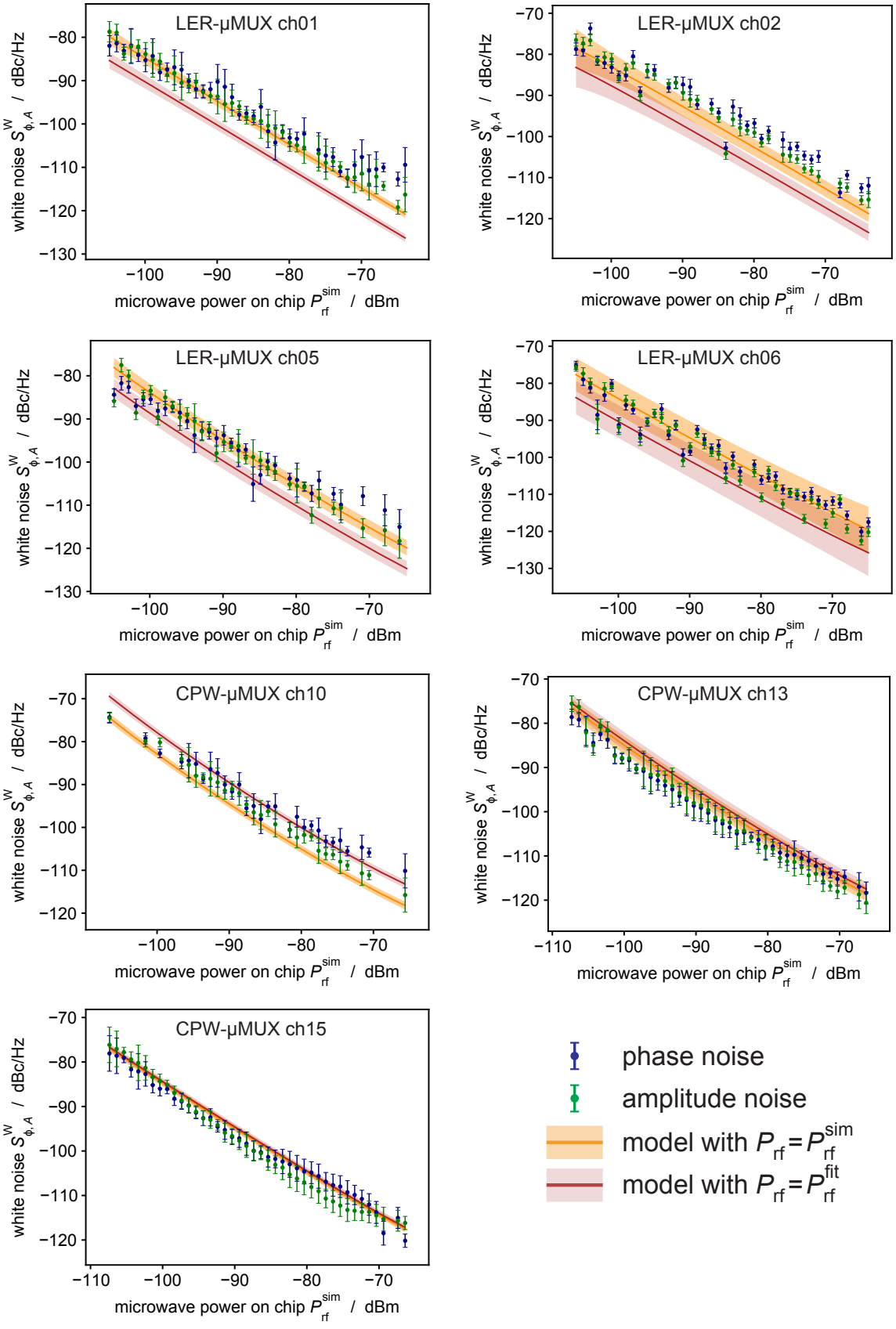

Figure 6.15: White phase noise S_ϕ^{W} and white amplitude noise S_A^{W} in dependence of the estimated microwave power on chip $P_{\mathrm{rf}}^{\mathrm{sim}}$.

not match the data very well is directly connected to the systematic issues with the experimental determination of the Tx attenuation of the cryogenic microwave read-out chain as described in section 6.2.3. Overall, for five out of the seven considered µMUX channels, the white noise model with $P_{\mathrm{rf}} = P_{\mathrm{rf}}^{\mathrm{sim}}$ describes the performance well, which demonstrates that the simulations of the Tx attenuation made during the design process of the cryogenic microwave read-out chain are mostly accurate within the systematic error of the noise measurement. Additionally, the good agreement of the measured data and the model for $P_{\mathrm{rf}} = P_{\mathrm{rf}}^{\mathrm{sim}}$ indicates that during the ECHo-100k phase of the ECHo experiment the cryogenic microwave read-out chain should perform as planned in terms of system noise temperature.

6.4.2 Apparent magnetic flux noise of the µMUX

One of the key quantities determining the energy resolution of an MMC detector read out by a µMUX channel is the signal-to-noise ratio, to which the µMUX contributes particularly at higher frequencies in terms of white noise. The apparent magnetic flux noise S_Φ, which references the noise of the whole read-out system to the rf SQUID, i.e. to the sensor registering a change in magnetic flux upon an event in the MMC, is therefore an important measure ultimately defining the noise performance of a µMUX set-up. Note that it is convention to specify the apparent magnetic flux noise in terms of $\sqrt{S_\Phi}$ in units of $\mu\Phi_0/\sqrt{\mathrm{Hz}}$ with the magnetic flux quantum Φ_0.

The measured phase noise and amplitude noise can be transformed into apparent magnetic flux noise using the transfer coefficient which is determined for each considered µMUX channel at each microwave power as discussed in section 6.3.4. Converting the measured white phase noise S_ϕ^{W} and white amplitude noise S_A^{W} presented in figure 6.15 into apparent white magnetic flux noise $\sqrt{S_{\Phi,\mathrm{W}}}$ yields the plots shown in figure 6.16. Additionally, the expected white magnetic flux noise curves based on the measured resonator and rf SQUID parameters are calculated with equation (3.67) for the LER-µMUX channels and with equation (3.71) for the CPW-µMUX channels. The expectation based on $P_{\mathrm{rf}} = P_{\mathrm{rf}}^{\mathrm{sim}}$ is plotted in orange and the expect-

µMUX channel:	ch01	ch02	ch05	ch06	ch10	ch13	ch14
mean deviation ($P_{\mathrm{rf}}^{\mathrm{sim}}$) / dB	2.1	3.5	1.8	2.3	3.6	2.1	1.5
mean deviation ($P_{\mathrm{rf}}^{\mathrm{fit}}$) / dB	7.3	7.6	4.6	5.7	2.2	3.0	1.7
average error / dB	±2.1	±2.1	±2.1	±3.6	±1.7	±2.2	±1.7

Table 6.5: Mean deviation of the measured white noise data from the model under the assumption of $P_{\mathrm{rf}} = P_{\mathrm{rf}}^{\mathrm{sim}}$ or $P_{\mathrm{rf}} = P_{\mathrm{rf}}^{\mathrm{fit}}$, and the average error of the mean absolute deviation.

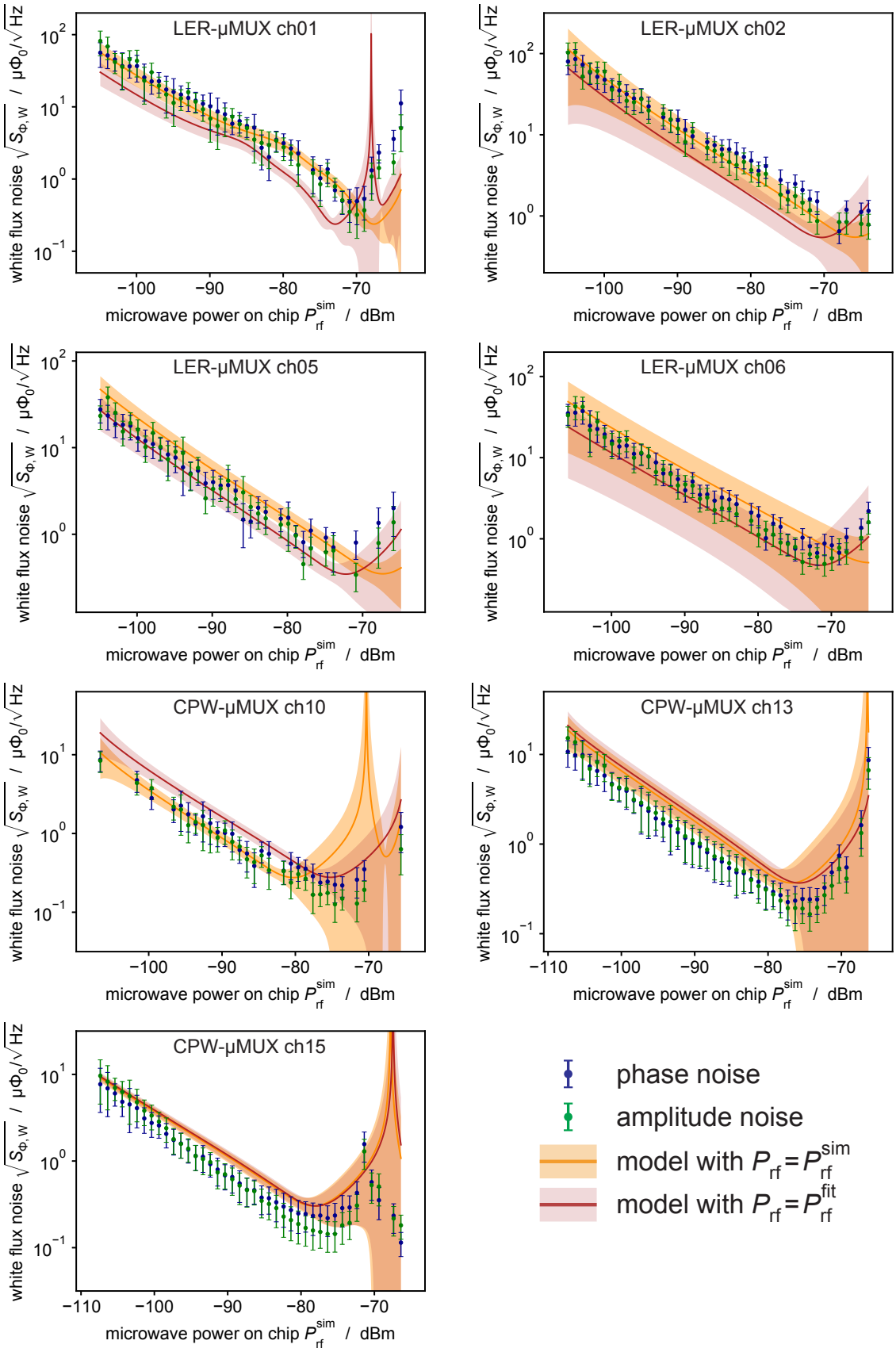

Figure 6.16: White flux noise $\sqrt{S_{\Phi,\mathrm{W}}}$ extracted from both the white phase and white amplitude noise in dependence of the estimated microwave power on chip $P_{\mathrm{rf}}^{\mathrm{sim}}$.

ation for $P_{\mathrm{rf}} = P_{\mathrm{rf}}^{\mathrm{fit}}$ in red. The errors for both the data and the expectation are derived by means of standard error propagation from the errors of the underlying quantities. For the data as well as for the expectation at low powers, the white noise level decreases with increasing microwave power which is due to the same behaviour of the underlying amplitude and phase noise. At larger microwave powers, the influence of the transfer coefficient starts to be significant. As the maximum frequency shift $\Delta f_{\mathrm{r}}^{\mathrm{max}}$ decreases for increasing microwave power as discussed in section 6.2.3, also the transfer coefficient decreases. This decrease of the transfer coefficient causes an increase of the apparent white magnetic flux noise, which from a certain point on overcomes the decrease of the underlying amplitude and phase noise, creating a local minimum of the white flux noise and, eventually, causing the white flux noise level to rise for higher microwave powers. When $\Delta f_{\mathrm{r}}^{\mathrm{max}} \to 0$ for microwave powers higher than at the noise minimum, the apparent white magnetic flux noise diverges, which can be observed in some of the depicted model curves. Comparing the position of the noise minima, it is apparent that the microwave power $P_{\mathrm{rf}}^{\mathrm{min,data}}$ at which a minimum occurs in the measured data does not for all µMUX channels coincide with the microwave power $P_{\mathrm{rf}}^{\mathrm{min,model}}$ at which the minimum occurs in the model curve. This reflects the fact, that true microwave power scale is known only with an uncertainty as shown in section 6.2.3 and observed in the previous section. It is important to note these uncertainties affect the modelled position of the microwave power $P_{\mathrm{rf}}^{\mathrm{min,model}}$, however, they do not change the apparent flux noise value of the minimum in the model.

For all considered µMUX channels, the minimal measured apparent white flux noise $\sqrt{S_{\Phi,\mathrm{W}}^{\mathrm{data,min}}}$ is extracted and plotted in figure 6.17a. The data is shown as a function of the resonance frequency f_{r} so that it groups by resonator geometry. For each µMUX channel, the minimal white flux noise value extracted from the phase noise (blue data points) is compatible within the error with the minimal white flux noise obtained from the amplitude noise (green data points). The average white flux noise is plotted for both resonator geometries and for both phase and amplitude based flux noise, respectively. As the resonator parameters are slightly different for different channels, also a slightly different noise performance is expected, and therefore, these average white flux noise performances are solely displayed to guide the eye. For the investigated µMUX chip *ECHo-MUX-04*, the white flux noise performance of CPW based µMUX channels is on average approximately three times better than the white flux noise performance of the LER-µMUX channels. As the LER-µMUX channels feature a lower intrinsic quality factor Q_{i} compared to the CPW-µMUX channels as discussed in section 6.2 and exhibit a smaller maximum frequency shift $\Delta f_{\mathrm{r}}^{\mathrm{max}}$, the observed difference in white flux noise performance is qualitatively not surprising. The white flux noise performance of the CPW-µMUX channels of $\sim 0.2\,\mu\Phi_0/\sqrt{\mathrm{Hz}}$ is competitive with the white flux noise performance of state-of-the-art dc SQUID

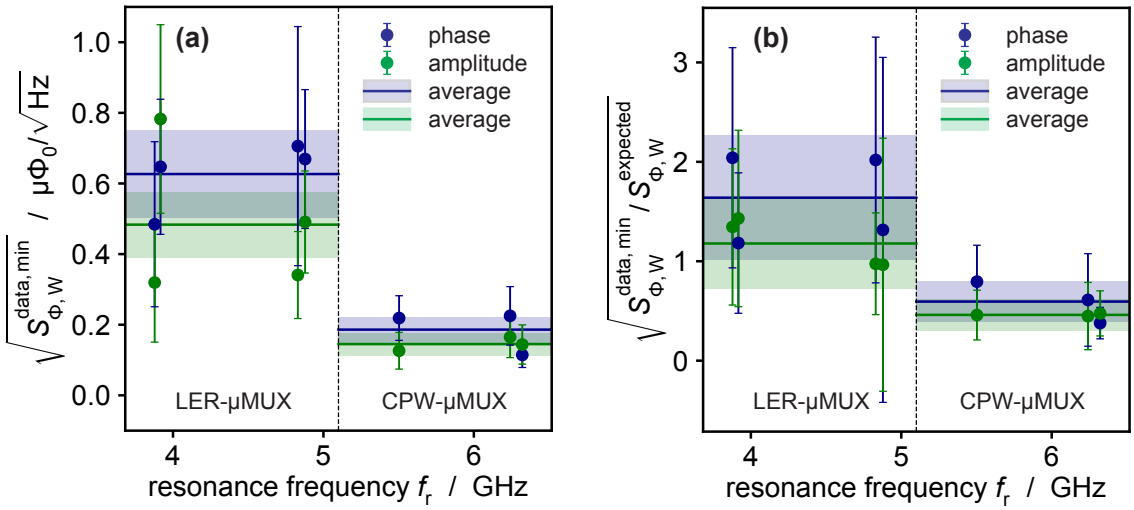

Figure 6.17: **(a)** The minimal measured white phase and white amplitude flux noise performances as a function of resonance frequency. **(b)** The ratio of the best measured noise performance and the corresponding expected value for all µMUX channels. For both figures, the average over all values for a given µMUX channel geometry is indicated as a solid line with error band in blue (phase noise) and green (amplitude noise).

based read-out systems for MMCs exhibiting $\sim 0.3\,\mu\Phi_0/\sqrt{\text{Hz}}$ [Man21b].

In order to analyse the noise performance further, the ratio of the measured apparent white flux noise $\sqrt{S_{\Phi,\text{W}}^{\text{data,min}}}$ and the expected apparent white flux noise $\sqrt{S_{\Phi,\text{W}}^{\text{expected}}}$ for each considered µMUX channel is plotted in figure 6.17b, where $\sqrt{S_{\Phi,\text{W}}^{\text{expected}}}$ corresponds to the minimum flux noise of the respective model curves in figure 6.16. The averaged ratios per resonator geometry and per phase/amplitude noise are depicted as solid lines with surrounding error band and are reported in table 6.6. The ratios connected to the LER-µMUX channels are each compatible with 1 within their respective errors indicating a match of the measured white flux noise with the model prediction for LERs. For the CPW-µMUX channels, however, only two out of six individual ratios are compatible with 1 within their respective errors and also the averages are not compatible with 1 either. They rather group around ~ 0.5, meaning that the measured white noise performance is about two times better than theoretically expected. As the noise performance measurements of the LER-µMUX channels and the CPW-µMUX channels have been carried out automatised and identically, i.e. using exactly the same measurement hardware and exactly the same data processing software, it is highly unlikely that the observed difference between the measured CPW-noise performance and the expected noise performance is caused by the measurement set-up and procedure. If the measured data is assumed to be cor-

channels	noise	$\langle\sqrt{S_{\Phi,\mathrm{W}}^{\mathrm{data,min}}}\rangle$ / $\frac{\mu\Phi_0}{\sqrt{\mathrm{Hz}}}$	$\langle\sqrt{\frac{S_{\Phi,\mathrm{W}}^{\mathrm{data,min}}}{S_{\Phi,\mathrm{W}}^{\mathrm{expected}}}}\rangle$	$\langle\sqrt{S_{\Phi,\mathrm{W}}^{\mathrm{rescaled}}}\rangle$ / $\frac{\mu\Phi_0}{\sqrt{\mathrm{Hz}}}$
LER-µMUX	ϕ	0.63 ± 0.12	1.64 ± 0.63	0.29 ± 0.11
LER-µMUX	A	0.48 ± 0.09	1.18 ± 0.45	0.21 ± 0.08
CPW-µMUX	ϕ	0.19 ± 0.04	0.59 ± 0.20	0.20 ± 0.07
CPW-µMUX	A	0.15 ± 0.03	0.46 ± 0.16	0.15 ± 0.05

Table 6.6: Averaged amplitude (A) and phase (ϕ) noise performance for both resonator geometries. The averages are taken from figures 6.17a, 6.17b and 6.18.

rect, following from equation (3.67) either the simulated system noise temperature $T_{\mathrm{N,system}}$ is overestimated by a factor 4, or due to some unconsidered physical effects the true theoretically predicted transfer coefficient has to be larger than calculated by means of equation (3.66) by a factor 2. As the system noise temperature has been simulated for the LER-µMUX channels and the CPW-µMUX channels in the same way and does not depend on the resonator geometry but solely on the frequency-dependent attenuation or gain of the rf components in the read-out chain and their respective noise temperature, a deviation by a factor 4 seems implausible, in particular as the system noise temperature would have to be smaller than the noise temperature of the HEMT amplifier in that case. Additionally, the results of the phase noise and amplitude noise measurements in the previous section exclude such a large deviation. Therefore, the most likely scenario is an underestimation of the transfer coefficient by a factor of 2. The transfer coefficient, given by equation (3.62), is comprised of three contributions out of which two are taking into account the resonator geometry and are therefore different for the CPW-µMUX channels compared to the LER-µMUX channels: the voltage $V_{\mathrm{rf}}(\Phi_{\mathrm{rf}})$ on the transmission line expressed in terms of rf magnetic flux Φ_{rf} in the rf SQUID, and the change of the resonance frequency upon a change in external magnetic flux $\partial f_{\mathrm{r}}/\partial\Phi_{\mathrm{ext}}$. As the model for the resonance frequency $f_{\mathrm{r}}(\Phi_{\mathrm{ext}}, \Phi_{\mathrm{rf}})$ has been successfully tested in section 6.2, the most likely source of the observed deviation is $V_{\mathrm{rf}}(\Phi_{\mathrm{rf}})$. However, no flaws in the derivation and no unconsidered physical effects accounting for a factor 2 could be identified. Therefore, up to this point, there is no explanation found for the mismatch between the measured white flux noise of the CPW-µMUX channels and the corresponding model based expectation and, hence, further investigation is required in the future. In order to be able to compare the measured flux noise performance of LER-µMUX channels and CPW-µMUX channels despite their different resonator and rf SQUID parameters, the measured minimal flux noise values are referenced to the ones of an ideal channel by rescaling. For this, the rescaled flux performance $S_{\Phi,\mathrm{W}}^{\mathrm{rescaled}} = S_{\Phi,\mathrm{W}}^{\mathrm{data,min}}/S_{\Phi,\mathrm{W}}^{\mathrm{expected}} \cdot S_{\Phi,\mathrm{W}}^{\mathrm{optimal}}$ is defined, where $S_{\Phi,\mathrm{W}}^{\mathrm{data,min}}$ is the minimum measured white magnetic flux noise and $S_{\Phi,\mathrm{W}}^{\mathrm{expected}}$ is the minimum white magnetic flux

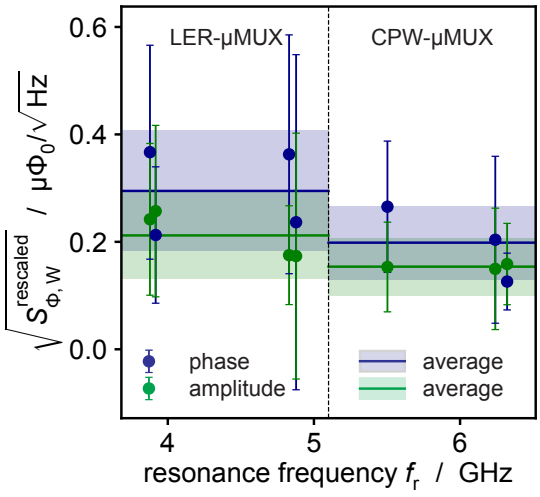

Figure 6.18: Rescaled white flux noise performance for all measured µMUX channels. The values extracted from the phase (amplitude) noise are plotted in blue (green). The average over the values is taken by µMUX channel geometry and is depicted as a solid line with error band.

noise expected from the model as described above. The optimal minimum white magnetic flux noise $S^{\text{optimal}}_{\Phi,\text{W}}$ is calculated with the theoretical model just as $S^{\text{expected}}_{\Phi,\text{W}}$, however, for both LER- and CPW-µMUX channels an ideal resonator with intrinsic quality factor $Q_\text{i} \to \infty$, i.e. $r = 1/2$ and matched bandwidth $\Delta f = 1\,\text{MHz}$ and maximum frequency shift, i.e. $\eta_0 = 1$ is assumed. The resonance frequency is set to $f_\text{r} = 6\,\text{GHz}$ reflecting the centre of the available frequency band in the cryogenic microwave read-out chain. For the rf SQUID a feasible inductance of $L_\text{S} = 45\,\text{nH}$ and a hysteresis parameter $\beta_\text{L} = 0.6$ are assumed. The system noise temperature $T_{\text{N,system}} = 4\,\text{K}$ is a typical value for the designed cryogenic microwave read-out chain. Note that the rescaling is insensitive to the influence of potentially missing numeric factors in the theoretical models, as the underlying models enter the calculation of both $S^{\text{expected}}_{\Phi,\text{W}}$ and $S^{\text{optimal}}_{\Phi,\text{W}}$. The rescaled results are plotted in figure 6.18 using the same colour code as in figure 6.17. The averages are depicted as solid lines with error bands and are reported in table 6.6. After rescaling the noise performance of all µMUX channels, it turns out that the potential noise performance of both the LER- and CPW-µMUX channels are almost identical within the error, i.e. $\sim 0.2\,\mu\Phi_0/\sqrt{\text{Hz}}$. For the flux-ramp modulated read-out of the µMUX during ECHo-100k, a minor degradation of the white noise performance compared to the values found in the scope of this thesis is expected [Mat12, Ric21], but in any case the potential noise performance of the µMUX for ECHo-100k is comparable to that of state-of-the-art dc SQUID-based read-out systems for MMCs with $\sim 0.3\,\mu\Phi_0/\sqrt{\text{Hz}}$ [Man21b].

6.4.3 Final remarks

The results of above analysis indicate that for an LER-based µMUX and a CPW-based µMUX, which exhibit an optimal set of resonator and SQUID parameters, the

noise performance is potentially identical within the analysis error and comparable to the noise performance of dc SQUID-based read-out systems for MMCs. The investigated CPW-µMUX channels with non-optimal parameters exhibit already an almost optimal noise performance, whereas the noise performance of the investigated LER-µMUX channels with non-optimal parameters still leaves room for improvement. As the radius of the resonance circle r and the matching parameter η_0 for all investigated LER-µMUX channels are significantly below the intended values, and as the white noise scales as $S_\Phi \propto (r\eta_0)^{-1}$, the noise performance of the LER-µMUX can be improved by tuning these two parameters. For this, it is essential to improve the intrinsic quality factor Q_i of the LERs, as r reaches its maximum value of $1/2$ for $Q_\mathrm{i} \to \infty$. Additionally, the design of the µMUX in terms of couplings should be adjusted in order to reach the target of $\eta = 1$ for the target bandwidth of $\Delta f = 1\,\mathrm{MHz}$. Currently, the coupling of the rf SQUIDs is suspected to limit Q_i of the LER-µMUX, as observed already in [Pal19, Ihs21], however, the exact mechanism is not understood yet. Possibly, the interruption of the ground plane for the connection of the LER to the rf SQUID allows for the formation of unwanted modes, which could potentially lead to radiative losses, and hence, future research should be focused on this effect.

If in the near future the LER-µMUX design can be optimised in terms of Q_i, and thereby in terms of noise performance, the decision on a microwave resonator geometry for the µMUX of the ECHo-100k phase of the ECHo experiment can be made considering solely aspects like the resonator size and the feasibility of a post-production resonance frequency adjustment. In this case, the preferred microwave resonator geometry would be the LER design due to is compactness and the comparably easy post-production resonance frequency adjustment.

If, however, in the near future such an optimisation of the LER design is not feasible, the CPW-µMUX could be a valid alternative. Although the resonator size is not as compact as the size of an LER, by now a resonance frequency fine-tuning technique has been developed (chapter 5), and the measured white noise performance of the CPW-µMUX is excellent and, in contrast to the theoretical expectation, it is not worse than the white noise performance of an optimised LER-µMUX.

7. Conclusion and outlook

The absolute neutrino mass scale is one of the most stringent open questions in particle physics. The ECHo experiment ultimately aims to reach a sub-eV sensitivity on the effective electron neutrino mass by analysing the shape of the end-point region of the ^{163}Ho electron capture spectrum being affected by the non-zero neutrino mass. In order to reach this ambitious goal, large arrays of magnetic microcalorimeters loaded with ^{163}Ho are planned to be operated in parallel to ultimately acquire a high-statistics calorimetric ^{163}Ho electron capture spectrum. A high energy-resolution and a fast detector response time are required, in order to allow for a precise reconstruction of the end-point region of the spectrum and a reduction of the unresolved pile-up fraction, respectively. Thus, the noise added by the read-out system should be kept as low as possible to preserve the energy resolution of the detectors, and the available bandwidth should be carefully tuned to avoid slowing down the rise time of the detector signals. For the current phase of the experiment, ECHo-100k, about 10^5 magnetic microcalorimeter pixels, each implanted with a ^{163}Ho activity of about 10 Bq, are planned to be simultaneously operated. As scaling up the commonly used dc SQUID-based single-channel read-out systems for MMCs would lead to an intolerable power dissipation in close vicinity to the detectors, and increase the system complexity dramatically, a multiplexed read-out approach is required. Different multiplexing approaches have been demonstrated for the read-out of cryogenic detectors, namely time-division, code-division and frequency-division multiplexing. Considering the above summarised requirements for the ECHo-100k experiment in terms of number of detectors to be read out simultaneously, and in terms of single detector performance, a multiplexing system with a high multiplexing factor, a high bandwidth per detector channel, a low power dissipation in the vicinity of the detectors and a low noise contribution is necessary. Among the available options, only the frequency-division multiplexing approach of microwave SQUID multiplexing proved to be suitable for ECHo-100k.

The development of a dedicated microwave SQUID multiplexer for the ECHo experiment is currently ongoing and it represents the framework of this thesis. In particular, the work presented here is focused on two fundamental aspects related to the development of a read-out for the current phase of the ECHo experiment, namely the design and realisation of a cryogenic microwave read-out system and the investigation of the optimal resonator geometry for the microwave SQUID multiplexer, meeting the strict requirements set by the ECHo experiment.

The dedicated cryogenic microwave read-out system must match all boundary condi-

tions set by the ECHo-100k phase, in terms of noise performance, microwave power levels and heat dissipation onto the cryogenic platform. Moreover, the intermodulation products should be minimised and mechanical and budget constraints must be taken into account. For this reason, a dedicated simulation framework has been set up and exploited to compare more than a million different system configurations. Subsequently, the optimal layout for the cryogenic microwave read-out chain, fulfilling all the above mentioned boundary conditions, while featuring the lowest possible system noise, has been selected. A mechanical design for the cryogenic microwave read-out chain has been developed and a demonstration system has been set up. The demonstration system has been exploited to experimentally show that the performance of the read-out chain matches the target. In particular, a system noise temperature of $\sim 4\,\mathrm{K}$ could be demonstrated, which allows for a white magnetic flux noise of $\sim 0.2\mu\Phi_0/\sqrt{\mathrm{Hz}}$ for an optimised microwave SQUID multiplexer, i.e. a white noise performance which is competitive with the white noise performance of state-of-the-art dc SQUID-based read-out systems for magnetic microcalorimeters [Kem15, Man21b]. The measured intermodulation distortion of the demonstration system would translate into a pseudo-noise floor, which for 400 read-out tones would correspond to a pseudo-noise temperature of $\sim 7\,\mathrm{mK}$. Hence, the additional pseudo-noise caused by the intermodulation distortion is negligible.

The second part of this work is devoted to the investigation of the most suited superconducting microwave resonator geometry for the microwave SQUID multiplexer (µMUX) for ECHo-100k. Two different planar resonator geometries have been compared, namely the well-established quarter-wave resonators based on coplanar waveguides (CPWs) and the more compact lumped element resonators (LERs), whose integration into the µMUX is still under development. In order to determine the best resonator layout, multiple aspects must be examined, starting from geometrical considerations, such as the size of the resonator, which defines the packing efficiency on chip. Secondly, the crosstalk level due to the Lorentzian tails of the resonance curves [Mat19] has to be kept at a minimum, while making the most efficient use of the available system bandwidth. Therefore, an equidistant frequency spacing between neighbouring resonances plays a crucial role, and thus, strategies to achieve this goal for the different resonator geometries should be pondered on. Finally, the noise performance in terms of white magnetic flux noise level should be precisely evaluated, as it has a direct impact on the detector energy resolution and thus, on the final sensitivity of the experiment.

The size of a CPW-based quarter-wave resonator is constraint by its resonance frequency, while the size of an LER depends ultimately on the structure size achievable with standard photolithographic methods. For the µMUX fir ECHo-100k, the area required by one CPW-based quarter-wave resonator is typically in the order of five

times larger than the area required by one LER. Taking into account, the transmission line and the rf SQUIDs on the µMUX chip, whose size is obviously independent from the resonator geometry, the size of an LER-based µMUX chip is about half the size of a CPW resonator-based µMUX chip. Therefore, an LER-based µMUX design would allow for a two times higher fabrication performance.

The equidistant resonance frequency spacing cannot be achieved relying solely on the resonator design, since microfabrication tolerances inevitably limit the precision of the resulting resonance frequencies, potentially causing shifts or even swaps of the resonance frequencies. For this reason, an additional resonance frequency fine-tuning step must be carried out to guarantee the desired resonance frequency spacing. A tile-and-trim procedure for the resonance frequency fine-tuning has already been demonstrated for LERs [Liu17b, McK19, Pal19] and even for an LER-based µMUX [Obe20, Nei21], but it cannot be adapted straightforwardly to the case of CPWs. Thus, a new tile-and-trim technique to fine-tune inductively terminated CPW resonators has been developed in this work. For that, a theory framework has been derived and the practical application of the fine-tuning has been successfully demonstrated for the first time. By means of this method, the accuracy of the resonance frequency placing for CPW-based quarter-wave resonators could be improved by more than a factor of five, which is competitive with the tile-and-trim technique for LERs [Pal19]. Based on this demonstration, the newly developed tile-and-trim technique has also been adopted for the resonance frequency fine-tuning of a µMUX based on CPW resonators [Nei21]. Therefore, by now, resonance frequency fine-tuning techniques for microwave SQUID multiplexers based on both CPW resonators and on LERs are available.

Finally, the noise performance of the two resonator geometries under investigation has been studied and compared. As the final microwave SQUID multiplexer will be read out employing a flux-ramp modulation scheme for the linearisation of the µMUX response, the white noise component of the magnetic flux noise of the µMUX will be dominant for the achievable energy resolution [Mat12]. According to the expectations based on theory, a µMUX based on LERs should be characterised by a lower white magnetic flux noise than a µMUX based on CPW resonators. The difference weakly depends on the resonance frequency, but in first approximation is expected to be about a factor of two. In order to compare the noise performance of the two geometries, a dedicated µMUX chip including channels based on both LERs and CPW resonators has been designed, fabricated and operated at cryogenic temperature. For the LER-based µMUX channels, a white magnetic flux noise level of $\sim 0.6\,\mu\Phi_0\sqrt{\mathrm{Hz}}$ was measured, which is compatible with the theoretical expectation, based on the measured µMUX parameters. The flux noise level for an LER-based µMUX with optimal resonator and rf SQUID parameters is, however, $\sim 0.2\,\mu\Phi_0\sqrt{\mathrm{Hz}}$.

The main reason, why this optimal performance was not reached in the framework of this thesis, are the low intrinsic quality factors of the fabricated LERs and hence, for an LER design with improved intrinsic quality factor, the optimal noise performance is within reach. For the CPW resonator-based µMUX channels, a white magnetic flux noise level of $\sim 0.2\,\mu\Phi_0\sqrt{\text{Hz}}$ has been measured, which is about two times better than expected from theory. As the CPW resonators and the LERs under investigation are located on the same chip, and as the experimental method for the determination of the white noise is identical for both resonator geometries, it is highly unlikely that this observation is caused by the measurement set-up and procedure. On the other hand, no flaw in the theoretical description of the white magnetic flux noise for the CPW-resonator based µMUX could be found, for which reason the cause of this mismatch is still under investigation. The measured white noise performance of the CPW-based µMUX channels is comparable to the optimal noise performance of LER-based µMUX channels.

As a conclusion, both considered resonator geometries, LERs and CPWs, are suitable for the microwave SQUID multiplexer for ECHo-100k. From the fabrication point of view, LERs offer a more compact layout, which would enhance the packing efficiency, and thus, the fabrication performance. Due to their potential white noise performance of $\sim 0.2\,\mu\Phi_0\sqrt{\text{Hz}}$ and their well-established resonance frequency fine-tuning technique, they would be the optimal choice for the µMUX for ECHo-100k. However, at the moment the noise performance of LERs is substantially limited by low intrinsic quality factors. If this issue cannot be solved in the near future, a CPW-based µMUX, at the expense of a lower packing density, could represent a valid alternative with a demonstrated white magnetic flux noise level comparable with state-of-the-art dc-SQUID read-out systems [Kem15, Man21b] and a newly established resonance frequency fine-tuning technique.

Once the final choice for the resonator geometry is taken, the microfabrication of the µMUX wafers for ECHo-100k can start, meaning the production of around 400 µMUX chips covering the frequency range from 4 GHz to 8 GHz for 15 distinct microwave read-out chains. The cryogenic part of the microwave read-out chains is being set up at the moment, and the software defined radio (SDR) system is currently being finalised [San19, Kar20]. Therefore, in the near future the entire microwave SQUID multiplexing read-out for ECHo-100k will be fully assembled and operational.

A. Appendix

A.1 Modulation function and expansion coefficients of the revised µMUX model

In the revised µMUX model [Weg21] a Taylor expansion of the current I_S running in the rf SQUID yields an analytic approximate expression describing the inductance modulation and thereby the resonance frequency modulation of a µMUX channel upon a change in normalised rf magnetic flux φ_rf or normalised external magnetic flux φ_ext. The associated modulation function following from the expansions is given by

$$D_\mathrm{revised}(\varphi_\mathrm{ext}, \varphi_\mathrm{rf}) = \frac{2\beta_\mathrm{L}}{\varphi_\mathrm{rf}} \sum_{i,j} p_{i,j}(\varphi_\mathrm{ext}, \varphi_\mathrm{rf}) \tag{A.1}$$

with summands

$$p_{i,j}(\varphi_\mathrm{ext}, \varphi_\mathrm{rf}) = a_{i,j} \beta_\mathrm{L}^{b_{i,j}} \cos\big(c_{i,j}\varphi_\mathrm{ext}\big) J_1(c_{i,j}\varphi_\mathrm{rf}) \tag{A.2}$$

where i indicates the order of the Taylor expansion and j addresses different contributions within one expansion order [Weg21]. $J_1(x)$ denotes the first Bessel function of first kind. The coefficients $a_{i,j}$, $b_{i,j}$ and $c_{i,j}$ are listed in table A.1. The first derivative of the modulation function with respect to the normalised external magnetic flux reads

$$\frac{\partial D_\mathrm{revised}(\varphi_\mathrm{ext}, \varphi_\mathrm{rf})}{\partial \varphi_\mathrm{ext}} = \frac{2\beta_\mathrm{L}}{\varphi_\mathrm{rf}} \sum_{i,j} \frac{\partial p_{i,j}(\varphi_\mathrm{ext}, \varphi_\mathrm{rf})}{\partial \varphi_\mathrm{ext}} = \frac{2\beta_\mathrm{L}}{\varphi_\mathrm{rf}} \sum_{i,j} p'_{i,j}(\varphi_\mathrm{ext}, \varphi_\mathrm{rf}) \tag{A.3}$$

with summands

$$p'_{i,j}(\varphi_\mathrm{ext}, \varphi_\mathrm{rf}) = -a_{i,j} c_{i,j} \beta_\mathrm{L}^{b_{i,j}} \sin\big(c_{i,j}\varphi_\mathrm{ext}\big) J_1(c_{i,j}\varphi_\mathrm{rf}). \tag{A.4}$$

The first derivative of the modulation function with respect to the normalised rf magnetic flux is given by

	$a_{i,j}$	$b_{i,j}$	$c_{i,j}$
$p_{0,0}$	$+1$	0	1
$p_{1,0}$	$-1/2$	1	2
$p_{2,0}$	$-1/8$	2	1
$p_{2,1}$	$+3/8$	2	3
$p_{3,0}$	$+1/8$	3	2
$p_{3,1}$	$-5/16$	3	4
$p_{4,0}$	$+1/16$	4	1
$p_{4,1}$	$-5/32$	4	3
$p_{4,2}$	$+9/32$	4	5
$p_{5,0}$	$-5/64$	5	2
$p_{5,1}$	$+3/16$	5	4
$p_{5,2}$	$-17/64$	5	6
$p_{6,0}$	$-15/512$	6	1
$p_{6,1}$	$+57/512$	6	3
$p_{6,2}$	$-115/512$	6	5
$p_{6,3}$	$-133/512$	6	7
$p_{7,0}$	$+24/512$	7	2
$p_{7,1}$	$-77/512$	7	4
$p_{7,2}$	$+137/512$	7	6
$p_{7,3}$	$-267/1024$	7	8
$p_{8,0}$	$+21/1024$	8	1
$p_{8,1}$	$-35/512$	8	3
$p_{8,2}$	$+103/512$	8	5
$p_{8,3}$	$-651/2048$	8	7
$p_{8,4}$	$+547/2048$	8	9
$p_{9,0}$	$-63/2048$	9	2
$p_{9,1}$	$+27/256$	9	4
$p_{9,2}$	$-1089/4096$	9	6
$p_{9,3}$	$+193/512$	9	8
$p_{9,4}$	$-1139/4096$	9	10
$p_{10,0}$	$-105/8192$	10	1
$p_{10,1}$	$+435/8192$	10	3
$p_{10,2}$	$-2595/16384$	10	5
$p_{10,3}$	$+5705/16384$	10	7
$p_{10,4}$	$-7317/16384$	10	9
$p_{10,5}$	$-4807/16384$	10	11

Table A.1: The expansion coefficients of the revised µMUX model [Weg21]

$$\frac{\partial D_{\text{revised}}(\varphi_{\text{ext}},\varphi_{\text{rf}})}{\partial\varphi_{\text{rf}}} = \frac{2\beta_{\text{L}}}{\varphi_{\text{rf}}}\sum_{i,j}\left(\frac{\partial p_{i,j}(\varphi_{\text{ext}},\varphi_{\text{rf}})}{\partial\varphi_{\text{rf}}} - \frac{p_{i,j}}{\varphi_{\text{rf}}}\right) = \frac{2\beta_{\text{L}}}{\varphi_{\text{rf}}}\sum_{i,j}\tilde{p}_{i,j}(\varphi_{\text{ext}},\varphi_{\text{rf}}) \tag{A.5}$$

with summands

$$\tilde{p}_{i,j}(\varphi_{\text{ext}},\varphi_{\text{rf}}) = a_{i,j}c_{i,j}\beta_{\text{L}}^{b_{i,j}}\cos\big(c_{i,j}\varphi_{\text{ext}}\big)\left[c_{i,j}J_0(c_{i,j}\varphi_{\text{rf}}) - \frac{2J_1(c_{i,j}\varphi_{\text{rf}})}{\varphi_{\text{rf}}}\right] \tag{A.6}$$

where the relation $\partial J_1(x)/\partial x = J_0(x) - J_1(x)/x$ relating the derivative of the first Bessel function of first kind to the zeroth Bessel function of first kind $J_0(x)$, has been used.

Bibliography

[All17] S. Allgeier, Entwicklung einer modularen 36-Kanal-Auslesekette mit rauscharmen SQUID-basierten Vorverstärkern für die 4k-Pixel-Molekülkamera MOCCA, Master's thesis, Kirchhoff-Institut für Physik, Universität Heidelberg, 2017.

[And63] P. Anderson and J. Rowell, Probable Observation of the Josephson Superconducting Tunneling Effect, *Phys. Rev. Lett.*, **10**, 230–232, 1963.

[And72] P. W. Anderson, B. I. Halperin, and C. M. Varma, Anomalous low temperature thermal properties of glasses and spin glasses, *Philos. Mag.*, **25**(1), 1–9, 1972.

[Aru19] F. Arute, K. Arya, and R. Babbush *et al.*, Quantum supremacy using a programmable superconducting processor, *Nature*, **574**, 505–510, 2019.

[Ban12] S. R. Bandler, K. D. Irwin, D. Kelly, P. N. Nagler, J.-P. Porst, H. Rotzinger, J. E. Sadleir, G. M. Seidel, S. J. Smith, and T. R. Stevenson, Magnetically coupled microcalorimeters, *Journal of Low Temperature Physics*, **167**(3), 254–268, 2012.

[Bar48] J. Bardeen and W. H. Brattain, The Transistor, A Semi-Conductor Triode, *Phys. Rev.*, **74**, 230, 1948.

[Bar09] R. Barends, Photon-detecting superconducting resonators, PhD Thesis, Technische Universiteit Delft, 2009.

[Bey09] J. Beyer, D. Drung, M. Peters, T. Schurig, and S. R. Bandler, A single-stage SQUID multiplexer for TES array readout, *IEEE Trans. Appl. Supercond.*, **19**(3), 505—-508, 2009.

[Cas17] D. Castelvecchi, Quantum computers ready to leap out of the lab in 2017, *Nature*, **541**, 9–10, 2017.

[Cla04] J. Clarke and A. I. Braginski (Ed.), The SQUID Handbook, WILEY-VCH, 2004.

[Coa19] Coax Co. Japan, thermal conductivity extracted from data provided by private communication, 2019.

[Col92] R. E. Collin, Foundations of Microwave Engineering, McGraw-Hill, New York, 1992.

[Day03] P. K. Day, H. G. LeDuc, B. A. Mazin, A. Vayonakis, and J. Zmuidzinas, A broadband superconducting detector suitable for use in large arrays, *Nature*, **425**, 817—821, 2003.

[DR82] A. De Rújula and M. Lusignoli, Calorimetric measurements of Holmium-163 decay as tools to determine the electron neutrino mass, *Phys. Lett. B*, **118**, 429–434, 1982.

[Dru07] D. Drung, C. Abmann, J. Beyer, A. Kirste, M. Peters, F. Ruede, and T. Schurig, Highly Sensitive and Easy-to-Use SQUID Sensors, *IEEE Transactions on Applied Superconductivity*, **17**, 699–704, 2007.

[DV10] P. De Visser, S. Withington, and D. J. Goldie, Readout-power heating and hysteretic switching between thermal quasiparticle states in kinetic inductance detectors, *J. Appl. Phys.*, **108**, 114504, 2010.

[Eli15] S. Eliseev, K. Blaum, M. Block, S. Chenmarev, H. Dorrer, C. E. Düllmann, C. Enss, P. Filianin, L. Gastaldo, M. Goncharov, U. Köster, F. Lautenschläger, Y. Novikov, A. Rischka, R. X. Schüssler, L. Schweikhard, and A. Türler, Direct Measurement of the Mass Difference of ^{163}Ho and ^{163}Dy Solves the Q-Value Puzzle for the Neutrino Mass Determination, *Phys. Rev. Lett.*, **115**, 1623—-1694, 2015.

[Esp21] M. Esposito, A. Ranadive, L. Planat, and N. Roch, Perspective on traveling wave microwave parametric amplifiers, *Appl. Phys. Lett.*, **119**, 120501, 2021.

[Fav20] M. Faverzani, E. Ferri, A. Giachero, A. Nucciotti, A. Puiu, and M. Sisti (Ed.), *J. Low Temp. Phys.*, **199**, Special Issue: Low Temperature Detectors LTD18, Part I & II, Springer Science+Business Media, 2020.

[Fey63] R. P. Feynman, The Schrödinger equation in a classical context: a seminar on superconductivity, in R. P. Feynman, R. B. Leighton, and M. Sands (Ed.), *The Feynman Lectures on Physics*, Volume 3, Addison-Wesley, 1963.

[Fla78] K. Flachbart, A. Feher, S. Jánoš, Z. Málek, and A. Ryska, Thermal Conductivity of Nb-Ti Alloy in the Low-Temperature Range, *phys. stat. sol. (b)*, **85**(3), 545, 1978.

[Fle05] A. Fleischmann, C. Enss, and G. Seidel, Metallic magnetic calorimeters, in C. Enss (Ed.), *Cryogenic Particle Detection, Topics in Applied Physics*, Volume 99, 151–216, Springer-Verlag, Berlin, Heidelberg, New York, 2005.

[Fle09] A. Fleischmann, L. Gastaldo, J. Porst, S. Kempf, A. Kirsch, A. Pabinger, C. Pies, P. Ranitzsch, S. Schäfer, F. Seggern, T. Wolf, C. Enss, and G. Seidel, Metallic magnetic calorimeters, *AIP Conf. Proc.*, **1185**, 2009.

[Fri44] H. T. Friis, Noise figures of radio receivers, *Proceedings of the IRE*, **32**(7), 419–422, 1944.

[Gam19] L. Gamer, Entwicklung und Charakterisierung des 4k-Pixel Detektorarrays MOCCA für die energie- und ortsaufgelöste Detektion neutraler Molekülfragmente, PhD Thesis, Kirchhoff-Institut für Physik, Universität Heidelberg, 2019.

[Gao08a] J. Gao, The Physics of Superconducting Microwave Resonators, PhD Thesis, California Institute of Technology, 2008.

[Gao08b] J. Gao, M. Daal, A. Vayonakis, S. Kumar, J. Zmuidzinas, B. Sadoulet, B. A. Mazin, P. K. Day, and H. G. Leduc, Experimental evidence for a surface distribution of two-level systems in superconducting lithographed microwave resonators, *Appl. Phys. Lett.*, **92**(15), 152505, 2008.

[Gao08c] J. Gao, J. Zmuidzinas, A. Vayonakis, P. K. Day, B. A. Mazin, and H. Leduc, Equivalence of the effects on the complex conductivity of superconductor due to temperature change and external pair breaking, *J. Low. Temp. Phys.*, **151**, 557–563, 2008.

[Gas13] L. Gastaldo, P. Ranitzsch, F. von Seggern, J.-P. Porst, S. Schäfer, C. Pies, S. Kempf, T. Wolf, A. Fleischmann, C. Enss, A. Herlert, and K. Johnston, Characterization of low temperature metallic magnetic calorimeters having gold absorbers with implanted ^{163}Ho ions Determination, *Nucl. Inst. Meth. A*, **711**, 2013.

[Gas17] L. Gastaldo and the ECHo Collaboration, The electron capture in ^{163}Ho experiment - ECHo, *Eur. Phys. J. Special Topics*, **226**, 1623—-1694, 2017.

[GG04] Q. García-García, Noise in lossless microwave multiports, *Int. J. RF Microw. Comput.-Aided Eng.*, **14**(2), 99–110, 2004.

[Giu12] A. Giuliani and A. Poves, Neutrinoless double-beta decay, *Advances in High Energy Physics*, **2012**, 2012.

[Glo57] R. E. Glover and M. Tinkham, Conductivity of Superconducting Films for Photon Energies between 0.3 and $40kT_c$, *Phys. Rev.*, **108**(2), 243, 1957.

[Gri22] M. Griedel, F. Mantegazzini, A. Barth, E. Bruer, W. Holzmann, R. Hammann, D. Hengstler, N. Kovac, C. Velte, T. Wickenhäuser, F. Fleischmann, C. Enss, L. Gastaldo, H. Dorrer, T. Kieck, N. Kneip, C. E. Düllmann, and K. Wendt, From ECHo-1k to ECHo-100k: Optimization of High-Resolution Metallic Magnetic Calorimeters with Embedded ^{163}Ho for Neutrino Mass Determination, *J.Low Temp. Phys.*, 2022.

[Hen18] S. W. Henderson, Z. Ahmed, J. Austermann, D. Becker, D. A. Bennett, D. Brown, S. Chaudhuri, H.-M. S. Cho, J. M. D'Ewart, B. Dober, S. M. Duff, J. E. Dusatko, S. Fatigoni, J. C. Frisch, J. D. Gard, M. Halpern, G. C. Hilton, J. Hubmayr, K. D. Irwin, E. D. Karpel, et al., Highly-multiplexed microwave SQUID readout using the SLAC Microresonator Radio Frequency (SMuRF) electronics for future CMB and sub-millimeter surveys, in J. Zmuidzinas and J.-R. Gao (Ed.), *Millimeter, Submillimeter, and Far-Infrared Detectors and Instrumentation for Astronomy IX*, Volume 10708, 170 – 185, International Society for Optics and Photonics, SPIE, 2018.

[Her17] A. Hertel, Optimierung kapazitiv gekoppelter supraleitender $\lambda/4$-Resonatoren für den Einsatz in einem Mikrowellen-SQUID-Multiplexer, Master's thesis, Kirchhoff-Institut für Physik, Universität Heidelberg, 2017.

[Ho78] C. Y. Ho, M. W. Ackermann, K. Y. Wu, S. G. Oh, and T. N. Havill, Thermal conductivity of ten selected binary alloy systems, *J. Phys. Chem. Ref. Data*, **7**(3), 959–1177, 1978.

[Igr04] R. Igreja and C. Dias, Analytical evaluation of the interdigital electrodes capacitance for a multi-layered structure, *Sensors and Actuators A: Physical*, **112**(2), 291–301, 2004.

[Ihs21] S. Ihssen, Messung des magnetischen Flussrauschens von Mikrowellen-SQUID-Multiplexern in Abhängigkeit von der eingesetzten Resonatortechnologie, Master's thesis, Kirchhoff-Institut für Physik, Universität Heidelberg, 2021.

[Irw04] K. D. Irwin and K. W. Lehnert, Microwave SQUID multiplexer, *Appl. Phy. Lett.*, **85**(11), 2107–2109, 2004.

[Irw10] K. D. Irwin, M. D. Niemack, J. Beyer, H. M. Cho, W. B. Doriese, G. C. Hilton, C. D. Reintsema, D. R. Schmidt, J. N. Ullom, and L. R. Vale, Code-division multiplexing of superconducting transition-edge sensor arrays, *Supercond. Sci. Technol.*, **23**(3), 034004, 2010.

[Jak64] R. C. Jaklevic, A. H. Lambe, J. Silver, and J. E. Mercereau, Quantum interference effects in josephson tunneling, *Phys. Rev. Lett.*, **12**(7), 159–160, 1964.

[Jos62] B. D. Josephson, Possible new effects in superconductive tunnelling, *Phys. Lett.*, **1**, 251–253, 1962.

[Jos64] B. D. Josephson, Coupled superconductors, *Reviews of Modern Physics*, **36**(1), 216, 1964.

[Kar20] N. Karcher, D. Richter, F. Ahrens, R. Gartmann, M. Wegner, O. Krömer, S. Kempf, C. Enss, M. Weber, and O. Sander, SDR-based readout electronics for the ECHo experiment, *Journal of Low Temperature Physics*, **200**(5), 261–268, 2020.

[Kau78] R. L. Kautz, Picosecond pulses on superconducting striplines, *Journal of Applied Physics*, **49**(1), 308–314, 1978.

[Kem12] S. Kempf, Entwicklung eines Mikrowellen-SQUID-Multiplexers auf der Grundlage nicht-hysteretischer rf-SQUIDs zur Auslesung metallischer magnetischer Kalorimeter, Phd thesis, Kirchhoff-Institut für Physik, Universität Heidelberg, 2012.

[Kem15] S. Kempf, A. Ferring, A. Fleischmann, and C. Enss, Direct-current superconducting quantum interference devices for the readout of metallic magnetic calorimeters, *Supercond. Sci. Technol.*, **28**, 045008, 2015.

[Kem18] S. Kempf, A. Fleischmann, L. Gastaldo, and C. Enss, Physics and applications of metallic magnetic calorimeters, *J. Low Temp. Phys.*, **193**, 2018.

[Kra20] M. Krantz, Development of a metallic magnetic calorimeter with integrated SQUID readout, PhD Thesis, Kirchhoff-Institut für Physik, Universität Heidelberg, 2020.

[Leh07] K. W. Lehnert, K. D. Irwin, M. A. Castellanos-Beltran, J. A. B. Mates, and L. R. Vale, Evaluation of a microwave SQUID multiplexer prototype, *IEEE transactions on applied superconductivity*, **17**(2), 705–709, 2007.

[Lik91] K. K. Likharev and V. K. Semenov, RSFQ logic/memory family: a new Josephson-junction technology for sub-terahertz-clock-frequency digital systems, *IEEE Trans. Appl. Supercond.*, **1**, 1991.

[Lil26] J. E. Lilienfeld, Method and apparatus for controlling electric current, *US Patent no. 1,745,175*, 1926.

[Liu17a] X. Liu, W. Guo, Y. Wang, L. F. Wei, C. M. McKenney, B. Dober, T. Billings, J. Hubmayr, L. S. Ferreira, M. R. Vissers, and J. Gao, Cryogenic LED pixel-to-frequency mapper for kinetic inductance detector arrays, *J. Appl. Phys.*, **122**, 034502, 2017.

[Liu17b] X. Liu, Y. Wang, M. Dai, L. F. Wei, B. Dober, C. M. McKenney, G. C. Hilton, J. Hubmayr, J. E. Austermann, J. N. Ullom, J. Gao, and M. R. Vissers, Superconducting micro-resonator arrays with ideal frequency spacing and extremely low frequency collision rate, *Appl. Phys. Lett.*, **111**, 252601, 2017.

[Man21a] F. Mantegazzini, Development and characterisation of high-resolution metallic magnetic calorimeter arrays for the ECHo neutrino mass experiment, Phd thesis, Kirchhoff-Institut für Physik, Universität Heidelberg, 2021.

[Man21b] F. Mantegazzini, S. Allgeier, A. Barth, C. Enss, A. Ferring-Siebert, A. Fleischmann, L. Gastaldo, R. Hammann, D. Hengstler, S. Kempf, D. Richter, D. Schulz, D. Unger, C. Velte, and M. Wegner, Multichannel read-out for arrays of metallic magnetic calorimeters, *JINST*, **16**, P08003, 2021.

[Man22] F. Mantegazzini, A. Barth, H. Dorrer, C. Düllmann, C. Enss, A. Fleischmann, R. Hammann, S. Kempf, T. Kieck, N. Kovac, C. Velte, M. Wegner, K. Wendt, T. Wickenhäuser, and L. Gastaldo, Metallic magnetic calorimeter arrays for the first phase of the ECHo experiment, *Nuclear Instruments and Methods in Physics Research Section A: Accelerators, Spectrometers, Detectors and Associated Equipment*, **1030**, 166406, 2022.

[Mar02] E. D. Marquardt, J. P. Le, and R. Radebaugh, Cryogenic Material Properties Database, in R. G. Ross (Ed.), *Cryocoolers 11*, Springer, Boston, MA, 2002.

[Mat58] D. C. Mattis and J. Bardeen, Theory of the anomalous skin effect in normal and superconducting metals, *Phys. Rev.*, **111**(2), 412, 1958.

[Mat11] J. A. B. Mates, The Microwave SQUID Multiplexer, PhD Thesis, University of Colorado, 2011.

[Mat12] J. A. B. Mates, K. D. Irwin, and L. R. t. Vale, Flux-Ramp Modulation for SQUID Multiplexing, *J Low Temp Phys*, **167**, 707–712, 2012.

[Mat17] J. A. B. Mates, D. T. Becker, D. A. Bennett, B. J. Dober, J. D. Gard, J. P. Hays-Wehle, J. W. Fowler, G. C. Hilton, C. D. Reintsema, and D. R. t.

Schmidt, Simultaneous readout of 128 x-ray and gamma-ray transition-edge microcalorimeters using microwave SQUID multiplexing, *Appl. Phys. Lett.*, **111**(6), 062601, 2017.

[Mat19] J. A. B. Mates, D. T. Becker, D. A. Bennett, B. J. Dober, J. D. Gard, G. C. Hilton, D. S. Swetz, L. R. Vale, and J. N. Ullom, Crosstalk in microwave SQUID multiplexers, *Appl. Phys. Lett*, **115**, 202601, 2019.

[Maz04] B. A. Mazin, Microwave Kinetic Inductance Detectors, PhD Thesis, California Institute of Technology, 2004.

[McK19] C. M. McKenney, J. E. Austermann, J. Beall, B. Dober, S. M. Duff, J. Gao, G. C. Hilton, J. Hubmayr, D. Li, J. N. Ullom, J. Van Lanen, and M. R. Vissers, Tile-and-trim micro-resonator array fabrication optimized for high multiplexing factors, *Rev. Sci. Instrum.*, **90**, 023908, 2019.

[McR20] C. R. H. McRae, H. Wang, J. Gao, M. R. Vissers, T. Brecht, A. Dunsworth, D. P. Pappas, and J. Mutus, Materials loss measurements using superconducting microwave resonators, *Rev. Sci. Instrum.*, **91**(9), 091101, 2020.

[Mor16] K. M. Morgan, B. K. Alpert, D. A. Bennett, E. V. Denison, W. B. Doriese, J. W. Fowler, J. D. Gard, G. C. Hilton, K. D. Irwin, and Y. I. Joe *et al.*, Codedivision-multiplexed readout of large arrays of TES microcalorimeters, *Appl. Phys. Lett.*, **109**(11), 112604, 2016.

[Nei21] M. Neidig, Nachbearbeitung und Messung des Übersprechens von Mikrowellen-SQUID-Multiplexern, Master's thesis, Kirchhoff-Institut für Physik, Universität Heidelberg, 2021.

[Nie10] M. D. Niemack, J. Beyer, H. M. Cho, W. B. Doriese, G. C. Hilton, K. D. Irwin, C. D. Reintsema, D. R. Schmidt, J. N. Ullom, and L. R. Vale, Code-division SQUID multiplexing, *Appl. Phys. Lett.*, **96**(16), 163509, 2010.

[Nis07] A. O. Niskanen, K. Harrabi, F. Yoshihara, Y. Nakamura, S. Lloyd, and J. S. Tsai, Quantum coherent tunable coupling of superconducting qubits, *Science*, **316**, 723–726, 2007.

[Nog19] T. Noguchi, A. Dominjon, M. Kroug, S. Mima, and C. Otani, Characteristics of Very High Q Nb Superconducting Resonators for Microwave Kinetic Inductance Detectors, *IEEE Trans. Appl. Supercond.*, **29**(5), 1–5, 2019.

[Nor13] O. Noroozian, J. A. B. Mates, D. A. Bennett, J. A. Brevik, J. W. Fowler, J. Gao, G. C. Hilton, R. D. Horansky, K. D. Irwin, and Z. Kang *et*

al., High-resolution gamma-ray spectroscopy with a microwave-multiplexed transition-edge sensor array, *Appl. Phy. Lett.*, **103**(20), 202602, 2013.

[Obe20] J. Obermeyer, Automatization of the characterization and trimming of microwave SQUID multiplexers based on lumped-element microwave resonators, Bachelor's thesis, Kirchhoff-Institut für Physik, Universität Heidelberg, 2020.

[Pal19] P. Paluch, Entwicklung, Herstellung und Charakterisierung von auf supraleitenden Mikrowellenresonatoren aus planaren, konzentrierten Elementen basierenden Resonatorarrays und eines Mikrowellen-SQUID-Multiplexers, Master's thesis, Kirchhoff-Institut für Physik, Universität Heidelberg, 2019.

[Pob92] F. Pobell, Matter and Methods at Low Temperatures, Springer Berlin Heidelberg New York, 1992.

[Por14] J.-P. Porst, S. R. Bandler, J. S. Adams, M. A. Balvin, S. E. Busch, M. E. Eckart, R. L. Kelley, C. A. Kilbourne, S. J. Lee, and P. C. Nagler *et al.*, Characterization and performance of magnetic calorimeters for applications in X-ray spectroscopy, *J. Low Temp. Phys.*, **176**(5), 617—623, 2014.

[Poz98] D. M. Pozar, Microwave Engineering, John Wiley & Sons Inc., 1998.

[Pro15] S. Probst, F. B. Song, P. A. Bushev, A. V. Ustinov, and M. Weides, Efficient and robust analysis of complex scattering data under noise in microwave resonators, *Rev. Sci. Instrum.*, **89**, 024706, 2015.

[Ric21] D. P. Richter, Multikanal-Auslesung von metallischen magnetischen Kalorimetern mittels eines vollständigen Mikrowellen-SQUID-Multiplexer-Systems, PhD Thesis, Kirchhoff-Institut für Physik, Universität Heidelberg, 2021.

[Ryh89] T. Ryhänen, H. Seppä, R. Ilmoniemi, and J. Knuutila, SQUID magnetometers for low-frequency applications, *Journal of Low Temperature Physics*, **76**(5), 287–386, 1989.

[San19] O. Sander, N. Karcher, O. Krömer, M. Kempf, S. an Wegner, C. Enss, and M. Weber, Software-Defined Radio Readout System for the ECHo Experiment, *IEEE Trans. Nucl. Sci.*, **66**, 1204–1209, 2019.

[Sch21] D. Schulz, Development and characterization of MOCCA, a 4k-pixel molecule camera for the energy-resolved detection of neutral molecule fragments, PhD Thesis, Kirchhoff-Institut für Physik, Universität Heidelberg, 2021.

[Sid05] I. Siddiqi, R. Vijay, F. Pierre, C. M. Wilson, L. Frunzio, M. Metcalfe, C. Rigetti, R. J. Schoelkopf, M. H. Devoret, D. Vion, and D. Esteve, Direct Observation of Dynamical Bifurcation between Two Driven Oscillation States of a Josephson Junction, *Phys. Rev. Lett.*, **94**, 027005, 2005.

[Sik20] T. Sikorsky, J. Geist, D. Hengstler, S. Kempf, L. Gastaldo, C. Enss, C. Mokry, J. Runke, C. Düllmann, P. Wobrauschek, K. Beeks, V. Rosecker, J. Sterba, G. Kazakov, T. Schumm, and A. Fleischmann, Measurement of the ^{229}Th Isomer Energy with a Magnetic Microcalorimeter, *Phys. Rev. Lett.*, **125**, 2020.

[Sim01] R. N. Simons, Coplanar Waveguide Circuits. Components, and Systems, Wiley-Interscience, 2001.

[Smi95] D. R. Smith and F. R. Ficket, Low-temperature properties of silver, *J. Res. Natl. Inst. Stand. Technol.*, **100**(2), 119–171, 1995.

[Weg18a] M. Wegner, Entwicklung, Herstellung und Charakterisierung eines auf metallischen magnetischen Kalorimetern basierenden Detektorarrays mit 64 Pixeln und integriertem Mikrowellen-SQUID-Multiplexer, PhD Thesis, Kirchhoff-Institut für Physik, Universität Heidelberg, 2018.

[Weg18b] M. Wegner, N. Karcher, O. Krömer, D. Richter, F. Ahrens, O. Sander, S. Kempf, M. Weber, and C. Enss, Microwave SQUID Multiplexing of Metallic Magnetic Calorimeters: Status of Multiplexer Performance and Room-Temperature Readout Electronics Development, *J. Low. Temp. Phys.*, **193**, 462–475, 2018.

[Weg21] M. Wegner, S. Kempf, and C. Enss, Analytical model of the readout power and SQUID hysteresis parameter dependence of the resonator characteristics of microwave SQUID multiplexers, *preprint*, doi:10.1088/1361-6668/ac6d15, 2021.

[Wil16] H. Wilckens, Untersuchung des Einflusses von Diskontinuitäten in den Masseflächen auf die Güte supraleitender, koplanarer Resonatoren, Bachelor's thesis, Kirchhoff-Institut für Physik, Universität Heidelberg, 2016.

[Won11] Y. Y. Wong, Neutrino mass in cosmology: status and prospects, *Ann. Rev. Nucl. Part. Sci.*, **61**, 69–98, 2011.